TESIS DE LA UNIVERSIDAD DE ZARAGOZA

2013

66

Clara Cuesta Soria

ANAIS-0: Feasibility study for a 250 kg NaI(Tl) dark matter search experiment at the Canfranc Undreground Laboratory

Departamento
Física Teórica

Director/es
Sarsa Sarsa, María Luisa

ISSN 2254-7606

Prensas de la Universidad
Universidad Zaragoza

Universidad Zaragoza
1542

Tesis Doctoral

ANAIS-0: FEASIBILITY STUDY FOR A 250 KG NAL (TI) DARK MATTER SEARCH EXPERIMENT AT THE CANFRANC UNDREGROUND LABORATORY

Autor

Clara Cuesta Soria

Director/es

Sarsa Sarsa, María Luisa

UNIVERSIDAD DE ZARAGOZA

Física Teórica

2013

ANAIS-0: Feasibility study for a 250 kg NaI(Tl) dark matter search experiment at the Canfranc Underground Laboratory

Memoria presentada por
Clara Cuesta Soria
para optar al grado de
Doctora en Física

Laboratorio de Física Nuclear y Astropartículas
Departamento de Física Teórica
Área de Física Atómica, Molecular y Nuclear
Universidad de Zaragoza

Marzo 2013

Contents

Chapter 1

Introduction

WMAP has measured the cosmological parameters with an impressive and unprecedented accuracy (section 1.1) supporting the standard cosmological model: a flat Universe, in accelerated expansion, and presently dominated by a 72% of dark energy over a 28% of matter. Despite the success of the model, many unknowns still remain, in particular, a new kind of matter, beyond the standard model of particle physics, should compose most of the Universe matter. A generic denomination for a broad sort of dark matter particle candidates is WIMPs: Weakly Interacting Massive Particles (section 1.2).

In order to know more about the dark matter nature, different experimental strategies have been applied to detect it (section 1.3). Products of the dark matter annihilation in the galactic halos or galaxy clusters could indirectly identify the dark matter, while direct detection experiments look for the interactions of the the dark matter particles with the nuclei of a convenient detector. The DAMA/LIBRA experiment has claimed a positive result with a very high confidence level ($8.9\,\sigma$) using NaI(Tl) as target and by searching the expected annual modulation in the interaction rate for 13 annual cycles (section 1.3.2). However, other very sensitive experiments, using different targets, claim to have ruled out most of the compatible WIMP parameter space.

The ANAIS (Annual Modulation with NaI(Tl) Scintillators) experiment aims at the confirmation of the DAMA/LIBRA signal using the same target and technique at the Canfranc Underground Laboratory (section 1.4). 250 kg of ultrapure NaI(Tl) crystals will be used as a target, divided into 20 modules, each coupled to two photomultipliers and inside an adequate shielding to minimize the contribution to the background from environmental radioactivity. The main experimental goals are: a very low background, low energy threshold, and very stable operating conditions.

1.1 Understanding of the Universe

The human interest for the Universe is common to all ages and cultures. Nevertheless, only very recently, cosmology has become a scientific issue, being able to confront data and theory. Several major changes in our understanding of the Universe can be reported, the first theories considered humans, and hence the Earth, as the center of the Universe, whereas at the moment, neither our place, nor even the matter we are made of plays a significant role.

The Copernican Revolution, supposed a shift from geocentric to heliocentric Universe model. Then, also the Sun was found to be out of the center of the Universe. Over the next two hundred years, it became increasingly understood that the nearby stars are not evenly distributed, but rather located in a disk-shaped assembly which we know now as the Milky Way galaxy. Besides, other galaxies were discovered, and we found that ours is not special in the Universe. The shift to the modern cosmology stems from the Einstein Theory of Relativity and comes up to the present precision cosmology era [1], thanks to specially designed very sensitive instruments, launched to space or based in Earth, able to measure cosmologically relevant magnitudes, that confronted with the standard cosmological model allow to derive high accuracy estimates of the different parameters of the model [2, 3].

1.1.1 The Standard Cosmological Model

Cosmology aims to obtain a physical description of the Universe, including its global dynamics and matter content; to measure the cosmological parameters describing the Universe, and to develop a fundamental understanding of as many of these parameters as possible; to understand the origin and evolution of cosmic structures and to probe the physics of the early Universe. An outstanding feature of the Universe is that it is expanding. First evidence of an expanding Universe came from Hubble. In 1929, he found out that galaxies move away with a velocity v which is directly proportional to its distance from us, r; this is known as Hubble's law:

$$v = H_0 r \tag{1.1}$$

The constant of proportionality H_0 is known as Hubble's constant. Hubble's law is not exact, but it describes extremely well the average behavior of all galaxies. In this expanding Universe everything is moving away from everything else, implying that in the

past everything was much closer together: the Universe was smaller and, then, hotter, till the initial instant, the Big Bang. We call Big Bang Cosmology [4] to a model of Universe evolution incorporating all these features. The Big Bang cosmology implies the Universe is an evolving entity, unlike other theories, as the Steady State Universe, which hold the Universe looked the same forever, with new material filling the gaps as the Universe expands. Observational support to Big Bang theory was overwhelming (see section 1.1.2).

The idea that the Universe should be homogeneous and isotropic, and hence all spatial positions essentially equivalent, led to the to the formulation of the Cosmological Principle in which have been based most of the past and present cosmological models. The cosmological principle is therefore a property of the global Universe, breaking down if one looks at local phenomena. Because of that, although the smoothness of the matter distribution on large scales has been a key assumption of cosmology for decades, it is only recently that it is at our hand convincing observational demonstration.

In the Standard Cosmological model [5–8], the overall geometry and evolution of the Universe are described in terms of two cosmological parameters: the spatial curvature and the expansion (or contraction) of the Universe. These two parameters appear in the Robertson-Walker metric as k and $a(t)$, respectively:

$$ds^2 = g_{\mu\nu}dx^\mu dx^\nu = -dt^2 + a^2(t)\left[\frac{dr^2}{1-kr^2} + r^2(d\theta^2 + \sin^2\theta d\phi^2)\right] \tag{1.2}$$

With a suitable definition of the units of r, in the above expression the curvature constant can be considered to have only three possible values: $k = 0$ for a spatially flat Universe, $k = 1$ for a closed Universe and $k = -1$ for an open Universe. The cosmological equations describing the evolution of the Universe are derived from the Einstein´s equations:

$$R_{\mu\nu} - \frac{1}{2}g_{\mu\nu}R = 8\pi G T_{\mu\nu} + \Lambda g_{\mu\nu} \tag{1.3}$$

being $R_{\mu\nu}$ the Ricci tensor, $R = g^{\mu\nu}R_{\mu\nu}$ the Ricci scalar and $T_{\mu\nu} = (p+\rho)u_\mu u_\nu + p g_{\mu\nu}$ the energy-momentum tensor, and Λ the cosmological constant, like an energy density of the vacuum and below referred to as dark energy. From here, taking $g^{\mu\nu}$ the Robertson-Walker metric and assuming the matter content of the Universe as a perfect fluid, the Friedmann equations are obtained:

$$\left(\frac{\dot{a}}{a}\right)^2 = \frac{8\pi G\rho}{3} - \frac{k}{a^2} \qquad \frac{\ddot{a}}{a} = -\frac{4\pi G}{3}(\rho + 3p) \tag{1.4}$$

with ρ the total matter and energy density of the Universe. Hubble's parameter is $\left(\frac{\dot{a}}{a}\right) = H(t)$ and its present value $H(t_0) = H_0$. Contributions to this density coming from matter, radiation and dark energy, with $\rho_\Lambda = \frac{\Lambda}{8\pi G}$, imply different solutions to Friedmann equations. The temporal evolution of the density can be derived from them:

$$\dot{\rho} = -3\frac{\dot{a}}{a}(\rho + p) \tag{1.5}$$

Matter, radiation, dark energy and any other component (i) of the energy density of the Universe, considered as an ideal fluid, having energy density (ρ_i) and pressure (p_i) related by the state equation $p_i = \omega\rho_i$, evolves differently, contributing at any time of the Universe evolution as:

$$\rho(t) \propto a(t)^{-3(\omega+1)} \tag{1.6}$$

For matter $\omega = 0$, for radiation $\omega = 1/3$ and for dark energy there are two different models: $\omega = -1$, which corresponds to a cosmological constant, or, more generally, any $\omega < -1/3$ (sometimes called quintessence), where it is even possible a dependence $\omega(t)$.

A critical density, ρ_c, can be defined from the Friedman equations that corresponds to $k = 0$ if $\Lambda = 0$. An adimensional parameter Ω_i can be built for each contribution to the Universe energy:

$$\rho_c = \frac{3H_0^2}{8\pi G} \qquad \Omega_i = \frac{\rho_i}{\rho_c} \tag{1.7}$$

Also the curvature can be considered as a contribution to the density, $\rho_k = -\frac{3}{8\pi G}\frac{k}{a^2}$, being for this case $\sum \Omega_i = 1$. However, it has to be stressed that this is not a real contribution to the Universe energy.

To complete the model, structure formation scenario has to be provided: this is done by the perturbed FRW model. Initial density fluctuations could be generated, for instance, by a period of inflationary expansion. There is broad consensus that the Standard Cosmological Model gives an excellent description of the observed data. A suitable baseline cosmological model to consider is the simplest one giving an adequate fit to current data.

It is a spatially-flat adiabatic ΛCDM model with six fundamental parameters described in next section.

1.1.2 Cosmological parameters

During the last twenty years, precision measurements of the fluctuations of the cosmic microwave background (CMB) radiation have allowed to compare cosmological models with observational data in order to fit the cosmological parameters of the model with high accuracy. When the temperature of the Universe fell down to $3 \cdot 10^6$ K, neutral atoms could form: the Universe changed from a plasma opaque to photons to be transparent for them, as their energy was not able to ionize hydrogen atoms. After this photon decoupling, radiation traveled freely, filling the Universe, and being redshifted by the expansion. The CMB radiation was discovered in 1965 by Penzias and Wilson and was soon identified as that radiation left over from an early stage in the development of the Universe (about 380,000 years after the Big Bang). This discovery was a benchmark to accept the Big Bang model. This radiation follows a black-body spectrum, and corresponds nowadays to a temperature of 2.72548 ± 0.00057 K [9].

Very specific and sensitive instruments have been searching for the fluctuations in this radiation, measuring them with increasing accuracy. COBE (Cosmic Background Explorer) satellite, developed by NASA, was the first satellite built to be devoted to cosmological studies. It was able to measure by the first time the small fluctuations of the CMB, less than 1 part in 10000, corresponding to the density inhomogeneities in the Universe at the photon decoupling time. These fluctuations, acting as seeds, grew after to become galaxies. COBE was launched in 1989 and the mission lasted 4 years. WMAP (Wilkinson Microwave Anisotropy Probe) is the successor instrument, also from NASA. It was launched in 2001 and orbits at 1.5 million km from the earth and has been taken data up to 2010. Final data have been already presented [10], corresponding to the total 9 years observation period, see Figure 1.1, enabling to test the different cosmological models and delivering very precise estimates of their parameters. Planck satellite from ESA was launched in 2009, and its main objective is also to measure the fluctuations of the CMB with a better detail. Only preliminary data from Planck [11] have been presented, and results are expected to be released soon.

Measurements of temperature and polarization anisotropy in the CMB have played a major role in establishing the standard ΛCDM model of cosmology: a six-parameter model based on a flat universe, dominated by a cosmological constant, Λ, and cold dark matter (CDM), with initial gaussian, adiabatic fluctuations seeded by inflation. Figure 1.2

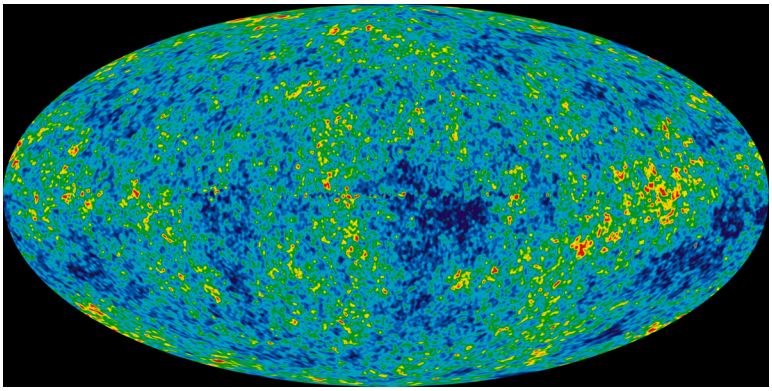

Figure 1.1: *The detailed all-sky picture of the infant Universe created from nine years of WMAP data. The image reveals 13.7 billion year old temperature fluctuations (shown as color differences) that correspond to the density inhomogeneities acting as seeds, that grew to become the galaxies. The signal from our Galaxy was subtracted using the multi-frequency data. The image shows a temperature range of* $\pm 0.2\,mK$ *[12]. The Figure has been taken from [10]*

shows the comparison between the measured power spectrum of the CMB temperature anisotropy and the predictions of the ΛCDM cosmological model fitted with WMAP data, in terms of the angular scale (or multipole moment).

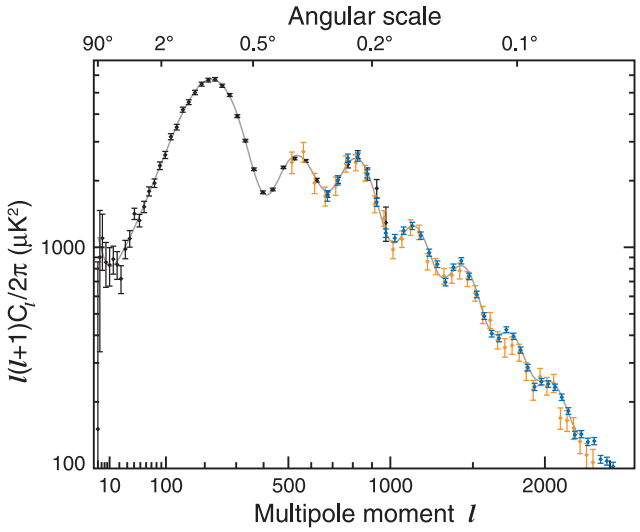

Figure 1.2: *A compilation of the CMB data used in the nine-year WMAP analysis. The WMAP data are shown in black, the extended CMB data set includes South Pole Telescope data in blue [13], and Atacama Cosmology Telescope data in orange, [14]. The* ΛCDM *model fit to the WMAP data alone (grey) successfully predicts the higher-resolution data. The Figure has been taken from [10].*

In Table 1.1, the six parameters obtained from the ΛCDM fit of the nine-year WMAP observations are shown, together with some of the parameters derived from them [10, 12]. Observational data supports a flat Universe, $\Omega_k = 0$. The six basic cosmological

parameters are: baryon density times h^2, where $H_0 = 100h\,\mathrm{km/s/Mpc}$; the CDM density times h^2; the dark energy density; the curvature perturbations amplitude (Δ^2_R) and the spectral index of the corresponding power law (n_s) are required to include a description of deviations from homogeneity; and finally, the ionization optical depth, τ, related with the probability that a given microwave photon scatters with ionized electrons in the interstellar medium, disturbing then the anisotropies pattern [15].

Curvature perturbations and the density perturbations spectral index have been measured as a complete model of the Universe should include a description of deviations from homogeneity, at least in a statistical way [16]. The universe is in accelerated expansion at present $\Omega_\Lambda = 0.72$, and with a matter content of only $\Omega_m = 0.28$, being negligible the present contribution from the radiation ($\Omega_{rad} \approx 10^{-4}$) to the universe energy content.

Parameter	Symbol	WMAP data
Fit parameters:		
Baryon density ($\times h^2$)	$\Omega_b h^2$	0.02264 ± 0.00050
Cold dark matter density ($\times h^2$)	$\Omega_c h^2$	0.1138 ± 0.00045
Dark energy density	Ω_Λ	0.721 ± 0.025
Curvature perturbations	$10^9 \Delta^2_R$	2.41 ± 0.10
Density perturb. spectral index	n_s	0.972 ± 0.013
Ionization optical depth	τ	0.089 ± 0.014
Derived parameters:		
Age of the Universe	t_0	$13.74 \pm 0.11\,\mathrm{Gyr}$
Hubble parameter	H_0	$70.0 \pm 2.2\,\mathrm{km/s/Mpc}$
Matter density	Ω_m	0.279 ± 0.025
Cold dark matter density	Ω_c	0.233 ± 0.023
Baryon density	Ω_b	0.0463 ± 0.0024

Table 1.1: *Some of the cosmological parameters derived from the WMAP measurements, obtained from [10].*

1.2 Dark matter need

If we center our interest in the matter content of the Universe, it is easily found out that it is much higher than the baryon (neutrons and protons) density predicted by the Big Bang nucleosynthesis [17] and confirmed by WMAP data, $\Omega_b = 0.0463 \pm 0.0024$ [10]. This implies the existence of other kind of matter, which neither emits nor absorb electromagnetic radiation, and represents an important contribution to the Universe density, $\Omega_c = 0.233 \pm 0.023$ [10].

A modification or replacement of Einstein's relativistic theory of gravity with some new, but not yet found, alternative could also solve the dark matter and, even, the dark energy issue, making unnecessary the introduction of further ingredients in the Universe content. However debate on this issue continues, the scientific community is more favorable to the dark matter hypothesis.

1.2.1 Dark matter evidences

First observational evidence of the existence of dark matter in spiral galaxies go back till goes back till 1975, when Vera Rubin was measuring galactic rotation curves. According to Newtonian dynamics, the rotation speed of the bodies bound to a mass distribution $M(r)$, assuming spherical symmetry, should show the following dependence in r:

$$v_{rot}^2(r) = \frac{GM(r)}{r} \tag{1.8}$$

with G the Newton gravitational constant and $M(r)$ the mass content in the sphere with radius r. However, Vera Rubin observed that rotation curves in the outskirts of the galaxies, where $M(r)$ should be constant, did not decrease with r, but reached an almost constant value [18]. This implied that the galactic mass distribution did not follow the visible mass distribution. Figure 1.3 shows two examples of her observations. Afterwards, many other galactic rotation curves were measured, obtaining similar results, as shown in [19]. The existence of a dark matter halo, extending much farther than the visible galaxy is the more extended explanation of these rotation curves.

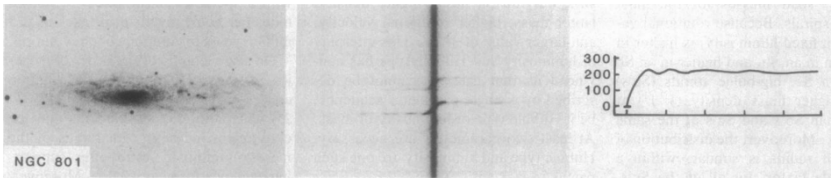

(a)

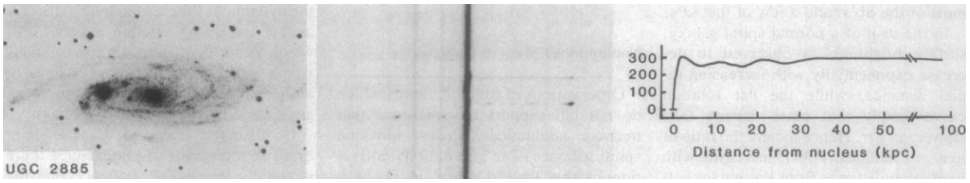

(b)

Figure 1.3: *Spectra and derived rotation curves for galaxies NGC 801 (a) and UGC 2885 (b). The curves at the right show the rotational velocities as a function of the distance to the galactic center, measured from the Doppler shift in the emission lines in the spectra. Images obtained from [18].*

In the galaxy cluster scale, many other observational evidences have accumulated since Zwicky used the virial theorem to infer the existence of unseen matter in the Coma galaxy cluster en 1933 [20]. He was the first to refer to such a matter as *dunkle Materie*. For instance, the gravitational lensing effect: the image of a far galaxy is distorted by a gravitational field generated by a very massive cluster, located between the telescope and the galaxy. The analysis of these images allows to determine the mass distribution of the interposed object, giving as general result much higher cluster masses than those estimated from the luminosity. Moreover, X-ray measurements reveal that the temperatures of the hot gas observed in the galaxy clusters can not be explained with the gravitational field caused by the visible matter of the clusters. Same argument would prevent clusters from being stable structures given the high velocities observed for the galaxies they contain.

The Bullet cluster has provided very robust arguments for the existence of dark matter and about its nature, see Figure 1.4. This cluster consists of two large colliding clusters of galaxies, one of the most energetic events known in the Universe since the Big Bang [21]. Hot gas detected by Chandra by the X-rays emissions is shown as two pink clumps in the image and traces the distribution of most of the baryonic matter. The bullet-shaped clump on the right is the hot gas from one cluster, which passed through the hot gas from the other larger cluster during the collision. An optical image from Magellan and the Hubble Space Telescope shows the galaxies in orange and white. The blue areas in this image depict where astronomers find most of the mass in the clusters, traced by the gravitational lensing analysis previously explained. The combination of information derived from observations using three different techniques evidenced a spatial offset of the center of the total mass distribution (blue) from the center of the baryonic mass peaks (pink), whereas the galaxies follow the total mass distribution. This is explained by the slowing down of the hot gas during the collision by a drag force, due to the electromagnetic interaction. If most of the invisible matter of the cluster was not slowed down, it should be collisionless matter: it can only interact gravitationally or very weakly. Therefore, during the collision the dark matter clumps from the two clusters moved ahead of the hot gas, without hindrance, producing the separation of the dark and normal matter seen in the image.

Observations of other galaxy cluster collisions, such as MACS J0025.4-1222, also show significant displacement between their hot gas distribution centers and their gravitational potential. However, there are other examples, like the merging galaxy cluster Abell 520, shown in Figure 1.5, formed by a violent collision of very massive clusters: dark matter, galaxies and hot gas distribution are shown [22]. Superimposed on the natural-color image

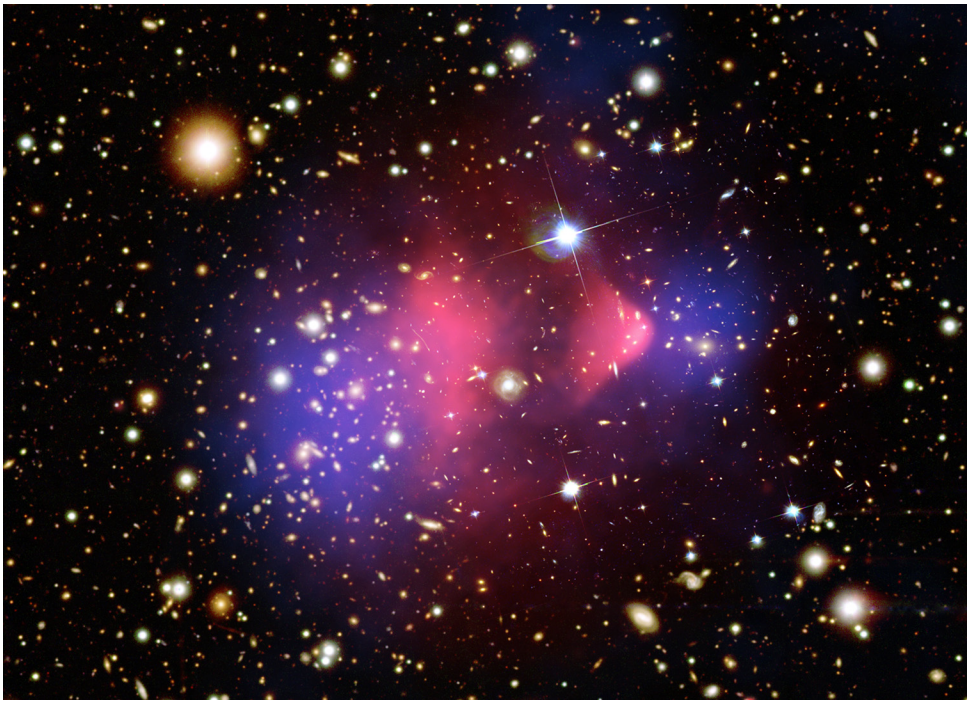

(a)

Figure 1.4: *This composite image shows the galaxy cluster 1E 0657-556, also known as the Bullet cluster. Hot gas detected by Chandra in X-rays is seen as two pink clumps in the image and contains most of the baryonic matter in the two clusters. The bullet-shaped clump on the right is the hot gas from one cluster, which passed through the hot gas from the other larger cluster during the collision. An optical image from Magellan and the Hubble Space Telescope shows the galaxies in orange and white. The blue areas depict where astronomers find most of the mass in the clusters. The concentration of mass is determined by analyzing the effect of gravitational lensing. Image obtained from [21].*

of galaxies are false-colored maps: in orange the starlight from galaxies (as detected by the Canada-France-Hawaii Telescope), in green hot gas (as detected by NASA's Chandra X-ray Observatory), and in blue the location of most of the mass in the cluster, which is dominated by dark matter. The dark matter map was derived from the Hubble Wide Field Planetary Camera 2 observations by gravitational lensing [22]. The dark matter is concentrated into a dark core containing far fewer galaxies than would be expected if the dark matter and galaxies mass distributions follow each other. Most of the galaxies apparently have sailed far away from the collision. This result could present a challenge to basic theories of dark matter, which predict that galaxies should be anchored to the invisible substance, even during the shock of a collision.

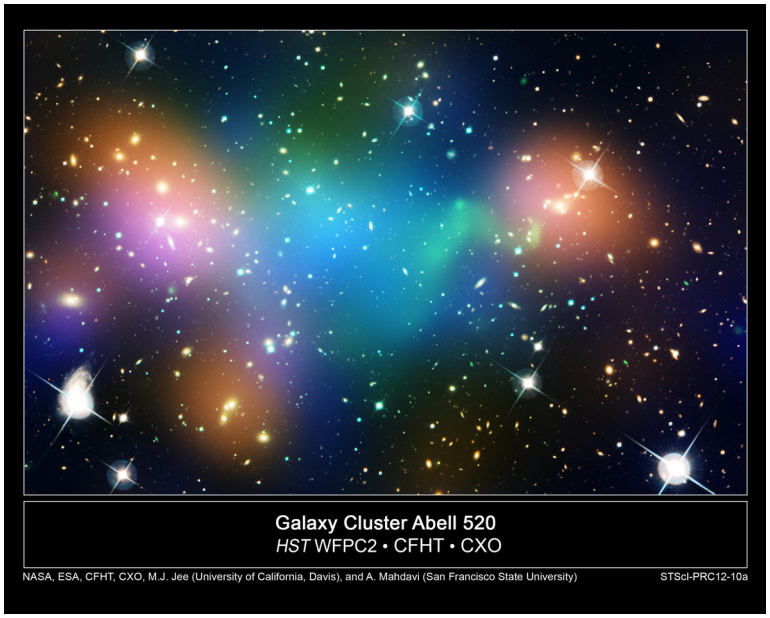

Figure 1.5: *Composite image showing the distribution of dark matter (blue), galaxies (orange), and hot gas (green) in the core from the Abell 520 galaxy cluster, formed from a violent collision of massive galaxy clusters. The blend of blue and green in the center of the image reveals that a clump of dark matter resides near most of the hot gas, where very few galaxies are found. Image obtained from [22].*

1.2.2 Dark matter candidates

In order to explain all the accumulated observational evidences from galaxy and galactic clusters dynamics, visible matter, baryonic content, cosmological data at large scales, etc. a very special kind of particle is required: stable (or very long lived, in the cosmological timescale), interacting only weakly with matter, non-relativistic at the decoupling moment, neutral and massive. Looking at the Standard Model of Particle Physics, only neutrinos fulfill partially these requirements, but they were relativistic at the decoupling moment, and they would not have been able to produce as much small scale structure in the universe as we observe.

Strong hints at physics beyond the Standard Model have been found. In some of those scenarios, compelling dark matter candidates appear [23–25]. In particular, a new particle, the axion, was postulated in 1977 by Peccei and Quinn to solve the CP conservation problem in QCD (quantum chromodynamics). Axion-like particles have become interesting dark matter candidates and are being searched for by different experimental strategies. However, the axion can only explain the dark matter if its mass is tuned in a small range of values. The supersymmetric (SUSY) extension of the Standard Model provides good dark matter candidates, although in a very model dependent way. SUSY

extensions are an appealing concept because of their remarkable properties, for example, with respect to gauge coupling unification, to solve the hierarchy problem, and the embedding of gravity. As superpartners of the Standard Model particles, new particles appear including fields that are electrically and color neutral. Since they have not been detected at particle accelerators, these sparticles must be heavy and/or extremely weakly interacting. In particular, the ligthest neutralino, the gravitino or the axino could be the Lightest Supersymmetric Particle, stable in many SUSY models, able to explain the non-baryonic dark matter. The neutralino is part of the Minimal Supersymmetric Standard Model which provides a solution to the hierarchy problem and allows for gauge coupling unification. Being the superpartner of the graviton and the gauge field associated with supergravity, the gravitino is equally well motivated with a mass that reflects the SUSY breaking scale. As the superpartner of the axion, also the axino appears naturally once the strong CP problem is solved with the Peccei-Quinn mechanism in a SUSY setting.

The fact that neutrinos have mass is suggestive of the existence of right-handed, gauge singlet sterile neutrinos, which may constitute also dark matter if their masses are small. It is worth noting that the number of particles types contributing to dark matter is unknown and it does not restrict to one single. In general, dark matter candidates in a model independent way can be referred to as WIMPs, acronym for Weakly Interacting Massive Particles.

These particles beyond the standard model of particle physics could be produced in accelerators [26], like the LHC, and many information about the nature of the dark matter could be obtained, because such a finding would imply new physics below the TeV scale. However, at the moment the data collected in pp collisions at $\sqrt{s} = 7\,\text{TeV}$ analyzed by the CMS [27, 28] and ATLAS [29] collaborations, corresponding to integrated luminosities of $5.0\,fb^{-1}$ and $4.6\,fb^{-1}$, respectively, do not show hints for new phenomena. As good agreement is observed between the data and the standard model predictions, the results are translated into exclusion limits on pair production of weakly interacting dark matter candidates.

1.3 Dark matter detection

Although a large amount of dark matter is required to explain the observations of the universe at different scales, deciphering the nature of these particles is a challenge for astrophysics, cosmology, particle and nuclear physics. There are different approaches to detect the elusive dark matter particle and several experiments have been designed

with such a goal. In the direct detection ones, the scattering of the WIMPs off a target nucleus in a convenient detector material is searched for, whereas in the indirect detection experiments the products of the WIMP annihilation are studied.

1.3.1 Indirect dark matter detection

The self-annihilation of WIMP particles in astronomical objects may leave observable imprints in several components of the cosmic rays. WIMPs are expected to annihilate efficiently in regions where they accumulate, such as the center of galactic halos or substructures as dwarf galaxies, because the annihilation rate depends on the square of the dark matter particles number density. Once they annihilate, they produce secondary particles, like quarks and gauge bosons, which subsequently fragment and decay in photons, protons, antiprotons, electrons, positrons and neutrinos. The typical energy of these final states is about a tenth of the dark matter particle mass, so to search indirectly for dark matter, an excess of photons (gamma rays), antimatter (positrons and antiprotons) or neutrinos in astrophysical data at energies between 1 GeV and 10 TeV have to be searched for. These experiments are complex instruments devoted to study gamma rays, cosmic rays or neutrinos and the study of dark matter is usually a byproduct of their main goal [30–33].

Gamma rays play an outstanding role among the possible messengers of a dark matter annihilation signal as they propagate almost unperturbed and directly point to their sources, hence, they could give distinctive spatial signatures, as well as sharp spectral signatures, in the case there is a direct annihilation channel to photons (a monoenergetic line at the WIMP mass would be expected) [34]. Gamma rays can be observed directly from space with satellites or indirectly, with ground-based telescopes via the Cherenkov light emitted by the showers of secondary particles produced by the interaction of very high energetic gamma rays hitting the upper part of the atmosphere. The Fermi Gamma-ray Space Telescope was launched in 2008 carrying the Large Area Telescope (LAT). The design life of the mission is 5 years. The LAT is an imaging high-energy gamma-ray telescope covering the energy range from about 20 MeV to more than 300 GeV. The Fermi-LAT collaboration has published upper limits at 95% C.L. from the absence of signal excess between 7 and 200 GeV [35]. However, there are recent claims of an observation of a 130 GeV line near the galactic center [36].

Due to the small area of detectors on satellites, higher energies can be only detected by ground-based Imaging Atmospheric Cherenkov Telescopes (IACTs) as HESS (High Energy Stereoscopic System), MAGIC with regular observations since 2009, and VERITAS, operational since 2007. None of them has found any excess and limits on the self-annihilation

cross section for WIMPS have been presented: by HESS from the Sculptor and Carina dwarf galaxies [37], by MAGIC from the dwarfs Willman [38] and Segue 1 [39], and by VERITAS also from Segue 1 [40], for example. The future Cherenkov Telescope Array (CTA) will provide a significantly improved sensitivity [41].

Positrons or antiprotons excess can be searched with cosmic rays telescopes [42]. The PAMELA (Payload for Anti-Matter Exploration and Light-Nuclei Astrophysics) satellite was launched in 2006, and two years later an excess of positrons was reported by the collaboration, which has been widely discussed [43, 44]. AMS-01 (Alpha Magnetic Spectrometer) confirmed this excess and new results will be released in the next future by the AMS-02 spectrometer which was installed in 2011 in the International Space Station, confirming or not the positron excess detected by PAMELA. Cosmic rays more energetic should be detected via the showers of secondary particles, as it is done from ground in the Pierre Auger Observatory [45] or will be done by JEM-EUSO from the space [46].

Neutrinos can be detected with the IceCube Neutrino Observatory at the geographic South Pole [47], whose construction ended in 2010. Charged particles produced in neutrino interactions in about $1\,\mathrm{km}^3$ of Antarctic ice are detected by the Cerenkov radiation, using a regularly spaced array of 5160 photomultiplier tubes buried between 1450 to 2450 meters of antarctic ice. Other experiment able to detect neutrinos is the ANTARES neutrino telescope, completed in 2008 [48]. It is located at a depth of 2475 m in the Mediterranean Sea, 42 km from the French coast. This detector consists of a tridimensional array of PMTs distributed along twelve detection lines, and is optimized for the detection of muons from high-energy astrophysical neutrinos. Moreover, the Galactic Center is accessible for ANTARES, being in the Northern Hemisphere. An important advantage of neutrino telescopes with respect to other indirect searches is that a potential signal would be very clean, since no other astrophysical explanations could mimic it (like pulsars can do in the case of the positron excess seen by PAMELA). As neutrino interactions are so rare, only the near annihilation sources could generate measurable fluxes: WIMPs gravitationally bound to the Sun or the Earth could produce an excess of neutrinos that could be detected by these experiments. No excess of neutrinos coming from the Sun, nor from the Earth, has been found for the moment

1.3.2 Direct dark matter detection

Detecting dark matter particles is not a simple issue, as it has been explained in section 1.2, they are expected to interact with matter mainly by elastically scattering off nuclei. Small

amounts of energy will be released in the target material in the form of nuclear recoil kinetic energy.

The expected dark matter interaction rate of WIMPs having a mass m_χ in a target consisting of one type of nucleus of mass m_N (and the total detector mass M_{det}) can be calculated as [7]:

$$\frac{dR}{dE_R} = \frac{\rho_0 M_{det}}{m_N m_\chi} \int_{v_{min}}^{v_{max}} v f(v) \frac{d\sigma_{\chi N}}{dE_R}(v, E_R)\, dv \tag{1.9}$$

where ρ_0 is the local WIMP density, $f(v)$ the WIMP speed distribution in the detector reference frame normalized to unity. Both depend on the astrophysical observations, in the Standard Halo Model the halo is described as an isotropic and isothermal sphere of collisionless particles with $\rho_r \propto r^{-2}$ and $f(v)$ Maxwellian in terms of the WIMP velocity in the halo reference frame:

$$f(v) = \frac{1}{\sqrt{v_0^3 \pi^{3/2}}} \exp\left(-\frac{v^2}{v_0^2}\right) \tag{1.10}$$

where v_0 is the most probable speed value, related with the root mean square velocity of such a distribution by $v_{rms} = \sqrt{3/2} v_0$. The differential cross section for the WIMP-nucleus scattering is $\frac{d\sigma_{WN}}{dE_R}(v, E_R)$.

Parameter	Typical value
ρ_0	$0.3\,\mathrm{GeV/cm^3}$
v_{esc}	$544\,\mathrm{km/s}$
v_0	$220\,\mathrm{km/s}$
v_{rms}	$270\,\mathrm{km/s}$
$\nu_\oplus$	$28.9\,\mathrm{km/s}$

Table 1.2: *Typical values used in the calculation of the WIMP interaction rate. Data obtained from [49, 50].*

As WIMP-nucleon relative speed is of order of $100\,km \cdot s^{-1}$, the elastic scattering occurs in the non-relativistic limit, and the recoil energy of the nucleus, depends on the scattering angle θ (calculated in the center of mass reference frame):

$$E_R = \frac{\mu_{\chi N}^2 v^2 (1 - \cos\theta^*)}{m_N} \tag{1.11}$$

with $\mu_{\chi N} = \frac{m_\chi m_N}{(m_\chi + m_N)}$. The lower limit of the WIMP speed integration is $v_{min} = \sqrt{\frac{m_N E_R}{2\mu_{\chi N}^2}}$, the minimum WIMP speed that causes a recoil energy E_R and the upper limit, $v_{max} = v_{esc}$, the maximum WIMP speed to be bound to the Milky Way. Then, the total rate (usually expressed in cpd/kg) is calculated by integrating from the smallest recoil energy that the detector is able to measure, E_T to the maximum recoil energy possible to detect (determined by kinematics):

$$R = \int_{E_T}^{E_{max}} dE_R \frac{\rho_0}{m_N m_\chi} \int_{v_{min}}^{v_{esc}} \vec{v} f(\vec{v}) \frac{d\sigma_{WN}}{dE_R}(v, E_R)\, d\vec{v} \tag{1.12}$$

The WIMP-nucleus differential cross section $\frac{d\sigma_{WN}}{dE_R}$ is computed from the Lagrangian that describes the interaction of a given WIMP with ordinary matter and encodes the particle physics input. In general, it can be separated into a spin independent (SI) and a spin dependent (SD) contribution:

$$\frac{d\sigma_{WN}}{dE_R} = \left(\frac{d\sigma_{WN}}{dE_R}\right)_{SI} + \left(\frac{d\sigma_{WN}}{dE_R}\right)_{SD} = \frac{m_N}{2\mu_{\chi N}^2 v^2}\left(\sigma_{SI} F_{SI}^2(E_R) + \sigma_{SD} F_{SD}^2(E_R)\right) \tag{1.13}$$

where σ_{SI} and σ_{SD} are the SI and SD components of the WIMP-nucleus cross sections at zero momentum transfer, and F_{SI} and F_{SD} are the form factors which account for the finite size of the nucleus, usually important at high momentum transfers. These nuclear point-like cross-sections can be expressed, in quite a general scenario, as:

$$\sigma_{SI} = \frac{4\mu_{\chi N}^2}{\pi}\left[Z f_p + (A - Z) f_n\right]^2 \qquad \sigma_{SD} = \frac{32\mu_{\chi N}^2}{\pi} G_F^2 \frac{J+1}{J}\left[a_p \langle S_p \rangle + a_n \langle S_n \rangle\right]^2 \tag{1.14}$$

where f_p,f_n,a_p, and a_n are the effective WIMP couplings to neutrons and protons in the spin-independent and spin-dependent case, respectively. They can be calculated using an effective Lagrangian of the theoretical model. They depend on the contributions of the light quarks to the mass of the nucleons and on the quark spin distribution within the nucleons, respectively, and on the composition of the dark matter particle. $\langle S_p \rangle$ and $\langle S_n \rangle$ are the expectation values of proton and neutron spin operators in the limit of zero momentum transfer, and must be determined using detailed nuclear model calculations. Usually, in the sensibility plots, SI coupling to protons and neutrons is not distinguished, and it is only consider the total spin-independent cross section; for the SD coupling they should be calculated individually depending on the nucleus considered. In general, in the spin-independent interaction is considered $f_p = f_n$, and then, the cross-sections depend

on the square of the total number of nucleons. The spin-dependent cross section is only different from zero for odd-even nuclei, having non-zero spin in their ground state.

Typical recoil energies released after a WIMP interaction are in the few keV range and can be detected in different forms. When a particle interacts in the detector three types of excitations can be produced: electron-hole or electron-ion pairs (ionization), phonons (heat) and scintillation photons (light). The detectors able to detect the phonons have to operate at low temperatures because, only in the mK temperature range a small energy deposition can produce a measurable temperature increase in a convenient absorber. The detectors sensitive to the scintillation photons use light detectors which can be, for instance, auxiliary bolometers or photomultipliers. In order to measure the ionization signal, an electric field has to be applied to collect the charge. The energy released can also be measured using superheated liquids: an energy deposition can destroy a metastable state, leading to the formation of bubbles, which can be recorded acoustically and optically.

An experiment designed to detect WIMP interactions should fulfill the following criteria [30]:

1. **Low energy threshold.** The spectrum of energy released by WIMPs in the target is almost exponential in shape, without distinctive features (see Figure 1.9). A small threshold improvement can imply a relevant increase in sensitivity. Thresholds lower than 10 keV (nuclear recoil energy) are usual for the dark matter direct detection experiments.

2. **Low radioactive background.** Environmental and intrinsic background contributing to the events rate at low energy should be as low as possible to avoid masking the very rare energy releases attributable to WIMP interactions. The radioactive background is composed by cosmic rays, external background and radioactive isotopes present in the components of the detector itself. Cosmic rays contribution is reduced by working in underground laboratories: hadronic components are easily suppressed by a few m.w.e., but muons are much more penetrating, and hence, the larger the rock overburden, the minor residual muon flux arrives at the laboratory. This residual muon flux produces not only direct events in the detectors, but induces other particles in the shielding or detector materials, as neutrons, that can produce an indirect, and sometimes delayed, signal. The environmental background contribution is prevented with convenient shielding, passive and/or active. A typical shielding will consist of lead and copper very radiopure to stop the gamma parti-

cles from laboratory walls, for instance, and other non low-background laboratory equipment (electronics, etc.). Water and polyethylene are typically used to moderate the neutrons and cadmium to capture them [51, 52]. Active shielding usually work in anticoincidence with the detectors, enabling to reject multiple scattering events: plastic scintillators can be used for instance to tag residual muon events arriving to the experimental layout, but the detector modules can work similarly, as far as WIMP candidates have negligible probability of having more than one interaction in the detector volume. Finally, the detector components have to be chosen in terms of their low radioactivity [53]. The isotopes more typically contributing to the background are: naturally occurring isotopes as ^{40}K and those constituent of the natural chains (^{238}U and ^{232}Th), but also others of cosmogenic origin or man-made produced as ^{60}Co. The materials to be used in detector building should be previously screened for their radiopurity by HPGe spectrometry, for instance, or using other analytical techniques. Of course, machining and handling of the different components in the detector building process should be also done by applying ultra-low background protocols, trying to avoid any contamination, for instance by radon isotopes deposition. Usually, total event rates of a few counts per day, per kg of detection mass and per keV energy window (cpd/keV/kg) are present in the dark matter experiments.

3. **Double read-out.** Detectors having the capacity of simultaneously measuring two of the channels allowed for the energy conversion, can distinguish the type of interaction by looking at the ratio of the two signal amplitudes [54]. Experiments able to measure ionization and phonons simultaneously consist of arrays of large Ge or Si detectors. In case of experiments able to measure scintillation photons and phonons at the same time, the detector consists of an array of double bolometers: a scintillating bolometer (target with heat sensor) facing to a secondary bolometer to detect the light produced in the former. There are also experiments able to measure the scintillation light and the ionization, they are usually non-segmented self-shielded detectors which use liquid noble elements as target material. Strong background reduction is typically achieved by this double readout scheme. For instance, CRESST experiment has only 0.092 cpd/kg in the 12-40 keV acceptance region for nuclear recoils [55].

4. **Sensitivity to a characteristic signature of dark matter particles.** Temporal and directional dependences in the dark matter interaction rate are expected. The Earth's motion around the Sun produces a variation in the differential event rate along the year. As seen in equation 1.12, the dark matter interaction rate depends

on the relative velocity WIMP-nucleus and this relative velocity changes along the year because of the Earth orbit around the Sun [50]:

$$\vec{v}_{\oplus}(t) = \nu_{\oplus} \left[\hat{e}_1 \sin\lambda(t) - \hat{e}_2 \cos\lambda(t)\right] \tag{1.15}$$

where $\nu_{\oplus}$ is the orbital speed of the earth, $\lambda(t)$ the Sun ecliptic longitude, and the unitary vectors in the direction of the Sun at the vernal equinox and at the summer solstice, respectively, in galactic coordinates are $\hat{e}_1 = (-0.0670, 0.4927, -0.8676)$ and $\hat{e}_2 = (-0.9931, -0.1170, 0.01032)$. In the galactic reference system it is obtained:

$$\vec{v}_{\oplus}(t) = (10, 225.25, 17) + (-2, 14.7 - 25.9)\sin\lambda(t) + (29.6, 3.49, -0.308)\cos\lambda(t) \tag{1.16}$$

The Earth's speed with respect to the Galactic rest frame is largest in summer when the component of the Earth's orbital velocity in the direction of solar motion is largest with the maximum the 1^{st} of June. As the Earth's orbital speed is much smaller than the Sun velocity around the galaxy, the amplitude of the modulation is small and the differential event rate can be written, for the standard halo model, in the k-th energy interval, as a first order Taylor approximation [56]:

$$R_k = R_{0,k} + R_{m,k}\cos\omega(t - t_0) \tag{1.17}$$

The amplitude of the modulation in the rate is expected to be less than 10% of the average rate. A diurnal modulation in the rate is also expected due to the Earth's motion around its own axis, but much lower (<1%) because the Earth acts as a shield in front of the detector, but the lower the interaction cross-section of the particle, the smaller modulation [57]. However, it is much more important, the periodic change expected in the direction of the WIMP-nucleus average velocity: it should peak in the direction of motion of the sun in the galactic frame, but change daily in the laboratory frame. Provided a directional detector with 3D readout is built, able to reproduce precisely the nuclear recoil direction, a very distinctive signature of the dark matter signal could allow sharp discrimination from the rest of expected isotropic backgrounds.

There are experiments devoted to dark matter detection since the eighties, but the detectors and techniques applied in this search have been continuously improving. Negative results have been presented in most of the cases. The most relevant among the current

dark matter experiments are briefly described in the following. Table 1.3 summarizes some of them, the technique(s), the available exposure and target material used.

Experiment	Technique	Target	Exposure	Reference
DAMA/LIBRA (*)	Scintillation	NaI	1170 kg × day	[56]
KIMS	Scintillation	CsI	24524.3 kg × day	[58]
XMASS	Scintillation	Xe	5591. kg × day	[59]
XENON100	Scint.& Ionization	Xe	2323.7 kg × day	[60]
ZEPLIN-III	Scint. & Ionization	Xe	1344 kg × day	[61]
CoGeNT (*)	Ionization	Ge	17.8 kg × day	[62]
EDELWEISS	Ioniz. & Phonon	Ge	384 kg × day	[63]
CDMS	Ioniz. & Phonon	Ge	241 kg × day	[64, 65]
CRESST (*)	Scint. & Phonon	$CaWO_4$	730 kg × day	[55]
COUPP	Superheated liquids	CF_3I	437.4 kg × day	[66]
SIMPLE	Superheated liquids	C_2ClF_5	14 kg × day	[67]
PICASSO	Superheated liquids	C_4F_{10}	114 kg × day	[68]

Table 1.3: *Selection of most relevant dark matter search experiments presently in operation and using different techniques. They have been chosen considering they provide the best exclusion limits or they have obtained positive hints (the latter are marked with *).*

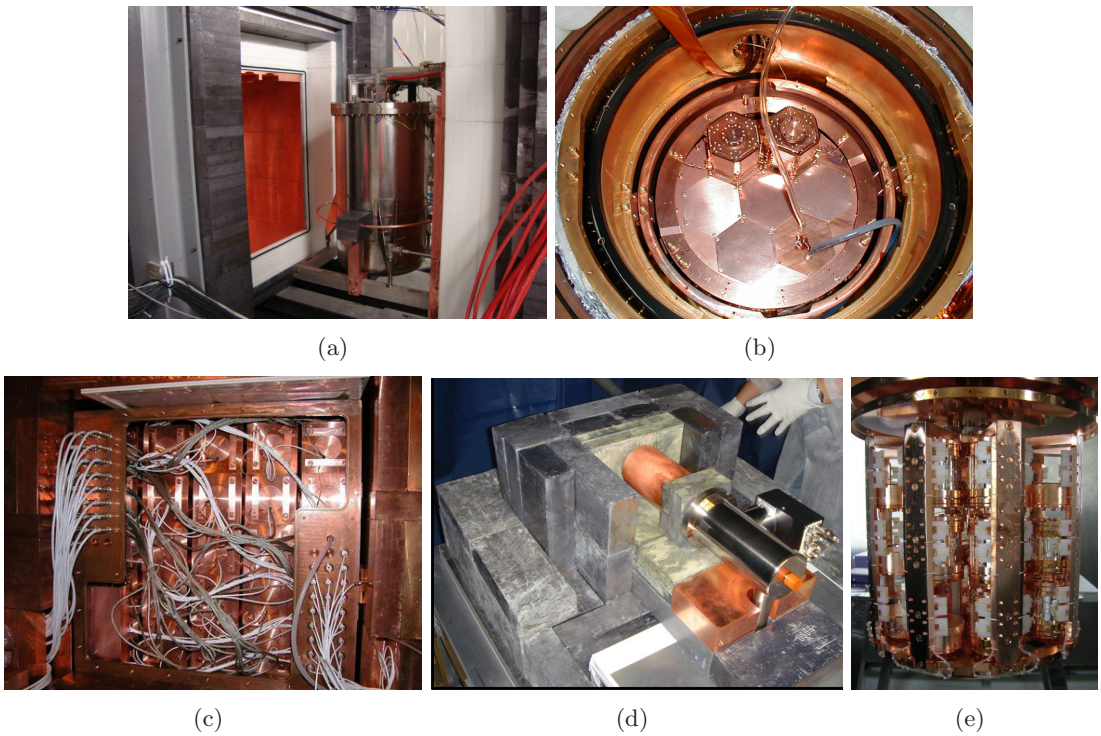

(a) (b) (c) (d) (e)

Figure 1.6: *Pictures of some of the dark matter experiments shown in Table 1.3: (a) the XENON100 experiment, (b) two towers of the CDMS II experiment, (c) the DAMA/LIBRA detectors placed into the shielding, (d) CoGeNT experiment and (e) CRESST detector carousel accommodating the 33 detector modules.*

The XENON100 [60, 69] experiment has achieved the lowest background but no hints of dark matter; in Figure 1.6.a a picture of the detector can be seen. Neither have done CDMS [64, 65] (see a picture in Figure 1.6.b), nor EDELWEISS experiments [63, 70]. Exclusion limits have been presented also by the XMASS [59] (with the lowest energy threshold for a massive experiment: 0.3 keV), SIMPLE [67], PICASSO [68], COUPP [66] and KIMS [58] experiments.

The DAMA/LIBRA [56] experiment has found evidence of an annual modulation in the interaction rate after 13 cycles of measurement with 8.9 σ statistical significance (combining the results with the previous phase of the experiment, DAMA/NaI) for the first time. The former DAMA/NaI [71] and the present DAMA/LIBRA (shown in Figure 1.6.c) setups use NaI as target, and the difference is that in DAMA/LIBRA the NaI mass was increased up to 250 kg using more radiopure crystals. Results corresponding to the 2-6 keVee residual rate are shown in Figure 1.7 for single hit scintillation events. The claim is supported by the following distinctive features: neither modulation is observed for multiple hits events, nor in energy regions above 6 keVee, and period and phase are those expected for the dark matter modulation effect.

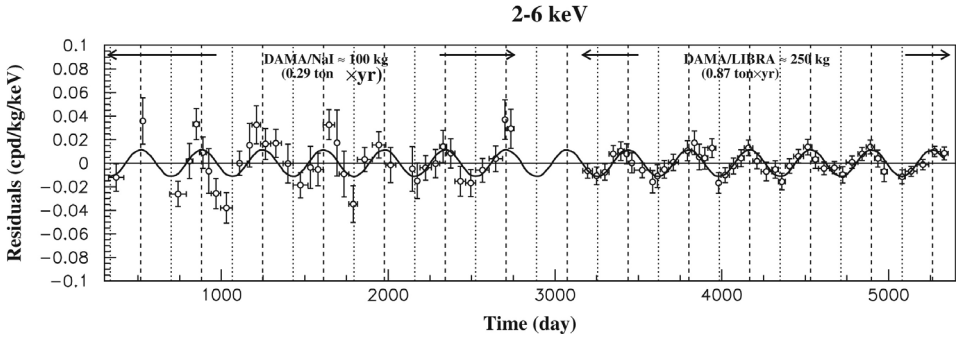

Figure 1.7: *Residual rate of the single-hit scintillation events, measured by the DAMA/NaI and DAMA/LIBRA experiment. An annual modulation of the residual rate is observed in the 2-6 keVee region. Figure obtained from [56].*

For years, DAMA/LIBRA has singled out among the dark matter search efforts with the only positive signal, and other very sensitive experiments using other targets did not find any hint in the same direction. This situation changed very recently, CoGeNT experiment has presented results of an excess of events at very low energy that can not be understood with the usual backgrounds (a picture of CoGeNT experiment can be seen in Figure 1.6.d). Moreover, an annual modulation in the rate of the experiment has been also identified [62]. However, the present experimental situation concerning possible hints, robust signals and negative results is still far from clear. Too many uncertainties and parametric dependences in the signals make model dependent the comparison among different

target results. The CDMS collaboration has also looked for annual modulation without positive result [72]. CRESST experiment (see Figure 1.6.e) has also found an excess of events [55], non-attributable to known backgrounds in the acceptance region where nuclear recoil events from WIMPs are expected. However, these events could be originated by a surface roughness effect [73]. None of these hints of dark matter can be easily accommodated with the negative results of the other experiments, however there are many dependences on the model considered for the comparison (halo model and WIMP particle model, mainly) and possible systematic error, for example in calibrations or rejection events procedures.

Next future seems to be really challenging for the dark matter searches: more than ever experiments are sensitive to very low interaction cross-sections and possible hints about event excesses require further understanding of the detection techniques at no precedent low background level. New experiments have been proposed or are already being commissioned in order to improve the experimental features (background and/or threshold) and to increase the detection mass. The corresponding discovery potential is very high. In Figure 1.8 most of these experiments/projects are shown according to the technique they use and highlighting the target.

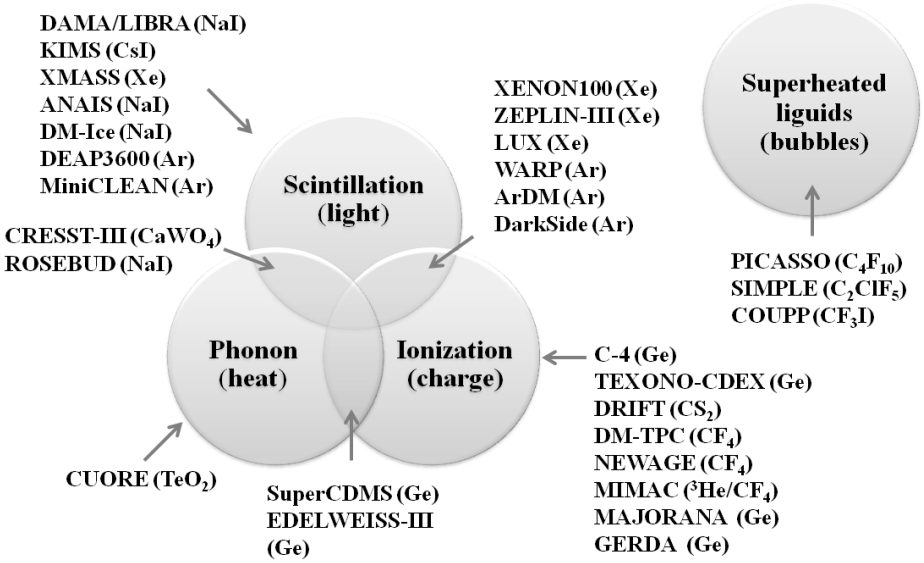

Figure 1.8: *Different experiments which are presently or will be in the next future devoted to dark matter direct detection.*

One of the most interesting lines of research is reproducing the DAMA/LIBRA result on the annual modulation using NaI(Tl) scintillators. It is the most robust hint to date and could be tested in a quite model independent way. This is the direction followed by

the projects ANAIS and DM-Ice. This work has been done in the frame of the ANAIS experiment, which will be briefly presented in the next section and the following chapters will detail the work carried out for the last years. The DM-Ice experiment will use also the same target and technique, with the particularity of the location: the South Pole. This experiment presents some advantageous features with respect to DAMA/LIBRA and ANAIS as are: the low operation temperature of the detectors, buried in the Antarctic ice, the high radiopurity and shielding offered by the surrounding ice and the southern position that inverts the possible correlation of any modulation in the signal with the temperature, allowing a better control of systematics. However, it has also some drawbacks as the impossibility to access to the detectors once buried, and hence, to calibrate them.

The CUORE experiment deserves a special mention because, although its main goal is the double beta decay search, it has achieved a low energy (3 keV) threshold in a test run [74] with a background of 2-25 cpd/keV/kg and will be able to look for annual modulation first with CUORE-0 setup, and later with the whole of CUORE detectors (amounting 741 kg TeO_2 bolometers).

A next generation of ton-target experiments has been planned. CRESST, EDELWEISS and ROSEBUD have rejoined efforts in the project EURECA [75], which could use Ge detectors (as those from EDELWEISS) or $CaWO_4$ scintillating bolometers (as those from CRESST), but could take into consideration the inclusion of other targets, in particular new scintillating bolometers being tested in the frame of ROSEBUD. The total mass of EURECA is planed to be 1 ton, and a multitarget approach could be envisaged. Combination of different target nuclei in the same set-up could bring interesting information in the case a positive signal is found. Moreover, the versatility of the target choice in the case of scintillating bolometers could allow to tune the target to the results of other experiments, in order to complement them and derive the parameters of the WIMPs, breaking degeneracies [76]. The XENON experiment will also be enlarged to 1 ton of fiducial mass. LUX and ZEPLIN will join efforts to build LZ with 7 t of liquid Xe. Also, SuperCDMS [77] will use improved Ge detectors, called iZIPs, to significantly improve the rejection of surface events, main background limitation in CDMS experiment. Moreover, EURECA and SuperCDMS have signed a Memorandum of Understanding in order to progress towards common goals and sharing know-how and results. Far into the future, two large scale experiments have been proposed: MAX [78] in the US using 40 t of liquid Ar and 20 t of liquid Xe and DARWIN [79] in Europe, using 10 t of liquid Xe and/or Ar.

1.4 ANAIS experiment

1.4.1 Scientific case

The ANAIS experiment will use NaI(Tl) as target material and will profit from its advantageous features in the search for dark matter. For instance, a low energy threshold can be achieved thanks to the high light yield, it is sensitive to Spin Dependent interactions because 100% of their isotopic content consists of nuclei having A-odd, and it combines light and heavy nuclei, that guarantees good sensitivity in the low and high mass WIMP ranges. Moreover, the state-of-the-art in the building of the detectors and the operation at normal temperature simplify the experimental challenge. ANAIS experiment will also profit from a large detection mass (it is easy to grow very large NaI(Tl) crystals) to analyze the annual modulation effect in the signal. Similar results to those obtained by DAMA/LIBRA collaboration (see previous section) should be found in ANAIS if WIMPs are responsible of such a signal. ANAIS experiment would confirm or refute that result in a model independent way.

NaI(Tl) scintillators are background limited because no discrimination between nuclear and electron recoils is possible in the low energy region [80, 81]. However, the main disadvantage of the NaI(Tl) scintillators is the low relative efficiency factor (or quenching factor, Q) for the conversion of the energy deposited by nuclear recoils into visible signal. It is well known that the scintillation yield strongly depends on the type of particle. The relative efficiency factor between nuclear recoils and electrons, is defined as the ratio between the scintillation signal produced by a nuclear recoil depositing an energy in the scintillator and that produced by an electron depositing the same energy.

Energies in the experiment are usually expressed as electron equivalent energies, because available calibration sources are beta/gamma sources. In the following chapters, we will refer to electron equivalent energies (keVee or just keV) unless it is otherwise stated. In order to compare with the expected dark matter interaction rates, conversion between nuclear recoil an electron equivalent energies is mandatory and Q should be well known. Q values of $\sim$0.3 for Na recoils and $\sim$0.1 for I recoils have been reported and were taken as constants in the low energy region [81–87]. Very recently, new measurements have been presented showing much lower values for that quenching factor for Na recoils in the low energy range, as well as strong energy dependence. Confirmation of such a result would imply important shift in the WIMP parameter space region within reach of ANAIS experiment [88]. Hence, a much better knowledge of this parameter is required in order to compare data from NaI experiments and those from other targets.

The expected dark matter signal in a NaI(Tl) target is shown in Figure 1.9 for different WIMP candidates: $\sigma_{SI} = 10^{-5}$ pb and WIMP masses of 10 and 50 GeV, and for different values of Q for Na and I nuclear recoils. The expected amplitude of the modulation is also shown in Figure 1.9. The relevance of the quenching factor considered is clearly observed in this Figure. However, this factor should not be important in the comparison between DAMA/LIBRA and ANAIS results, as far as the same target is used. By reaching 1 keVee threshold and a background low enough, compatibility with DAMA/LIBRA signal could be sought in the average rate, without waiting several cycles to analyze the annual modulation.

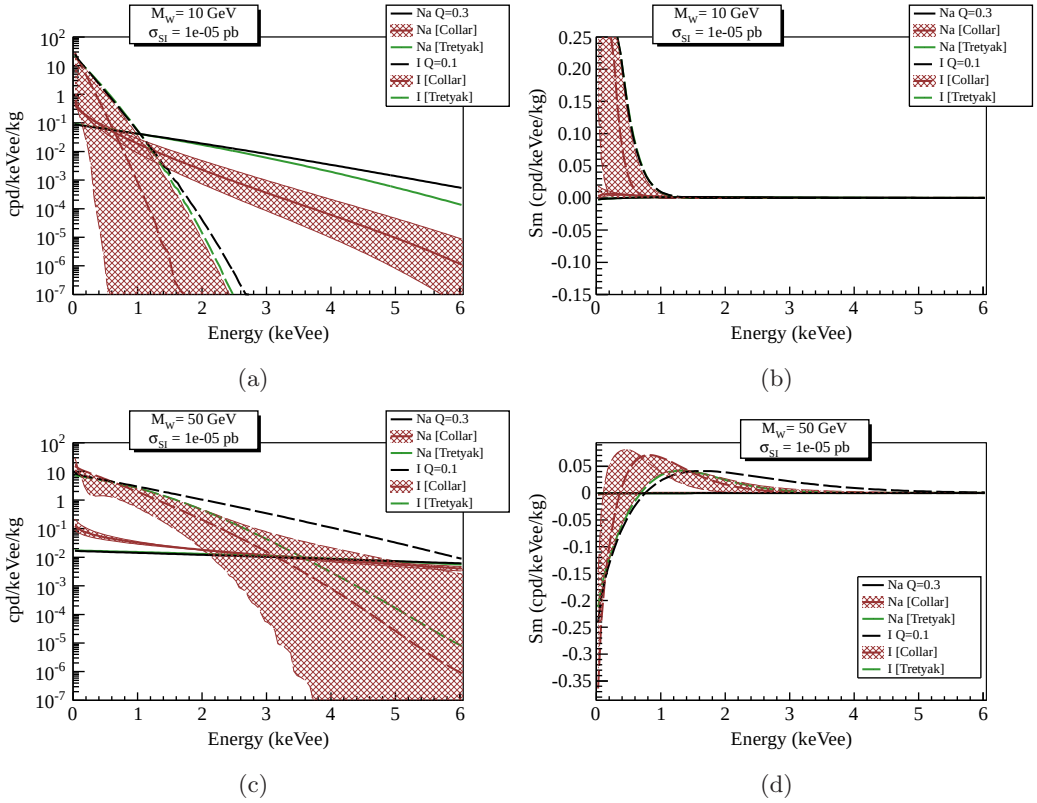

Figure 1.9: *Expected dark matter rates in NaI, energy is shown in electron equivalent units. Different signals for WIMPS of $M_w = 10GeV$ and $M_w = 50GeV$ with $\sigma_{SI} = 10^{-5}$ pb and different values of Na and I nuclear recoils quenching factor (as reported on [85, 88]) have been considered [89].*

It is interesting to mention here the possibility of building a NaI scintillating bolometer, able to simultaneously measure the heat and light signals. With this technique, it would be possible to discriminate between nuclear and electron recoils [90], and the DAMA/LIBRA positive signal could be confirmed even with low exposures. This possibility has been studied in the frame of the ANAIS and ROSEBUD experiments [91]. With the long-term goal of developing a scintillating NaI bolometer, we have tested NaI(Tl) crystals coated

by vapor-deposited poly-p-xylylene (parylene) and studied their optical and mechanical behaviour in the mK range.

1.4.2 Technical aspects of the project

The ANAIS experiment is the large scale conclusion of previous studies carried out with different prototypes. ANAIS was conceived to be made with 10 hexagonal NaI(Tl) crystals of 10.7 kg each made by BICRON (now Saint Gobain) (see Figure 1.10). These detectors were part of the 14 detectors used in an experiment which looked for the ^{76}Ge $\beta\beta$ decay to the first excited state at the Modane Underground Laboratory first, and then at the Canfranc Underground Laboratory. They have been stored underground at the LSC since the late eighties.

After that, the NaI32 experiment searched for dark matter at the LSC with 3 of these detectors (amounting 32.1 kg) and accumulating two years of data taking. Bounds on WIMP masses and cross-sections were derived from the absence of positive hints, neither in the usual analysis of the total rate, nor in a pioneer modulation analysis [92–94].

Then, one of the NaI crystals was chosen to be further studied and modified: it was used to build ANAIS prototype I [95], and after decoupling the PMT and removing the original stainless-steel encapsulation (see Figure 1.10) it was used in prototypes II [89] and III. In prototype II a copper box was used to allow testing easily different light guides geometries, lengths, optical couplings and reflector/diffuser materials, see Figure 1.11.a, whereas in prototype III (PIII) a tight copper encapsulation was designed and PMTs and/or light guides were coupled in a second step, see Figure 1.11.b. As main result of the study of these prototypes the natural potassium content of the bulk crystal was measured to be too high to allow their use in a dark matter search experiment. Subsequently, all the available crystals were characterized, see section 4.1.2, resulting contaminations of the same magnitude. This result implied a significant change in the ANAIS experiment timeline.

The ANAIS experiment had then to be redefined and, in order to reach the experimental goals, the final proposal consisted of 250 kg of ultrapure NaI(Tl) crystals to study the expected annual modulation in the galactic dark matter signal. An ultrapure powder provider and manufacturer of the ultra-low-background crystals had to be searched for, see section 5.1. The total NaI(Tl) mass will be divided into 20 modules of 12.5 kg each. Each module will be coupled to two photomultipliers to increase the light collection efficiency and reduce the photomultipliers events rate. A copper housing will close tightly

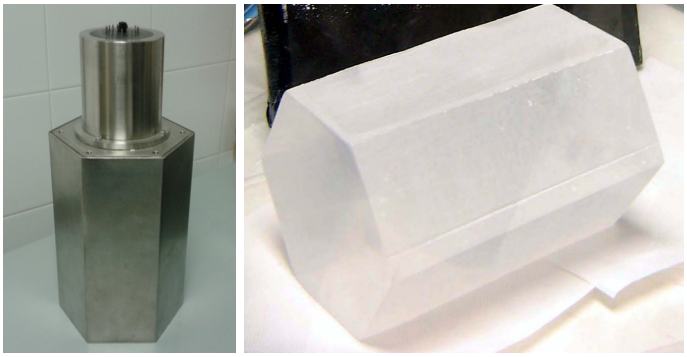

(a) (b)

Figure 1.10: *10.7 kg NaI(Tl) crystal from BICRON. Original detector configuration: stainless steel encapsulation and PMT coupled (a), and bare NaI(Tl) crystal (b).*

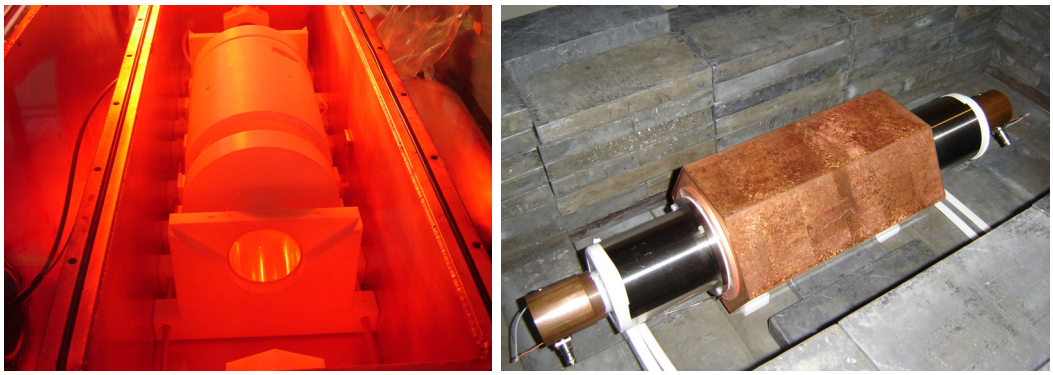

(a) (b)

Figure 1.11: *(a) Prototype II, a 10.7 kg NaI(Tl) crystal from BICRON inside a Teflon cylinder used as light diffuser material and coupled to light guides, all inside a copper box tightly closed to keep a low relative humidity atmosphere. (b) Prototype III uses the same crystal enclosed in a copper encapsulation with the PMTs directly coupled to 1 cm quartz windows, in a second step.*

the crystals (NaI is highly hygroscopic), which will be covered by a Teflon layer as light diffuser to increase the light collection efficiency.

In order to preserve the NaI(Tl) ANAIS detectors from the environmental background sources, the crystals must be conveniently shielded. The ANAIS shielding will be very similar to the shielding of the ANAIS-0 module, which will be described in section 2.3. The Figure 1.12 shows an artistic view of the ANAIS experiment, with the different parts of the shielding. It will consist of the following layers:

- The first layer of the shielding consists of lead: 10 cm of ancient lead plus 20 cm of low activity lead to attenuate the γ background. All the lead required for the

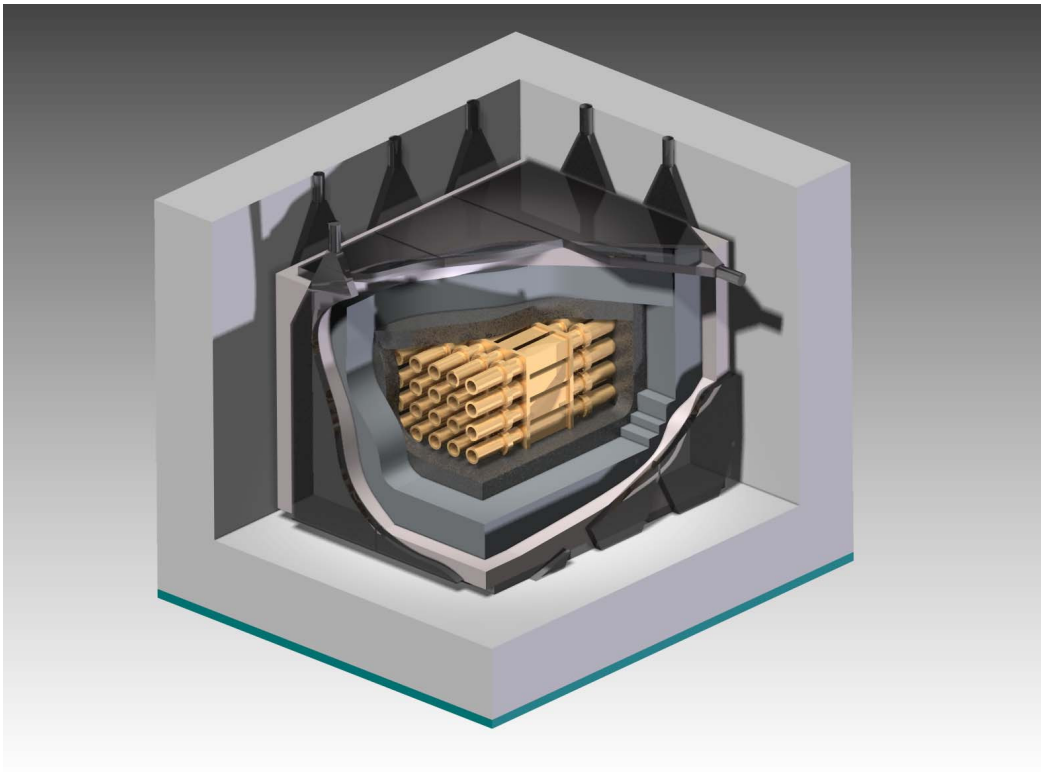

Figure 1.12: *ANAIS experiment artistic view.*

whole ANAIS shielding is already available underground, at the LSC, ready for the mounting.

- An anti-Rn box is required to allow tightly closing the shielding to prevent the entrance of airborne radon inside the experimental space (being continuously flushed with radon-free nitrogen furnished by the LSC). The box has been tested in ANAIS-0 and an expansion of it could house the whole ANAIS shielding. However, other options are still being considered.

- Plastic scintillators covering maximally the ANAIS shielding to act as active muon vetoes have been especially designed: six vetoes are ready to be used in the ANAIS experiment (three of them were used in the ANAIS-0 setup) and the other 10 have been already ordered.

- Finally, a neutron shielding combining boron-loaded water and Polyethylene blocks which are also stored at the Canfranc Underground Laboratory. This neutron shielding is designed in such a way that a part could be easily removed to allow weekly calibrations.

The electronics to be used in the ANAIS experiment is the same designed for ANAIS-0, see section 2.5 and [96], and ANAIS-25 experiments, but scaled to 20 modules and 2 PMTs/module. It has been already tested with up to 2 modules simultaneously and further tests are in progress with a higher modularity. Fine-tuning of some of the components is still to be done. Acquisition and analysis programs have been already prepared and tested. Robust analysis procedures can be concluded after all the work carried out and presented mainly in chapters 3 to 6.

The ANAIS experiment plans to start measuring as soon as the new ultrapure NaI(Tl) crystals are available. An stable measurement during several years is required to look for the annual modulation signal with a high enough confidence level.

1.4.3 Experimental requirements

The ANAIS experiment has three main requirements: keeping energy threshold and radioactive background as low as possible, and operation in stable conditions. To study the feasibility of the ANAIS experiment, with the ANAIS-0 prototype we have worked in the corresponding directions:

- **Energy threshold below 2 keV should be achieved.** This goal is required in order to improve sensitivity for the annually modulated WIMP signal (see Figure 1.13.a and b) and it has been addressed by testing new photomultiplier tubes: with high quantum efficiency PMTs and very low radioactive background PMTs that could allow to avoid the use of light guides, see section 5.2. Also low energy events filtering analysis has been developed in order to reject non-bulk-NaI scintillation events, that dominate the background below 10 keVee, see section 3.1. Reaching a threshold at the 1 keV range would really increase the ANAIS sensitivity for the dark matter signal, see Figure 1.13.c and d.

- **Background at low energy should be kept as low as possible.** After the full background assessment of the hexagonal NaI(Tl) crystals, of 10.7 kg each, which were originally thought as ANAIS target, the measured ^{40}K bulk crystal contamination appeared as the most dangerous at the very low energies of interest for ANAIS (see section 4.4) and forced us to look for more radiopure crystals, implying the development of NaI powder purification techniques and the search for new providers (see section 5.1). The ANAIS-0 crystal contamination, and with a special care the ^{40}K activity, has been thoroughly studied in this work, and the same analysis has been applied to the new radiopure ANAIS-25 crystals (see sections 4.1 and 6.2).

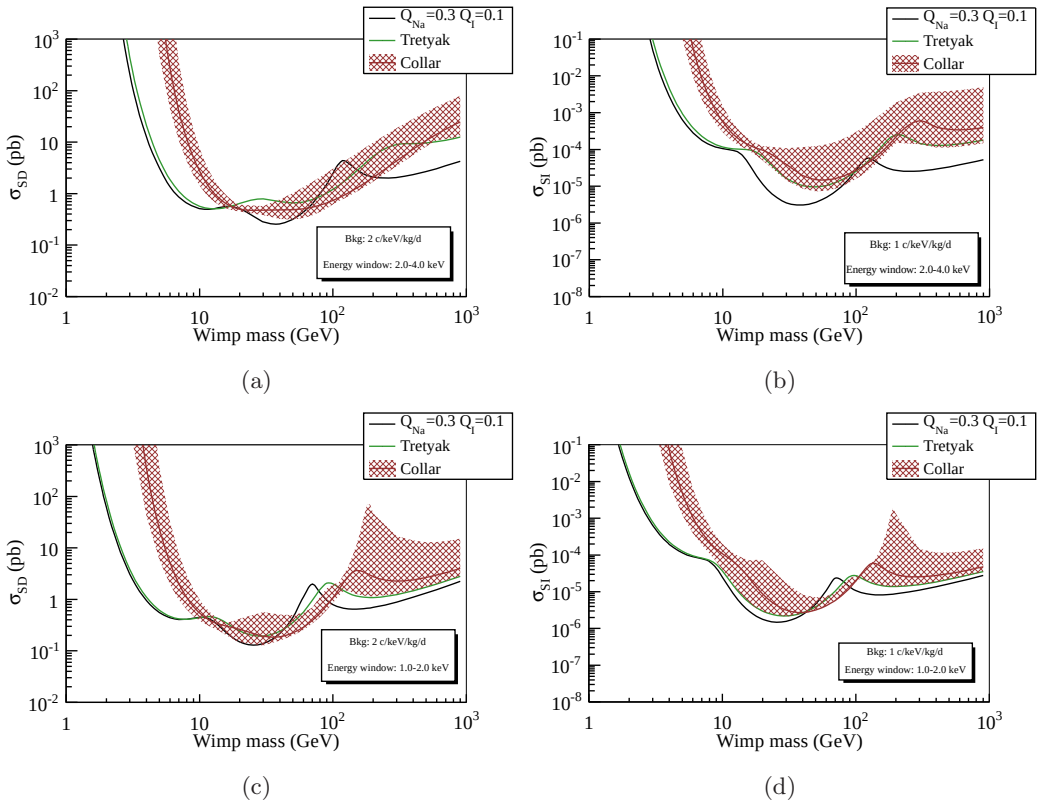

Figure 1.13: *Annual modulation sensitivity curves estimated for NaI considering different energy windows, different backgrounds and quenching factors [89].*

The materials to be used in the ANAIS experiment must be selected in terms of radioactivity. All of the ANAIS-0 module components have been screened with HPGe spectrometry at the LSC. A Geant4 simulation of the background has been carried out and a background model has been proposed, see section 4.3. This background model has allowed to understand much better the different background contributions present in ANAIS-0 and such a knowledge has been applied in the design of the new modules. The same simulation code will be applied, with few modifications, to the whole ANAIS experiment. The ANAIS shielding has been tested with ANAIS-0 module, showing good performance. In particular, the muon veto system (although only having partial shielding coverage) has been setup and muon related events have been studied with ANAIS-0 module.

- **Very stable operation conditions should be guaranteed.** The ANAIS experiment plans to measure continuously during several years and any kind of instability could jeopardize the final result. Monitoring every relevant parameter has been implemented with the ANAIS-0 module at the LSC - Hall B (see sections 2.4 and 2.6) in order to discard environmental interferences in the events rate that could

affect the annual modulation analysis. Weekly calibrations at high and low energy have been carried out (see section 2.7) and the same will be done when running the ANAIS experiment. An stable electronic chain, and acquisition system are required. They have been upgraded, during the ANAIS-0 operation. The electronics design is compact and homogeneous consisting on VME and NIM modules, providing a solid performance. Some problems concerning channels cross-talk due to the HV power supply are still unsolved. For the acquisition system part, it has overcome satisfactory stress tests and long runs, see section 2.5.

Chapter 2

ANAIS-0 experimental procedure

This chapter presents the experimental details relevant to guarantee the required low background conditions in the operation of the ANAIS-0 module. The ANAIS-0 module consists of a 9.6 kg NaI(Tl) crystal grown by Saint Gobain and encapsulated in copper at the University of Zaragoza (section 2.1). Several setups have been operated to test different photomultiplier tubes (PMTs), and the effect of coupling some of them through 10 cm light guides (section 2.2). A convenient shielding has been designed in order to reduce the different contributions of the environmental radioactive sources to the background (section 2.3).

All the measurements have been carried out in the Canfranc Underground Laboratory (LSC), in Spain, under 2450 m.w.e. (section 2.4). The new installations of the LSC were re-opened in 2010, after the starting of the measurements with ANAIS-0 module at the old LSC facilities. As soon as it was possible, all the ANAIS-0 experimental layout was moved to the Hall B of LSC.

The stability of the experimental parameters has been monitored during ANAIS-0 operation (section 2.6), specially in the new LSC facilities where the ANAIS experiment will be placed. The experimental parameters monitored are: radon air content in Hall B; temperature inside Hall B, at ANAIS electronics and at ANAIS hut; pressure; humidity; nitrogen flux and HV power supply. Muon interaction rate in the vetoes has been also monitored and the coincident events in the NaI crystal have been studied (section 2.8).

The ANAIS-0 module has been calibrated weekly (section 2.7) at low and high energy. Calibration data have been used, for instance, to check the operation stability, to have reference NaI(Tl) scintillation events for the data analysis, to search for systematic effects in the simulations, and to study the energy resolution.

2.1 ANAIS-0 module assembly

The NaI(Tl) crystal was encapsulated in ETP (Electrolytic Tough Pitch) copper, closing tightly the detector, and using two synthetic quartz windows to get the light out to the photomultiplier tubes. A Teflon sheet as diffuser and a Vikuiti reflector layer wrap the crystal to increase light collection efficiency. This design allowed the direct coupling of different PMT models to these quartz windows or the additional inclusion of light guides, enabling to have data about light collection efficiency in the different configurations tested, as well as about the corresponding PMT background contribution. For the final design of the detectors of the ANAIS experiment a compromise between these two criteria, clearly anticorrelated, should be achieved: the highest light collection compatible with the least PMT background contribution. Low background voltage dividers were specially designed for ANAIS using SMD (Surface Mount Technology) components on Teflon.

The ANAIS-0 module has been taking data at the LSC in different setups in order to characterize and fully understand ANAIS background at low and high energy, to optimize NaI scintillation events selection, to determine the calibration method, and to test the electronics.

2.1.1 NaI(Tl) crystal

The ANAIS-0 module was made with a parallelepipedic 9.6 kg NaI(Tl) crystal bought to Saint Gobain in 2003. The size of the crystal is 254.0 x 101.6 x 101.6 mm^3. Size and shape are the same of DAMA/LIBRA crystals, made also by Saint Gobain [97].

It was stored, hermetically closed, at the University of Zaragoza until 2009 when it was encapsulated. The crystal had not been manipulated till the encapsulation, and then, only the square faces were cleaned with isopropanol before coupling the quartz windows. The NaI(Tl) crystal used in ANAIS-0, partially covered in Teflon sheet, can be seen in Figure 2.1.a.

2.1.2 NaI(Tl) crystal encapsulation

The NaI(Tl) crystal was encapsulated in ETP copper at the University of Zaragoza. Two quartz windows (1 cm thick) allow to couple two PMTs in a second step, so that different PMTs, and eventually light guides, can be tested while keeping the crystal hermetically closed.

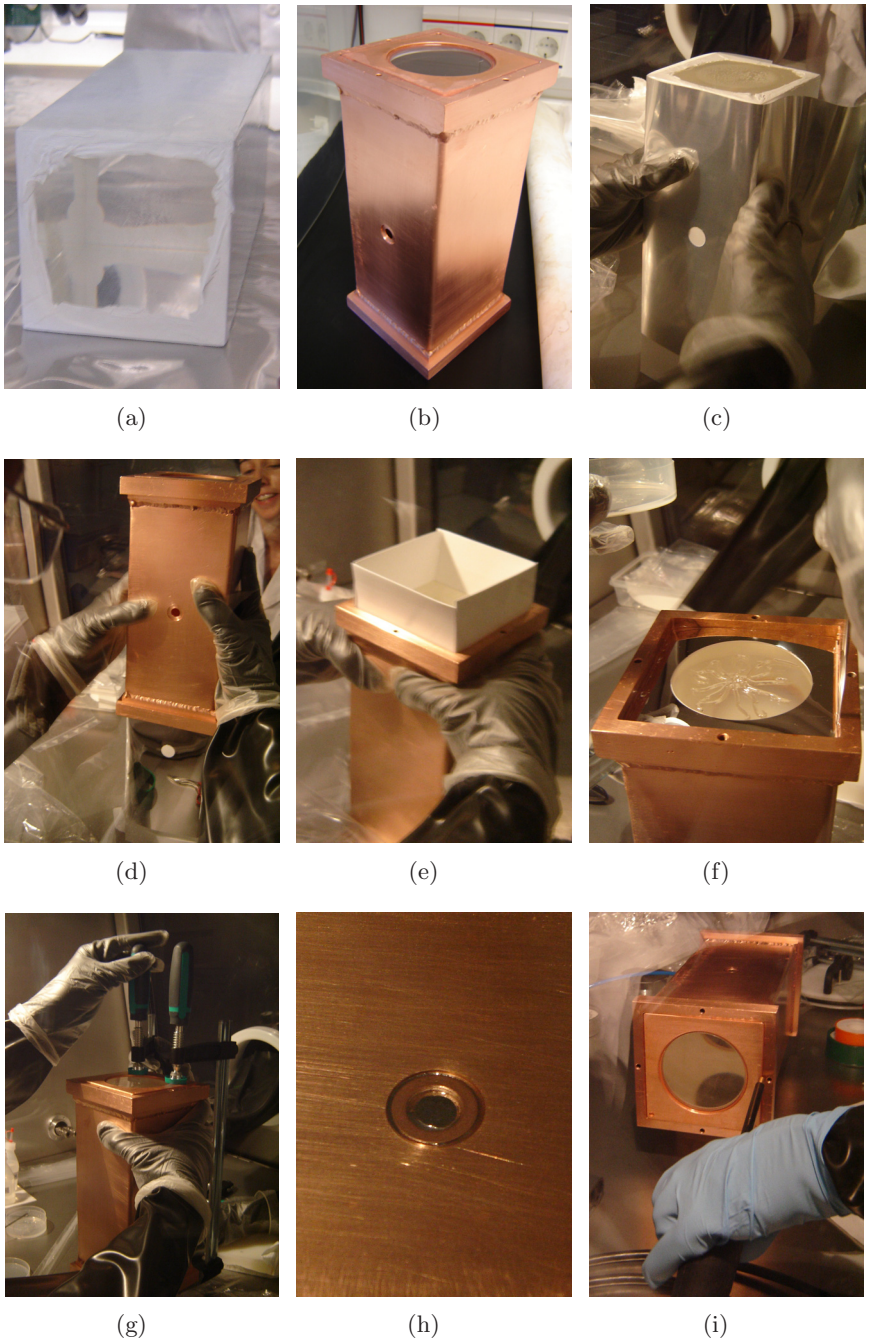

Figure 2.1: *Pictures of the ANAIS-0 encapsulation procedure. (a) The NaI(Tl) crystal covered with a Teflon sheet as arrived from Saint Gobain. (b) The copper encapsulation with a copper lid and a quartz window glued. Placing the reflector around the Teflon (c), the copper encapsulation (d) and the second Teflon layer (e). (f) Detail of the optical coupling grease and reflector before coupling the synthetic quartz window. (g) Two clamps fixed the quartz window and copper encapsulation till the glue hardened, tightly sealing the detector. (h) Detail of the Mylar window that allows low energy calibrations. (i) Checking the tightness.*

The encapsulation procedure was done inside a glove box with less than 0.9% of relative humidity and temperature in the range from 20 to 22 °C.

All the materials used in the assembly of the ANAIS-0 module were carefully selected in terms of radioactive isotopes content. They had been previously screened using a High Purity Ge (HPGe) spectrometer in the LSC; results of these measurements for the different ANAIS-0 module components are shown in Table 2.1 (only upper limits at 95% C.L.). The HPGe spectrometer used has an active mass of about 1 kg and was built by Princeton Gamma Tech Instruments in collaboration with the Pacific Northwest National Laboratory and the University of South Carolina with detector components of ultra low background. Since the last eighties this detector has been underground, at the LSC, shielded from cosmic rays, and hence avoiding cosmogenic activation. All the measurements are carried out in an ultra-low background environment, inside a low radioactivity lead shielding.

The main constituents of the encapsulation are:

- Copper lining consisting of a lateral surface made with a folded ETP copper sheet (1 mm thick) sidelong sealed by TIG (Tungsten Inert Gas) welding without additional material incorporation (other than ETP copper), and two copper lids having 3" diameter synthetic quartz windows glued on each side (see Figure 2.1.b). Two clamps eased the optical coupling between NaI(Tl) crystal and quartz windows while mounting the detector (see Figure 2.1.g).

- Two optical windows with cylindrical shape (3" diameter and 1 cm height) made of synthetic quartz Suprasil 2 grade B from Heraeus [98]. Synthetic quartz with high optic quality and purity was chosen to avoid the anomalous events attributed to scintillation in natural quartz, observed in [99].

- First Teflon sheet wraps the NaI(Tl) crystal acting as light diffuser.

- Reflecting layer of Vikuiti Enhanced Specular Reflector [100] surrounds the Teflon wrapped crystal (see Figure 2.1.e). The thickness of the layer is 65 μm and the reflectance 98% for $400\,nm < \lambda < 1000\,nm$. It helps to increase the light collection efficiency [89].

- Second Teflon sheet (Gore Tex, 1 mm thick) acts as mechanical pad, between the Vikuiti and the copper lining, to prevent the constituents from moving after mounting (see Figure 2.1.c).

- Aluminized Mylar foil (10 μm thickness, 16 mm diameter) closes tightly a hole in the copper lining to allow low energy calibrations. The Mylar window is held by a copper washer glued to the copper encapsulation (see Figure 2.1.h).

- Epoxy glue Loctite Hyson RE2039 and hardener HD3561 are used to glue the quartz windows to the copper lids, the copper lids to the copper encapsulation and the Mylar window.

- Thixotropic optical gel from Fiber Optic Center Inc. is used to couple the quartz windows to the crystal and to the PMTs (see Figure 2.1.f).

To finish, the encapsulated NaI(Tl) crystal was checked for leaks, before taking it out from the glove box, see Figure 2.1.i.

Detector component	Units	^{40}K	^{232}Th	^{238}U	^{226}Ra	^{60}Co	^{137}Cs
Copper lining	mBq	< 11	< 4.1	< 140	< 2	< 0.94	< 1.4
Suprasil quartz	mBq/kg	< 12	< 2.2	< 100	< 1.9	< 0.3	< 1
Thixotropic gel	mBq/kg	< 200	< 200	< 2000	< 30	< 20	< 30
Reflector Vikuiti	mBq/m^2	< 34	< 5.5	< 150	< 4.4	< 1	< 2.5
Mylar	mBq/kg	< 125	< 37	< 1500	< 66	< 5	< 10
Epoxy Loctite	mBq/kg	< 120	< 3.7	< 100	< 7.8	< 1	< 2
Teflon	mBq/kg	< 15	< 3	< 50	< 2	< 0.5	< 1

Table 2.1: *Upper limits given at 95% C.L. for the content on the main radioactive isotopes for the different components of the ANAIS-0 module, measured with a HPGe spectrometer at the LSC.*

2.1.3 Photomultiplier tubes

Different photomultipliers have been tested in the frame of the ANAIS project before the final choice for ANAIS has been taken. Compromise between high quantum efficiency and low background features of the different PMT models was looked for: high quantum efficiency PMTs could allow lowering the threshold, but the low radioactivity levels in the PMTs are crucial to minimize their contribution to the background, and could enable, for instance, the removing of the light guides. The cost of each photomultiplier must be also taken into account, because the budget is limited.

The following five models of PMTs have been studied (main features of each model are summarized in Table 2.2):

- ETL: Low background photomultipliers from Electron Tubes Limited, model 9302B, were thought as the first option for ANAIS. Typical quantum efficiency (QE) of this model was 25%. The technical data sheet can be found in [101].

- HQE: New photomultipliers from Hamamatsu of very high quantum efficiency, larger than 42%, (R6233-100 SEL) were tested with the aim of lowering the threshold of the ANAIS experiment. However, they did not satisfy any low background requirement. The technical data sheet can be found in [102].

- LB: Hamamatsu low background PMTs (R6233-100 MOD), quite similar in performance to the very high quantum efficiency ones (but nominal quantum efficiency was only guaranteed to be larger than 35%), seemed to be a good option combining low background and good efficiency. Moreover, their cost was lower than the ETL ones.

- ULB: The excellent radiopurity level of the ultra-low background Hamamatsu (Ham) PMT model R11065 SEL made it very interesting for ANAIS goals because light guides could be avoided, improving the light collection and lowering the threshold. They had been specially designed for low background experiments, with a window made of synthetic silica and glass body replaced by Kovar metal. Several low background experiments like LUX [103] and DarkSide [104], among others, are using them. Typical quantum efficiency of this model was 25%, but selected PMTs with higher quantum efficiency could be requested (>30%). Nevertheless, their cost is too high and hardly could be afforded with the ANAIS budget. Hamamatsu loaned us a faulty PMT unit (ZK5171) specifically for the low background screening, and after checking its radiopurity, two units were bought and tested (BA0057 and BA0086). The technical data sheet can be found in [105].

- VLB: Hamamatsu technical staff offered an additional option to ANAIS research team: VLB PMTs (R6956 MOD), having less radioactive content than LB model and being less expensive than the ULB one. The window is made of borosilicate glass. Selected PMTs of this model with quantum efficiency over 33% could be guaranteed by HAMAMATSU. This model is similar to the recently installed by DAMA/LIBRA collaboration [106].

Table 2.3 shows the main technical information of the PMT models tested, as given by Hamamatsu or Electron Tubes Limited. All the PMTs tested have the same photocathode size (3" diameter) and their response is optimized at 420 nm. Table 2.4 summarizes

Name	Manufacturer	Model	Serial number
ETL	Electron Tubes Limited	9302B	1034
HQE	Hamamatsu	R6233-100 SEL	1062DA 1066DA
LB	Hamamatsu	R6233-100 MOD	ZE5331 ZE5336
ULB	Hamamatsu	R11065 SEL	ZK5171 BA0086 BA0057
VLB	Hamamatsu	R6956 MOD	ZK5902 ZK5908

Table 2.2: *Different photomultipliers studied throughout this work: Low background PMTs from Electron Tubes Limited (ETL), Hamamatsu high quantum efficiency (HQE), low background (LB), ultra low background (ULB) and very low background (VLB) photomultipliers. Names shown in the first column have been given by the ANAIS research team for internal use, attending to the main properties of each model. Manufacturer, model and serial number are indicated for each of them.*

(a) (b) (c) (d) (e)

Figure 2.2: *Different photomultipliers studied: (a) Low background PMTs from Electron Tubes Limited (ETL), (b) Hamamatsu high quantum efficiency (HQE), (c) low background (LB), (d) ultra low background (ULB) and (e) very low background (VLB) PMTs. See Table 2.2 for more details about each model. Ham LB, ULB and VLB PMT models present flying leads.*

the main features for each PMT unit as given by Hamamatsu. The minimum quantum efficiency values requested and quoted by Hamamatsu are also shown in this table.

A couple of units of each model were bought to study the corresponding performance, and, if first tests were good enough, they were installed in the ANAIS-0 module at the LSC to test them in a real situation. In a previous step, all the PMTs were characterized at the University of Zaragoza (results will be presented in section 5.2) and were screened for radiopurity with HPGe spectrometry at LSC. Results of such radioactive screening are

	Units	ETL 9302B	HQE, LB R6233-100	ULB R11065	VLB R6956
GENERAL					
Diameter	*in*	3	3	3	3
Spectral response	*nm*	285-630		200-650	300-650
λ of max. response	*nm*		420	420	420
PK material			SBA	BA	BA
PK Min. Effective	*mm*		70	64	70
Dynode structure		L	B+L	B+L	B+L
Number of Stages		9	8	12	10
Operating Ambient T	*C*	-30/+60		-186/+50	-30/+50
Max. Supply Voltage	*V*	1300	1500	1750	1500
Max. Av. Anode Curr.	*mA*	0.1	0.1	0.1	0.1
CHARACTERISTICS AT 25° C					
Cathode Luminous Sens.	$\mu A/lm$	75	130	90	100
QE @ peak	%	30	35	25	
QE @ 420 nm	%		34		
Cath. Blue Sens. Index			13.5	10	11
Anode Luminous Sens.	A/lm	50	30	450	100
Gain	$\cdot 10^5$	7	2.3	5	10
Anode Dark Curr. (max.)	*nA*	0.5(5)	10(30)	10(100)	6(60)
Dark Current Rate	s^{-1}	500			
Anode Pulse Rise Time	*ns*	7.5	6.0	5.5	9.5
Electron Transit Time	*ns*	125	52	46	60
Transit Time Spread	*ns*	15		6.5	13
Pulse Linearity	*mA*	30 (±5%)		20 (±2%)	30 (±2%)

Table 2.3: *Technical information of the different PMT models tested. The PMT model R6233-100 shares main features with HQE and LB PMTs, the main difference is the selection of special building materials in the LB PMT model that makes them suitable for low background applications. SBA stands for Super Bialkali and BA for Bialkali. B means Box, and L Linear focused. Transit time spread is given as the FWHM of the electron transit time distribution.*

presented in Table 2.5. On view of the high radioactivity level of the HQE PMTs, they were not tested in ANAIS-0.

Copper caps were designed and specially manufactured to house the PMTs and the voltage dividers. They are made of copper specifically electroformed at the University of Zaragoza with such a purpose. Because of the different shape of Ham and ETL PMTs, both casings are different (see Figure 2.3).

After the moving of ANAIS to the new LSC installations all the coupling and decoupling of the PMTs to the ANAIS-0 module was done inside the LSC clean room

Name	Serial N.	Sensitivity Luminous C.	A.	Blue C.	D.C. Rate	A.	Q.E. min. 420 nm	meas. 420 nm	peak
		$\mu A/lm$	A/lm	Index	s^{-1}	nA	%	%	%
ETL	1034								
HQE	1062DA	125	16.5	13.7		3.12	40		
	1066DA	143	71.6	14		20.9	40		
LB	ZE5331	127	38.9	13.9		8.5	32		
	ZE5336	132	43.8	13.9		18	32		
ULB	BA0086	115	516	14.7		15	$\langle 30 \rangle$	28.68	
	BA0057	145	1120	11.9		8.1	$\langle 30 \rangle$	32.90	
VLB	ZK5902	111	225	14.4	577	2.6	33	34.90	38.20
	ZK5908	99	66	14.3	57	0.1	33	34.30	37.20

Table 2.4: *Main features of the PMT units tested in this work, as indicated by the manufacturer. C. stands for cathode, A. for anode and D.C. for dark current. The first column of the quantum efficiency indicates the minimum QE guaranteed by Hamamatsu, whereas the other two columns show particular values of the PMT units purchased (only given by the manufacturer for ULB and VLB units). Values shown between $\langle\rangle$ indicate that only the average value for the purchased units had been guaranteed.*

Component		^{40}K	^{232}Th	^{238}U	^{226}Ra	^{60}Co	^{137}Cs
		$mBq/unit$					
PMTs:							
ETL	1034	420 ± 50	24 ± 4	220 ± 12	-	-	-
HQE	1062DA	$(185 \pm 1)10^3$	420 ± 40	5100 ± 30	-	-	-
LB	ZE5331	678 ± 42	68 ± 3	100 ± 3	-	-	-
	ZE5336	647 ± 56	75 ± 4	109 ± 5	-	-	-
ULB	BA0086	12 ± 7	3.6 ± 1.2	47 ± 28	8.0 ± 1.2	4.1 ± 0.7	-
	BA0057	24 ± 9	1.8 ± 1.0	59 ± 28	6.1 ± 1.2	5.1 ± 0.8	-
VLB	ZK5902	97 ± 19	20 ± 2	128 ± 38	84 ± 3	-	-
	ZK5908	113 ± 13	20 ± 2	150 ± 34	88 ± 3	-	-
Light guide		< 21	< 4.1	< 120	< 4.7	< 1.4	< 1.1
SMD V.D.		-	-	22.0 ± 1.5	-	-	-
PMT C.E.		< 10	< 1.0	< 26	< 1.6	< 0.7	< 1.0

Table 2.5: *Values or upper limits given at 95% C.L. for the content on the main radioactive isotopes for the PMTs, light guides, corresponding PMT copper encapsulations (PMT C.E.) and SMD voltage dividers (SMD V.D.).*

(class 10000), see section 2.4.3. A copper cleaning protocol (based on that of the CUORE

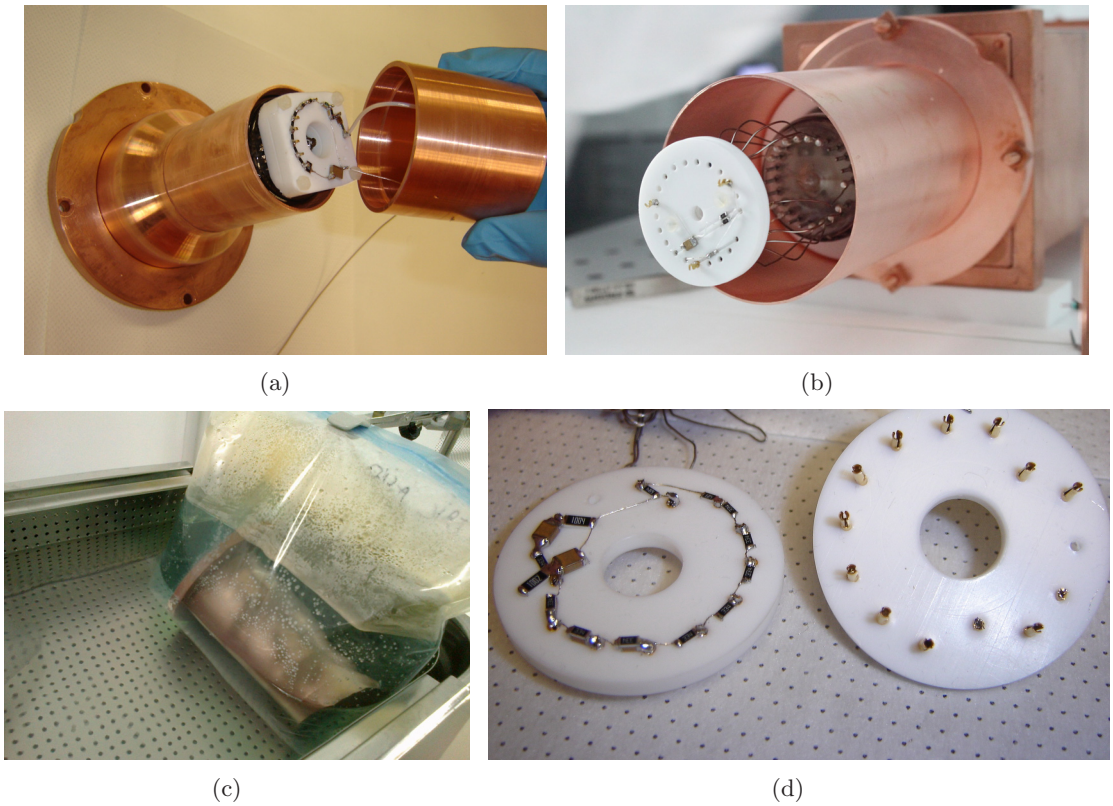

(a) (b)

(c) (d)

Figure 2.3: *Images of the PMTs and voltage dividers inside their electroformed copper casings: ETL PMT (a) and Ham PMT (b). PMT copper casing during the cleaning process, using nitric acid inside an ultrasonic bath (c). Voltage dividers, both sides can be seen: showing the SMD components and the connectors for the PMT leads (d).*

experiment [107]) was applied to all the copper pieces after machining them. It consists of the following steps:

1. Mechanical cleaning: Grinding should be done when machining left-overs remained.

2. Soap cleaning: Pieces are put into a polyethylene bag together with a solution of ultra-pure (deionized) water and 5% of Micro 90 basic soap. The bag with the piece should be in the ultrasonic bath at 40 °C for 1 hour and then, be rinsed with ultra-pure water. Pieces are put into another polyethylene bag together with a solution of ultra-pure water and 5% of Elma 60 acid soap. The bag with the piece should be in the ultrasonic bath at 60 °C for half an hour and afterwards, be rinsed again with ultra-pure water.

3. Acid etching: Pieces are put into a polyethylene bag together 0.5 M of nitric acid in ultra-pure water. The bag with the piece should be in the ultrasonic bath at 40 °C for half an hour and then, be rinsed with ultra-pure water.

4. Passivation: The pieces are then put into a polyethylene bag with a solution at 10% of citric acid in ultra-pure water. The bag is kept in the ultrasonic bath at 60 °C for 1 hour. The piece should be rinsed with ultra-pure water and dried with clean nitrogen gas. A picture of the acid nitric bath step is shown in Figure 2.3.c.

5. After drying the pieces, they should be enclosed into tight plastic bags filled with nitrogen gas, radon-free quality, for storing till use.

The same protocol will be applied to the cleaning of the copper pieces to be used in the encapsulation of the ultrapure ANAIS crystals.

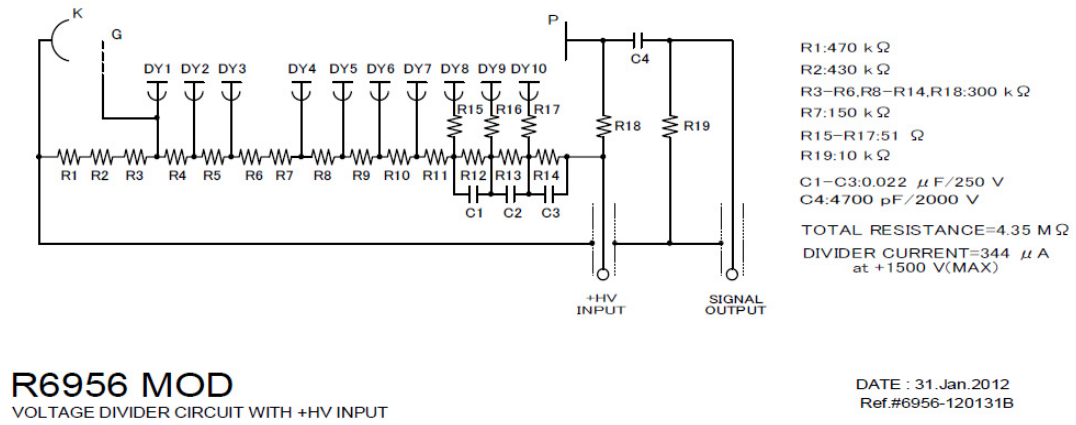

Figure 2.4: *Scheme of a voltage divider circuit used for the VLB Ham PMTs, following Hamamatsu recommendations.*

PMTs voltage dividers were designed in Teflon boards with SMD components. The electric circuits used were adapted to each model, following the recommendations of the manufacturer (either Hamamatsu or ETL) [108]. The scheme of the voltage divider used for the Ham VLB PMT model is shown in Figure 2.4 as an example. Radioactivity screening results for the voltage divider mounted are also presented in Table 2.5 and some images in Figure 2.3.d. Ham LB, ULB and VLB PMT models present flying leads, min. 65 mm long, in order to reduce the voltage divider contribution to the background.

2.1.4 Light guides

Two cylindrical light guides made of methacrylate (3" diameter and 10 cm length) were optionally used with the ANAIS-0 module, between the quartz window and the PMT, in order to evaluate, and eventually reduce, the contribution of the PMTs to the background. They were encapsulated individually in copper. Figure 2.5 shows a light guide and its encapsulation.

The light guide encapsulation consists of an electroformed copper cylinder and two commercial ETP copper clamps fixed under pressure on every side of the piece. Once the clamps were fixed on the cylinder, their joint was reinforced by depositing electroformed copper onto the juncture. All the electroformation work has been done at the University of Zaragoza.

The radiopurity of the light guide together with its encapsulation was measured in the HPGe spectrometer, see results in Table 2.5. Only upper limits on the different radioactive isotopes searched for were derived.

(a) (b) (c)

Figure 2.5: *Methacrylate cylindrical light guide 3" diameter and 10 cm long (a), copper casing for the light guide (b), view of the encapsulated light guide to be coupled in ANAIS-0 module (c).*

2.2 ANAIS-0 Setups

ANAIS-0 module was brought underground the 21/04/09 and up to the 27/11/12 it has been taking data continuously at the LSC. During this time it has been operated in various setups. As explained before, different photomultipliers coupled to ANAIS-0 module with or without light guides have been tested in order to choose the optimum configuration in terms of threshold and background. Table 2.6 summarizes those setups.

A special set-up to measure the ^{40}K content of the crystal has been also taken data in that period, intersperse with the setups shown in Table 2.6, the results will be presented in section 4.1.2. The ANAIS-0 module measured in coincidence with the previously studied PIII, see section 1.4.2. This set-up had three phases because the PMTs were changed twice. Phases I and II took place between set-up 1 and 2 at the old LSC facilities, with the aim of determining the ^{40}K content of ANAIS-0, see section 4.1.2. Phase III took place at the Hall B of the new LSC, after the set-up 5, and the main goal was to measure

Set−up	PMTs	Light guides	Installation date	Live time (days)
1	ETL	No	21/04/09	31.32
2	LB	Yes	22/01/10	178.9
3	ULB	Yes	03/05/11	43.40
4	ULB	No	21/06/11	126.4
5	VLB	No	22/03/12	31.90

Table 2.6: *Main features of the different setups of the ANAIS-0 module: PMT model used, whether light guides are or not coupled, beginning of the installation date and live time of measurement available.*

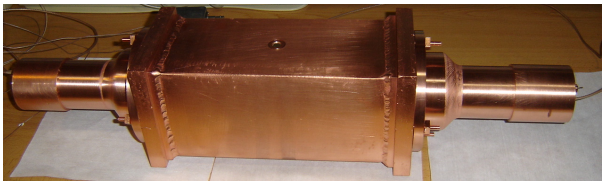

(a)

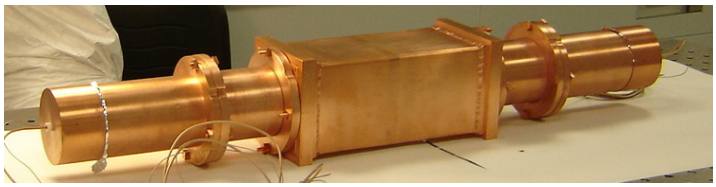

(b)

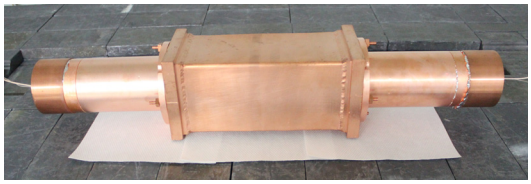

(c)

Figure 2.6: *Pictures of the ANAIS-0 module in the different setups shown in Table 2.6: (a) set-up 1, (b) set-up 3 (set-up 2 had the same external appearance), (c) set-up 4 (set-up 5 had the same external appearance).*

the long NaI scintillation constants also for the PIII, see section 3.6. Table 2.7 summarizes those ^{40}K-coincidence setups.

Some upgrades of the ANAIS-0 experimental layout have been implemented during this time:

- During set-up 2, the 26/04/10, active vetoes anti-muons (see section 2.4) were installed.

Phase	ANAIS-0 PMTs	PIII PMTs	Installation date	Live time (days)
I	ETL	ETL and LG	15/07/09	51.20
II	LB	ETL and LG	08/10/09	57.82
III	VLB	ULB	01/08/12	39.30

Table 2.7: *The dedicated set-up to measure the ^{40}K activity of the ANAIS-0 crystal had three phases. Light guides (LG) were used only with the PIII during phases I and II. Installation date, PMTs used at each detector module, and live time of each phase are shown.*

- The 18/02/11, also during the set-up 2 measurement, the ANAIS experiment was moved to the new installations of the LSC (see also next section). Live time of set-up 2 indicated in Table 2.6 refers only to measurements after the vetoes installation and before the moving to the new LSC facilities.

- The 14/12/11, while measuring with set-up 4, the ANAIS electronic chain was upgraded (see section 2.6).

2.3 ANAIS-0 Shielding

The ANAIS-0 module was placed underground to be shielded from cosmic radiation. Additional active and passive shielding was designed to reduce the environmental radioactivity contribution to the background. The Figure 2.7 is an artistic view of the ANAIS-0 module experimental layout at LSC, consisting of active and passive shielding. During the measurement time some improvements were done, as it has been summarized in the previous section. The ANAIS-0 shielding consisted of the following layers (from inside out):

- The most inner layer of the shielding consists of 10 cm of ancient lead to attenuate the γ background, see Figure 2.8. As explained in [109], lead is an excellent shielding material due to its high Z, price, mechanical properties, and low activation cross section for environmental neutrons. However, even for the highest purity lead, the presence of ^{210}Pb implies an important contribution to the background. The advantage of ancient lead, as the one found in wrecks of Roman ships sunk in the Mediterranean sea, is that ^{210}Pb is expected to be absent because, as the lifetime is 22.3 years, it has completely decayed and the overburden of water has prevented the lead to be activated by cosmic ray neutrons.

- Then, a second layer of low activity lead, 20 cm thick, see also Figure 2.8.

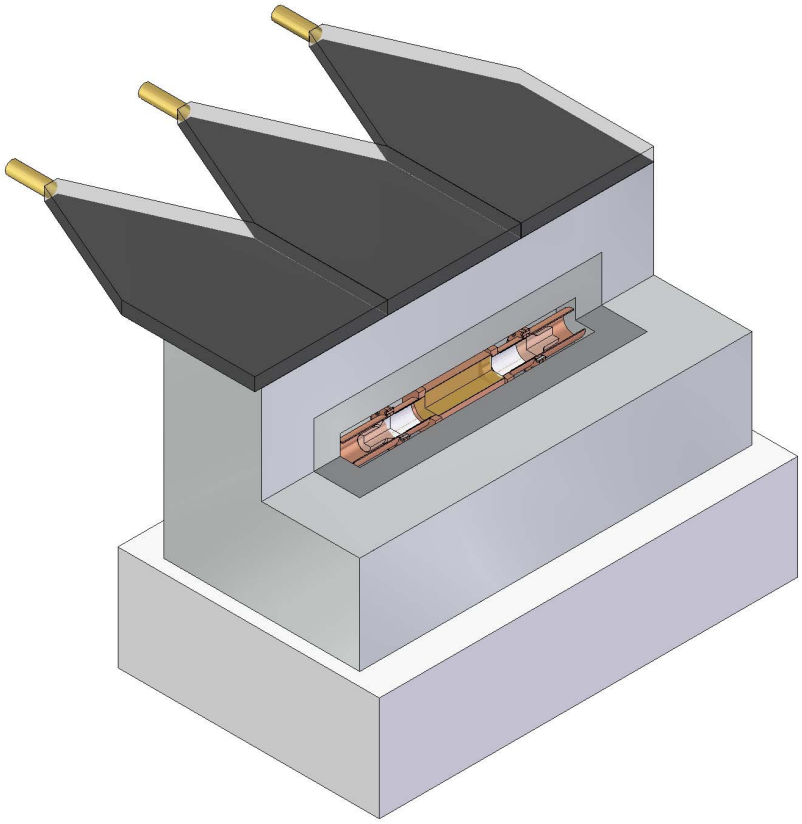

Figure 2.7: *Schematic drawing of the ANAIS-0 experimental layout. It can be seen the NaI(Tl) crystal, the copper encapsulation, light guides, PMTs, ancient lead, low activity lead, a polyethylene base, and three vetoes anti-muons.*

(a) (b)

Figure 2.8: *The ANAIS-0 lead shielding over the polyethylene base. In (a) the ANAIS-0 module over the lead and in (b) the complete lead shielding are shown.*

- An anti-Rn box allows closing the shielding to prevent the entrance of airborne radon inside the experimental space (by continuously flushing with radon-free nitrogen gas which keeps an slight overpressure). First, an anti-Rn bag was used, upgraded for

the set-up 5 to a box made of aluminum and PVC and expandable to house the whole ANAIS shielding. Figure 2.9 shows the two anti-Rn systems used.

(a)

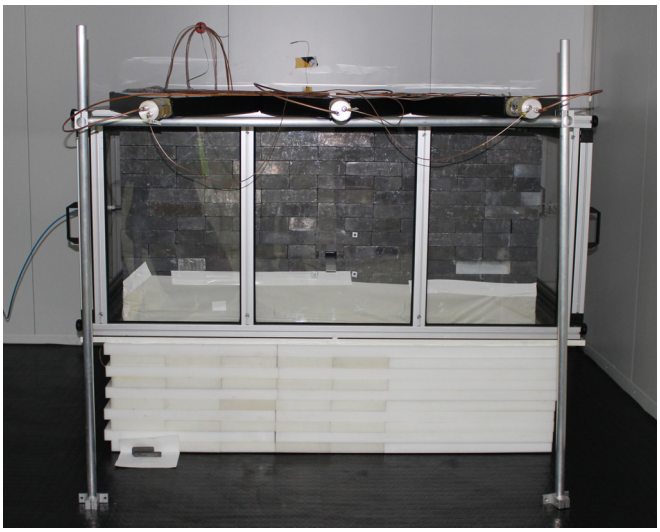

(b)

Figure 2.9: *ANAIS-0 experimental layout in two different configurations: (a) set-up 2, at old LSC facilities using an anti-Rn plastic bag to close the shielding; (b) set-up 5 at the new LSC facilities using an anti-Rn box. In both setups, active vetoes anti-muons can be seen on top of the shielding.*

- The lead is placed over a polyethylene base (see Figure 2.9), which is part of the neutron shielding that will be used for the whole ANAIS experiment, but that was not completed during ANAIS-0 measurements.
- 3 plastic scintillators ($0.5 \times 1 \times 0.05\,m^3$) were installed, during the set-up 2 measurement, to monitor the muon rate in the laboratory at the shielding position,

reject the corresponding contribution to the background and evaluate any possible related seasonal variation. Only partial coverage of the shielding (the upper part) was accomplished. They are also shown in Figure 2.9.

2.4 Canfranc Underground Laboratory

The Canfranc Underground Laboratory (LSC) [110] is an underground scientific facility located in a railway tunnel in disuse crossing from Spain to France, under the Pyrenees. The laboratory is 2450 m.w.e. down from Monte Tobazo. It is mainly devoted from the beginning to study rarely occurring phenomena such as the double beta decay of some nuclei or the interactions of the hypothetical dark matter particles with atomic nuclei. Figure 2.10.a shows a longitudinal section of the rock overburden profile along the Somport railway tunnel and the location of the different facilities.

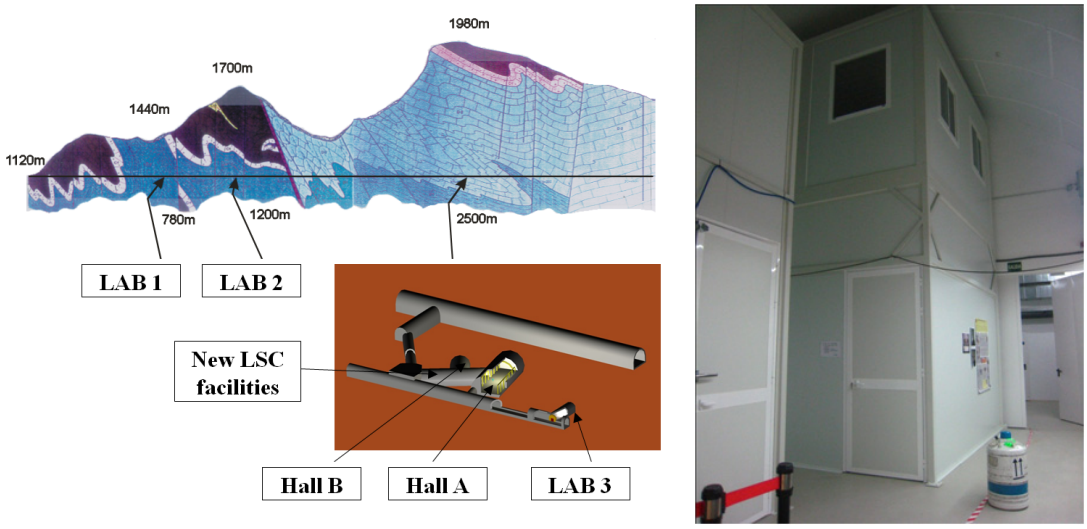

(a) (b)

Figure 2.10: *(a) Profile of the rock coverage along the Somport tunnel. Maximum rock overburden is achieved below the Tobazo (1980 m high). The different locations of LSC facilities along the railway tunnel are marked. (b) ANAIS hut in the new LSC facilities.*

2.4.1 Old LSC facilities

The research activities of the LSC go back till 1985. The laboratory was devised by professor Ángel Morales and developed by researchers of the Nuclear and Astroparticle Physics Group of the University of Zaragoza. Since then, different locations and upgrades of the laboratory have taken place. The first laboratory facilities were two old stores (24 m^2 in total) located under a rock overburden of 675 m.w.e. (LAB 1). Some years later

two new sites were conditioned moving to higher rock overburden: LAB 2, 27 m^2, under 1380 m.w.e. and LAB 3, 120 m^2, under 2450 m.w.e., the maximum coverage the mountain profile allows along the tunnel.

These old LSC facilities housed several experiments with international relevance aiming at the dark matter direct detection (NaI32 [94], COSME [111], or ROSEBUD [54,112–116]) or the $\beta\beta$ decay of nuclei as ^{78}Kr and ^{76}Ge ($\beta\beta/\gamma$ [117], Krypton [118], and IGEX [119]).

The ANAIS-0 module was first installed at the old LSC facilities (LAB 3) and took data there from April 2009 to February 2011.

2.4.2 New installations of the LSC

The new facilities of the LSC have 1250 m^2 of total area divided in two experimental halls: 40 x 15 x 12 m^3 (Hall A) and 15 x 10 x 7 m^3 (Hall B), as well as offices, a clean room (class 10000), a mechanical workshop and a gas storage room. External space is also available at LSC, an external building houses headquarters, administration, workshops and additional laboratories.

There are several experiments currently running in the LSC: ANAIS, ROSEBUD [120] and ArDM [121] to look for dark matter; BiPo [120], NEXT [122] and SuperKGd involved in the the study of neutrino properties; and GEODYN devoted to Geoscience. There is also a proposal for an Underground Nuclear Astrophysics Facility, CUNA.

The new facilities of the LSC are managed by a consortium formed by the Government of Aragón, the Ministry of Economy and Competitiveness and the University of Zaragoza. The LSC has a Scientific Committee formed by scientist of international reputation whose purpose is to study the experiments proposals as well as follow up the progress of those experiments already approved.

2.4.3 Moving ANAIS-0 to the new LSC facilities

Shielding, electronics, plastic scintillator vetoes and ANAIS-0 module were moved from the old LSC facilities into the Hall B from 16^{th} to 18^{th} February, 2011. ANAIS was the first experiment that moved to the new facilities and began taking data there.

The ANAIS experiment, and hence the ANAIS-0 module, are housed in Hall B in a specially designed hut (see Figure 2.10.b). It has removable walls to allow the convenient

access to the experimental space (lower part of the cabin) and a control room, placed at the upper part of the ANAIS cabin, is reached by external metallic stairs.

2.5 Signal processing

When a particle interacts in the NaI(Tl) crystal, the scintillation process converts a fraction of the energy released in the interaction into light. This light propagates, experimenting reflections in the faces of the crystal and the surrounding materials (Teflon and reflector) until it is transmitted to the PMT photocathode. Light losses should be minimized in order to achieve the best performance of the detector. The light is finally converted into an electrical pulse and, at the same time, amplified by photomultiplier tubes. This electrical signal has to be processed in order to draw as much information as possible from the energy release. The signal processing can be divided into three main steps: the first one is the electronic chain used to treat the analogical signal coming out from the photomultiplier and convert it into digital, the second is the acquisition program which controls the different electronic modules and stores the data in an appropriate format, and the third one is the analysis program which processes digitally the acquired data to derive useful parameters, apply filtering procedures off-line, etc.

During the ANAIS-0 module operation, the electronic chain was upgraded to a combination of VME and NIM electronics, and a new acquisition and analysis software was developed [96]. Before the installation at LSC, hardware and software of the new acquisition system were tested in Zaragoza with the PIII.

2.5.1 Electronic hardware

In a first approach, the electronic chain can be divided in two main parts: one is dedicated to obtain information about the interaction (energy and shape of the signal) and the other to generate a trigger.

The new VME acquisition was moved and mounted at LSC, with the ANAIS-0 module, the 15^{th} December 2011, during set-up 4. The VME electronics conceptual design is very similar to the previous, with the advantage that it is fully configurable and easier to scale up to 20 modules, as required for the whole ANAIS experiment.

Diagrams of both electronic chains are shown in Figures 2.11 (first) and 2.12 (new).

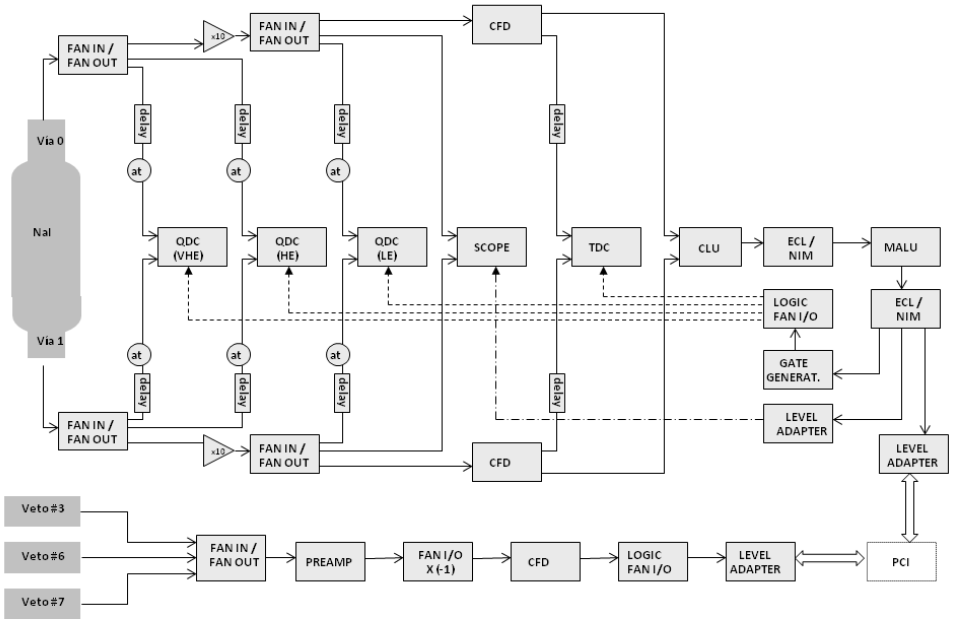

Figure 2.11: *First ANAIS-0 electronic chain scheme.*

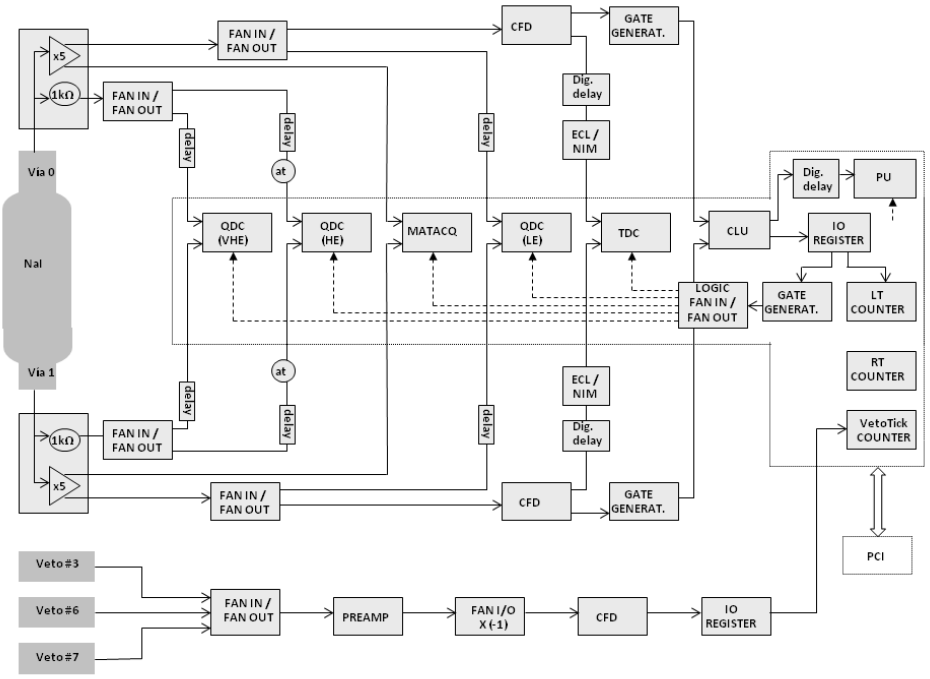

Figure 2.12: *VME electronic chain scheme for one module.*

Each ANAIS module generates two independent signals, one from each PMT, to be processed. The signal of each PMT is divided into three parts: two are sent, conveniently delayed, to the QDC (Charge Digital Converter) modules with different attenuations to record the high (E <2 MeV) and the very high energy (E <20 MeV) regions, while the other is amplified. The amplified signal is also divided in three: one is sent, delayed, to the low energy (E <200 keV) QDC, other to an oscilloscope Tektronix TDS5034B, where the pulse is digitized, and the third is used to generate the trigger. The first step of the trigger chain is a Constant Fraction Discriminator (CFD). If the signal is over the CFD threshold, that is adjusted in order to trigger at photoelectron level, a 200 ns gate is generated and sent to a coincidence logic unit, in mode AND: a trigger is generated if the gates opened by the two PMT signals overlap in the coincidence logic unit. This implies that signals triggering have at least one photoelectron per PMT in a 200 ns window.

Some improvements in the first steps of the chain shown in Figure 2.12 (similar to that shown in Figure 2.11) were introduced to increase the signal to noise ratio. Instead of using FAN-IN/FAN-OUT module for the signal division (see Figure 2.11), the direct PMT signal is divided into two branches by a resistive passive splitter: 19/20 of the input signal is sent to a specially designed for such a purpose preamplifier and the remaining 1/20 is used as input of the very high energy QDC. After passing through the preamplifier, the signal is divided in other two branches: one is the direct input signal of the digitizer and the other is treated as before.

The vetoes signals are added, conveniently amplified, and sent to a CFD to generate a trigger signal that resets and starts a counter. The CFD threshold is adjusted so that only residual cosmic muons arriving to the LSC generate a trigger.

In the following, the main modules used in the electronic chain are briefly described:

- **HV power supply.** PMTs require voltages between 1000 and 1500 V, depending on the model, provided by a very stable HV power supply. A LeCroy multichannel HV power supply was used at the beginning of the operation of ANAIS-0 module, but was upgraded to a new CAEN HV power supply (A1833BP board housed in a Universal Multichannel Power Supply System SY2527). The latter was the option chosen for the whole ANAIS experiment, because it profits from a high density of channels. However, important noise and cross-talk effects were identified as coming from this HV source and efforts in collaboration with CAEN technical staff were carried out in order to solve them. Specially designed filters were incorporated in

the HV output and improvement in the noise levels proved to be significant, but further work is still required to completely solve the problem.

- **Constant Fraction Discriminator (CFD).** A 200 ns digital window output is generated by this module (CAEN N843) when the signal overcomes a determinate voltage, parameter that is configured at the beginning of any data taking and defines the hardware trigger level. The trigger is produced at the position the signal reaches a given fraction of the signal maximum. This implies that the trigger position (in time) is independent of the size of the signal.

- **Coincidence Logic Unit (CLU).** The CLU module (CAEN N455) can be configured in mode AND or OR. The outputs of the CLU modules corresponding to each detector pass through the CLU in AND mode.

- **Dual OR.** If several detectors are used, the output of the CLU modules pass through a dual OR module (CAEN N133) to generate a global trigger.

- **Input/Output Register.** When a coincidence is generated by the CLU, this module (CAEN V977B) is in charge of raising a level which, read by the acquisition software, launches the beginning of the event acquisition routines. This level is reset when the software has finished the event acquisition. With the old acquisition, this step was done by a MALU (Lecroy MAjority Logic Unit, CAMAC 4532) module.

- **Pattern Unit (PU).** When several detector modules are used, this unit (CAEN V259N) identifies which detector(s) made the trigger and assigns a mask to the event with that information. In the old acquisition the MALU module saved itself this information.

- **Gate Generator.** This module (NIM 222 and CAEN V993B) generates a fixed gate, 1 μs width in our case, to establish the QDCs and TDC integration time.

- **Amplifiers.** Fast amplifiers (Lecroy NIM 612A and CAEN N979) were used to improve the signal to noise ratio. During the ANAIS-0 operation they were replaced by preamplifiers placed inside the ANAIS hut, very close but outside the ANAIS shielding. They are ultrahigh speed current feedback amplifiers with a good slew rate, enabling the resulting preamplifier to have a good bandwidth. They were specially designed for ANAIS, providing two main outputs, one for triggering and one for digitalization.

- **Signal Attenuators**. In order to keep spectral information in several dynamic ranges, the QDC input signals are attenuated to fit in the desired energy ranges

(low, high and very high energy) by a resistors set, conveniently adjusted to the desired energy ranges.

- **Charge Digital Converter (QDC).** It is a device that converts the input charge signal into a channel number by integration in the chosen gate ($1\,\mu s$ in our configuration), keeping the proportionality with the charge in the dynamic range. A fixed value of charge (pedestal) is always injected by the module itself to the signal, in order to guarantee the proper working of the QDC. The channel range goes from 0 to 2048 for the old QDCs (Canberra ADC 8713) and from 0 to 4096 for the new QDCs (CAEN V792). The CAEN QDCs require a decoupling board (A992) in the input signal, which eliminates the DC level of the signal.

- **Time to Digital Converter (TDC).** The information of the arrival time of each signal, is saved by the TDC modules (CAMAC 2229 and CAEN V775) to study the chance coincidences. The time lapsed from the beginning of the gate up to the arrival of the signal is saved as a digital number.

- **Digitizer.** In order to obtain all the information from the shape of the pulse, each event is digitized. First, a scope from Tektronix series TDS5034 was used. It presents a bandwidth of 350 MHz, a sampling rate up to 5 GS/s with 8 bits of resolution, and records from 500 to $2 \cdot 10^6$ points of temporal resolution. A choice of 0.8 ns/point sampling was done for the ANAIS-0 data taking. With the upgrading of the electronics, a MATACQ CAEN V1729 digitizer card was installed. It presents a bandwidth of 300 MHz, a sampling rate of 2 GS/s, 2520 points of temporal resolution and a dynamic range of 1 V (in this case, it is fixed) with 12 bits of resolution.

- **Time Counters.** For the ANAIS experiment a precise determination of the live time is required. Dedicated counters (CAEN V560) have been installed with that purpose. Independent time counters are used for the registering of the time after a veto signal in the plastic scintillators.

- **FAN-IN/FAN-OUT.** Analogic (CAEN N625) and Logic (CAEN N454) FAN-IN/FAN-OUT modules are used to obtain up to four outputs from the same input. They are also used to add the three vetoes signals first, and then to invert the subsequent preamplifier output before entering the CFD (see Figures 2.11 and 2.12).

- **NIM-ECL converter.** This converter (CAEN N638) is needed to adapt the TDC and MALU input signals.

- **Delays.** Analogical delays are needed to retard the QDCs input signals till the trigger is done and the QDC integration windows are open. This analogical delays

are implemented by using long cables and adjusting conveniently their length. The scope inputs also needed to be delayed, unlike the MATACQ signals. Digital delays are required for the TDC and PU inputs. A module has been specially designed for the ANAIS electronic chain with such a purpose [108].

2.5.2 Acquisition software

The acquisition program used in ANAIS-0 is easily scalable to a large number of detectors and it can be configured, i.e. some parameters can be changed without compiling the program. Data are saved in binary files (*.raw), organized in blocks. This program was described in [89, 123]. The information saved for each event is:

- General information: live time counter value, real time counter value, time after last veto event, mask informing about the trigger (useful if more than one detector is taking data).
- Specific information for each PMT output signal (two signals for each detector triggering): three QDC values, one TDC value, and the digitized pulse.

In parallel to the upgrading of the electronic chain, a completely new environment was developed in C++. It is fully configurable: with a single configuration file many different hardware configurations can be controlled. Sampling rate, number of detectors and signals, file size and pretrigger are some of the parameters that can be configured, but also the graphical interface can be chosen and some conditions for the acquisition can be imposed, as for example, in calibration mode digitized pulses are not saved to reduce the measurement dead time, or an energy window can be selected in order to only store pulses in that region of interest.

All the information is directly saved into root files (see section 2.5.3) for off-line analysis. Drivers for the control of many VME modules have been specially developed, tested and optimized. The software was tested to avoid bottlenecks and stability problems. Dead time was estimated with pulser generated signals and measured with counters, resulting a value of 2 ms/event, mainly dominated by the digitization conversion time, improving the 4 ms/event obtained with the old acquisition [89].

2.5.3 Analysis software

The data analysis is done with ROOT [124]. It is a framework for data processing, born at CERN, to be used in the field of high energy physics. However, the versatility and functionality of the package has triggered a broad spread of its use, being nowadays the reference analysis code in different particle physics applications. It can be used to save, access and process data as well as to show results, either in interactive mode or by developing specially designed scripts.

In the old version of ANAIS acquisition software, raw data were produced that had to be converted into root format, as first analysis step. The upgraded acquisition saves the data directly in root format, although an off-line analysis is still required in order to get the relevant pulse information without increasing the acquisition dead time.

There are some configurable parameters in this off-line analysis procedure that depend on the particular acquisition configuration: analysis threshold to define the start of the pulse, pretrigger region where baseline is calculated, threshold for the peak search algorithm (and also peak width) related to the SER of the PMTs used, etc. Some of the more relevant parameters resulting from the analysis for each pulse are:

- **Baseline and root mean square.** The mean value and standard deviation of the baseline noise are obtained from the first points (pretrigger region) of the pulse.
- **T0.** The pulse onset is assigned to the point the point where the pulse overtakes the analysis threshold.
- **Pulse areas.** The pulse area in a chosen pulse region is calculated as the addition of the points in that region, subtracting the corresponding DC contribution. Different parts of the pulse can be of interest and, hence, different pulse areas are calculated in the off-line analysis: total pulse area (from T0 to the end of the pulse), SER area (50 ns around the last peak in the pulse) or some partial areas, that are used to build pulse timing parameters, as for instance P1s (see section 3.1).
- **Maximum and minimum of the pulse**. The minimum (and maximum) of the pulse are calculated and its positions in the pulse are also saved. Subtracting the DC level to the minimum of the pulse, the amplitude of the pulse is calculated. It is worth noting that the pulse is a negative voltage signal.
- **Number of peaks in the pulse.** An algorithm that determines the number of peaks in the pulse has been developed. It is based on the TSpectrum ROOT class

and the Search method [125]. Peaks are considered gaussian with a minimum height and width, which are selected specifically for every data set. Information about the position of the peaks in the pulse is also saved. In section 3.1 this variable will be studied. This variable makes sense only for very low energy pulses where single photoelectrons can be distinguished.

Figure 2.13 shows an example of a digitized pulse corresponding to a low energy event, in which some of the parameters derived from the off-line analysis are remarked: baseline (horizontal red line), T0 (green line), minimum position (blue line) and the peaks identified (red triangles).

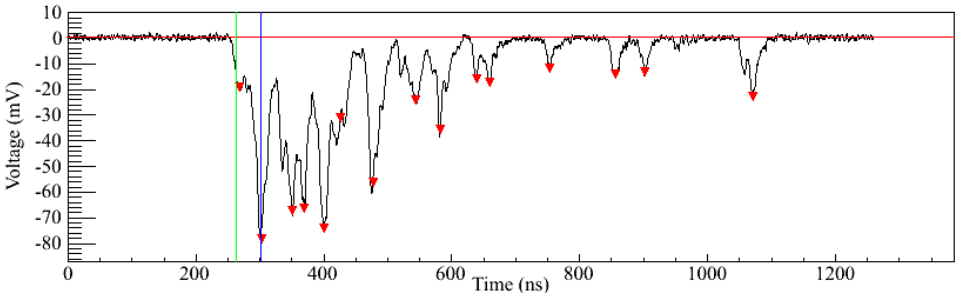

Figure 2.13: *Example of digitized pulse with the MATACQ board and some of the parameters derived from the analysis: baseline (horizontal red line), T0 (green line), minimum position (blue line) and the peaks identified (red triangles).*

2.6 Slow-control

To monitor the stability of all the environmental and experimental parameters is mandatory for an experiment aiming at being sensitive to the annually modulated dark matter signal. Tuning of the probes and test measurements with some of them have been carried out since the beginning of ANAIS-0 operation. Environmental operation conditions at the old LSC facilities were not optimal, but they improved noticeably after moving at the new facilities. However, also some problems were detected, as it will be commented later.

Continuous monitoring of different environmental parameters has being carried out since the moving of ANAIS-0 to the new LSC facilities (March 2011): radon air content, pressure, humidity, temperature in the ANAIS electronics rack, temperature in ANAIS experimental room, temperature in Hall B, evaporated nitrogen flux coming into ANAIS shielding, PMT High Voltage Supply values, intensity of the HV supply source and total trigger rate of the ANAIS-0 module.

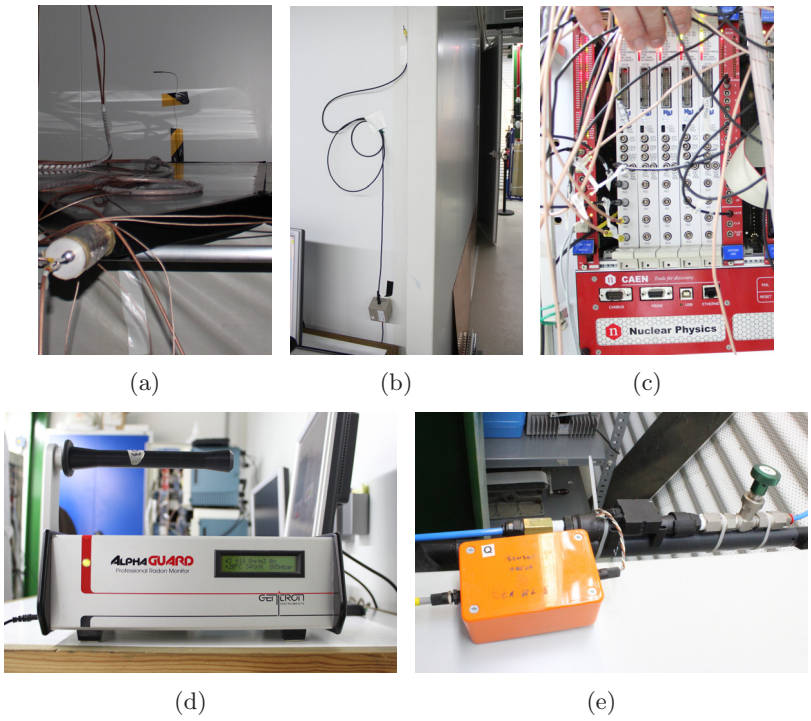

(a) (b) (c)

(d) (e)

Figure 2.14: *Temperature probes: at ANAIS hut (a), at Hall B (b), and at the electronics rack (c). AlphaGUARD meter placed in Hall B (d). Nitrogen flux meter before the entrance of the gas pipeline into the ANAIS hut (e).*

Radon air content, pressure and relative humidity are measured with an AlphaGUARD system [126] every 10 minutes. The temperatures, controlled with PT100 probes, and the nitrogen flux that enters into the shielding are monitored every 3 minutes with a specially designed program [123]. Figure 2.14 shows the AlphaGUARD meter, the temperature probes and the flux meter in the new LSC facilities.

During May of 2011, the radon activity was simultaneously measured in Hall B and inside the ANAIS hut. Average activities of $88.0 \pm 0.5\,Bq/m^3$ and $86.5 \pm 0.5\,Bq/m^3$ were measured in Hall B and inside the ANAIS hut, respectively. Hence, similar radon activity is expected in both locations. The radon content inside the ANAIS shielding, in overpressure and continuously flushed with radon-free nitrogen gas, should be much lower to that of Hall B (upper limits are estimated in section 4.2.3, but they have not been directly measured).

After 19 months of measurements, radon air content in Hall B of LSC averaged per day and month is shown in Figure 2.15, also pressure and relative humidity measurements are shown in Figure 2.16. Corresponding mean values and their standard deviations are reported in Table 2.8. A seasonal fluctuation can be clearly identified in the radon and humidity values along the measurement period and they have been fitted to a sinusoidal

function, letting as free parameters the amplitude of the fluctuation, the mean value, the period and the phase:

$$y = y_0 + A \cdot sin\left(\frac{2\pi}{T}(x - x_c)\right) \tag{2.1}$$

The values obtained in the fit are shown in Table 2.9. They are compatible with an annual modulation, having the maximum around the 25^{th} July (with an error of more than ten days). Both modulations are clearly correlated, although the amplitude is higher for humidity (30.9%) than for radon (15.5%). Nevertheless, more data are needed to confirm such a modulation and to identify its origin.

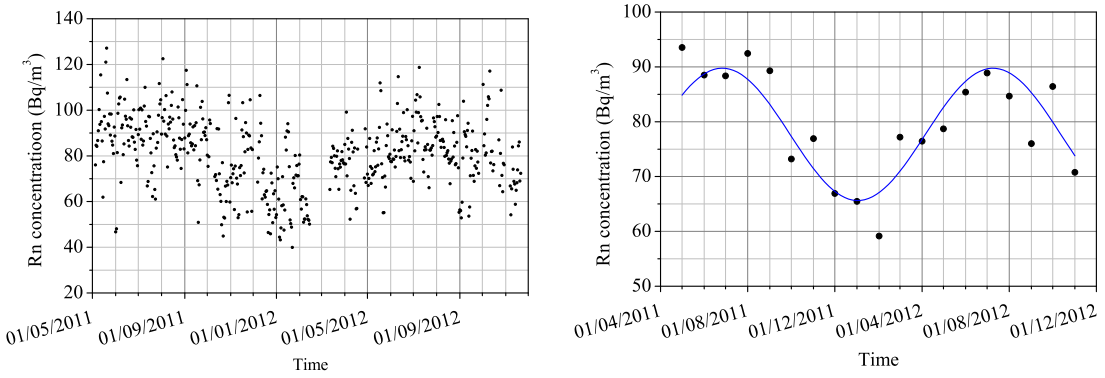

(a) (b)

Figure 2.15: *Rn air content in Hall B from May 2011 to November 2012. Data are averaged on days (a) and months (b). Result of the data fit to a sinusoidal function is shown in blue, and the parameters of the fitted function are shown in Table 2.9.*

Parameter	Mean value	σ
Radon	$80.9 \pm 0.3\, Bq/m^3$	$29.9 \pm 0.4\, Bq/m^3$
Pressure	$882.84 \pm 0.02\, mbar$	$5.41 \pm 0.02\, mbar$
Relative humidity	$44.8 \pm 0.7\,\%$	$9.9 \pm 0.9\,\%$

Table 2.8: *Mean values of the radon air content, pressure and relative humidity monitored during the ANAIS-0 operation (from May 2011 to December 2012) at the new LSC facilities, measured with an AlphaGUARD system.*

However, the radon activity in Hall B (or inside ANAIS hut) does not affect directly to the ANAIS background, because the radon content inside the ANAIS shielding, in overpressure and continuously flushed with radon-free nitrogen gas, should be much lower to that of Hall B (upper limits are estimated in section section 4.2.3). Therefore, even in the case of confirmation of such an annual modulation effect in the radon air content,

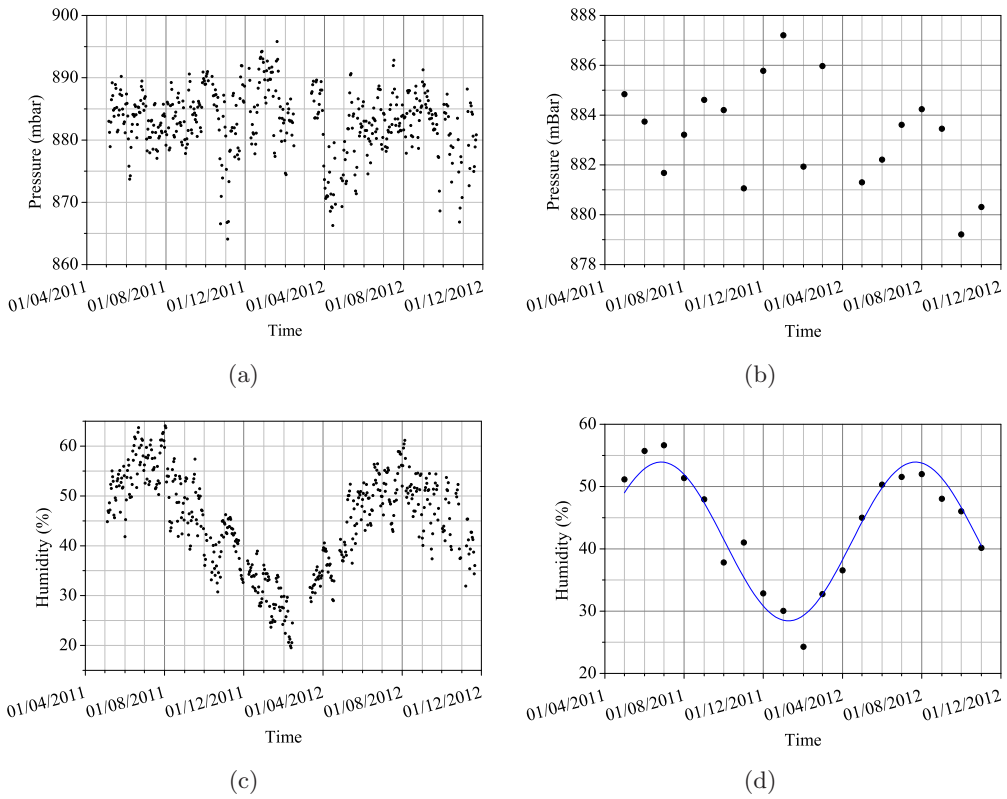

Figure 2.16: *Pressure (a,b) and humidity (c,d) measurements obtained with an AlphaGUARD system in Hall B. Data are averaged on days (a,c) and months (b,d). Result of the relative humidity data fit to a sinusoidal function is shown in blue, and the parameters of the fitted function are shown in Table 2.9.*

Parameter	Radon	Relative humidity
y_0	$77.70 \pm 1.34\, Bq/m^3$	$41.19 \pm 0.68\%$
A	$12.07 \pm 1.89\, Bq/m^3$	$12.75 \pm 0.96\%$
T	$379 \pm 20\, days$	$392 \pm 11\, days$
x_c	$22^{nd}\ April \pm 20\ days$	$19^{th}\ April \pm 10\ days$
$Maximum$	$26^{th}\ July \pm 21\ days$	$23^{th}\ July \pm 11\ days$

Table 2.9: *Parameters obtained from the sinusoidal fit of the radon and humidity measurements.*

neither a relevant contribution to the ANAIS background, nor a modification in the ANAIS prospects are expected.

The temperature is monitored in different locations around ANAIS experimental space: in ANAIS electronics, inside ANAIS hut and in Hall B, using PT100 probes. With the AlphaGUARD the temperature of Hall B is also measured, but with lower precision. In Figure 2.17 the behaviour of the monitored temperatures is shown. In particular, it has

to be remarked the presence of sudden changes in the Hall B temperature, some of them corresponding to changes in LSC thermostat configuration: from 17 °C to 20 °C the 3^{rd} of August and from 20 °C to 19 °C the 15^{th} of September, for instance. Modifications on the ventilation system operation conditions are responsible of other changes. The temperature at the ANAIS electronics decreased significantly after the installation of the new VME electronics (December 2011), thanks to the better ventilation system of the modules. Good agreement between both measuring systems, PT100 probes and AlphaGUARD, can be observed (see Figures 2.17.a and b)

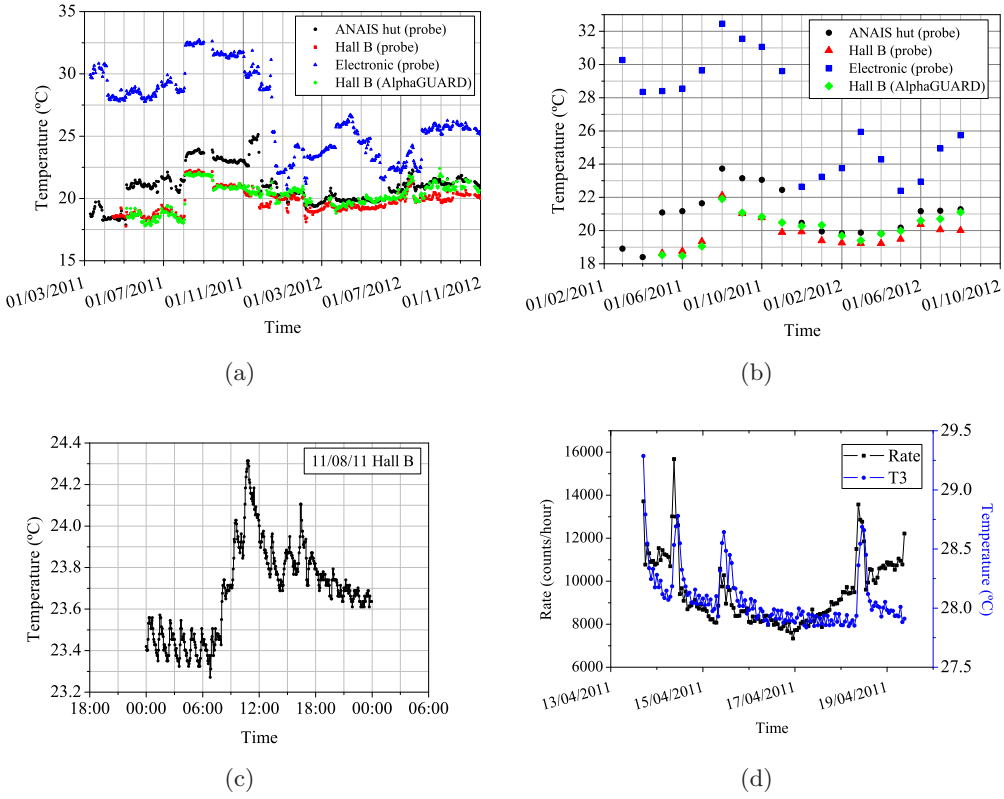

Figure 2.17: *Measurements of the temperature in three different locations at LSC for the whole monitored period; data averaged in days are shown in (a) and averaged in months in (b). Variation of temperature in Hall B along one day, arbitrarily chosen, without averaging is shown in (c). It can be clearly seen the period of the thermostat regulation. Correlation between temperature at ANAIS electronics and trigger rate is shown in (d).*

In Figure 2.17.c a 24 h zoom of the temperature variations along the 11/08/11 is shown. It can be observed that the thermostat seems to work pretty well and can correct changes of 0.1 °C, in about one hour. However, there is only one thermostat for all the laboratory and is placed in Hall A, therefore, local temperature variations related, for instance, to the human presence in Hall B can not be corrected.

Correlation of ANAIS-0 trigger rate with temperature at the electronics rack was observed in some periods of ANAIS-0 data taking, disturbing considerably the acquisition. An example of that correlation is shown in Figure 2.17.d. In this case, the origin of the effect was found in the QDC module DC input level and was avoided by the use of an specific decoupling board (see section 2.5). Similar effects were also observed in the Dual OR module. In this case, the module needed to be repaired by CAEN (two diodes and one integrated circuit malfunctioned).

The nitrogen gas flux that enters into the ANAIS-0 shielding has also been monitored. At the moment, the LSC furnishes radon-free nitrogen gas (evaporated from liquid) to all the experiments, but previously ANAIS had its own nitrogen supply system. An average of $0.830 \pm 0.011\, l/min$ can be reported.

The PMT High Voltage Supply values and intensity of the HV supply source were monitored during set-up 2 at the old LSC and during set-up 4 at the new facilities. Fluctuations of only 0.25 V (<0.02%) have been observed.

2.7 Detector calibrations

Radioactive sources have been used to calibrate the ANAIS-0 module, to check the gain stability, to get reference NaI(Tl) scintillation events for the data analysis, to search for systematic effects in the simulations, etc. An aluminized Mylar window was included in the detector design to allow calibration at very low energy (below 20 keV) with external gamma sources, it can be seen in Figure 2.18.a. The radioactive source is introduced into the shielding and placed just in front of the Mylar window with the help of a Teflon tray, see Figure 2.18.b. The radioactive sources used for high and low energy calibrations are listed in Table 2.10, together with their main emission lines and intensities. Typical calibration spectra for most of them are shown in Figure 2.19.

Stability of the gain (through periodic calibration at high and low energy) along the ANAIS-0 data taking has been studied. A ^{57}Co source has been chosen for weekly calibrations of the prototype because its low energy X and gamma lines (at 6.4 keV, 14.4 keV and 122.1 keV) reach the crystal through the calibration window built in the copper encapsulation. The deviation in % from the average channel value for each of these lines is shown in Figure 2.20.a. A ^{22}Na source has been also used for calibration and the high energy stability is shown in Figure 2.20.b for the 511 keV and 1275 keV lines.

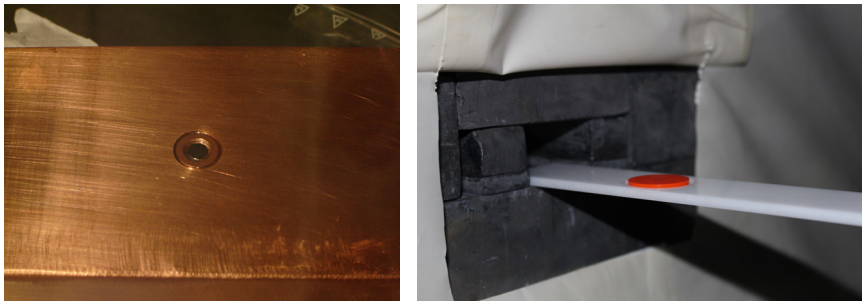

(a) (b)

Figure 2.18: *(a) Aluminized Mylar window in ANAIS-0 copper encapsulation and (b) Teflon tray to introduce the radioactive sources into the shielding and to position them precisely in front of the Mylar window.*

Deviations are small in all cases, but more stability will be required for the ANAIS experiment. It is worth noting that during the ANAIS-0 operation it was required to switch off and on the PMTs HV supply several times. That probably had an effect on gain stability. In data from setups 2 and 4, a gain drift can be observed. Its origin has not been established, but could be due to a malfunction of the old QDC modules or the HV power supply.

One of the most important issues for ANAIS is to guarantee a good energy calibration at the lowest energies, down to the threshold. In Figure 2.21.a a linear fit (energy vs QDC channel) is shown; all the available energy lines below 150 keV have been used (from ^{57}Co, ^{55}Fe, ^{133}Ba and ^{109}Cd) as well as the 3.2 keV line from ^{40}K, the origin of this line is explained is section 4.1.2. Residuals from the fit are also shown in Figure 2.21.a. In Figure 2.21.b it is shown a linear fit with all the lines used in 2.21.a except the 5.9 and 6.4 keV ones. It can be noticed a reasonable linearity down to 14.4 keV, but residuals at 6.4 and 5.9 keV are much larger (and both positive), specially considering them in percent, than those obtained for the other lines, including the 3.2 keV one. Although non-linearity effects had been previously reported in NaI(Tl) detectors, they cannot explain such a large effect as that seen in Figure 2.21.b. (5.9 keV line appears with an effective energy of 3.5 keV and 6.4 keV line with 4.0 keV), that however, could be explained by superficial effects either in the light yield or in the light collection efficiency (or both), that would not contribute for bulk energy depositions as that from ^{40}K.

Non-proportionality in the scintillation yield with respect to the deposited energy has been observed in inorganic scintillators [128, 129]. In particular, in NaI(Tl) scintillators some non-linear effects are expected at the K-shell Iodine binding energy (33.2 keV) because photoelectrons emitted following a K-shell photo-absorption do have less kinetic energy and ionize less. This fact has been observed experimentally [129–133] but it is

Source	Energy	Intensity
	keV	%
^{57}Co	6.4(*)	56.1 ± 1.0
	14.4	9.2 ± 0.2
	122.1	8.5 ± 0.1
	136.5	10.7 ± 0.2
^{109}Cd	22.6(*)	101.5 ± 1.5
	88.0	3.6 ± 0.3
^{133}Ba	31.7(*)	119.6 ± 1.4
	81.0	32.9 ± 0.3
^{137}Cs	32.9(*)	6.9 ± 0.2
^{55}Fe	6.0(*)	28.4 ± 0.5

Source	Energy	Intensity
	keV	%
^{22}Na	511	90.4 ± 0.2
	1275	99.9 ± 0.1
	1786 (A)	
^{60}Co	1173	99.9 ± 0.0
	1332	100 ± 0.0
	2506 (A)	
^{133}Ba	303	18.3 ± 0.1
	356	62.1 ± 0.2
^{137}Cs	662	85.0 ± 0.2
^{54}Mn	835	100 ± 0.0
^{152}Eu	245	7.6 ± 0.1
	344	36.6 ± 0.1
	444	3.1 ± 0.2
	779	13.0 ± 0.1
	964	14.5 ± 0.1
	1086	10.1 ± 0.1
	1112	13.4 ± 0.1
	1408	20.9 ± 0.1

Table 2.10: *Radioactive calibration sources used in ANAIS and their main γ and X emissions. Low energy lines are shown at left and high energy lines at right. Those energies marked with an (*) are average values from several lines that our detector can not resolve. Those energies marked with an (A) correspond to the addition of two lines that are emitted in cascade, producing a peak in the energy spectrum that can be used for calibration. No intensity is assigned, because it would depend strongly on the position of the source and geometry of the detector. Intensity of the very low energy lines will depend also on the location of the source, and the intensity of the 511 keV will also be related with the source-detector geometry. Only lines with an intensity over 3% are shown. Data have been obtained from [127].*

an effect smaller than 5% in the amplitude response. Similarly, at around 5 keV (L-shell Iodine binding energy) we should expect the same effect, but experimental data at that energy region are scarce [133].

Several groups working with large size NaI(Tl) detectors, aiming at the detection of dark matter, have observed good linearity at low energies, but reductions in the response to 5.9 keV energy X-rays from an external source, that were attributed to superficial effects [71,81]. In Ref. [81] a Compton scattering experiment was designed in order to obtain a volume-distributed low-energy population whose results supported such assumption.

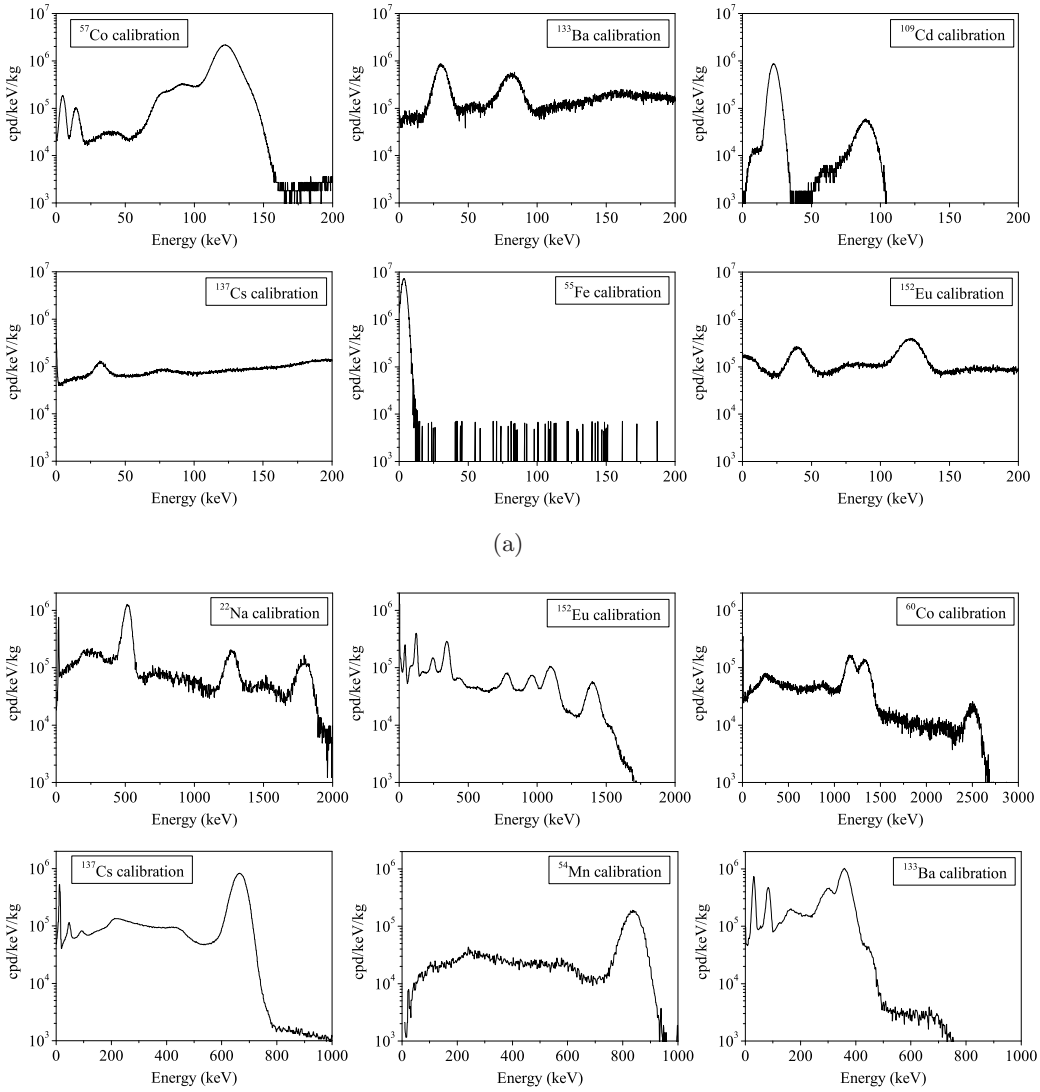

Figure 2.19: *Typical calibration spectra for the radioactive sources used with the ANAIS-0 module in the low (a) and high (b) energy ranges.*

Because the dark matter region of interest in NaI(Tl) scintillators is below 10 keVee, it was decided to calibrate the low energy range using only 3.2 keV, 14.4 keV and 22.6 keV lines trying to minimize possible non-linear effects in the detector response. In Figure 2.21.c are shown the linear fit and residuals corresponding to the low energy calibration for the set-up 4 data, used in the following chapters is:

$$E(keV) = (0.105 \pm 0.006) \cdot Ch - (7.4 \pm 1.2) \tag{2.2}$$

It has to be remarked that ANAIS-0 crystal has shown an anomalous behavior after excitation with a high energy radioactive source: it seems that long-life excited states

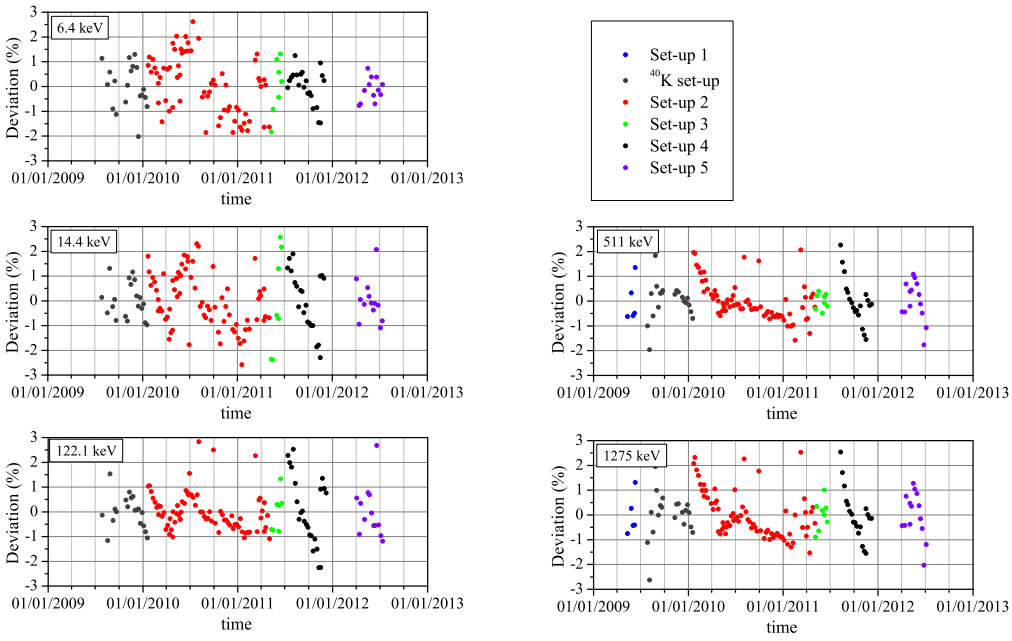

Figure 2.20: *Percentage of deviation in the position of the X and gamma lines from ^{57}Co (a) and ^{22}Na (b) weekly calibrations along the different ANAIS-0 setups.*

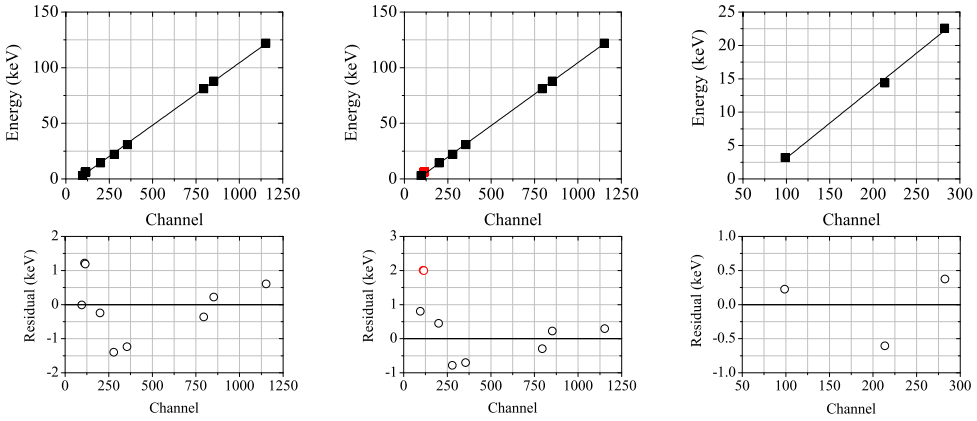

Figure 2.21: *Linear fit energy versus QDC channel and corresponding residuals using all the available lines below 150 keV coming from ^{57}Co, ^{109}Cd and ^{133}Ba radioactive sources and ^{40}K in the bulk (a). 5.9 keV and 6.4 keV lines from external origin could be strongly affected by superficial effects, and are not used in the fit shown in (b); in the residuals, those lines appear in red. The calibration chosen for the low energy region uses only 3.2 keV, 14.4 keV and 22.6 keV, trying to minimize possible non-linear effects in the detector response; it is shown in (c).*

are activated in the crystal, producing in their decay a large number of photons in a few hours following the irradiation. The number of photons is so large that increases strongly

the probability of chance coincidence in the 200 ns window and trigger rate shows an exponential behavior, see Figure 2.22.a. Most of the events contributing to this trigger rate increase have only two photoelectrons (one per PMT) and are easily identified and hence, rejected. However, in these periods data taking suffers from strong disturbance. For that reason, calibrations with high energy radioactive sources should be as short as possible and if full deexcitation of the crystal is not accomplished before the starting of the next background acquisition, those data are removed as first analysis step, before the background analysis (see section 3.1). This effect was observed since the beginning of ANAIS-0 operation underground, but had not been observed in other crystals as PIII, for instance, see also Figure 2.22.a.

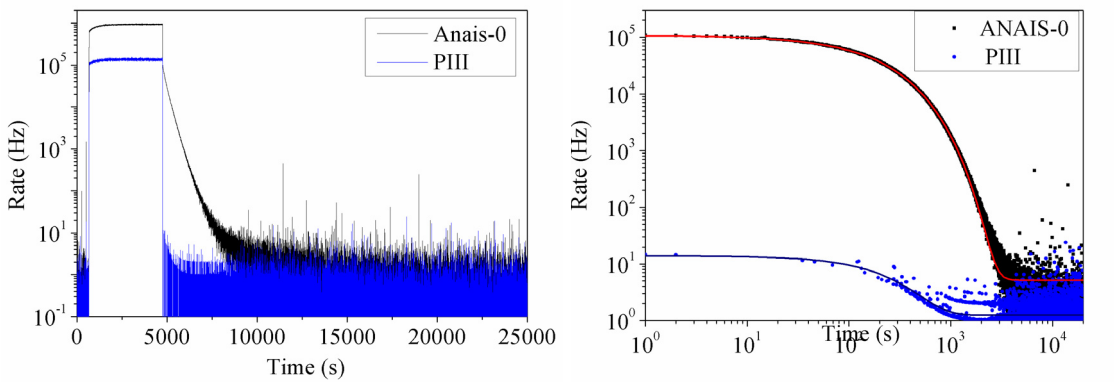

(a) (b)

Figure 2.22: *(a) Trigger rate before, during and after a ^{22}Na calibration for ANAIS-0 and PIII modules. It can be clearly observed the very high trigger rate after removing the radioactive source in ANAIS-0, lasting several hours. (b) Trigger rate after a ^{22}Na calibration and exponential decay fit for ANAIS-0 and PIII modules. Fit results are shown in Table 2.11.*

In Figure 2.22.b total trigger of ANAIS-0 just after a ^{22}Na calibration has been fitted to three exponential decays (the best fit achieved):

$$y = y_0 + A_1 \exp(-x/\tau_1) + A_2 \exp(-x/\tau_2) + A_3 \exp(-x/\tau_3) \tag{2.3}$$

and the results derived are shown in Table 2.11. The moment of taking out the source has been considered the initial time of the fit. When trying to fit similarly the PIII rate, taking data under equivalent conditions, only the slowest time constant can be fitted, but with a much smaller amplitude.

A full explanation of this effect has not been found, however, it seems to be related to the long scintillation time constants (tens and hundreds of milliseconds range) observed

Detector	τ_1 (s)	A_1 (kHz)	τ_2 (s)	A_2 (kHz)	τ_3 (s)	A_3
ANAIS-0	25.9 ± 0.4	12.1 ± 0.1	141 ± 1	45.3 ± 0.6	294.9 ± 1.1	52.6 ± 0.7 kHz
PIII	-	-	-	-	234.2 ± 8.3	12.7 ± 0.4 Hz

Table 2.11: *Exponential decay fit results of the trigger rate after a ^{22}Na calibration for ANAIS-0 and PIII modules. Fit function is shown in equation 2.3.*

after the interaction of very high energy particles in the crystal. This very slow scintillation components are also much more important in ANAIS-0 than in PIII, as it will be described in section 3.6.

2.8 Muon coincident events in ANAIS-0

Active plastic scintillator vetoes were installed on top of the ANAIS-0 shielding to reject the residual cosmic muon flux contribution to the background of ANAIS and also to monitor the muon rate in the laboratory at the shielding position in order to evaluate any possible seasonal variation. As mentioned in section 2.3, only partial coverage of the shielding was accomplished.

A good comprehension of the muon related events in ANAIS experiment is required, because annual modulation in the muon rate is well known [134, 135], and it should be discarded as responsible of any modulation observed in the very low energy events rate, and hence attributable to dark matter candidates. This issue has been discussed in the frame of the DAMA/LIBRA experiment [136, 137], and is even more important for the ANAIS experiment, because at the LSC rock overburden residual muon flux is significantly larger than at Gran Sasso Laboratory.

Muon coincident events have been identified using the time after the last muon event in the plastic scintillators: a counter is reset by any event triggering one (or more) of the active vetoes and its value read and associated to every event in the NaI(Tl) detector. Because of the different delays in the signals from plastic scintillators and NaI(Tl) crystal, coincident events appear after ~ 15 ms (see Figure 2.23). The large events accumulation below 3 ms is due to the over range of the counter time-scale, because the NaI signal rate is much higher than the veto trigger rate.

Figure 2.24 shows the muon coincident events rate in different experimental conditions: for set-up 2 after the installation of the vetoes in the old LSC facilities, for set-up 2 after the moving to the new installations, and for setups 3 and 4. The average rates in the

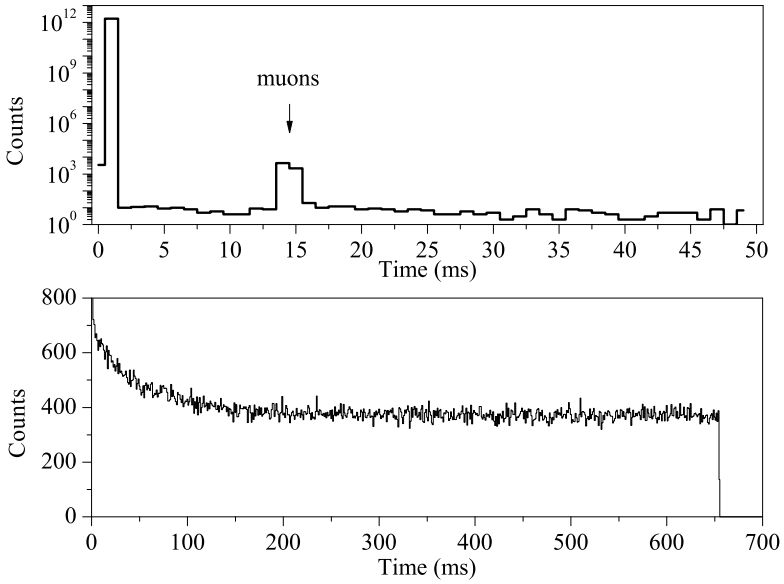

Figure 2.23: *Distribution of the time after the last trigger in the active vetoes for all the events in ANAIS-0 set-up 2 measurements. In the zoom (top), coincident events between vetoes and NaI(Tl) crystal appear after* ~ 15 *ms. The large accumulation of events near 0 is due to the over range of the counter, because the trigger rate in the NaI(Tl) crystal is much higher than that of the vetoes.*

different setups are shown in Table 2.12. An increase in the muon coincident events rate is observed after the moving to the new LSC facilities, as expected, since there is less rock overburden, and according to the available measurements: the muon rate at the old LSC facilities was measured to be $(2.47 \pm 0.3(stat) \pm 0.98(syst)) \cdot 10^{-3}\mu/m^2/s$ [51], while at the new facilities has been recently measured to be $(5.04 \pm 0.25) \cdot 10^{-3}\mu/m^2/s$ (preliminary results) [138]. The rate of events in coincidence with muons in the plastic vetoes increases in 8 cpd ($\sim$20%) when light guides are used (the only difference from setups 3 and 4), pointing to muon interactions in the light guides producing scintillation able to trigger ANAIS acquisition and contributing to the low energy background.

Set-up	LSC facilities	PMTs	LG	Muon coincident events rate
2	old	LB	Yes	37.1 ± 6.4 cpd
2	new	LB	Yes	46.0 ± 8.3 cpd
3	new	ULB	Yes	51.3 ± 10.8 cpd
4	new	ULB	No	43.4 ± 7.5 cpd

Table 2.12: *Average rate of events in ANAIS-0 coincident with the active vetoes in the different setups.*

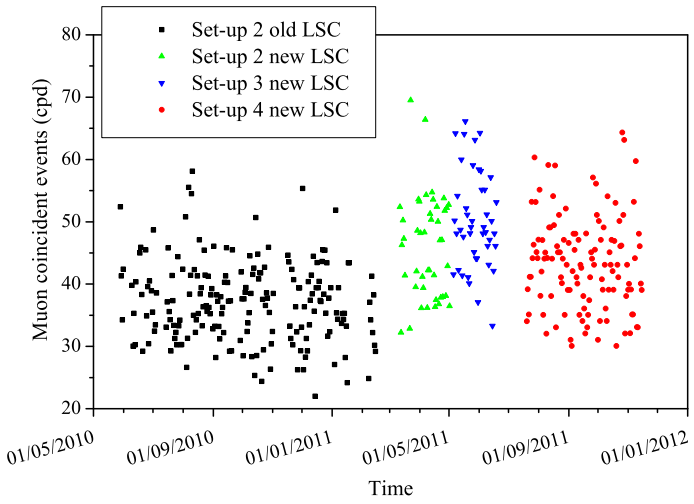

Figure 2.24: *Rate of events in ANAIS-0 crystal in coincidence with muons in the plastic vetoes at the old and new LSC facilities in different setups.*

In Figures 2.25 and 2.26, the energy distribution of the events coincident with a muon interaction in the plastic scintillator vetoes besides the total background of the ANAIS-0 module can be seen for setups 3 and 4. Because of the partial coverage of the plastic vetoes used, about 30% of the events above the alpha region in the NaI crystal data (and, hence, attributable mostly to muon interactions in the crystal) were not coincident with the vetoes. A relatively high rate of coincident events is observed at the lowest energies, especially when using light guides, as commented before. The rate from 1 to 100 keV shows an 86% increase when light guides are present (comparing setups 3 and 4), pointing at a scintillation effect in the methacrylate. Such events are not compatible with NaI(Tl) typical scintillation, supporting again the hypothesis of scintillation in the light guides. In sections 3.3, and 3.6 this issue will be discussed again. It is worth noting that total event rate attributed to muon coincident events in the dark matter region of interest is clearly further down the rest of the background contributions ($< 0.1\%$ in the 2-10 keV region.

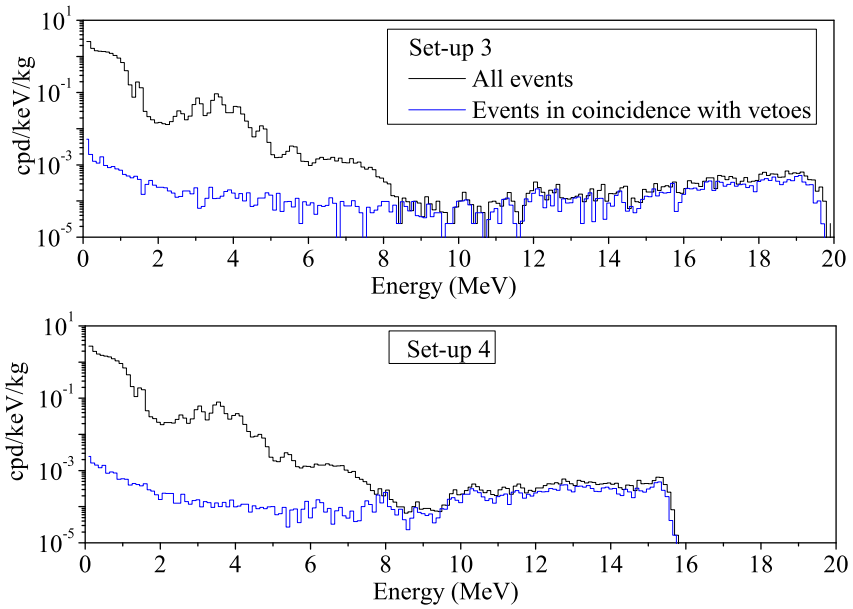

Figure 2.25: *Background spectrum measured with the ANAIS-0 module at very high energy, up to about 20 MeV. PMTs signals saturate (more in set-up 4 than in set-up 3), implying that the shape of the muon spectrum is modified and proportionality with energy is lost above 8 MeV.*

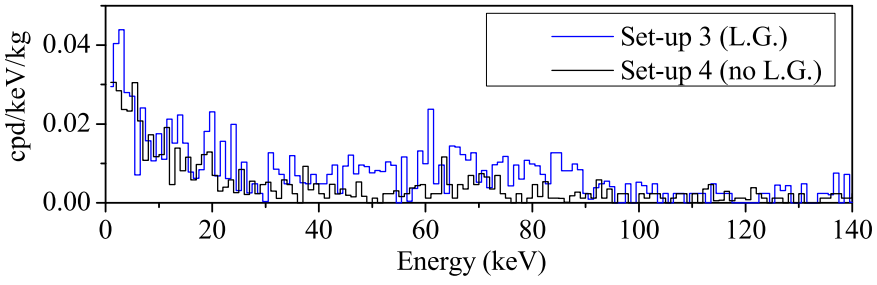

Figure 2.26: *Distribution of events at low energy coincident with a muon in the active vetoes. Clear contribution from events in the light guides can be observed.*

Chapter 3

Data analysis

Low energy events are of utmost interest for the ANAIS experiment because dark matter particles are expected to produce very small energy depositions in the detector: below 100 keV of nuclear recoil energy, and depending on the candidate at much lower energies (see section 1.3.1). This implies electron equivalent energies below 30 keV for Na recoils and below 10 keV for I recoils. For this reason, a very good knowledge of the detector response function for real scintillation events in the active volume of the detector and a good understanding and characterization of other anomalous or noise event populations in that energy region is required. Efficiently filtering all the low energy events populations non attributable to dark matter interactions is one of the main issues for ANAIS. Among them, events having scintillation time constants other than NaI(Tl) one or events in coincidence with a signal in the plastic scintillator vetoes or in coincidence between at least two ANAIS modules should be rejected. Specific protocols to reject such events have been developed and applied to data from ANAIS-0 module corresponding to setups 4 and 5 (section 3.1).

The low energy region has been carefully studied: old neutron calibration data from ANAIS Prototype III have been reanalyzed (section 3.2), asymmetry in the energy sharing has been investigated with ANAIS-0 and prototype III data (section 3.3), several low energy estimators have been compared to determine the one with the best resolution and performance (section 3.4) and, as trigger at the photoelectron level in the experiment is mandatory, the trigger efficiency in the different setups is discussed (section 3.5).

The NaI scintillation constants have been determined for alpha, beta/gamma and neutron interactions very precisely. In particular, very slow scintillation in NaI(Tl), sparsely known previously, has been precisely measured in ANAIS-0 and PIII crystals (section 3.6). Finally, quenching factor for alpha particles vs. beta/gamma particles has been determined (section 3.7).

3.1 Bulk NaI scintillation low energy events selection

Strong rejection of non bulk NaI scintillation events is required to reduce the effective threshold down to 2 keV. Dark matter particles are expected to interact in our detector by elastic scattering off Na and I nuclei in the NaI crystal. Hence, the energy is deposited through the interaction of the corresponding recoiling nucleus in the crystal. Dark matter events are expected to be very similar to those produced by neutrons, and to share some features with those having beta/gamma origin; both can be produced using calibration sources in order to have reference populations that allow a good NaI(Tl) bulk scintillation event characterization.

However, dark matter events neither should be correlated with muon interactions in the vetoes, nor appear in coincidence between two or more modules, nor accumulate in short time periods, nor show anomalous scintillation time constants in the pulse shape, for instance. All these events populations, non attributable to dark matter interactions can be rejected before the dark matter analysis.

The goal is to find a compromise between a high acceptance of bulk NaI scintillation events and low contribution of other events, not rejected by the filtering. In some of the cuts, the filtering implies an effective reduction in the acquisition live time, while in others, the efficiency of the cut to preserve the bulk scintillation events in NaI(Tl) active volume has to be estimated by studying populations of bulk scintillation events, specially at very low energies. ^{57}Co, ^{109}Cd, and ^{133}Ba source events and the 3.2 keV events following ^{40}K decay in the bulk (see section 4.1.2) have been used for that purpose.

We describe below in detail the filtering procedure followed with ANAIS-0 data. Table 3.1 shows the number of events, as well as the available live time, before and after each cut for setups 4 and 5. All the cuts have been applied consecutively and in the order presented in the text to every set-up data.

1. **Periods of anomalous high rate.**
   Dark matter interaction rates are so low, that the probability of two events occurring in a short time period is negligible. Because of that, periods of anomalous high rate can be discarded. In this category of events are some electronic noise related events and events following high energy calibrations, see section 2.7. During the ANAIS-0 operation period, some problems in the experimental conditions appeared (for instance, just after moving ANAIS-0 to the new LSC facilities or while testing the

Cut	Set-up 4		Set-up 5	
	Number of Events	Live Time (s)	Number of Events	Live Time (s)
0	6924171	11216800	1272028	2755985
1	6642571	10918900	1272028	2755985
2	6470283	10649269	1272028	2755985
3	6326697	10648800	1259000	2755660
4	6323129	10648800	1259000	2755660
5	6322944	10648800	1173911	2755660
6	2121342	10648800	748640	2755660

Table 3.1: *Total number of events and live time remaining after the different cuts described in the text.*

new VME electronics) and these data are not considered, and the corresponding time is discounted.

2. **Periods of non-correlation between analog electronics and digitized data.** Because in the analysis we combine information from the digitized pulse with QDC data, for instance, we have to reject such uncorrelated periods. They affected full blocks of data, that were discarded and their corresponding acquisition time discounted from the total live time. In set-up 4, there were 673 blocks of 256 events each rejected as uncorrelated, 97.53% of the live time remains after applying this cut, as it is shown in Table 3.1. In set-up 5, using the new acquisition, uncorrelated events are not present, which entails a significant improvement.

3. **Cut on events after a muon (very high energy) event.**
When a very high energetic particle interacts in the ANAIS-0 module, due to the slow NaI(Tl) scintillation (see more details in section 3.6) photons in the tail of the pulse are able to trigger again the acquisition (because of the triggering at the photoelectron level) and the total acquisition rate increases (see Figure 3.1). For that reason, events triggering during 0.5 s after a high energy event (over 9 MeVee to guarantee to be well above the usual alpha and gamma backgrounds) are rejected and the corresponding live time deducted. As in set-up 5 PMTs signals saturated at energies much below 9 MeVee and then, muon events could not be tagged and discriminated from the high energy gamma and alpha background, it was decided (in a conservative way, because the muon veto coverage is not complete) to reject 0.5 s after the arrival of a muon at the plastic vetoes (see cut 4). The spectra of events rejected by this cut in setups 4 and 5 is shown in Figure 3.2. The different shape of the rejected events spectra is attributed to the different PMTs used in each

set-up; in particular, VLB PMTs of set-up 5 present a higher quantum efficiency and can be more effective in triggering at those events. However, the different criterion used to tag the high energetic events could be blamed on it.

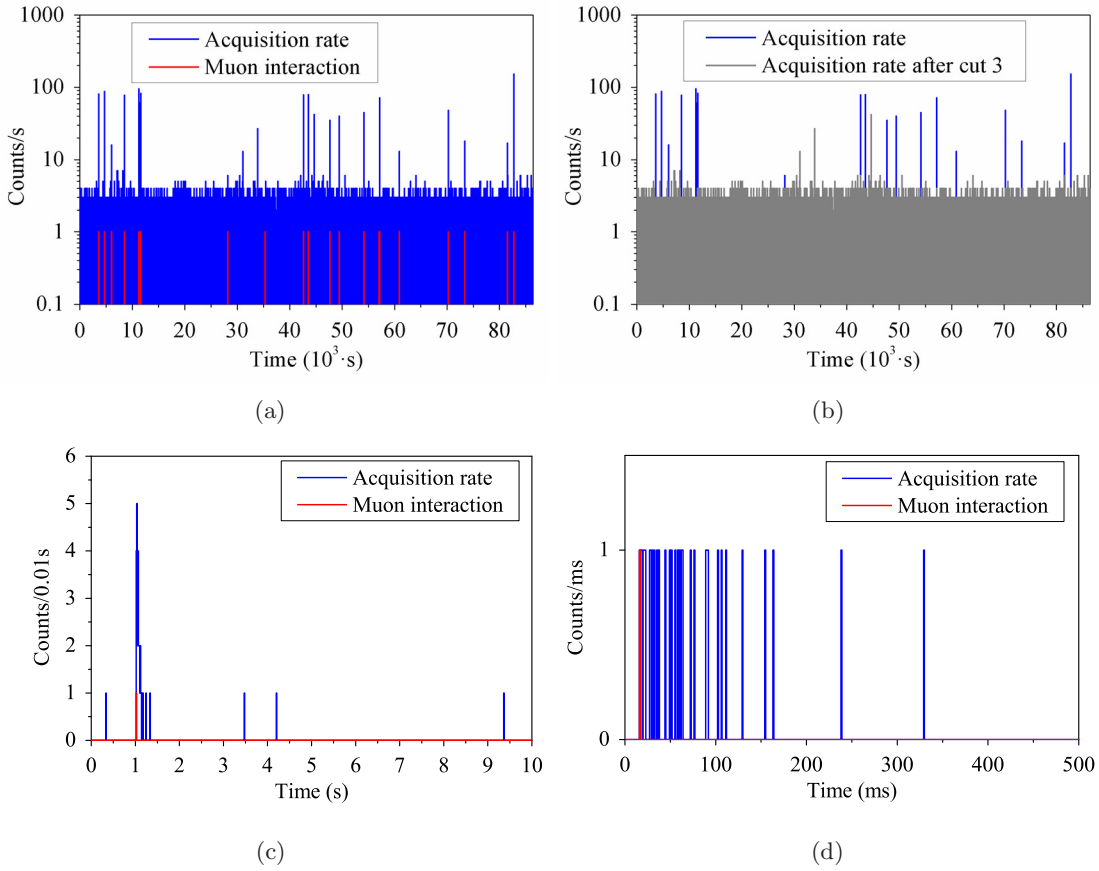

Figure 3.1: *Total acquisition rate (in blue) with ANAIS-0 module along a week (a), and in a zoom at different timescales (c) and (d). In red, very high energy events (above 9 MeVee) are marked. It can be observed the clear correlation between these events (mostly attributable to muon interactions in the NaI(Tl) crystal) and the increase in the trigger rate. In (b) the acquisition rate before (blue) and after applying cut 3 (gray) are shown.*

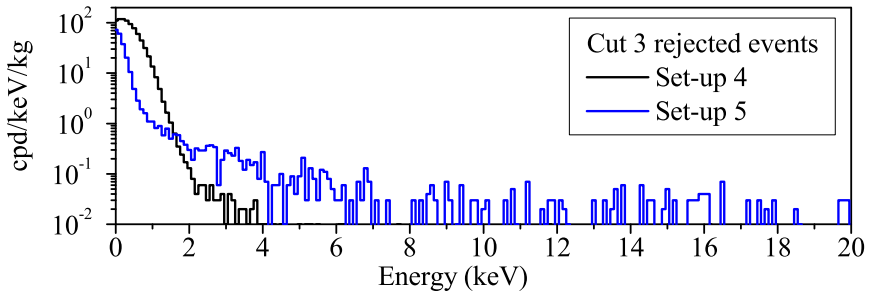

Figure 3.2: *Spectrum of the events rejected by cut 3 (0.5 s after a very energetic event) for setups 4 (black) and 5 (blue).*

4. **Cut on events coincident with a a plastic veto signal.**
   In section 2.8 muon related events in ANAIS-0 module coincident with a plastic veto signal were identified, both at high and low energies. Hence, these events are also rejected, without implying efficiency or live time corrections. For set-up 5 this cut is unnecessary, being done at the same time than cut 3, due to the PMT signals saturation. The spectrum of the events rejected by this cut has been shown in Figure 2.26.

5. **Cut on events with anomalous baseline estimate.**
   As explained in section 2.6, the baseline is calculated for each pulse with the first points before the beginning of the pulse. If a photon arrives in the pretrigger region, the baseline won't be properly calculated and hence, neither other related parameters. These events are identified by their anomalous low baseline level and they are not considered for the analysis, see Figure 3.3. They can be attributed to tails of previous pulses or to dark current photons, see an example of each case in Figure 3.4. VLB PMTs present a higher dark current rate than ULB PMTs and hence, more events are rejected by this cut in set-up 5.

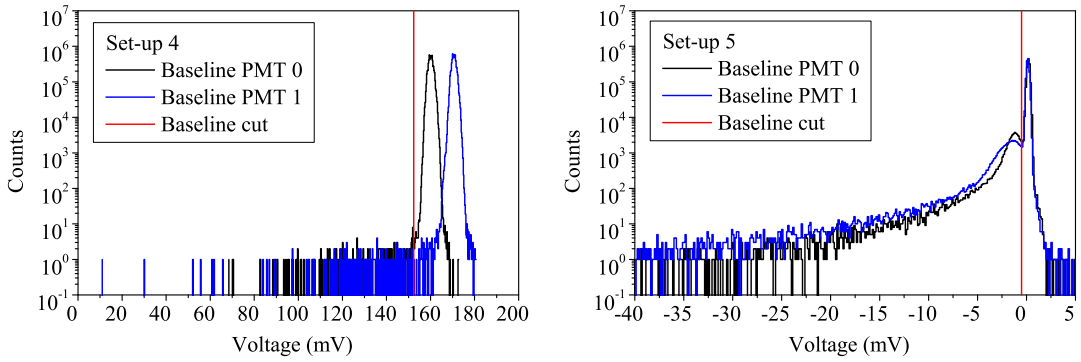

(a) (b)

Figure 3.3: *Distribution of baseline parameter for PMT0 and PMT1 data corresponding to setups 4 (a) and 5 (b). Cut applied to reject events having anomalous estimated baseline is shown in red. Set-up 4 data were digitized with the scope, and set-up 5 with the MATACQ, implying different absolute values of the typical baseline values.*

6. **Cut on the peaks number of the event.**
   Profiting from the good sampling rate of the digitized data, the discrete arrival of the scintillation photons to the PMT photocathode can be distinguished at low energies. An algorithm has been applied in order to count them, see section 2.5. The algorithm requires two parameters: a threshold voltage and a width for the peak. By choosing these parameters according to the S.E.R. of the PMT, peaks are properly found,

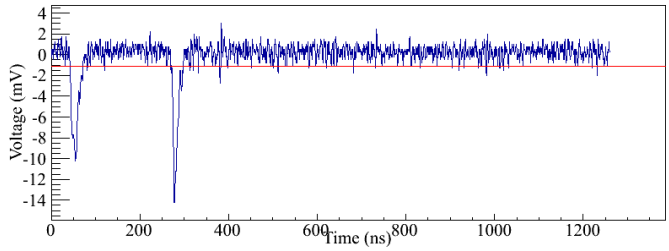

(a)

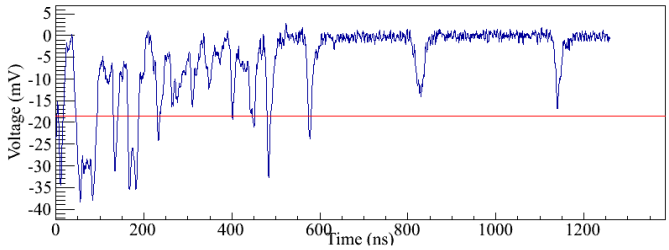

(b)

Figure 3.4: *Examples of events where the baseline (red) has not been properly calculated, due to the early arrival of a single photon (a) or to a previous pulse tail triggering (b).*

counted and their positions saved. In Figure 3.5, a low energy pulse is shown and the peaks identified by the algorithm are marked.

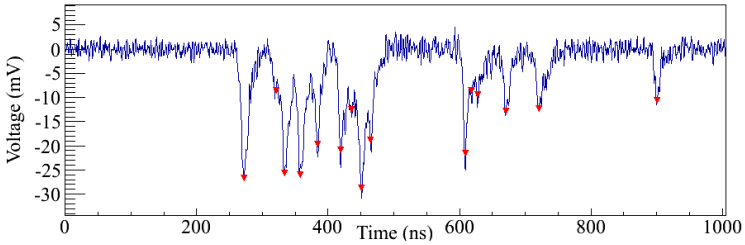

Figure 3.5: *Low energy pulse (corresponding to the population of 3.2 keV events after ^{40}K decay, selected by coincidence, see section 4.1.2) showing peaks identified by the peak search algorithm corresponding to individual photoelectrons. They are counted independently for each PMT signal and their positions saved. The shown pulse corresponds to set-up 5 (data taken with the MATACQ).*

We reject events having less than 3 peaks in any of the PMTs. This implies an effective analysis threshold of about 1 keV (see section 5.2.4 where the photoelectrons/keV are calculated for each set-up). This cut allows to reject events due to chance coincidences (directly related to the dark current of the PMTs), or other events having their origin in the PMTs (possible Cerenkov light emission in the PMT glass, for instance), that are expected to produce a signal very similar to SER, except in amplitude/area. Events rejected by this cut cannot be attributed to NaI

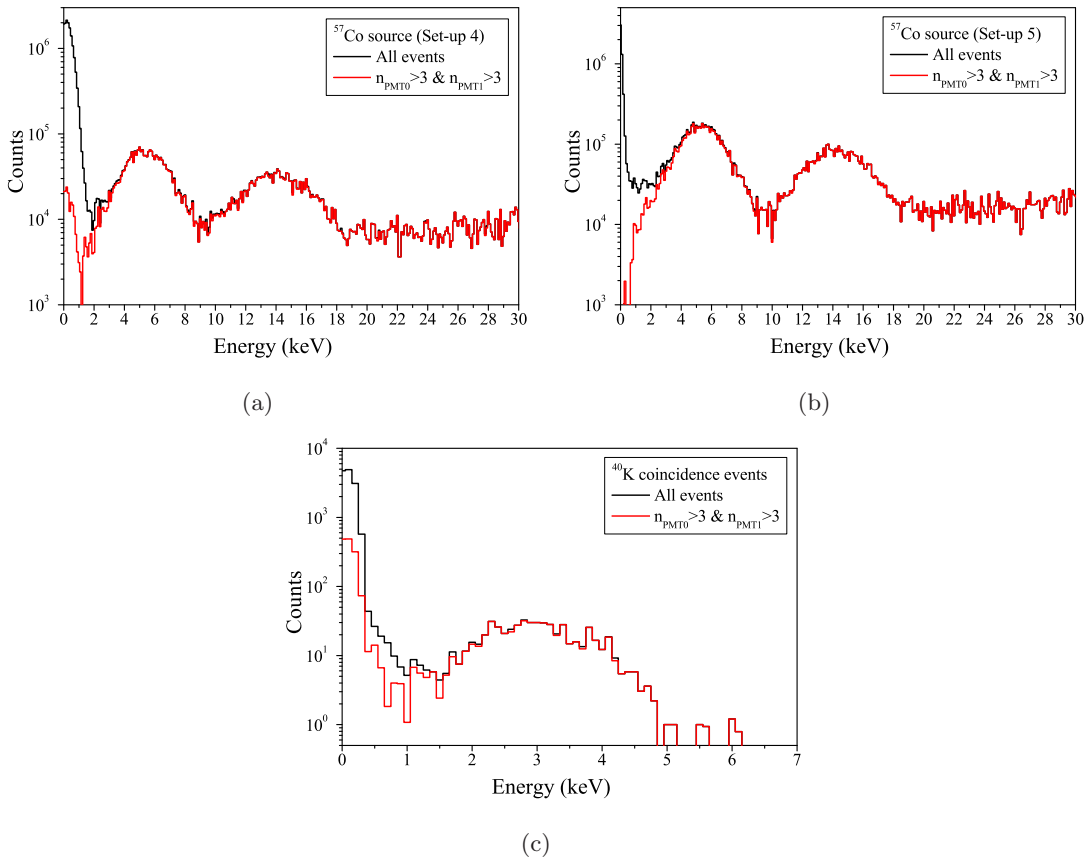

Figure 3.6: *Low energy spectra of set-up 4 (a) and 5 (b) corresponding to a ^{57}Co calibration and low energy spectrum coincident with the ^{40}K high energy gamma at low energy (showing the 3.2 keV line), corresponding to the phase III of the ^{40}K-coincidence set-up (c), before (in black) and after (red) the application of cut 6.*

scintillation. The effect of this cut in data of a ^{57}Co calibration is shown in Figure 3.6 for setups 4 and 5. This cut is only removing events below 2 keV, and 6.4 and 14.4 keV lines are not affected at all by the cut. Similarly, events from ^{40}K corresponding to 3.2 keV, selected by the coincidence with the high energy gamma (see section 4.1.2), are not affected by the cut. They are shown before and after the application of the cut in Figure 3.6.c. On view of the results it does not seem necessary to add an efficiency to this cut above 2 keV.

The low energy background spectra before and after cut 6 are shown in Figure 3.7 for setups 4 and 5. Also the spectra of the events rejected by this cut are shown. It can be seen that this cut allows to reject background events up to 20 keV equivalent energy. The spectra corresponding to the events rejected by this cut for setups 4 and 5, sharing some features, are different. As both setups use different PMT models, that supports our hypothesis that these events have a PMT origin.

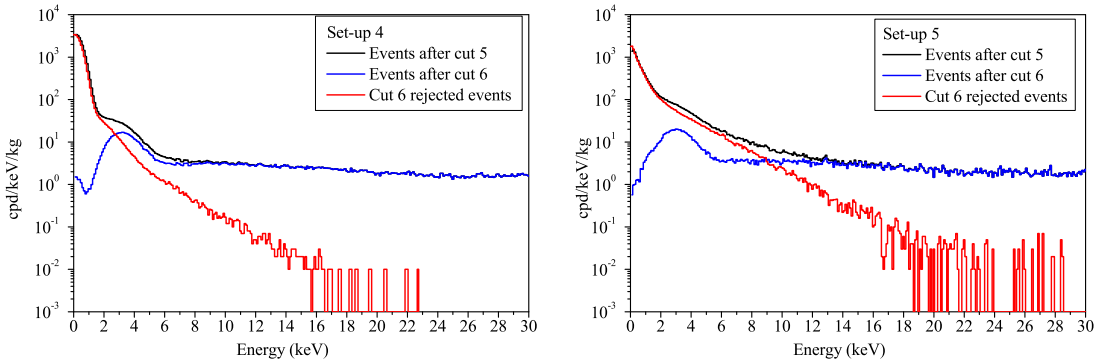

(a) (b)

Figure 3.7: *Low energy spectra of set-up 4 (a) and 5 (b) after cut 5 (black), after cut 6 (blue) and events rejected (red) because the number of photoelectrons is below 3 in at least one of the two PMT signals.*

7. **Cut on events faster than typical NaI(Tl) bulk scintillation.**

   With the purpose of rejecting events clearly faster than typical NaI(Tl) bulk scintillation pulses, different parameters depending on the scintillation time (pulse decay constant) have been studied. P1 has been determined as the one that works better: P1 is the ratio between the pulse area from 100 to 600 ns after the pulse onset and the area from pulse onset till 600 ns after. In previous works [89], P1 was calculated for each PMT signal individually, but, in this work, in order to profit from the total number of photoelectrons at the lowest energies, a new parameter P1s has been built with the addition of both pulses, featuring much better discrimination ability. Hence, the P1s timing parameter has been defined:

$$P1s = \frac{Area1(100-600ns) + Area2(100-600ns)}{Area1(0-600ns) + Area2(0-600ns)} \tag{3.1}$$

   This parameter is expected to be around 0.7 for the NaI(Tl) scintillation events, even though it shows an slight dependence on the energy (see Figure 3.8 where this parameter is shown for ^{57}Co calibration data up to 100 keV.)

   In order to apply an additional cut based on this parameter, data from ^{57}Co and ^{109}Cd calibrations (set-up 4) have been used: mean values and standard deviation of P1s in different energy windows (1 keV width) have been calculated by fitting to a gaussian function the P1s parameter distribution (see Figure 3.9 and Table 3.2). During set-up 5 no ^{109}Cd calibration was available, but data from ^{57}Co and ^{133}Ba were used instead. In principle, the values of this parameter should be characteristic of the NaI(Tl) scintillation and do not depend on the special set-up features. However, small differences have been observed in the P1s values corresponding to

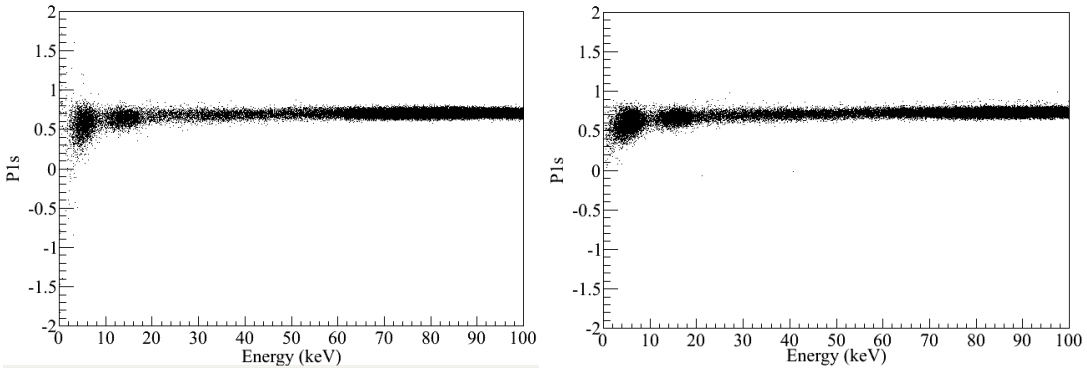

(a) (b)

Figure 3.8: *P1s parameter distribution as a function of the energy for ^{57}Co calibration data, after the application of the 6 cuts explained in the text. Data in (a) correspond to set-up 4 and in (b) to set-up 5.*

data from setups 4 and 5 (see Table 3.2), that could be attributed, for instance, to the better resolution of the MATACQ (see Figure 3.11). Only data up to 16 keV are shown because this is the main region of interest and variation of the parameter is strongly reduced for higher energy pulses. An analysis energy threshold of 2 keVee is imposed hereafter because there are not enough good calibration events below such an energy to allow the definition of an useful acceptance region (see Table 3.2).

After testing different cut criteria, an acceptance region of good scintillation events at 97.7% is defined by selecting events having P1s value larger than the mean minus $2\,\sigma$ at every energy window. Figure 3.10 shows the distribution of the P1s parameter as a function of the energy for background data together with the mean P1s value derived from calibration data and the chosen cut value.

The goodness of the so calculated efficiencies and cut is checked with the 3.2 keV bulk events coming from the internal ^{40}K disintegration, which have been selected by the coincidence method (see section 4.1.2). These events are bulk NaI scintillation events and are not rejected with the cuts, as expected, see Figure 3.10.c. In the energy region from 2 to 10 keV, there are 553 events. After applying the cut, 537 events remain that correspond to 549 events after applying the efficiency factor. It can be stated that the efficiency of the cuts is well estimated down to 2 keVee.

To finish, this cut on P1s parameter has been applied to the background data, obtaining the filtered spectra shown in Figure 3.12. The main factor limiting the analysis threshold is the availability of data to estimate the efficiency of this last cut, because there are very few events from 0 to 2 keV in the calibrations. In the 2-3 keV region, the cut is probably not rejecting many non-bulk scintillation events,

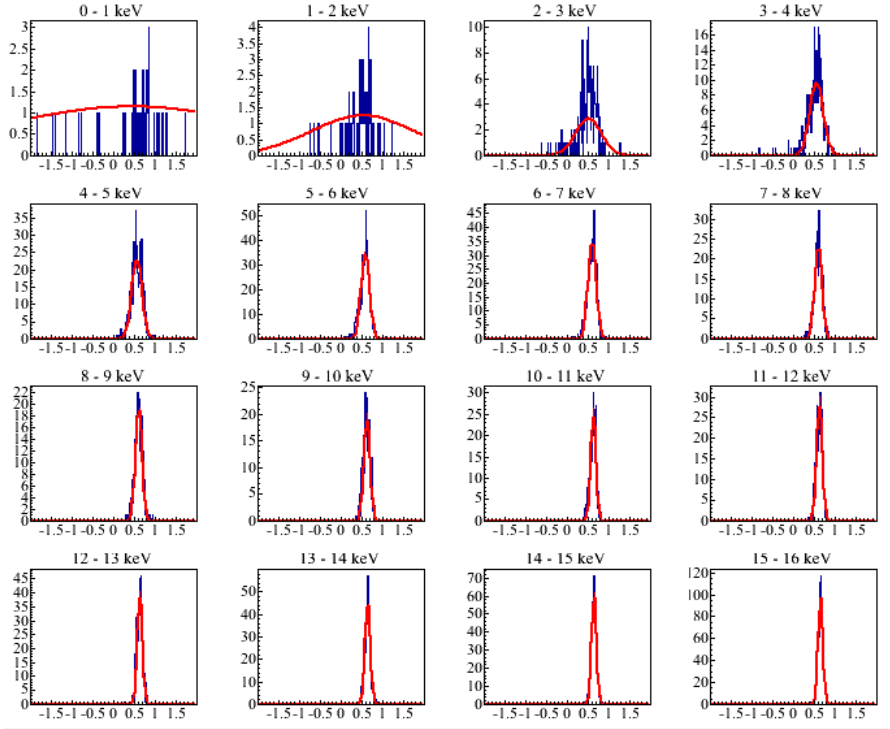

(a)

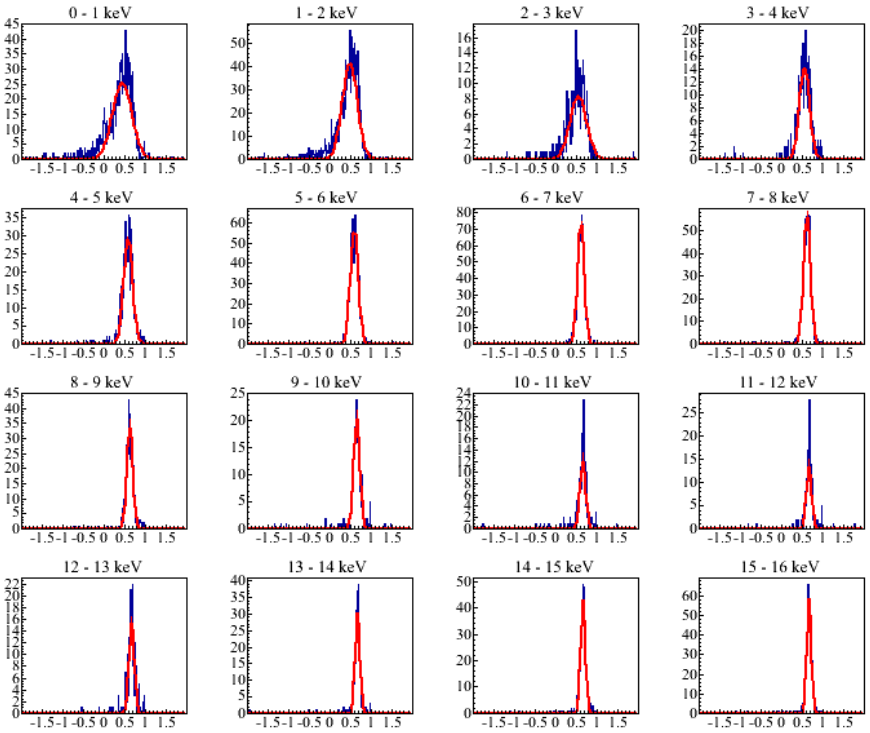

(b)

Figure 3.9: *P1s parameter distribution and corresponding gaussian fits for events corresponding to calibration data. They are shown for 1 keV width windows, from 0 up to 16 keV for set-up 4 (a) and 5 (b). Mean values and standard deviations corresponding to the fits are shown in Table 3.2.*

Energy region	Set-up 4		Set-up 5	
	Mean	σ	Mean	σ
0 - 1 keV	0.439 ± 2.935	3.229 ± 5.145	0.441 ± 0.09	0.233 ± 0.09
1 - 2 keV	0.525 ± 0.587	1.237 ± 1.095	0.485 ± 0.05	0.184 ± 0.04
2 - 3 keV	0.511 ± 0.036	0.314 ± 0.065	0.547 ± 0.12	0.203 ± 0.13
3 - 4 keV	0.555 ± 0.010	0.166 ± 0.011	0.558 ± 0.06	0.124 ± 0.05
4 - 5 keV	0.560 ± 0.005	0.126 ± 0.004	0.585 ± 0.04	0.111 ± 0.03
5 - 6 keV	0.584 ± 0.004	0.105 ± 0.003	0.595 ± 0.03	0.098 ± 0.02
6 - 7 keV	0.599 ± 0.004	0.101 ± 0.003	0.613 ± 0.02	0.083 ± 0.02
7 - 8 keV	0.602 ± 0.004	0.091 ± 0.004	0.620 ± 0.03	0.086 ± 0.02
8 - 9 keV	0.608 ± 0.004	0.081 ± 0.004	0.626 ± 0.03	0.074 ± 0.02
9 - 10 keV	0.625 ± 0.004	0.077 ± 0.004	0.653 ± 0.04	0.077 ± 0.04
10 - 11 keV	0.629 ± 0.003	0.066 ± 0.003	0.659 ± 0.05	0.072 ± 0.05
11 - 12 keV	0.627 ± 0.004	0.071 ± 0.003	0.666 ± 0.05	0.066 ± 0.05
12 - 13 keV	0.634 ± 0.003	0.063 ± 0.002	0.671 ± 0.04	0.067 ± 0.05
13 - 14 keV	0.641 ± 0.002	0.066 ± 0.002	0.671 ± 0.03	0.060 ± 0.03
14 - 15 keV	0.644 ± 0.002	0.061 ± 0.002	0.662 ± 0.02	0.060 ± 0.02
15 - 16 keV	0.650 ± 0.002	0.060 ± 0.001	0.667 ± 0.02	0.056 ± 0.02

Table 3.2: *Mean value and standard deviation for the P1s parameter corresponding to bulk NaI(Tl) scintillation events obtained from calibration data, for set-ups 4 and 5, with the corresponding errors, in 1 keV width energy windows up to 16 keV. The windows below 2 keV are not considered in the analysis.*

because of the very conservative acceptance region ($2\,\sigma$) chosen. However, most of the bad events in these region had already been rejected by cut 6 and we do not see many anomalous events present in the filtered data, see Figure 3.12.

Events rejected by this last cut have a scintillation faster than NaI(Tl). Their origin is not clear, but they could be related to surface events in the NaI(Tl) crystal from isotopes implanted, for instance, after ^{222}Rn deposition (confirmed to be faster than gamma events in CsI(Tl) [139] and proposed as solution to similar fast anomalous events populations identified in old NaI(Tl) experiments [81]) or scintillation in the quartz windows [99], for instance.

Figure 3.13 shows the filtered spectra of setups 4 and 5 after having applied the previous cuts and correcting with the corresponding efficiencies. The 3.2 keV line coming from the ^{40}K disintegration is dominating the low energy spectrum (from 2 to 6 keV) in both set-ups. From 6 keV up to 30 keV a rate of 2 - 3 cpd/keV/kg is measured without light guides with both PMT models, which is on the limit of the ANAIS experiment requirements. VLB PMTs do not seem to contribute more than ULB down to 10 keV. Nevertheless,

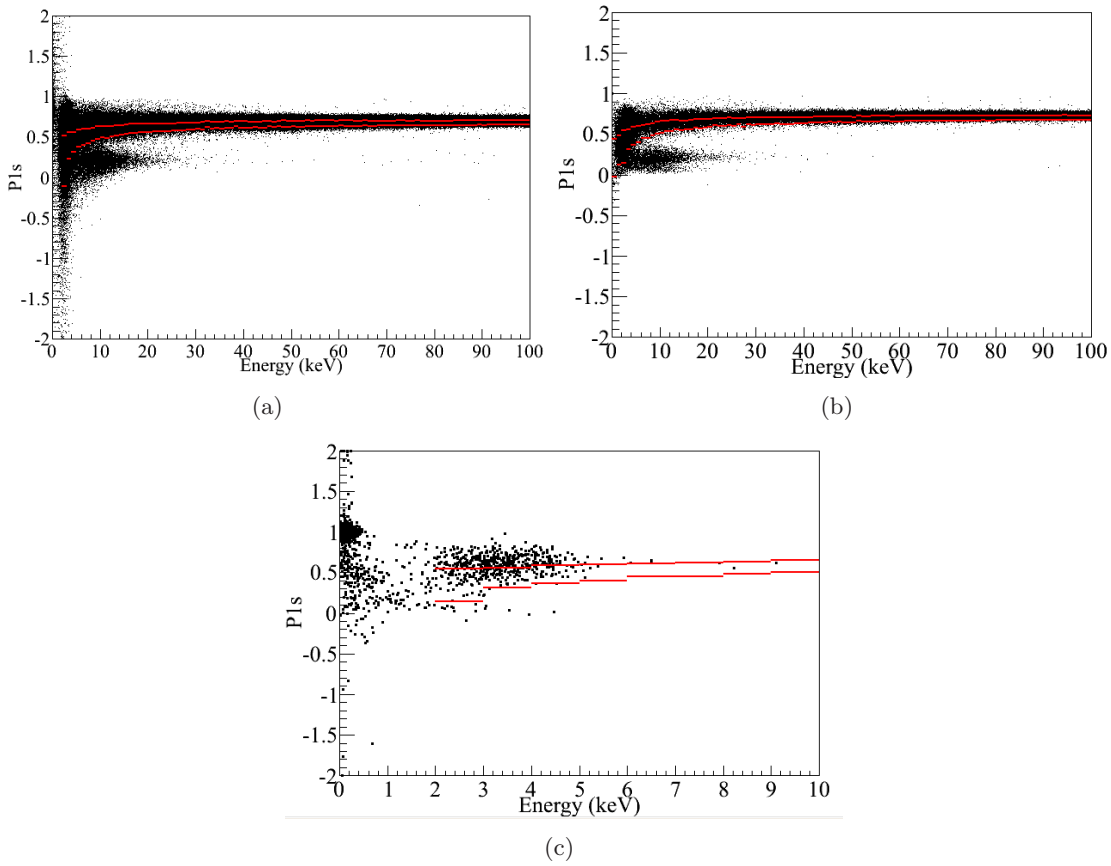

Figure 3.10: *P1s parameter distribution versus energy for events passing all the 6 cuts referred in the text corresponding to background data from setups 4 (a) and 5 (b), as well as for 3.2 keV events coming from the internal ^{40}K disintegration and selected by the coincidence with the high energy gamma (c). The upper red line represents the P1s mean value obtained from the calibrations and the lower red line the cut value chosen for cut 7 in order to have an acceptance of 97.7% for bulk scintillation in NaI(Tl) events.*

this issue will be further studied with the ANAIS-25 modules, made with ultrapure NaI crystals, in section 6.2.1.

3.2 Neutron calibration

Neutron interactions are relevant for a dark matter experiment because they produce nuclear recoils of the target constituent nuclei as the WIMPs do. Nuclear recoil events in NaI are slower than β/γ ones [80, 81], however at low energies there is only a slight difference in pulse shape and particle discrimination can not be done on an event by event basis.

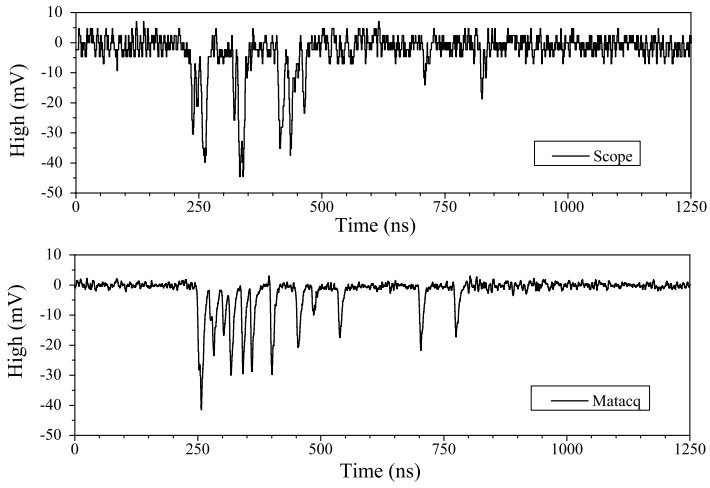

(a)

Figure 3.11: *Pulses at very low energy (6.4 keV line from ^{57}Co calibration) obtained with the MATACQ digitizer (bottom) compared to those obtained with the previously used oscilloscope (top) in similar experimental conditions (set-up 4, i.e. ULB PMTs). The different resolution in amplitude from both digitizer systems can be clearly noticed.*

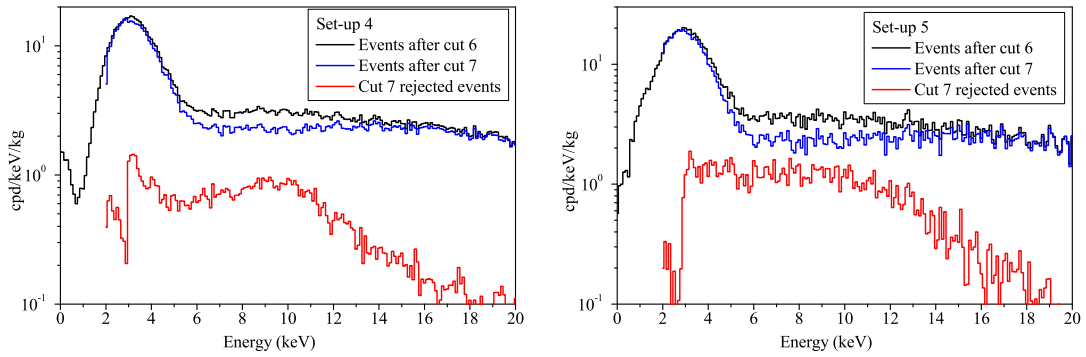

(a) (b)

Figure 3.12: *Low energy spectra corresponding to setups 4 (a) and 5 (b). Events remaining after cut 6 are shown in black and after applying cut 7 in blue. Events rejected in cut 7 are also shown in red.*

Unfortunately, neutron sources are not easily brought to an underground facility and ANAIS experiment had only the chance to do a neutron calibration in 2007 using a ^{252}Cf source. At that moment, only the prototype III was taking data. Because of that, we have reanalyzed those data in order to obtain information about nuclear recoils pulse shape and then, the effect of the previously explained cuts on such a population. Figure 3.14 shows the low energy spectrum obtained with the ^{252}Cf source. Threshold effects are observed at

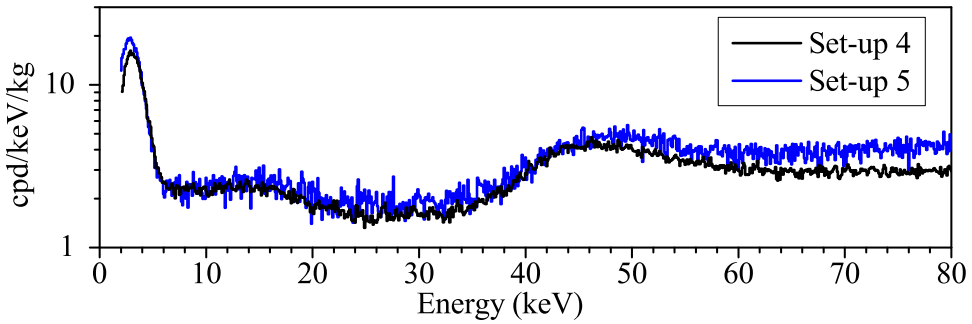

Figure 3.13: *Low energy spectra of set-up 4 (a) and 5 (b) after having applied all the cuts described in text. Main differences are observed above 60 keV and are due to the higher PMTs background contribution in set-up 5.*

energies lower than 10 keV. According to specific Geant4 simulations, up to 30 keV most of the events in the spectrum can be attributed to nuclear recoils.

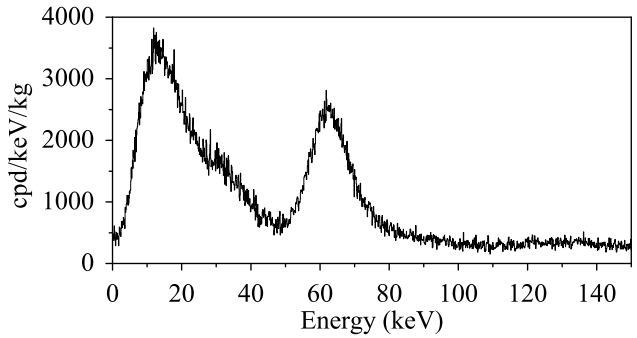

Figure 3.14: ^{252}*Cf neutron source calibration spectrum taken with prototype III. Only low energy (below 150 keV) is shown.*

Data have been reanalyzed to include the calculation of the P1s parameter and to study its mean value in 1 keV width energy windows as it was done in section 3.1 for the β/γ calibrations. The gaussian fit for the P1s distribution in energy windows up to 16 keV are shown in Figure 3.15 and the corresponding parameters in Table 3.3. Above this energy no relevant differences in the mean value and standard deviation of the P1s parameter have been observed.

Figure 3.16.a shows the P1s parameter as a function of the energy for the ^{252}Cf calibration data and Figure 3.16.b shows data from added ^{109}Cd and ^{57}Co calibration data superimposed to ^{252}Cf data; the former are shown in blue and the latter in black. Corresponding cut values defining 97.7% bulk scintillation acceptance regions are shown in red and green, respectively. It can be seen that neutrons are slower than β/γ particles but a cut can not be established to distinguish them. No filtering has been applied to the ^{252}Cf

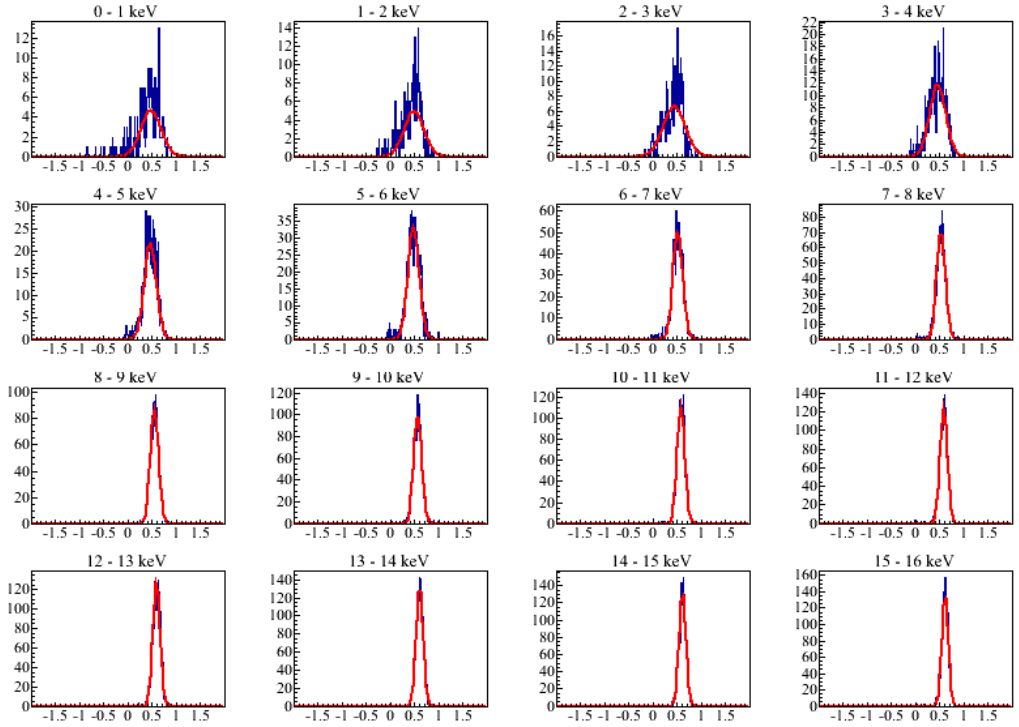

Figure 3.15: *P1s parameter distribution in 1 keV regions (blue) and gaussian fits (red) for ^{252}Cf neutron calibration data taken with prototype III. Although threshold effects are present below 10 keV, good scintillation events are found at those energies and we have decided to show also for them the P1s distribution.*

calibration data and some pulse tails and single photoelectron events are present with P1s ≈ 0, but they only amount a 0.2% of the total number of events, and they do not affect to conclusions derived below. For ^{109}Cd and ^{57}Co calibration data, cuts 1 to 6 have been applied.

From the neutron calibration data analysis it can be concluded that an additional efficiency factor should be taken into account for the selection of possible dark matter events. Figure 3.16 shows clearly that nuclear recoil events would be rejected by the cut on the P1s parameter with an efficiency different than that estimated from beta/gamma calibrations. The cut value chosen with beta/gamma events (lower limit at $2\,\sigma$ confidence level) is equivalent to a lower limit at $1.59 \pm 0.37\,\sigma$ for neutron events, if data data from 5 to 30 keV are averaged. Hence, in the 5 to 30 keV energy window we should replace our acceptance efficiency for the selection of events using cut 7 (see section 3.1) by 0.944 instead of 0.977 in order to select conveniently nuclear recoils in the dark matter analysis.

Energy region	^{252}Cf calibration	
	Mean	σ
0 - 1 keV	0.469 ± 0.018	0.213 ± 0.027
1 - 2 keV	0.480 ± 0.017	0.208 ± 0.029
2 - 3 keV	0.429 ± 0.008	0.232 ± 0.017
3 - 4 keV	0.449 ± 0.005	0.170 ± 0.008
4 - 5 keV	0.457 ± 0.004	0.128 ± 0.004
5 - 6 keV	0.469 ± 0.003	0.120 ± 0.003
6 - 7 keV	0.505 ± 0.002	0.104 ± 0.002
7 - 8 keV	0.520 ± 0.002	0.093 ± 0.002
8 - 9 keV	0.545 ± 0.002	0.087 ± 0.001
9 - 10 keV	0.558 ± 0.002	0.085 ± 0.001
10 - 11 keV	0.572 ± 0.002	0.080 ± 0.001
11 - 12 keV	0.579 ± 0.002	0.077 ± 0.001
12 - 13 keV	0.587 ± 0.002	0.076 ± 0.001
13 - 14 keV	0.598 ± 0.002	0.073 ± 0.001
14 - 15 keV	0.605 ± 0.002	0.072 ± 0.001
15 - 16 keV	0.606 ± 0.001	0.068 ± 0.001

Table 3.3: *Parameters obtained from the gaussian fit of the P1s parameter distribution corresponding to ^{252}Cf calibration data taken with prototype III.*

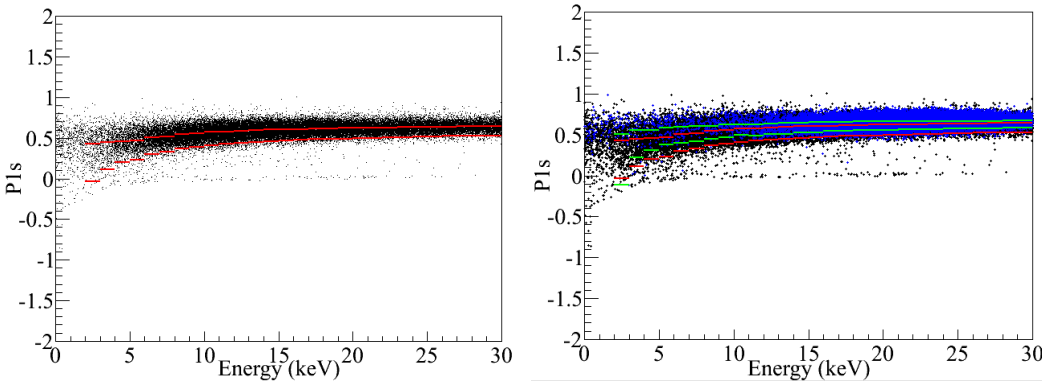

(a) (b)

Figure 3.16: *(a) P1s parameter versus energy for ^{252}Cf calibration data taken with prototype III. The upper red line represents the P1s mean value obtained in 1 keV width windows and the lower red line the cut value chosen to define the acceptance region (the mean minus 2σ). (b) ^{252}Cf calibration (black), ^{109}Cd and ^{57}Co calibrations (blue), P1s mean value and the cut value chosen to define the acceptance region (the mean minus 2σ), for the ^{252}Cf (red) and ^{109}Cd and ^{57}Co (green) calibrations. No filtering has been applied to the ^{252}Cf calibration data. Cuts 1 to 6 have been only applied to ^{109}Cd and ^{57}Co calibration data.*

3.3 Asymmetric events

Asymmetric events have been observed in background and calibration data from ANAIS-0 by looking at the different sharing of light between the two PMT channels, see Figure 3.17.

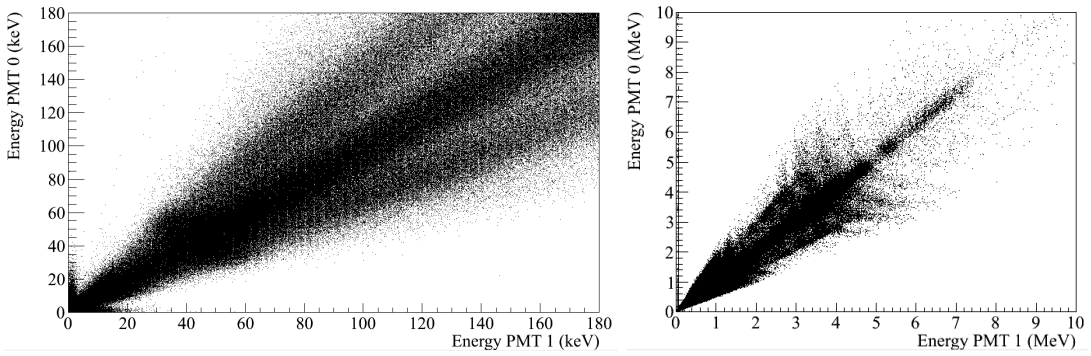

Figure 3.17: *Energy sharing between the two PMT signals at low (a) and high (b) energy in background data taken with the ANAIS-0 module set-up 4. Similar data have been obtained with the other ANAIS-0 setups.*

Two different kinds of asymmetric events have been identified in the data and are further studied:

1. Bulk scintillation events are observed to produce different sharing of the light collected by the two PMT channels depending on the interaction position along the crystal axis. This effect can be caused by the spatial dependence of the light collection efficiency for every PMT channel and has been characterized with radioactive sources placed in different positions along the crystal axis in ANAIS-0 and in the PIII, observing important differences, as it will be reported later in this section.

2. Very strongly asymmetric events are identified in both channels at low energy (see Figure 3.17.a). These events are not compatible with bulk NaI scintillation events. They show a much larger pulse area in one PMT channel than in the other, hinting at chance coincidences or at light emission at or very near one of the PMTs, hindering a significant amount of light reaches the other PMT.

In order to understand the asymmetric bulk scintillation events, calibration sources have been used, placing them in different positions along the crystal axis (see Figure 3.18). Figure 3.19 shows the QDC values obtained for each PMT signal and and the corresponding average values when calibrating with a ^{137}Cs source in different positions along the crystal axis: near the PMT 0 (position 1), near the PMT 1 (position 7) and centered (position 4). By looking at the average of the two PMT signals, spatial dependence is strongly

reduced but does not disappear and we have characterized it by studying a parameter A, measuring the asymmetry of the light sharing:

$$A = \frac{Q_0 - Q_1}{Q_0 + Q_1} \tag{3.2}$$

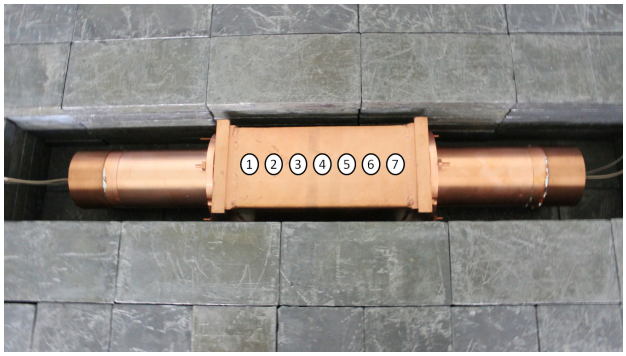

Figure 3.18: *Calibration source positions along the axis of ANAIS-0 module used to characterize the asymmetric bulk scintillation events.*

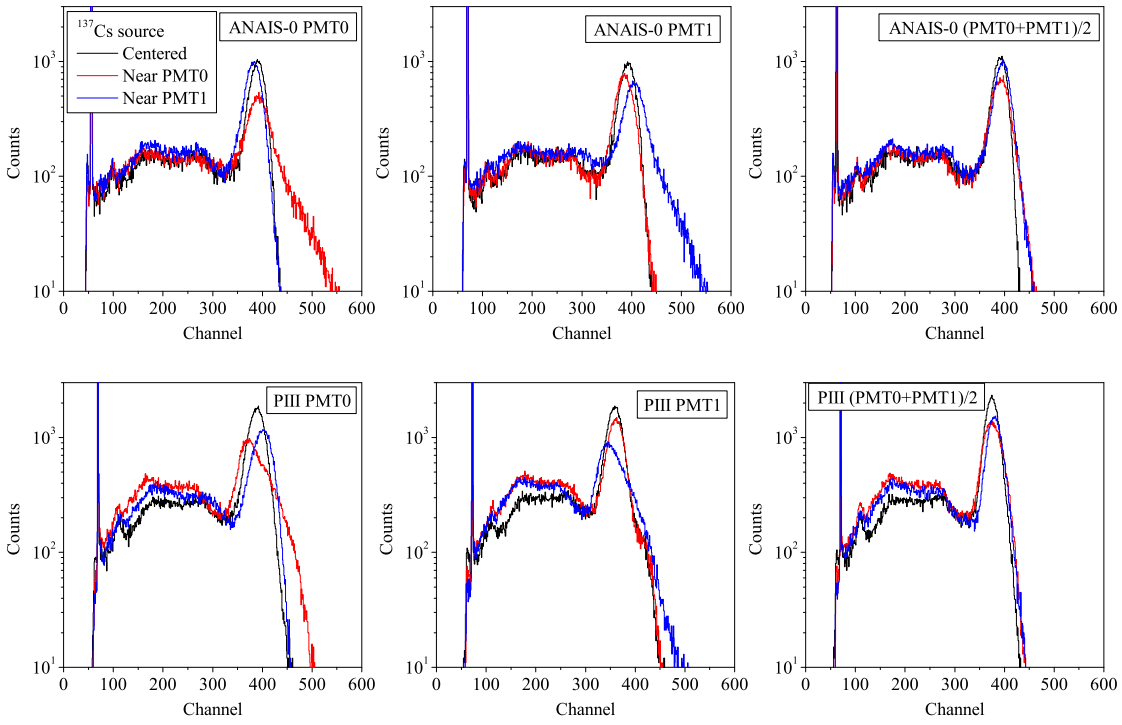

Figure 3.19: *Spectra obtained from each PMT signal and the corresponding average for ANAIS-0 (top) and PIII (bottom) modules when calibrating with a ^{137}Cs radioactive source at different positions along the crystal axis: centered (position 4), near PMT 0 (position 1) and near PMT 1 (position 7).*

being Q_0 and Q_1 the mean channel associated to a determined gamma line as seen by PMT0 and PMT1, respectively. This parameter has been studied with the 662 keV gamma line from a ^{137}Cs source, which was moved along the crystal axis, both in ANAIS-0 and in PIII modules. Because of the different gain in the PMT 0 and PMT 1 channels, see Figure 3.19, the parameter A is not distributed around zero, as should be expected if it had been defined in energy instead of QDC channel, and is corrected by subtracting the mean value ($< A >$). This $A - < A >$ parameter is plotted as function of the source position along the axis in Figure 3.20, for ANAIS-0 and PIII modules. A very different behavior for the two detectors, probably with a geometrical origin, is observed. This effect is very small ($< 2\%$) but clearly observable in both detectors. The PMT which is nearest to the energy deposition is expected to see more light in a very plain light propagation model, however PIII data shows the opposite behavior, requiring a deeper understanding of the light collection efficiencies. The crystal shape (ANAIS-0 has a square section while PIII has an hexagonal section and both crystals have different ratio length over cross-section) could be the origin of this effect, that will be also studied with ANAIS-25 modules as soon as the background assessment is finished.

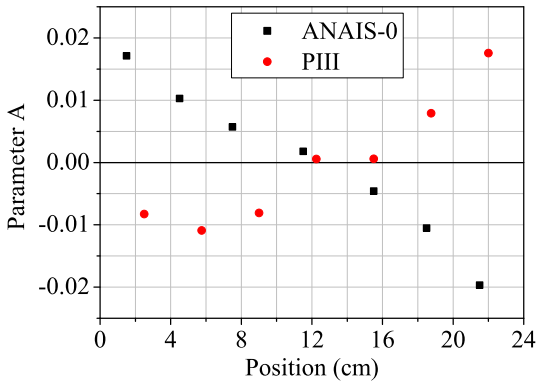

Figure 3.20: *Parameter A, after subtracting the average value, calculated as a function of the ^{137}Cs radioactive source position for ANAIS-0 (black points) and PIII (red points) modules.*

Figure 3.21 shows the different sharing of the collected light between the two PMT signals for events from a ^{137}Cs calibration source in the center of the crystal (position 4), near PMT 0 (position 1), and near PMT 1 (position 7). The different behavior already commented with the parameter A is also observed in this representation. As the observed asymmetry in background data is very similar to that obtained from the combination of calibration data shown in Figure 3.20, and comparing data from setups 1 and 2, the fraction of events in the lateral bands reduce from 15 to 10% when using light guides

in the low energy region, we hypothesize that the contribution from the PMTs to the background is responsible of the high and low bands seen in Figure 3.17. Contaminations homogeneously distributed at or around the crystal are not expected to generate such asymmetric sharing of the light.

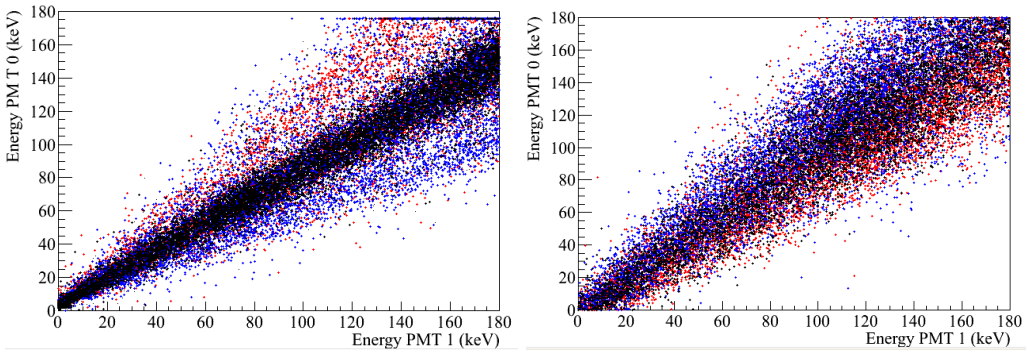

(a) (b)

Figure 3.21: *Repartition of the energy between PMT 0 and PMT 1 in data from ANAIS-0 set-up 1 (a) and PIII (b) with a ^{137}Cs calibration source placed in position 4, in the center of the crystal (black); in position 1, near PMT 0 (red); and in position 7, near PMT 1 (blue).*

This asymmetric events population can not be rejected because they are NaI crystal scintillation events. However, it could be possible to define an active volume region, rejecting the most asymmetric events, but at the expense of losing sensitivity in the search for dark matter, by reducing the active mass. Moreover, it has to be noticed that the asymmetry reduces at the low energy regime.

On the contrary, the second asymmetric events population is due to a scintillation faster than that of NaI. Light guides have been observed to contribute to these population, as can be seen in Figure 3.22, corresponding to the energy sharing between the two PMTs for a background measurement with the set-up 3 of ANAIS-0 module.

It can also be observed a high asymmetry in veto-coincident events at low energy, specially in the case of set-up 3 data, which used light guides, see Figure 3.23. Tagging events as asymmetric when one PMT detects more than the double of the light signal than the other, asymmetric events rate has been quantified to be 9 cpd in set-up 3 and 3 cpd in set-up 4. In section 2.8, it was stated that set-up 3 presented 8 cpd in coincidence with active vetoes more than set-up 4, being the use of light guides the only difference between both setups. Here, it is established that the majority of these events (6 cpd) are asymmetric, as expected to correspond to interactions in the light guides. On view of these results, scintillation in light guides and quartz windows due to muon interactions

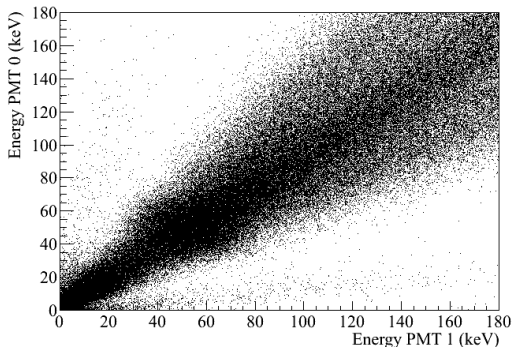

Figure 3.22: *Energy sharing between PMT 0 and PMT 1 for background data from the set-up 3 of ANAIS-0. A population of strongly asymmetric events, having energy equivalent up to 200 keV, is clearly identified and attributed to scintillation in the light guides, because these events were not present in data from setups 4 and 5 (see Figure 3.17).*

could be responsible of such asymmetric events. One quartz window could scintillate more than the other (the one near PMT 0), because in Figure 3.23.b there are more asymmetric events with few energy in PMT 1 than in the inverse band.

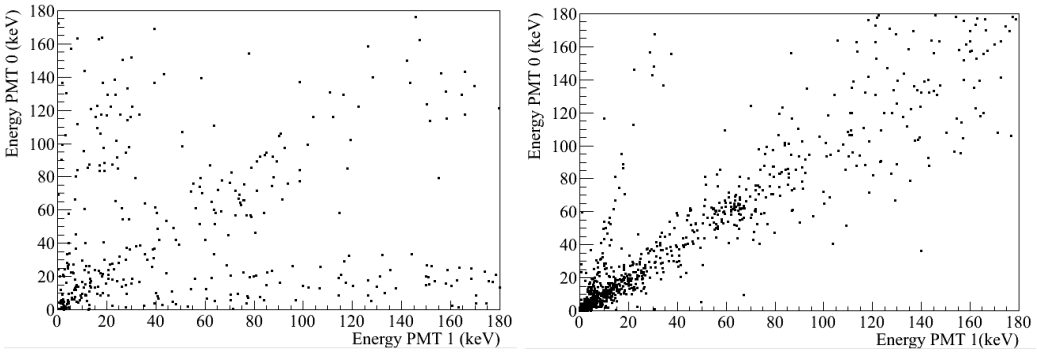

(a) (b)

Figure 3.23: *Energy sharing between PMT 0 and PMT 1 for the events coincident with a muon in the plastic vetoes. In (a) data from set-up 3 (43.4 days, 2184 events), using light guides, and in (b) data without light guides, from set-up 4 (126.4 days, 5689 events), are shown.*

Although it had been studied, an specific cut for asymmetric events at very low energy is finally not required in the filtering of ANAIS-0 data because it adds nothing to the cut 7, previously described. All the strongly asymmetric events have been filtered by cuts 6 and 7, see Figure 3.24.

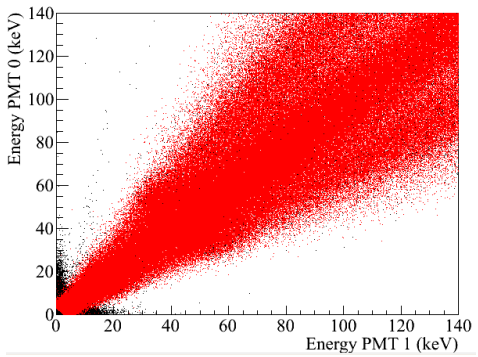

Figure 3.24: *Energy sharing for PMT 0 and PMT 1 in set-up 4 before (black) and after (red) the cuts described in section 3.1. It can be observed how the strongly asymmetric events are efficiently rejected by the cuts proposed there (in particular by cuts 4, 6 and 7).*

3.4 Energy estimators

Different low energy estimators have been studied: Charge converted signal (QDC), area of the digitized pulse (area), number of peaks in the pulse (n), and area of the peaks in the pulse (area-p). The aim is to reconstruct the event energy with the best accuracy down to the threshold, which implies having the best resolution for monoenergetic events. For the high energy events, QDCs values are taken as energy estimators. In this regime, n and area-p are not defined, and even total area is usually useless because of the adjustment of the digitization scale, up to a few hundreds of keV, that prevents to record full pulses above some hundreds of keV in most of the setups.

- QDC: The PMT charge output signal is integrated in a microsecond window at the QDC module and converted into a digital channel. QDCs inject a small charge amount (pedestal), resulting in a non-zero value for a zero energy deposition. The pedestal should be very stable to guarantee a very low and stable threshold.

- Area: It is the integral of the pulse from the pulse onset (T0) up to the end of the digitized window subtracting the baseline, see section 2.5.

- n: The number of peaks in the pulse, see section 2.5, could be a low energy estimator. However, this parameter in general underestimates the energy because two photons can arrive too close in time producing only one peak.

- Area-p: This parameter is constructed by integrating the pulse around every identified peak (50 ns window around the peak position), and the baseline contribution is subtracted afterwards. This estimator has been tested trying to avoid the energy underestimate associated to the previous parameter.

Usually, QDC output is the best energy estimator and the most widely used. However, due to the excellent resolution of the MATACQ digitizer, the other parameters have been found to be competitive, not being the case with the previous scope data. Figure 3.25 shows the spectra obtained with ^{57}Co (a), ^{109}Cd (b) sources and the 3.2 keV population selected by the coincidence measurement (c) using the different energy estimators proposed: QDC channel, area and area-p. Parameter n will be studied later on.

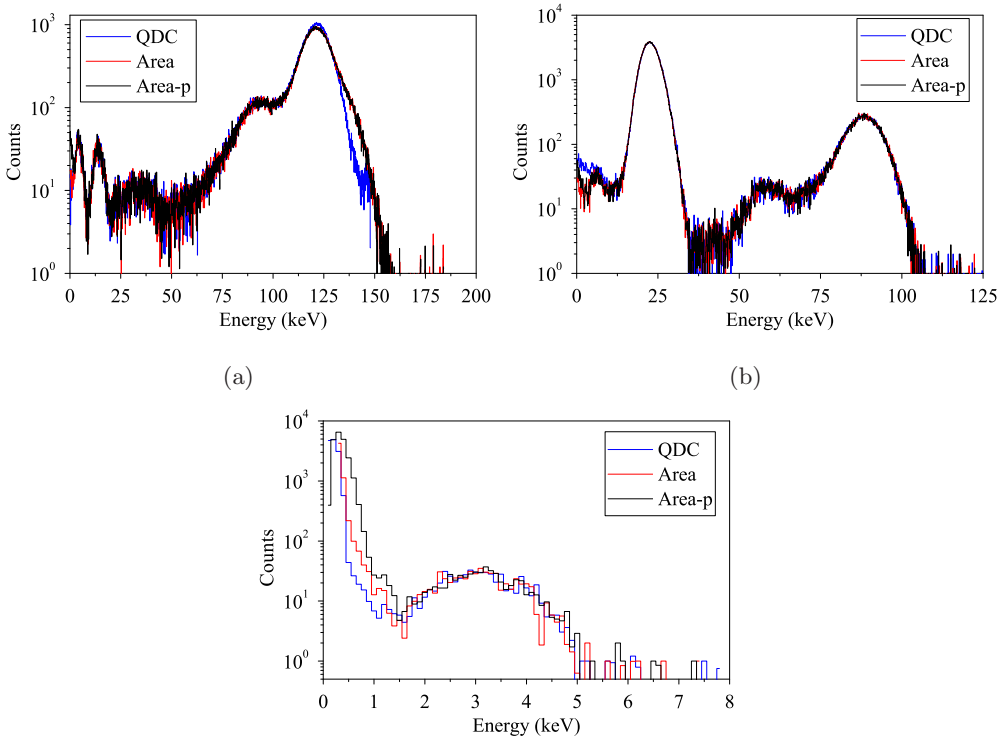

Figure 3.25: *Comparison of spectra built with different energy estimators at low energy: QDC channel, area and area-p, for (a) ^{57}Co calibration data, (b) ^{109}Cd calibration data, and (c) 3.2 keV population selected by the coincidence technique. In (a) the QDC signal saturates at about 120 keV and above this energy the spectrum is distorted.*

The three parameters show similar results in terms of energy resolution, see data in Table 3.4. Hence, area can be used as a good energy estimator in the energy region where the pulse is digitized, making the use of QDC modules in the same dynamic range redundant. As conclusion, low energy range QDCs could may be skipped in next ANAIS phases.

As expected, data shown in Table 3.4 confirm that area-p is the best energy estimator in the very low energy window (below 10 keV). However, it can be observed in Figure Figure 3.25.c that the distribution of baseline noise is clearly broader than for the other energy estimators: this is due to the fact that the peak search algorithm sometimes identifies

noise fluctuations as peaks. In the absence of real peaks attributable to photoelectrons, area-p integrates only the positive noise fluctuations, without compensating them with the negatives, as occurs in area or QDC estimates.

Energy (keV)	Resolution(%)		
	QDC	Area	Area-p
3.2	22.98 ± 1.68	22.58 ± 2.34	20.60 ± 1.71
6.4	23.26 ± 7.56	23.70 ± 8.09	18.74 ± 5.85
14.4	14.6 ± 0.80	14.05 ± 0.72	14.55 ± 0.61
22.6	11.79 ± 0.10	11.72 ± 0.06	11.70 ± 0.06
88.0	5.74 ± 0.04	5.71 ± 0.05	5.71 ± 0.04
122.1	5.07 ± 0.03	5.04 ± 0.05	5.13 ± 0.05

Table 3.4: *Resolution values for the different lines studied with the energy estimators: QDC, area and area-p.*

Moreover, the linear dependence between these energy estimators has been checked with ^{57}Co calibration data and the 3.2 keV events population selected by the coincidence measurement (see Figure 3.26). All the three energy estimators present a linear dependence between them.

The number of peaks in the pulse has been also studied as an energy estimator at the lowest energies, where single peaks can be distinguished. However, this number is not a good energy estimator, as can be seen in Figure 3.27: 3.2 keV events population is shown in the number of peaks vs energy plot and the n distribution for the same data. Very poor energy reconstruction is achieved with this parameter, although it has proven to be very useful to reject non-bulk NaI scintillation events (as explained in section 3.1).

3.5 Trigger efficiency.

As it has been already explained, lowering the threshold as much as possible is mandatory in any experiment devoted to the direct search for dark matter. The lowest achievable threshold requires to trigger at the single photoelectron level in each PMT signal. To guarantee the trigger at this level is really an important experimental issue.

We have studied the trigger level in the different ANAIS-0 setups by different methods: first the distribution of amplitude of the S.E.R. is compared to the amplitude of the first peak (at the trigger position), and second the 3.2 keV events, selected by the coincidence, have been profited to study how many of them trigger effectively our acquisition.

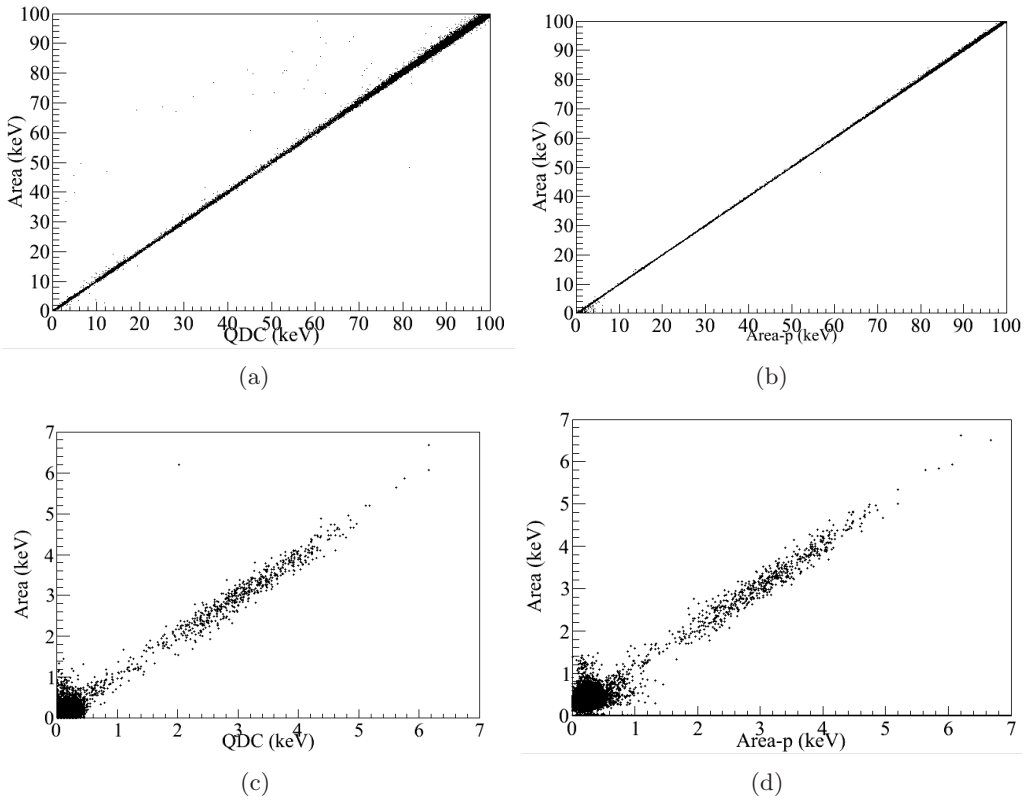

Figure 3.26: *Linear dependences between the different energy estimators studied: area vs QDC and area versus area-p for* ^{57}Co *calibration data (shown in (a) and (b), respectively), and for the 3.2 keV population selected by the coincidence (in (c) and (d)).*

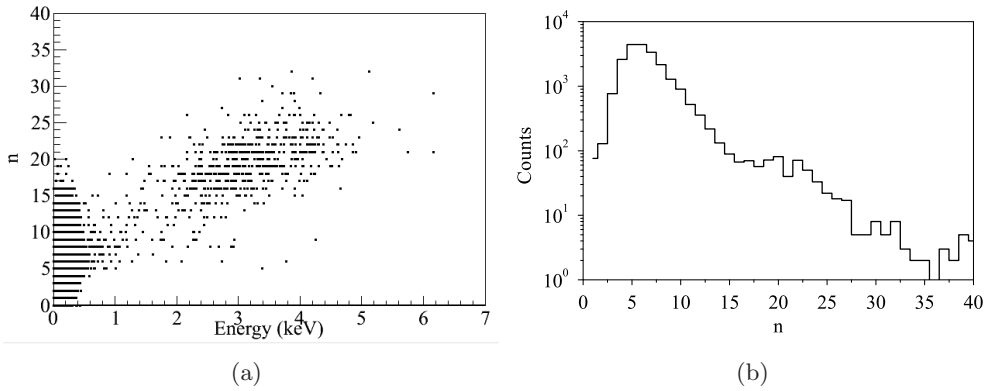

Figure 3.27: *Number of peaks in the pulse vs. energy (estimated with the QDC) (a) and n spectrum (b) for the 3.2 keV selected population.*

The S.E.R. parameters (amplitude, area, etc.) are determined from a population of single photoelectron peaks built by selecting the last identified peak in pulses having a low number of peaks (algorithm is described in section 2.5). Hence, these peaks are found in the last part of the pulse in order to avoid any bias related to the real trigger efficiency. However, some bias remains, because of the threshold used in the peak search algorithm.

As far as this threshold can be changed along the analysis and the S.E.R. can be built for different threshold values, the final effect in the S.E.R. is thought to be minor.

Figure 3.28 shows the amplitude distribution of photoelectrons derived from the last peak of pulses having a low number of peaks and that corresponding to the first peak (responsible of the trigger) for pulses having only one peak per PMT. The spectra for the different PMTs and setups, shown in Figure 3.28, have been conveniently scaled.

The photoelectron amplitude spectra have been gaussian fitted: mean values and standard deviations are shown in Table 3.5 (labeled as trigger level). From the first peak amplitude distribution an effective threshold (an amplitude that effectively triggers) can be deduced and is also shown in Table 3.5. Comparing this threshold with the mean value and standard deviation of the S.E.R. amplitude distribution gaussian fit, the number of sigmas below (or even above) the mean corresponding to such a threshold is calculated and, hence, the percent of the S.E.R. distribution effectively triggering.

Set-up	Signal	S.E.R. Mean	S.E.R. σ	Trigger level		Over T.L.
		mV	mV	mV	$n \cdot \sigma$	% of S.E.R.
1	PMT 0	31.15 ± 0.16	12.75 ± 0.17	40	0.69 ± 0.02	24.4
	PMT 1	33.10 ± 0.17	13.64 ± 0.19	35	0.14 ± 0.01	44.5
2	PMT 0	16.04 ± 0.06	4.47 ± 0.07	16	-0.01 ± 0.01	50.4
	PMT 1	13.42 ± 0.10	3.63 ± 0.10	14	0.16 ± 0.03	43.7
3	PMT 0	22.26 ± 0.08	7.18 ± 0.09	12	-1.43 ± 0.02	92.3
	PMT 1	28.86 ± 0.11	11.73 ± 0.12	12	-1.44 ± 0.02	92.5
4	PMT 0	19.52 ± 0.07	7.32 ± 0.07	12	-1.03 ± 0.01	84.7
	PMT 1	22.69 ± 0.09	7.99 ± 0.09	12	-1.34 ± 0.02	91.0
5	PMT 0	11.41 ± 0.03	6.33 ± 0.03	10	-0.22 ± 0.01	58.8
	PMT 1	16.11 ± 0.07	10.89 ± 0.08	10	-0.56 ± 0.01	71.2

Table 3.5: *Photoelectron amplitude, standard deviation and trigger level, together with the percent of the photoelectron distribution that triggers (fraction of the S.E.R. above trigger level). Data are shown for all the ANAIS-0 setups.*

In the first two setups, trigger was only partially done at the photoelectron level, having a poor trigger efficiency, perhaps because of the electronic noise caused by the worse operation conditions at the old LSC facilities. However, when using the ULB PMTs (setups 3 and 4) a very good trigger efficiency has been achieved and only a few percent of the photoelectron distribution is lost. The VLB PMTs produce a different photoelectron distribution: mean amplitude and specially standard deviation are bigger, making more difficult fully triggering at photoelectron level. As a conclusion of this analysis, we could

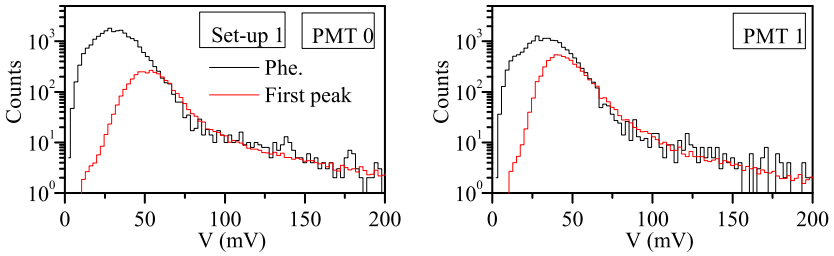

(a)

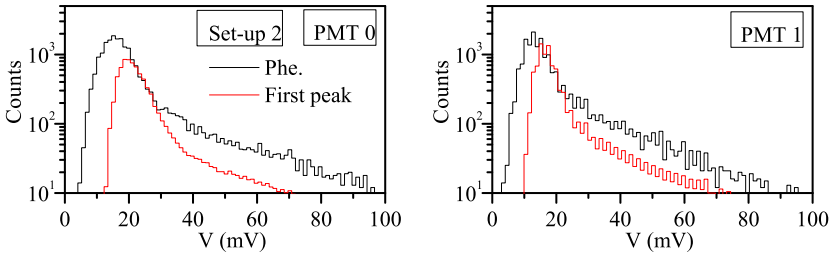

(b)

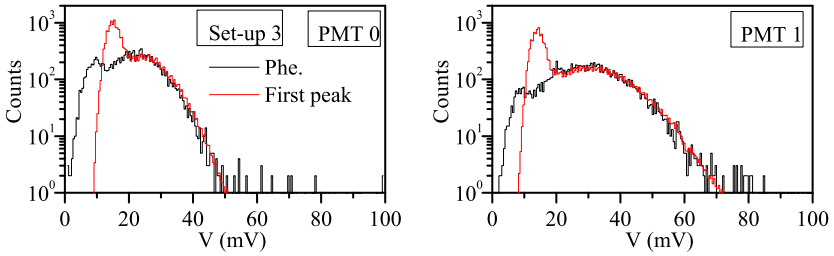

(c)

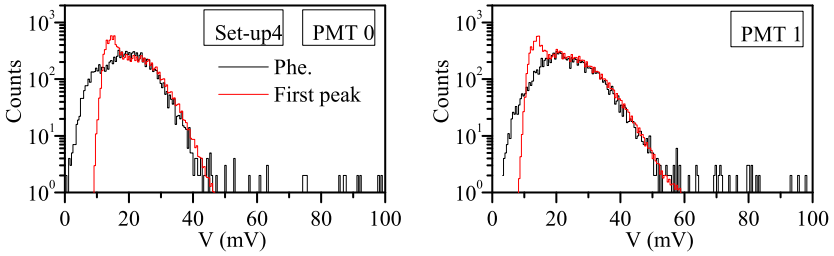

(d)

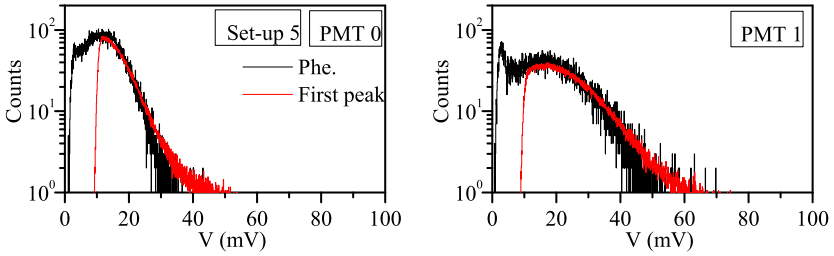

(e)

Figure 3.28: *Photoelectron and first peak amplitude distribution for the different ANAIS-0 setups.*

say that the VLB PMTs hardware trigger level has to be reduced in order to effectively triggering at photoelectron level.

The availability of the selected population of 3.2 keV after ^{40}K decay, which is a population of bulk scintillation events at very low energy, has also been profited to study the trigger efficiency of the experiment as a function of the deposited energy. The Pattern Unit module (see section 2.5) saves the trigger configuration of the event (with the old acquisition this was done with a MALU module) in a variable that we call T. To check the effective threshold of the acquisition, the variable T is studied (see Table 3.6 for the possible values of T).

T	Detector triggering
1	ANAIS-0
2	PIII
3	ANAIS-0 and PIII

Table 3.6: *Possible values of the T variable depending on which detector(s) triggered the acquisition.*

In Figure 3.29 spectra of the ANAIS-0 module in coincidence with the 1461 keV line in the prototype III are shown. All events (in black), events having T = 3 (in red) and T = 2 (in blue) are shown. No events with T = 1 are found in this population, because the imposition of the coincidence implies that PIII always triggers. ^{40}K events should make trigger in both detectors, if a 2 keVee threshold has been achieved.

For phases I and III of the coincidence set-up, the expected behaviour is observed: events in the peak at 3.2 keV triggered with almost full efficiency, supporting a very high trigger efficiency at or even below 2 keVee. Nevertheless, phase II presents much worse trigger efficiency. Summarizing, very good trigger efficiency down to 2 keVee is shown, even though triggering at photoelectron level is only partially achieved.

3.6 Precise determination of the NaI(Tl) scintillation constants.

Main scintillation time constants of NaI(Tl) are well reported in the bibliography [128, 140, 141]: the dominant decay time of the scintillation pulse is usually considered in the range 230-250 ns [142–144] but a slower component of 1.5 μs [142] and a phosphorescence component with characteristic 0.15 s decay time have been also reported [145]. Other

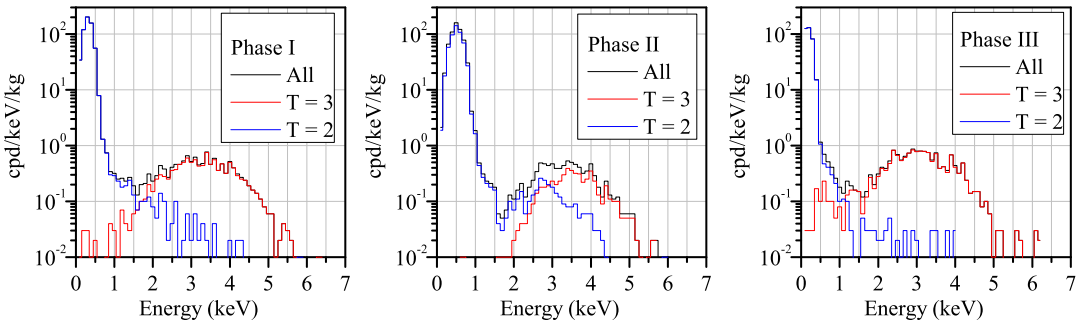

Figure 3.29: *Low energy spectra selected by the coincidence with the ^{40}K gamma considering T variable for the different phases of measurement (see section 2.2).*

possible phosphorescence components could be present at much longer timescales [146]. It was observed that after the interaction of a very high energetic particle in the ANAIS-0 module, the acquisition rate increased considerably (see section 3.1). This effect lead us to make a special measurement digitizing very high energy events during longer time than the usual (1 μs) and in different amplitude ranges. Measurements were carried out with ANAIS-0, but also with PIII, in order to check whether the effect is intrinsic to NaI(Tl) or corresponds to a particular behavior of the ANAIS-0 module.

Differences in the scintillation time constants for particles interacting in NaI(Tl) detectors are also well known and have been used for discrimination purposes: alpha vs. gamma interactions at high energy [97, 147–150] and nuclear recoils vs electron recoils at very low energies [80, 81, 97, 151, 152]. In the latter case, differences between both kind of events are quantified with an effective mean decay time constant, and are so small that only an statistical discrimination of events can be pursued. Dependence of the time constants with the energy deposited by the particle has also been clearly established.

A special branch in the electronic chain was designed for data acquisition in the very long timeline basis. Figure 3.30 shows the branch added to digitize pulses using two Tektronix phosphor scopes (TDS5034B) in two different horizontal scales and two different vertical ranges: Tektronix Scope 207 is configured to record pulses at photoelectron level in the longest timescale allowed ($8 \cdot 10^6$ points per pulse sampled at 40 ns/point) and Tektronix Scope 208 is configured to fully record high energy pulses in order to allow the reconstruction of their energy. Figure 3.31 shows an example of pulse measured with the Tektronix Scope 207. The scopes were only triggered by very high energetic events (above 2 MeVee). Measurements were done for one detector each time and scintillation decay time constants have been studied in different temporal scales and for different interacting particles. The short timescale is studied with data obtained with the usual electronic chain

(and the MATACQ as digitizer), but corresponding to an special run: dynamic range of the digitization was adjusted to fully record high energetic events. In Table 3.7 the main parameters of the different digitized data are described.

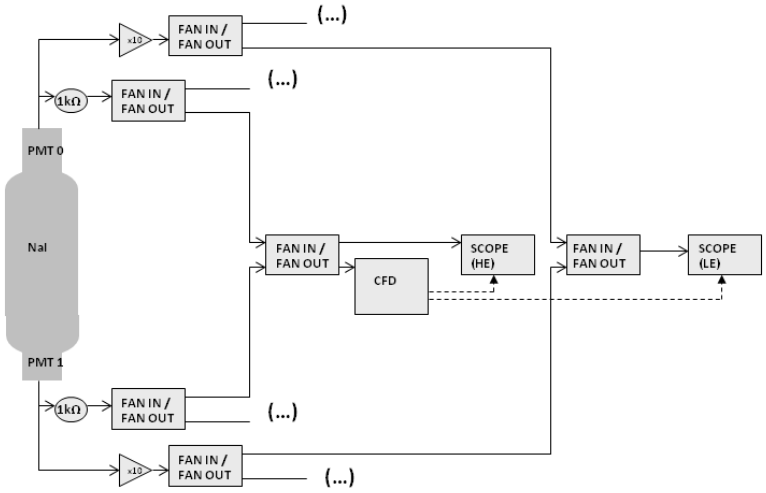

Figure 3.30: *Branch added to the electronic chain to digitize very energetic events in longer timeline basis.*

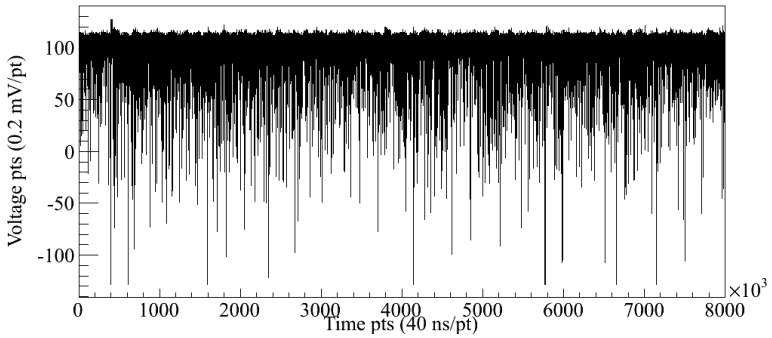

Figure 3.31: *Example of pulse corresponding to an alpha interaction in the ANAIS-0 crystal recorded in the long timescale (320 ms) by the Tektronix Scope 207.*

Alpha events are separated from beta/gamma/muon events by a discrimination based on the different relationship between pulse height and area of the pulse, see section 4.1.2. Two populations can be clearly distinguished, estimating as 100% the efficiency of the discrimination at energies above 2 MeVee and up to the saturation of the PMT readout circuit. No assumptions about the respective timing constants are required to apply such a discrimination. Muon events are distinguished from the gamma ones by the tagging of the plastic scintillators veto signals (only for the shortest timescales, using MATACQ data).

Digitizer	sampling rate	N of x points	vertical scale	N of y points
Tektronix Scope 207	25 MS/s	$8 \cdot 10^6$	50 mV	256
Tektronix Scope 208	250 MS/s	10^4	200 mV	256
MATACQ	2 GS/s	2520	1 V	4096

Table 3.7: *Summary of the configuration values for the main digitization parameters relevant in the analysis of the NaI(Tl) scintillation constants: sampling rate, number of points in the horizontal scale, dynamic range and number of points in the vertical scale.*

In the following, we will show events having pulse area in a region corresponding from about 2.5 to 3 MeVee (equivalent to the region from 4.2 to 5 MeV for alphas). In Figure 3.32.a, the average pulses built for alpha, gamma and muon interactions in a 1 μs temporal scale, recorded by the MATACQ digitizer, with ANAIS-0 module are shown. No difference between gamma and muon events has been found, as expected, and gammas and muons will be considered in the following analysis as the same population, as far as it is not expected different behavior in the longer timescales.

We will work with average pulses for the two populations in the cases of the fast and medium timescales, see Figure 3.32. For the longest timescale, a different approach has been followed: photoelectrons have been identified individually, at a given position of the pulse, and an histogram has been produced with the corresponding temporal distribution for all the events in the R.O.I., separately for alpha and beta/gamma/muon events, for ANAIS-0 and PIII modules. The corresponding pulses can be seen in Figure 3.33, conveniently normalized to the same fast pulse area and averaged according to the number of events in the ROI for each population.

In order to derive the different scintillation time constants, a fitting procedure has been followed in three steps. First, a fit has been done in the longest timescale to two exponential decays using the range from 4 to 320 ms after the onset of the pulse. Fits have been carried out for alpha and gamma/muon events, both in independent and dependent ways, for ANAIS-0 and in independent way for PIII data and are shown in Figure 3.34. According to the chi-squared value of the fits for ANAIS-0 data, the same time constants fit properly pulses from both populations, although with different relative amplitudes, being the significance of the fit limited by the poor statistics in the gamma/muon population. The results of the fits are summarized in Table 3.8, showing very similar results in ANAIS-0 and PIII for the fitted time constants. The most relevant difference between alpha event pulses and gamma/muon event ones in this long timescale is the total number of photoelectrons in these slow components: gamma or muon events excite much more efficiently

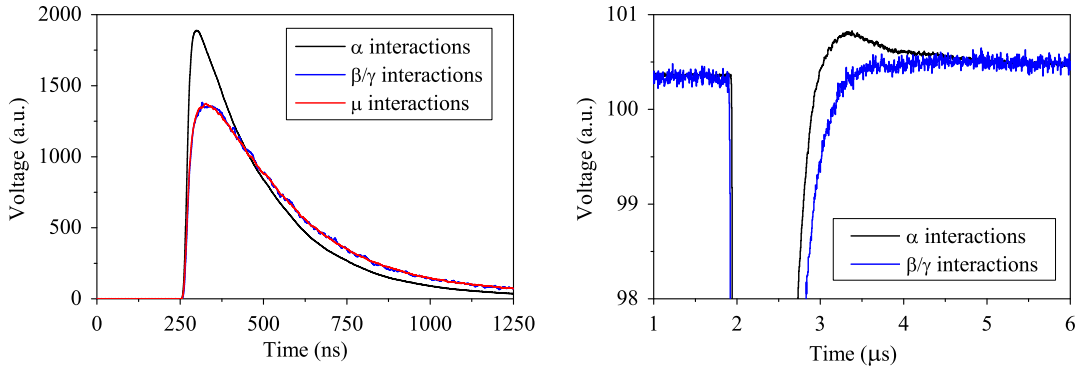

(a) (b)

Figure 3.32: *(a) Pulses corresponding to the interaction of alpha particles (black), gammas (blue) and muons (red) in a 1 μs window, recorded by the MATACQ digitizer. (b) Pulses corresponding to alpha particles (black) and gammas/muons (blue) in a 40 μs window, recorded by the Tektronix 208. Only data taken with ANAIS-0 are shown. All the pulses shown have been normalized to the same pulse area.*

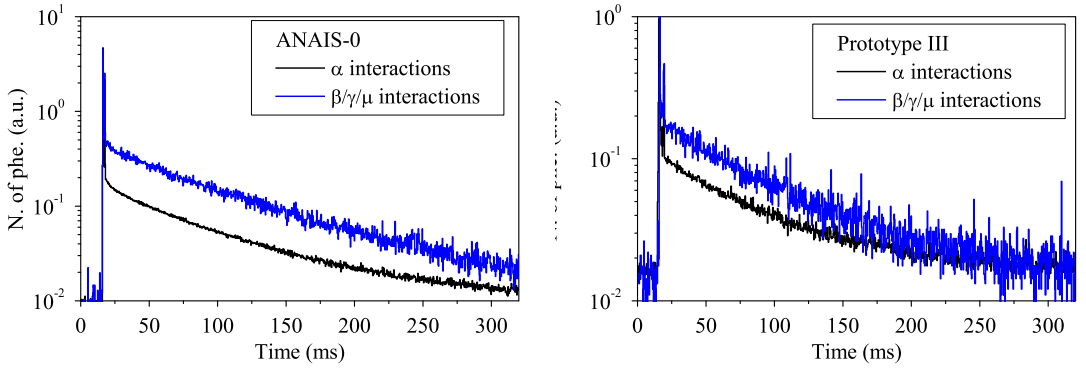

(a) (b)

Figure 3.33: *Pulses corresponding to the interaction of alpha particles (black) and gammas and muons (blue) in a 320 ms window, registered with the Tektronix 207 for the ANAIS-0 (a) and PIII (b) crystals. Events from both populations correspond to the same pulse area, dominated by the fast scintillation components.*

the long-lived states contributing to this very slow light emission. The distributions of the total number of photoelectrons for events of the alpha and gamma/muon populations are shown in Figure 3.35. In ANAIS-0, there is more than a factor of two different average values (0.050 ± 0.016 for alpha particles vs. 0.118 ± 0.029 for gammas/muons), however in PIII this difference is not so high (0.055 ± 0.011 for alpha particles vs. 0.068 ± 0.011 for gammas/muons). This is also evidenced in the different relative amplitudes for the slow scintillation components (see Table 3.8): gammas and muons produce more scintillation in a factor of 2 (3.5) for the 30 ms (95 ms) components. Because of the quenching factor for alpha particles vs beta/gamma events in NaI(Tl) and the fact that we have normalized

to the pulse area and not to the energy deposited, in terms of photoelectron production per unit of energy, the referred effect is still much more important. It has to be noted that, by cause of the scope sampling and peak search algorithm required for building the photoelectron distribution, we can not rely on the absolute number of photoelectrons assigned to a given energy depositions. However, relative values between the both analyzed populations should be trustworthy.

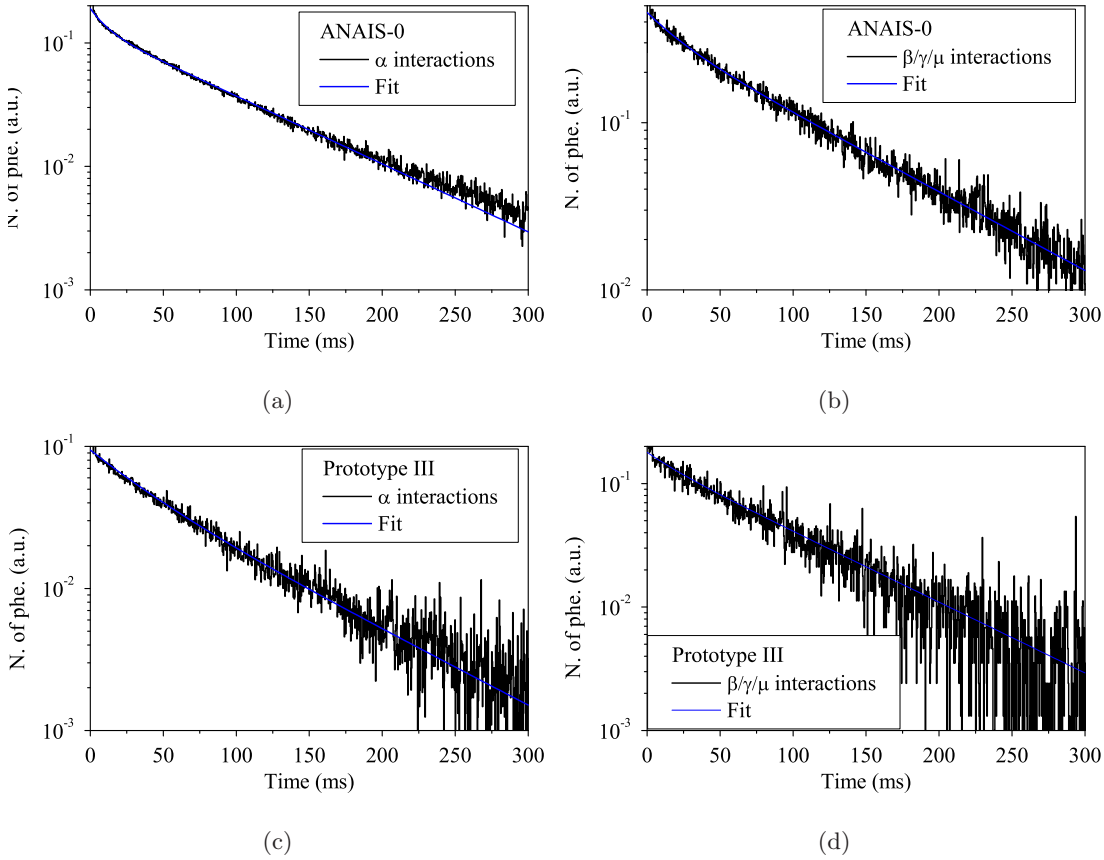

Figure 3.34: *Pulses corresponding to the interaction of alpha particles, (a) and (c), and gammas and muons, (b) and (d), in a 320 ms window, registered with the Tektronix 207 for the ANAIS-0, (a) and (b), and PIII, (c) and (d) crystals are shown in black. The fit of the data shown in Table 3.8 are shown in blue. Events from both populations correspond to the same pulse area, dominated by the fast scintillation components.*

Second, in the medium timescale, important effects of the RC time constant of the PMT readout circuit can be observed, limiting the conclusions derived for possible additional time constants in the microseconds range. Corresponding pulses are shown in Figure 3.32.b. Clearly pulses overshoot the baseline being not recovered in the 40 μs studied range, but in the first milliseconds. This effect sweep any relevant scintillation temporal behavior. However, it can be clearly seen that it is much more important in alpha pulses than in gamma/muon ones of the same fast pulse area. We will modify in

	ANAIS-0				PIII	
	Independent fit		Dependent fit		Independent fit	
	α	$\beta/\gamma/\mu$	α	$\beta/\gamma/\mu$	α	$\beta/\gamma/\mu$
τ_1 (ms)	10.7 ± 0.3	22.7 ± 2.3	29.0 ± 2.0		34.2 ± 4.7	19.8 ± 10.33
τ_2 (ms)	79.0 ± 0.3	92.3 ± 1.6	94.4 ± 1.5		81.7 ± 4.1	75.77 ± 2.7
A_1/A_2	0.44	0.35	0.73	0.38	0.59	0.16

Table 3.8: *Results of the fit between 4 and 320 ms after the pulse onset for ANAIS-0 and PIII. Fits have been carried out for alpha and gamma/muon events, both in independent and dependent ways, for ANAIS-0 and in independent way for PIII data.*

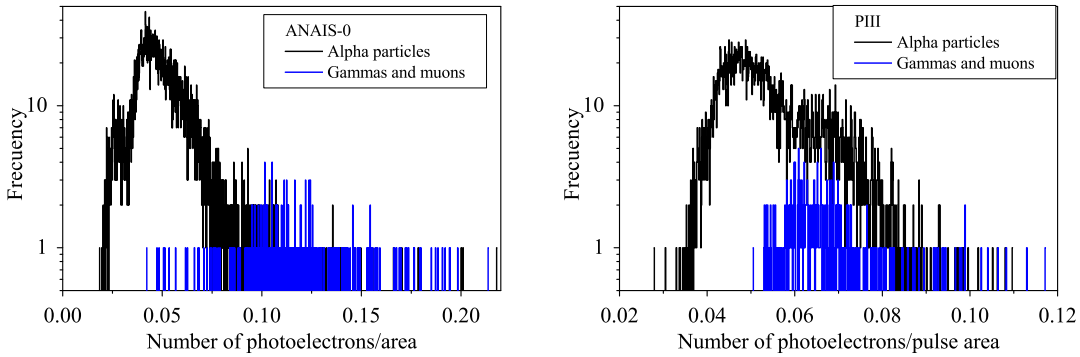

(a) (b)

Figure 3.35: *Distribution of the number of photoelectrons per area unit identified in the longest timescale for alpha particles (black) and gammas/muons (blue) interacting in ANAIS-0 (a) and PIII (b).*

the future the PMT readout circuit to solve this problem, that it also slightly affect the shortest timescale pulses (see below).

And finally, the shortest time scale pulses from ANAIS-0 have been fitted in the range from 0 to 1000 ns after the onset of the pulse to a combination of exponential decays. Fits have been done only in independent mode for both kind of events: from alpha and gamma/muon origin. In the case of the alpha pulse, the best fit is achieved when using only two exponential components: one for the rise and other for the decay, this fit is shown in Figure 3.36.a However, a slower component seems to be present in the pulses, that the fitting procedure is not able to take it out from the data; other possibility is an alteration of the pulse shape due to the pulse overshoot commented before. The same procedure has been applied for the fitting of the average gamma pulse, being most of the previous comments valid in that case also. The results of the fits are shown in Table 3.9 and the slow component no fitted can be seen in Figure 3.36.b. It is very probable that a

time constant in the microsecond range is present in the data, but the effect of the signal overshoot in this range prevents from deriving any estimate.

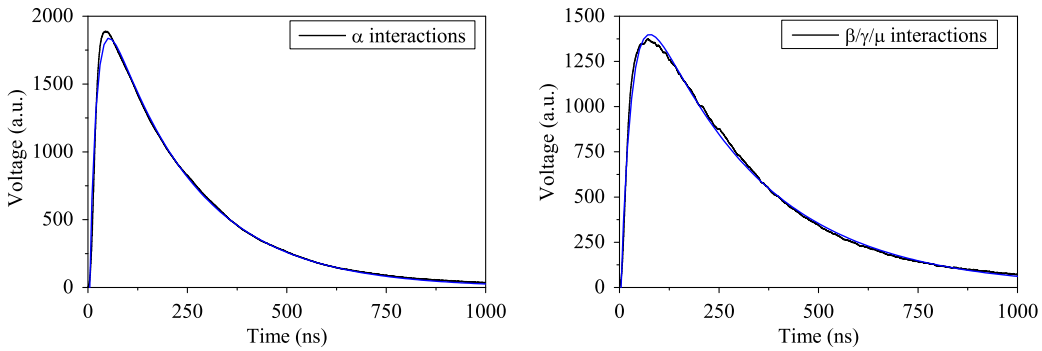

(a) (b)

Figure 3.36: *(a) Pulses produced by the interaction of alpha particles (a) and of gammas/muons (b) in the ANAIS-0 module in a 1 μs temporal scale, registered with the MATACQ card, shown in black. The fit of the data shown in Table 3.9 are shown in blue. Events from both populations correspond to the same pulse area.*

	α	$\beta/\gamma/\mu$
τ_1 (ns)	17.98 ± 0.12	28.23 ± 0.14
A_1	3119 ± 11	2275 ± 6
τ_2 (ns)	219.28 ± 0.52	291.85 ± 0.60
A_2	2551 ± 6	287.35 ± 0.51

Table 3.9: *Results of the fit from 0 to 1000 ns after the pulse onset for ANAIS-0 module. The fit takes every data set in an independent way. The first values correspond to an exponential growth and the second to an exponential decay.*

We can conclude that for alpha particles, the scintillation constant derived from our analysis is 220 ns, compatible with results from the bibliography. The rise time of the pulses is compatible with the rise time of the S.E.R. pulse, being an indication that no delay in the light emission is taking part in the scintillation mechanism. However, for the gamma pulse, some more complicated mechanisms are coming into play: an slower rise time of the pulse is found, that could be attributed to a delayed scintillation by an intermediate non-scintillating state decay, for instance; in addition, the decay time constant value of 290 ns, could be also explained by a combination of a faster constant and a longer one, but the fit is not able to converge in this scenario. This constant is somehow longer than typical values in the bibliography, but it is worth remarking that in many of the published results, the mean time of the pulse and not a decay constant is given.

Summarizing, the fast components of the NaI(Tl) scintillation pulses for alpha and beta/gamma particle interactions have been fitted, given results compatible with those published [128, 140–144]. However, for the first time, the slow scintillation constants in NaI(Tl) are measured with this accuracy. The effect is observed in ANAIS-0 and PIII crystals, although there are differences between them, specially in the amplitude of the effect, pointing to impurities or defects in the crystalline lattice as the origin of the scintillation.

3.7 Quenching factor for α particles.

Quenching factor for the conversion into visible energy of the energy deposited by alpha particles with respect to that converted by gammas has been determined with ANAIS-0 data. Alpha particle events are selected by Pulse Shape Analysis, and the corresponding spectrum has been autocalibrated, because no external calibration is possible (see section 4.2). Hence, from the position of the alpha peaks in electron equivalent energy (using the gamma calibration at very high energy) it is possible to determine the quenching factor for alpha particle interactions with respect to gamma ones. The alpha lines are observed with electron equivalent energies shown in Table 3.10.

E_α(MeV)	E_{ee} (MeVee)	E_{ee}/E_α
4.2	2.56	0.610
4.78	3.016	0.631
5.3	3.54	0.668
6	4.04	0.673
6.29	4.33	0.688
6.78	4.71	0.695

Table 3.10: *Quenching factor determination for the different α lines observed with the ANAIS-0 module.*

Both, visible energy (in terms of electron equivalent energy) for the alpha lines observed in the ANAIS-0 module and quenching factor are plotted as a function of the alpha energy in Figure 3.37 and fitted linearly. Results of the fit are shown in equations 3.3 and 3.4. The alpha particle quenching factor derived is compatible with the one obtained by the DAMA/LIBRA experiment [97]: $E_\alpha/E_{ee} = (0.0257 \pm 0.010) \cdot E_\alpha(MeV) + (0.467 \pm 0.006)$ and with the predicted by Tretyak in [85].

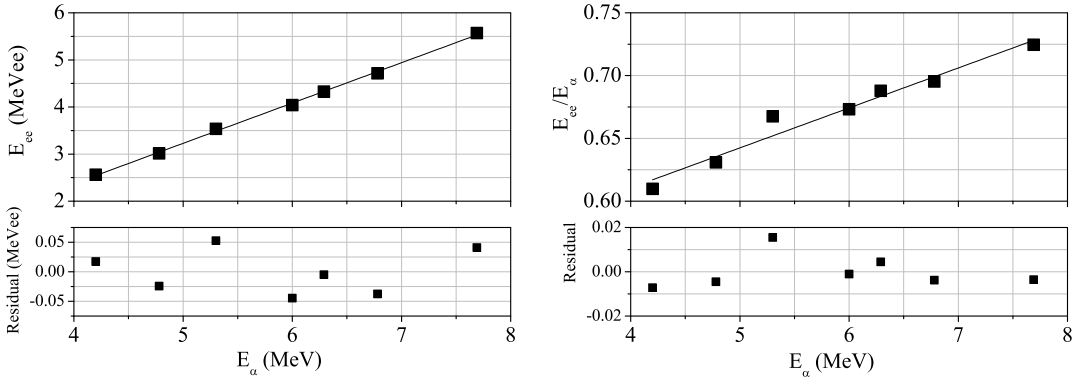

(a) (b)

Figure 3.37: *(a) Visible energy (in terms of electron equivalent energy) for the alpha lines observed in the ANAIS-0 module background as a function of the alpha energy. (b) Quenching factor for alpha events with respect to beta/gamma events is shown as a function of the alpha energy. Linear fits for both and corresponding residuals are shown and results of the fits are in equations 3.3 and 3.4.*

$$E_{ee} = (0.855 \pm 0.014) \cdot E_\alpha(MeV) - (1.050 \pm 0.085) \tag{3.3}$$

$$E_{ee}/E_\alpha = (0.032 \pm 0.003) \cdot E_\alpha(MeV) + (0.483 \pm 0.017) \tag{3.4}$$

Chapter 4

Background understanding

This chapter presents the background model for the ANAIS-0 module, described in chapter 2. First, the ANAIS-0 prototype background in different set-up conditions is shown and compared (section 4.1.1). Then, we summarize the main bulk contaminants contributing to the background, that have been precisely identified and quantified by different techniques: discrimination of alpha particles vs beta/gamma background by Pulse Shape Analysis (PSA) for the uranium and thorium natural radioactive chains and coincidence technique for the ^{40}K bulk contamination (section 4.1.2). Cosmogenic isotopes present in the NaI crystal have been also identified and estimates are presented (section 4.1.2).

Secondly, we describe the Monte Carlo simulations using Geant4 package, that have been accomplished for the different contributions and the tests carried out to validate the code (section 4.2). Then, we show the comparison between simulated and experimental data. Only a few assumptions are required in order to explain most of the measured background at high energy, supporting the goodness of the proposed model for ANAIS-0 whose background is dominated by ^{40}K bulk contamination. At low energy, some non-explained background components are still present and additional work is required to improve background understanding, but some plausible background sources contributing in this range have been studied and, under some hypotheses, its contribution to the background is considered in an improved background model (section 4.3).

4.1 Background measurements and radioactive contaminants identification

ANAIS-0 module has been operated in various set-ups. Different photomultipliers coupled to ANAIS-0 module with or without light guides have been tested in order to choose the optimum configuration in terms of threshold and background, as it will be detailed in section 5.2.

The background spectra measured for each configuration have been thoroughly studied in order to understand the origin of the main background contributions, specially in the low energy region. As result, it can be stated that bulk contaminations of the NaI crystal are responsible of most of the background.

4.1.1 Background measurements

During the ANAIS-0 operation the energy spectra have been registered in three different energy ranges using different QDC channels: low energy (from 2 keV up to 100 keV), high energy (from 100 keV up to 2 MeV) and very high energy (from 2 MeV up to 40 MeV), as it was stated on section 2.5.

In Table 2.6 main features of the different ANAIS-0 set-ups were summarized (see section 2.1.2 for more details). The main goal of ANAIS-0 was to determine the best configuration in terms of light collection and background at low energy, to be applied in the final design of the modules of the ANAIS experiment. Different types of photomultipliers were tested and their contribution to the background was studied. PMTs are complex devices that, traditionally were built with components non-specially selected in terms of radiopurity, so they used to be an important contribution to the radioactive background of any experiment using them. Recently, R+D in this field has allowed to develop ultralow background models that are changing this framework [153].

The normalized background spectra for the different ANAIS-0 setups are shown in Figure 4.1 for the high energy region and in Figure 4.2 for the low energy region. The set-up 1 data were taken just after the installation underground of the ANAIS-0 module and cosmogenic lines are observed (see section 4.1.2). It is worth remarking that these spectra correspond to raw data, and no filtering at low energies has been applied. Hence, no threshold comparison between the different set-ups can be derived from these plots.

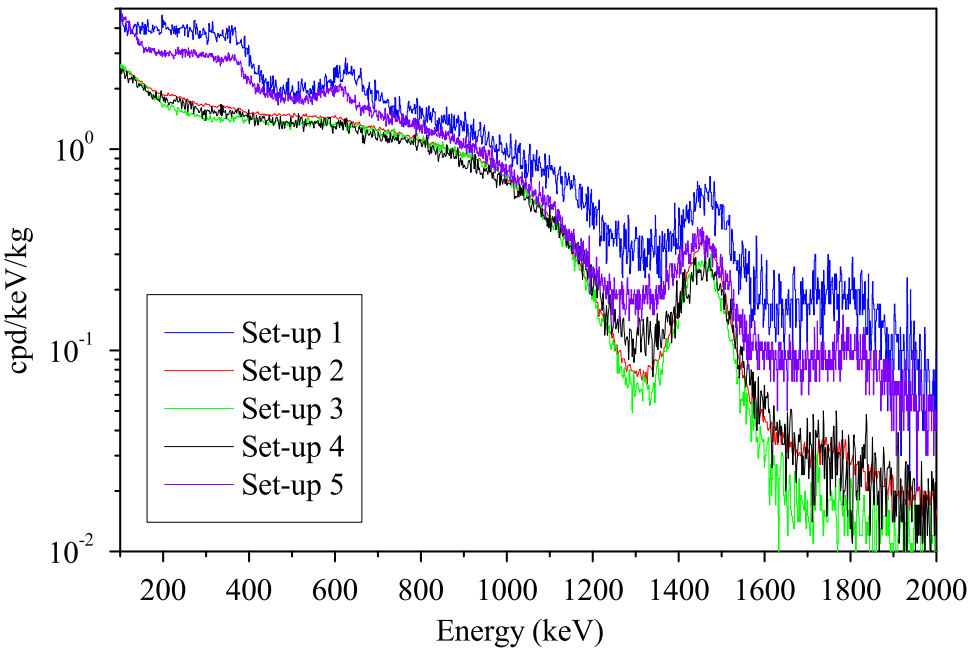

Figure 4.1: *Comparison of the high energy spectra for the different ANAIS-0 set-ups (see Table 2.6).*

From these direct background measurements, we can conclude that ETL (an hence, also LB, that have very similar radiopurity) photomultipliers contribute strongly to the background and will be hardly used without light guides without jeopardizing the experiment background goal. ULB PMTs scarcely contribute to the background at the present level of sensitivity and light guides will not be probably required (improving light collection according to results presented in section 5.2.5). LB PMTs with light guides are a similar option in terms of background. A compromise between background contribution, light collection efficiency and PMT price has to be taken. In this sense, last tested option (VLB PMTs) could be an affordable option, being the background contribution at low energy probably acceptable even without light guides. Anyway, because in these measurements background at low energy is clearly dominated by bulk NaI contributions, we will revise later this issue in the light of the simulations of the absolute PMT contribution to the background (see section 4.2.2).

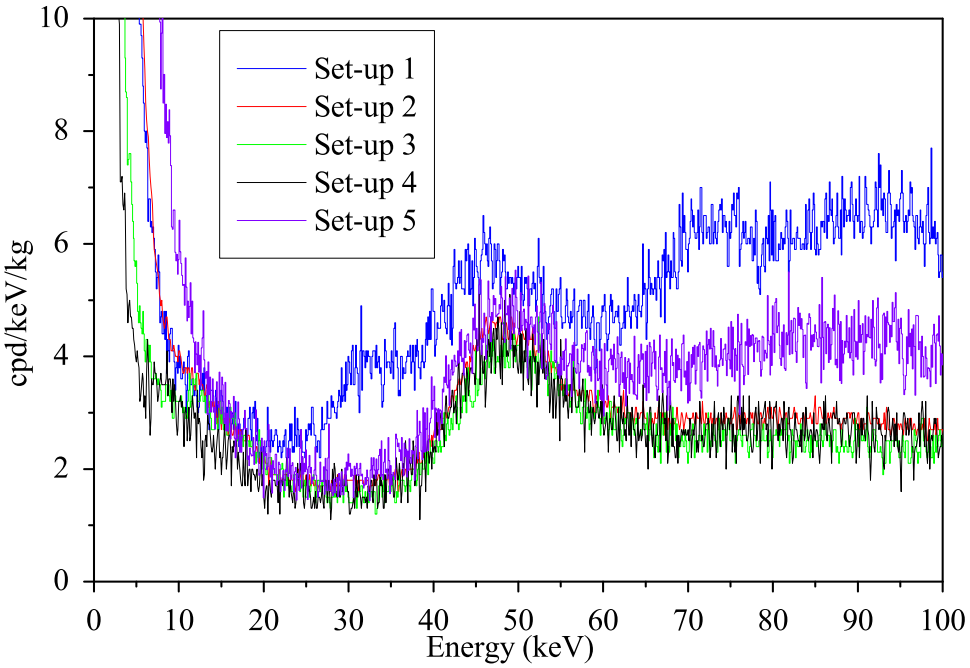

Figure 4.2: *Comparison of the low energy spectra for the different ANAIS-0 set-ups (see Table 2.6). Only raw data are shown. Set-up 1 data were taken just after the installation underground of the ANAIS-0 module and cosmogenic lines are observed.*

4.1.2 Radioactive contaminants in ANAIS-0 crystal

^{40}K bulk content

^{40}K is probably the most relevant radioactive contaminant in the bulk for NaI(Tl) detectors. It is specially important the ^{40}K contribution to the background at the very low energy, as it will be shown later. Because of that, a very good knowledge of such a contamination is required in order to properly estimate the sensitivity prospects achievable with the new ANAIS crystals, grown using potassium-purified NaI powder.

The technique used to estimate the ^{40}K activity in the bulk of the NaI crystal is the coincidence measurement. It consists in measuring in one detector X-ray/Auger electron emissions of argon amounting a total energy release of 3.2 keV following the K-shell EC of ^{40}K (Ar binding energies are listed in Table 4.1) in coincidence with a 1461 keV gamma fully absorbed in another detector sharing the experimental space, inside a common shielding. Besides a few accidental coincidences, the 3.2 keV peak is clearly observed. From the measured coincidence rates and Geant4 estimated efficiencies, the ^{40}K activity of the NaI crystals can be deduced. In Figure 4.3 a simplified ^{40}K decay diagram is shown and more details on the ^{40}K decay channels can be found in Table 4.2.

Shell:	K	L_1	L_2	L_3	M_1	M_2	M_3
Energy (keV):	3.2060	0.3263	0.2507	0.2486	0.0292	0.0159	0.0158

Table 4.1: *Atomic electron binding energies for argon obtained from [127].*

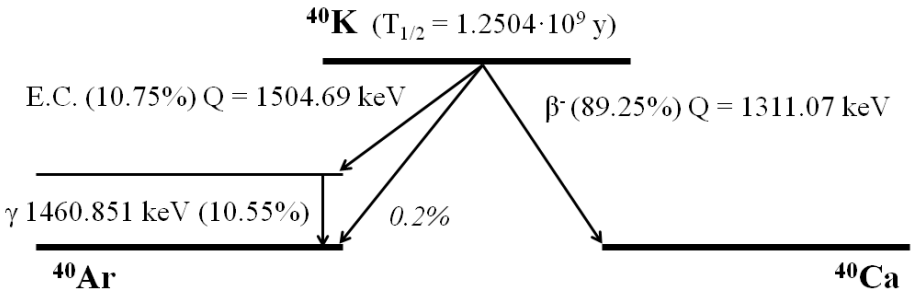

Figure 4.3: *Simplified ^{40}K decay diagram. Data have been taken from [127]. See Table 4.2 for more details about the branching ratios and decay channels.*

	Energy (keV)	Probability (%)	P_K	P_L	P_M
$\epsilon_{0,1}$	44.0 ± 0.3	10.55 ± 0.11	0.763	0.209	0.027
$\epsilon_{0,0}$	1504.69 ± 0.19	0.2 ± 0.1	0.88	0.086	0.013
$\beta^+_{0,0}$	489.3 ± 0.3	0.00100 ± 0.00012			
$\beta^-_{0,0}$	1311.07 ± 0.11	89.25 ± 0.17			
$\gamma_{1,0}$	1460.822 ± 0.006	10.55 ± 0.11			

Table 4.2: *Q-value energies and branching ratios for the different decay channels of ^{40}K: EC to the first excited state ($\epsilon_{0,1}$), EC to the ground state ($\epsilon_{0,0}$), beta plus (β^+) and beta minus (β^-). Only EC to the first excited state is followed by a gamma emission. In the case of the EC channels, the relative probabilities of K/L/M capture is also shown (P_K, P_L, P_M). Data have been obtained from [127].*

It is worth noting that the rate of the direct decay of ^{40}K to the ground state to ^{40}Ar through electron capture (0.2%) has not been experimentally measured and hence, the uncertainty on the corresponding branching ratio is very high [154]. This decay is important for the final ANAIS background because it can not be rejected by the coincidence method. However, at the moment it is not possible to measure it in the frame of the ANAIS project.

Different set-ups were operated at the LSC with the objective of determining the ^{40}K content of all the NaI(Tl) available crystals. 11 NaI(Tl) detectors from BICRON of 10.7 kg

each, were previously screened; some of them were placed in two different set-ups as cross-check. In Figure 4.4 one of these set-ups is shown.

Results of the ^{40}K bulk content for all the BICRON crystals are presented in Table 4.3. All of them have very similar ^{40}K contents, far too high to allow their use in a dark matter experiment as ANAIS and new ultrapure NaI(Tl) crystals have to be used.

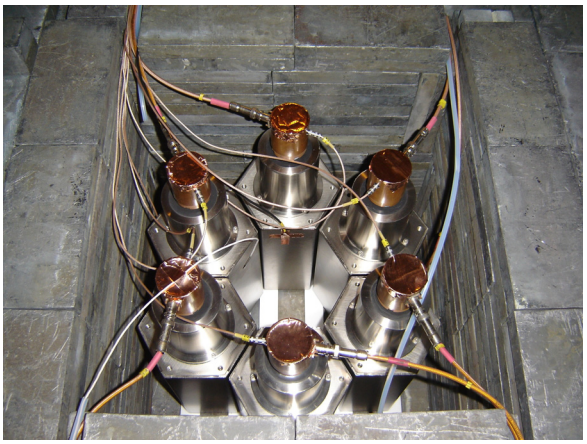

Figure 4.4: *Set-up at old LSC with six NaI BICRON crystals for the estimate of their ^{40}K bulk crystal content by the coincidence technique.*

Detector	^{40}K Activity (mBq/kg)
EP054	13.7 ± 0.3
EP055	15.2 ± 0.1
EP056	18.8 ± 0.2
EP057	20.9 ± 0.4
EP058	16.2 ± 0.3
EP059	16.6 ± 0.2
EL214	17.9 ± 0.4
EM301	21.2 ± 0.4
EL604	16.5 ± 0.3
EL603	14.5 ± 0.2
EL607 (PIII)	15.7 ± 0.5

Table 4.3: *Results for ^{40}K bulk activity in the previously characterized BICRON - 10.7 kg NaI(Tl) crystals.*

The estimate of the ^{40}K bulk content of the ANAIS-0 crystal, was also done afterwards in a dedicated set-up (see section 2.2), measuring in coincidence with the previously studied Prototype III (the corresponding set-up is shown in Figure 4.5). Measurements were carried out at the old LSC in two phases: ANAIS-0 was coupled to two ETL PMTs in phase I, and to two LB PMTs in phase II. Live time available of each phase is shown in

Table 2.7. Phase III had another purpose, see section 2.2, but these data will be revised at the end of the chapter, see section 4,4. Trigger was done in logic OR mode of the the two detector signals, being both recorded independently of the detector(s) triggering. Data have been analyzed separately for each phase and ^{40}K bulk content of the PIII has been also determined as cross-check.

Figure 4.5: *Set-up at LSC with PIII (top) and ANAIS-0 (bottom) for the estimate of their* ^{40}K *bulk content.*

The first step is to select the ^{40}K high energy events in one detector: Different windows ($1\,\sigma$, $2\,\sigma$ and $3\,\sigma$) at the 1461 keV gamma line have been considered to select the coincident events in the other detector. High energy spectra for the two phases of ANAIS-0 and PIII are shown in Figure 4.6 (left) and a zoom around the 1461 keV line (right). The different windows studied are also shown in Figure 4.6 (right), and in the following σ will refer for each detector to the corresponding to that 1461 keV line. The low energy spectra in coincidence with $1\,\sigma$ window around the 1461 keV line in the other detector are shown in Figure 4.7. The gain of PIII along phase II was probably not stable enough and the 1461 keV line is distorted; this could lead to a decrease in the efficiency of the coincidence in an undetermined way, compromising the validity of the derived result.

Only a small fraction of the events selected by the coincidence are attributable to ^{40}K decay, and are distributed in a peak around 3.2 keV, the rest are mostly baseline noise and a few fortuitous coincidences. A simple selection of ^{40}K events is done, considering those above a threshold. Table 4.4 shows the analysis thresholds chosen for each phase and detector. The choice is done just by visual inspection. It must be remarked that this is not the threshold of the experiment.

In order to check the ^{40}K origin of the low energy events selected by the coincidence, the effect of changing the high energy window above and below the 1461 keV position

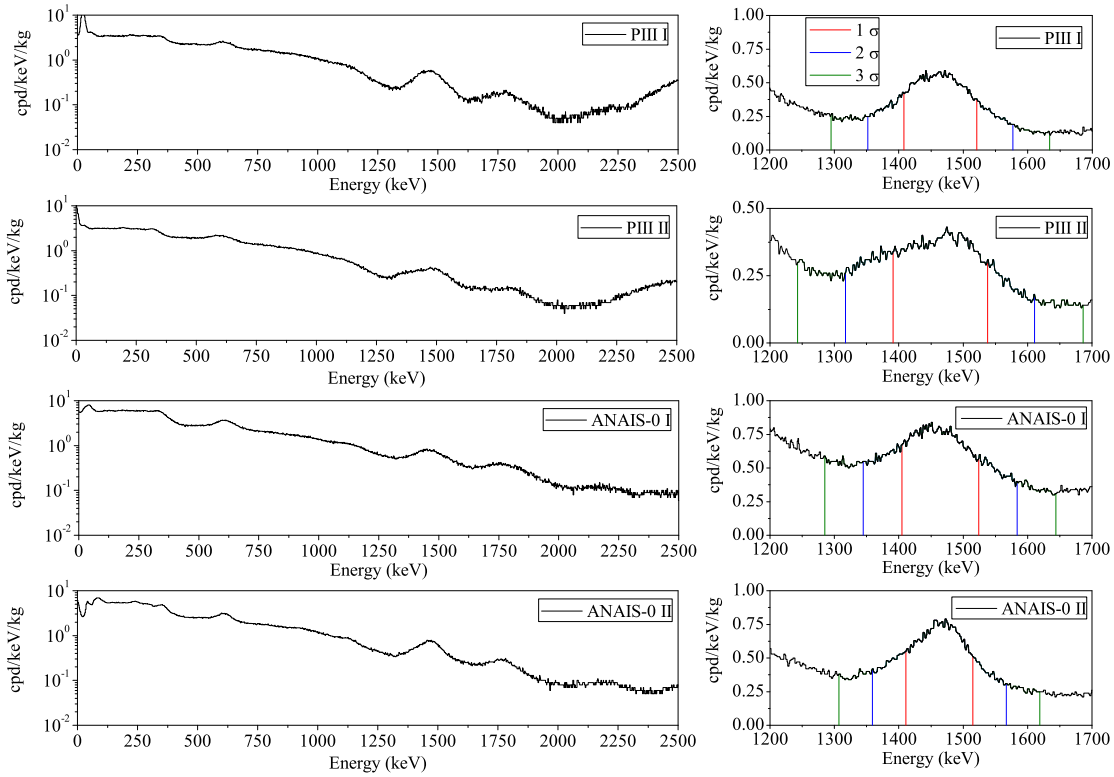

Figure 4.6: *High energy spectra of PIII and ANAIS-0. Left, the whole spectra and right, a zoom showing the 1461 keV gamma line following ^{40}K EC decay for the two considered phases. The 1 σ (red), 2 σ (blue) and 3 σ (green) coincidence windows are also shown.*

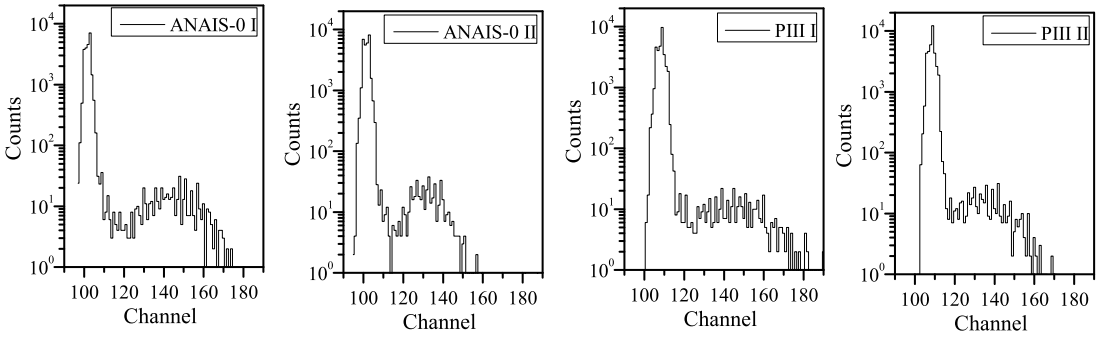

Figure 4.7: *Low energy spectra in coincidence with 1σ windows around the 1461 keV line in the other crystal, shown in Figure 4.6, for the two detectors and two phases considered in this study.*

has been studied. For this purpose, the coincidence is done with 1 σ windows centered in channels 2 σ above and below 1461 keV. Also another window more energetic is selected, centered 11 σ above the 1461 keV position (see results in Figure 4.8). Assuming gaussian shape for the 1461 keV line, the corresponding percentage of real ^{40}K events selected in each window should be 68% for $\mu \pm \sigma$, 16% for $\mu + 2\sigma \pm \sigma$ and 0 for the $\mu + 11\sigma \pm \sigma$. The

Detector	Phase	Threshold (Channel)
ANAIS-0	I	115
ANAIS-0	II	115
PIII	I	125
PIII	II	120

Table 4.4: *Threshold (in channels) considered for the selection of ^{40}K events from noise events in the low energy spectra for the different phases and detectors.*

highest window should only present fortuitous coincidences and could allow us to estimate their contribution in the other windows.

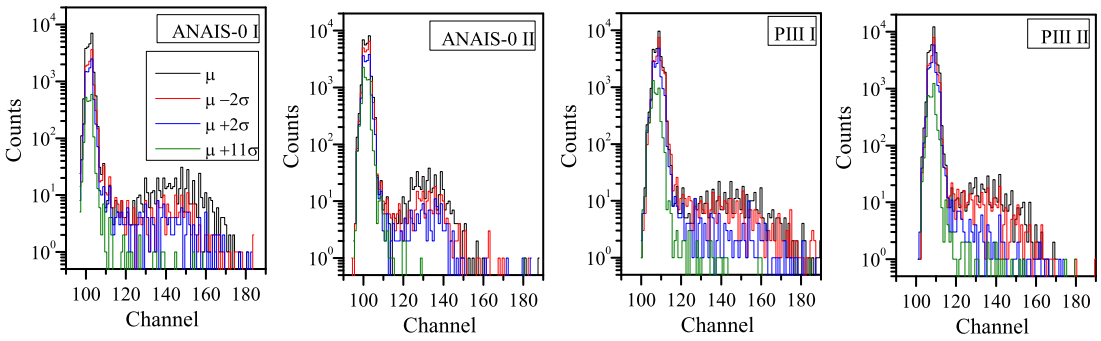

Figure 4.8: *Low energy spectra in coincidence with high energy windows in the other detector (all of them having the same width, $\pm\sigma$) are shown for the different phases and detectors: centered at 1461 keV peak (μ) in black, centered 2σ above ($\mu + 2\sigma$) in blue, centered $\mu - 2\sigma$ below ($\mu - 2\sigma$) in red, and centered further above ($\mu + 11\sigma$) in green.*

Detector	Phase	μ	$\mu + 2\sigma$	$\mu - 2\sigma$	$\mu + 11\sigma$
		Events			
ANAIS-0	I	726	95	312	8
ANAIS-0	II	713	142	253	26
PIII	I	706	146	358	22
PIII	II	766	137	205	12

Table 4.5: *Number of events selected by the coincidence above the threshold, shown in Table 4.4, in the different windows studied (all of them having the same width $\pm\sigma$).*

In Table 4.5 the results are presented considering only events above the thresholds shown in Table 4.4. As expected, events at low energy coincident with the $\mu+11\sigma$ window correspond to chance coincidences. The $\mu + 2\sigma$ window presents results compatible with the expected 16% of the total number of coincident events, but slightly underestimated. Events found in coincidence with the $\mu - 2\sigma$ window are much more than expected for

a pure gaussian peak contribution, but this is probably due to the presence of compton events with partial energy deposition from the ^{40}K gamma line.

The setup has been simulated with Geant4, version geant4.9.1.p02 [155], in order to evaluate the probability that, after a ^{40}K disintegration in one crystal, the 1461 keV photon escapes and releases the full energy in the other detector.

500000 photons of 1460.8 keV have been simulated assuming homogeneous distribution of the contaminant in the bulk in ANAIS-0 and PIII crystals. The absolute branching ratio for the ^{40}K K-shell EC followed by the emission of the 1460.8 keV photon is 0.080325729, as given by Geant4 [155]. The number of events with the full gamma energy absorbed in PIII or ANAIS-0 crystals when emitted in ANAIS-0 and PIII, are 8258 and 6998, respectively. Thus, the efficiencies for the respective coincidences are $1.33 \cdot 10^{-3}$ and $1.13 \cdot 10^{-3}$.

The ^{40}K activity of every crystal is estimated with the area of the 3.2 keV peak (Area), the total available live time (LT), the crystal mass (m), efficiency of the coincidence (eff) and the fraction of the total number of events selected by the coincidence window (F).

$$Activity(Bq/kg) = \frac{Area(counts)}{LT(s) \cdot m(kg) \cdot eff \cdot F} \tag{4.1}$$

The area of the 3.2 keV peak (Area) is obtained by fitting to a gaussian the events above the threshold. The fits are shown in Figure 4.9.

The ^{40}K activity is calculated for each phase individually and using all the available data for the three different coincidence window widths (1σ, 2σ and 3σ) around 1461 keV energy. Results for each phase and detector are shown in Table 4.6.

Detector	Phase	^{40}K Activity (mBq/kg)		
		$1\,\sigma$	$2\,\sigma$	$3\,\sigma$
ANAIS-0	I	14.3 ± 0.8	15.1 ± 0.9	17.2 ± 1.1
	II	11.1 ± 0.5	12.4 ± 0.5	13.4 ± 0.6
	I and II	12.7 ± 0.5	13.6 ± 0.5	15.2 ± 0.6
PIII	I	13.5 ± 0.9	16.8 ± 1.13	20.1 ± 1.4
	II	13.9 ± 0.9	16.1 ± 1.1	19.0 ± 1.4
	I and II	13.7 ± 0.6	16.4 ± 0.7	19.5 ± 1.0

Table 4.6: *^{40}K activity calculated for ANAIS-0 and PIII using different width coincidence windows. Combined values derived for each detector are also shown.*

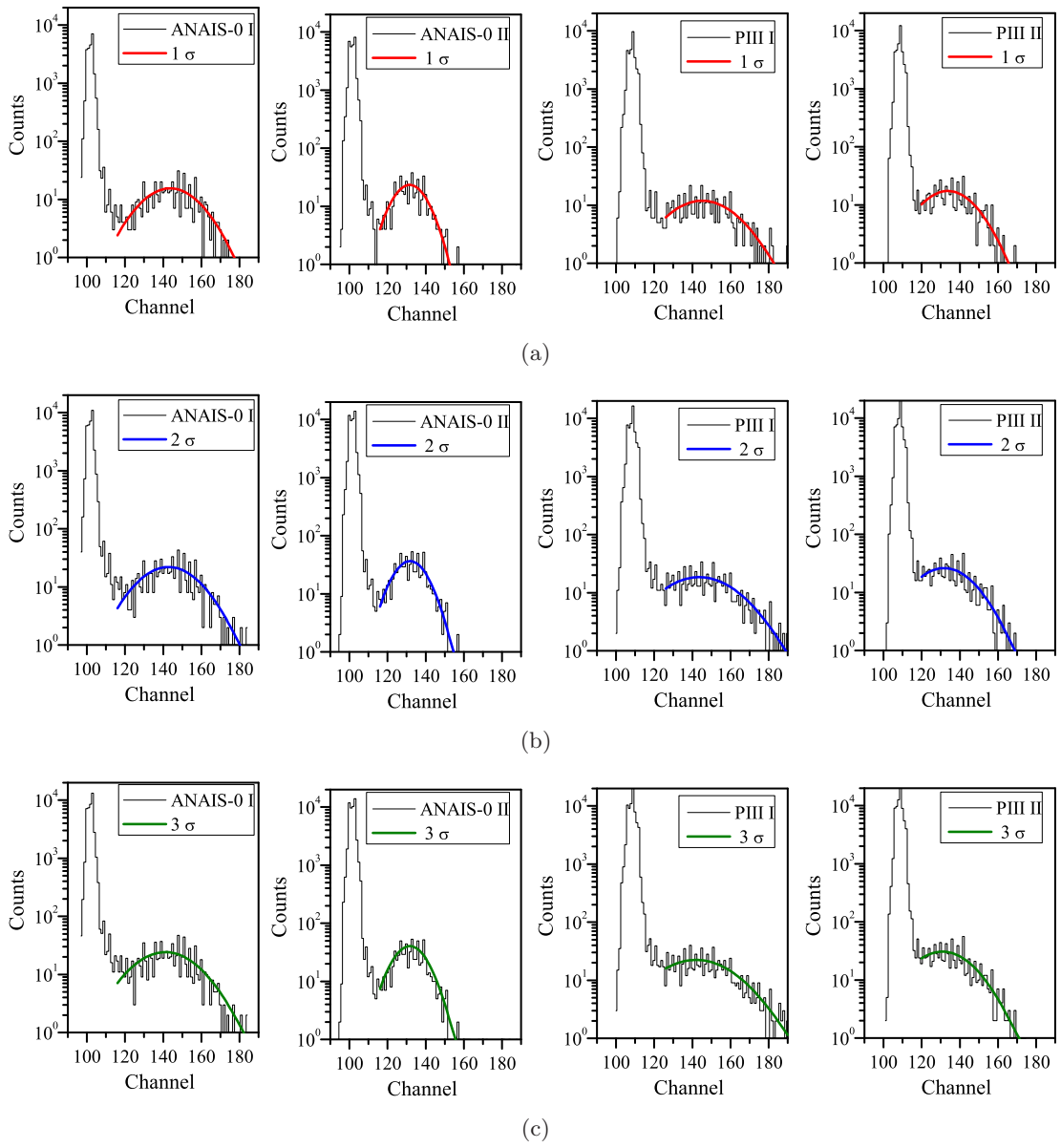

Figure 4.9: *Low energy coincident events for the* 1σ *(a),* 2σ *(b) and* 3σ *(c) coincidence windows, and gaussian fits of the events above the threshold.*

Results derived from the different windows and phases analyzed are mostly compatible. As expected, larger windows have a larger contribution from chance coincidences and Compton events. Hence, results of the $1\,\sigma$ window have been taken in the following as the most reliable. Phase II presented a non gaussian shape for the 1460 keV gamma line of PIII which might have been caused by gain instabilities. However, phase I showed a higher discrepancy between the results determined with the different sigma windows and in Figure 4.9 it can be seen that the 3.2 keV peak is wider in phase I and more contribution from chance coincidences is expected. In PIII both phases were similar. Then, the average

of phase I and II results for every detector has been taken as final result of our analysis, being shown in Table 4.7.

Detector	^{40}K Activity (mBq/kg)
ANAIS-0	12.7 ± 0.5
PIII	13.7 ± 0.6

Table 4.7: *^{40}K activity estimated for ANAIS-0 and PIII crystals by the coincidence technique.*

We checked that these results were compatible with the intensity of the 1461-1464 keV gamma line seen at ANAIS-0 background. There are contributions to this line coming from K-shell EC decay of ^{40}K, producing 1464 keV (1460.8 keV + 3.2 keV = 1464.0 keV) total energy release, but also from L and M-shell EC decays, with energy depositions that can not be distinguished from the 1461 keV line. For this comparison we chose data from ANAIS-0 set-up 4 to minimize contributions from external components contaminated in ^{40}K to the photopeak and fitted it to a gaussian, comparing its area with the prediction of the previously introduced simulation. For 500000 isotropic 1460.8 keV photons simulated, the ANAIS-0 crystal detects 135294 photons in the photopeak (27.1%). Taking into account that only in 10.55% of the ^{40}K decays a high energy gamma is emitted, if the ANAIS-0 set-up 4 result for this 1461-1464 keV peak is $32.38 \pm 0.32\, cpd/kg$, the activity of ^{40}K derived is $12.32 \pm 0.18\, mBq/kg$ assuming that only ^{40}K in the crystal bulk is contributing to this peak. This result is compatible with the activity derived from the coincidence measurement and implies that the ANAIS-0 background is dominated by ^{40}K in the bulk.

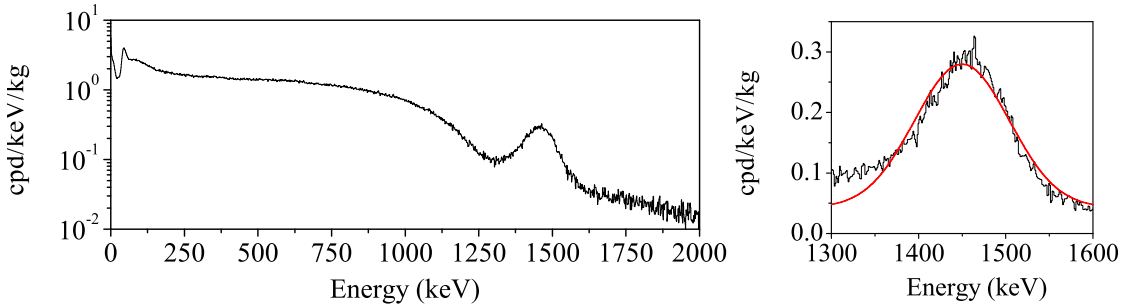

Figure 4.10: *High energy spectrum for the ANAIS-0 set-up 4 (not a coincidence set-up) used to derive the ^{40}K bulk content from the intensity of the background line at 1461-1464 keV, assuming negligible contributions from external ^{40}K sources.*

At last, the temporal distribution of ^{40}K events at low energy selected by the coincidence above the threshold is shown in Figure 4.11. Average values of 9.32±3.63 counts/day for ANAIS-0 and of 8.46±3.11 counts/day for PIII crystals are reported without significant fluctuations.

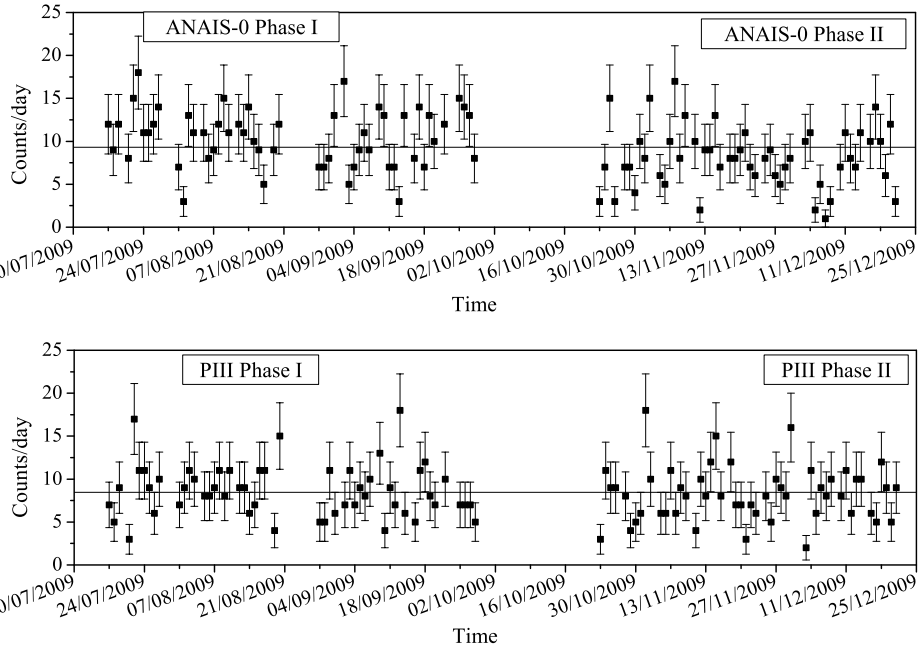

Figure 4.11: *Rate of the 3.2 keV events selected by the coincidence above the threshold. Average values of* 9.32 ± 3.63 *counts/day for ANAIS-0 and of* 8.46 ± 3.11 *counts/day for PIII crystals are shown as horizontal lines in both plots.*

^{238}U and ^{232}Th chains

Activities of the different branches in the ^{238}U and ^{232}Th chains have been quantified after identifying their alpha emissions. Tables 4.8 and 4.9 show the type of decay, lifetimes and energies of the different alpha emissions for all the isotopes of both chains. The visible energy corresponding to these disintegrations should be: $E_\alpha \cdot Q_\alpha + E_{recoil} \cdot Q_{recoil}$ because all the energy is absorbed in the detector. However, as Q_{recoil} for so heavy nuclei should be really low [85] we have not considered this contribution in the following.

The acquisition dead time per event (≈ 4 ms, see section 2.5) complicates the observation of some alpha emissions, as ^{214}Po and ^{212}Po. However $^{212}Bi - Po$ events sequence can be identified in the same digitization window, because of the very short lifetime of ^{212}Po. In Figure 4.12, one example of such a pulse sequence is shown, corresponding to an special run of set-up 4 in which the digitization dynamic range was adjusted to match

$T_{1/2}$	Isotope	E_α(MeV)	I (%)	Activity
$4.468 \cdot 10^9\, y$	^{238}U			
	$\downarrow \alpha$	4.18	99.9	A0
$24.1\, d$	^{234}Th			
	$\downarrow \beta$			
$1.17\, m$	^{234m}Pa			
	$\downarrow \beta$			
$2.455 \cdot 10^5\, y$	^{234}U			
	$\downarrow \alpha$	4.75	99.8	A1
$7.538 \cdot 10^4\, y$	^{230}Th			
	$\downarrow \alpha$	4.66	99.7	A2
$1600\, y$	^{226}Ra			
	$\downarrow \alpha$	4.78	94.4	A3
$3.8\, d$	^{222}Rn			
	$\downarrow \alpha$	5.49	99.9	A3
$3.10\, m$	^{218}Po			
	$\downarrow \alpha$	6.00	99.9	A3
$26.8\, m$	^{214}Pb			
	$\downarrow \beta$			
$19.9\, m$	^{214}Bi			
	$\downarrow \beta$			
$164.3\mu\, s$(*)	^{214}Po			
	$\downarrow \alpha$	7.69	99.9	A3
$22.3\, y$	^{210}Pb			
	$\downarrow \beta$			
$5.01\, d$	^{210}Bi			
	$\downarrow \beta$			
$138.4\, d$	^{210}Po			
	$\downarrow \alpha$	5.30	100	A4
Stable	^{206}Pb			

Table 4.8: *Summary of the ^{238}U chain general information with more details in alpha decays [127]. The type of decay and lifetime of every isotope are shown, as well as the energies of the alpha emissions. If two or more alpha lines are closer than the energy resolution, the weighted average energy is shown. A0 - A4 are the possibly independent activities, if secular equilibrium in the chain is not imposed. (*) The acquisition dead time per event (≈ 4 ms, see section 2.5) complicates the observation of this line, that should be strongly inhibited.*

high energy events. This population can be identified by the difference of the positions of the minimum and pulse onset.

As α events are faster in NaI(Tl) than β/γ ones (see section 3.6), they can be discriminated by Pulse Shape Analysis (PSA) techniques. The digitalization scale is optimized for the study of the low energy events and in most of the available data the alpha events

$T_{1/2}$	Isotope	E_α(MeV)	I (%)	Activity
$1.405 \cdot 10^{11}\,y$	^{232}Th			
	$\downarrow \alpha$	3.99	99.9	A5
$5.75\,y$	^{228}Ra			
	$\downarrow \beta$			
$6.15\,h$	^{228}Ac			
	$\downarrow \beta$			
$1.9116\,y$	^{228}Th			
	$\downarrow \alpha$	5.37	99.4	A6
$3.66\,d$	^{224}Ra			
	$\downarrow \alpha$	5.69	94.9	A6
$55.6\,s$	^{220}Rn			
	$\downarrow \alpha$	6.29	99.9	A6
$0.145\,s$	^{216}Po			
	$\downarrow \alpha$	6.78	99.9	A6
$10.64\,h$	^{212}Pb			
	$\downarrow \beta$			
$60.55\,m$	^{212}Bi			
	$\downarrow \alpha_{36\%}$	6.06	35.9	0.36·A6
	$\downarrow \beta_{64\%}$			
$0.299\,\mu s$(*)	^{212}Po			
	$\downarrow \alpha$	8.78	100	0.64·A6
$3.053\,m$	^{208}Tl			
	$\downarrow \beta$			
Stable	^{208}Pb			

Table 4.9: *Summary of the ^{232}Th chain general information with more details in alpha decay [127]. The type of decay and lifetime of every isotope are shown, as well as the energies of the alpha emissions. If two or more alpha lines are closer than the energy resolution, the weighted average energy is shown. A5 and A6 are the possibly independent activities to be determined if secular equilibrium is not imposed. (*) The acquisition dead time per event ($\approx 4\,ms$) prevents the observation of this line, but $^{212}Bi - Po$ events are clearly identified in our data (see Figure 4.12).*

are out of the digitizer dynamic range. Hence, we decided to choose as discrimination parameter a polygonal cut in two variables: QDC energy estimate in the very high energy window and pulse area, see Figure 4.13. The parameter pulse area is clearly saturated at the alpha events region. However, the signal arriving to the QDC has been attenuated and after integration in a microsecond window does not saturate. For this reason, a faster pulse with the same QDC value presents a smaller area. The total high energy spectrum and the alpha events selected with the referred polygonal cut (see Figure 4.13) are shown in Figure 4.14. The alpha events have as origin bulk crystal contaminations since α particles have a very short mean free path in NaI.

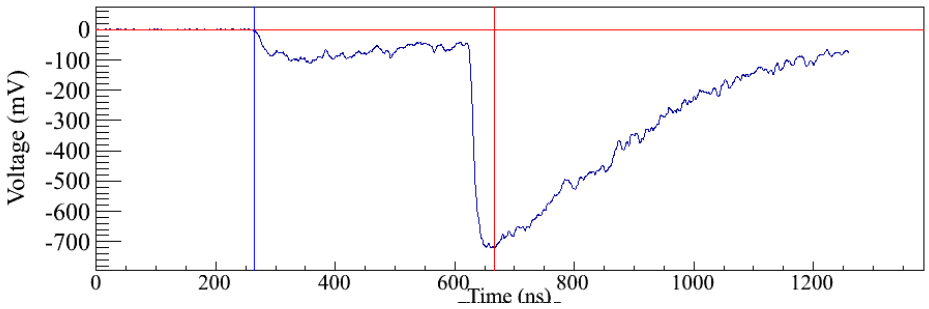

Figure 4.12: *Example of $^{212}Bi - Po$ event. The position of the minimum of the pulse is shown as a vertical red line and the pulse onset is shown as a vertical blue line. From the difference between both positions, events associated to this $^{212}Bi - Po$ sequence can be identified.*

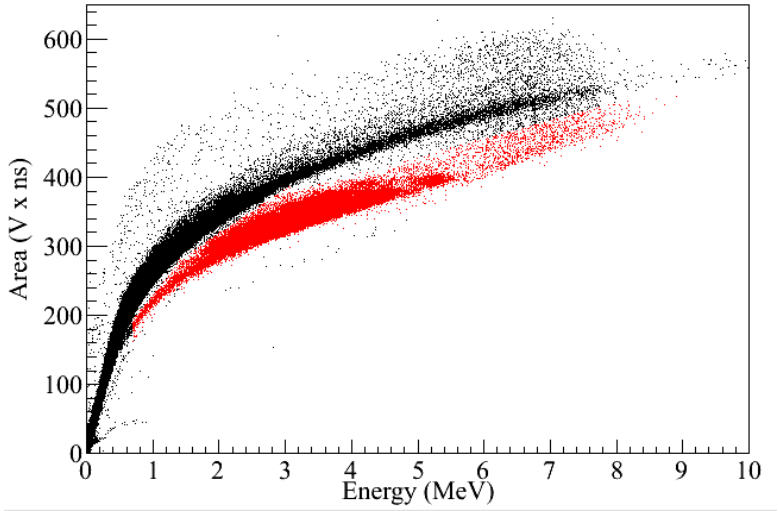

Figure 4.13: *Plot of the pulse area vs. electron equivalent energy (estimated with the QDC and calibrated with gamma lines) in the very high energy range for set-up 2 of ANAIS-0. Only the PMT 1 signal is shown because PMT 0 signal was not stable, see Figure 4.15. Alpha events (selected by a polygonal cut in these two parameters and shown in red in the figure) have a smaller area for a given QDC than beta/gamma (black) ones.*

The data studied here were taken with the set-up 2 (see Table 2.6), i.e. ANAIS-0 module with Hamamatsu LB PMTs coupled to 10 cm light guides, measuring at the old Canfranc Underground Laboratory facilities. Only data from one of the two PMTs (PMT 1) have been considered in the following because the other (PMT 0) showed fluctuations in gain along the measurement (see Figure 4.15).

If radioactive secular equilibrium in both chains is not imposed, there are seven possibly independent activities (A0 - A6) to be determined (see Tables 4.8 and 4.9). If there are two or more alpha lines from the same isotope closer than the energy resolution, the weighted average is shown.

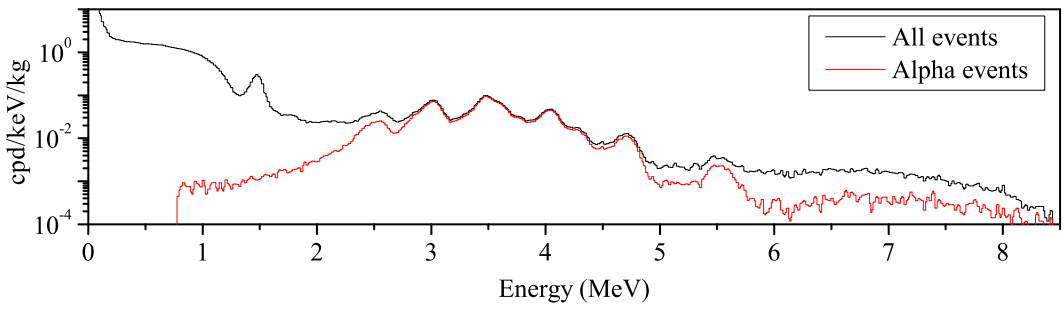

Figure 4.14: *The total high energy spectrum (black) of ANAIS-0 and the alpha spectrum built with the events selected by the polygonal cut shown in Figure 4.13 (red).* $^{212}Bi - Po$ *events (between 5 and 9 MeV) are only partially identified by this cut, because they are not pure alpha events. The energy is shown in electron equivalent energy units.*

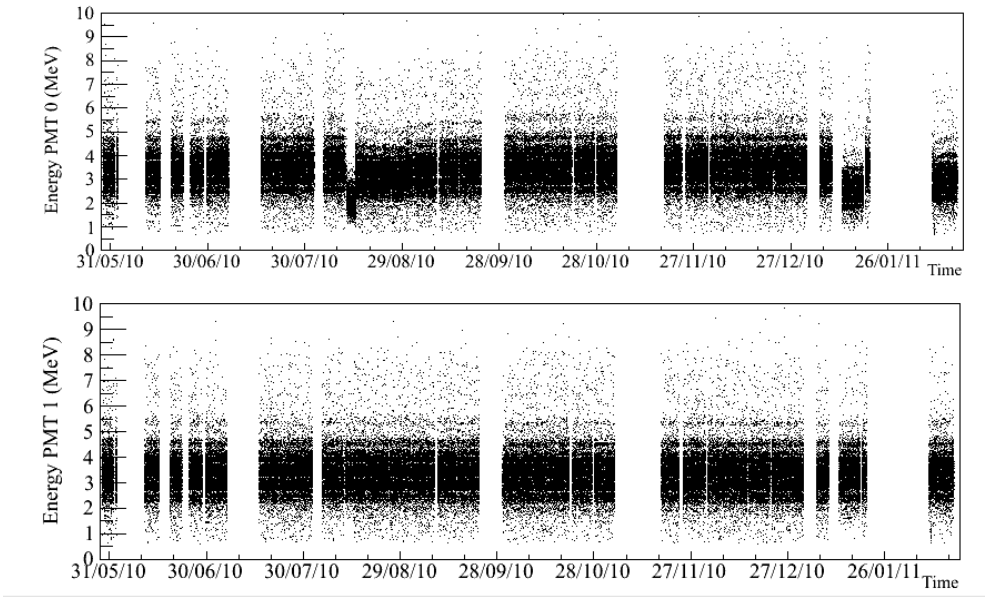

Figure 4.15: *Energy vs time for alpha selected events for each PMT signal for data corresponding to ANAIS-0 setup 2. PMT 0 signal (top) was not stable and has not been considered for the analysis.*

As the energy scale of the alpha events is different from that of β/γ events, because of the different quenching, specific calibration of the alpha spectra is mandatory, and external sources cannot be used with such a purpose. Because of that, an autocalibration procedure has been followed, using only information from background data. First, ^{220}Rn and ^{216}Po lines have been identified in the following sequence of fast alpha decays:

$$^{220}Rn \xrightarrow{55.6s} {}^{216}Po \xrightarrow{0.145s} {}^{212}Pb \tag{4.2}$$

Looking at the time interval between one alpha event and the following (Δ_{post}) or previous (Δ_{pre}) alpha event, ^{220}Rn (if $\Delta_{pre} < 55\,s$ and $\Delta_{post} < 0.15\,s$) and ^{216}Po (if $\Delta_{pre} < 0.15\,s$) lines are identified in the alpha spectrum (see Figure 4.16).

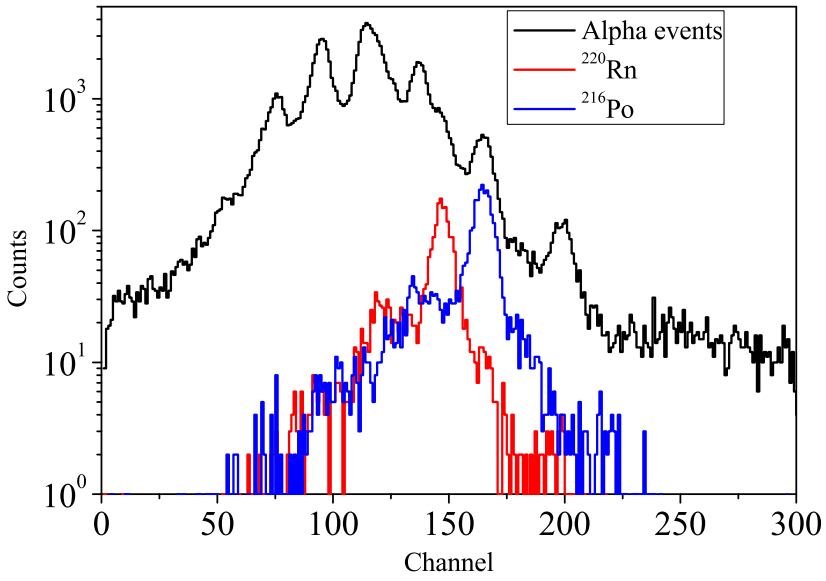

Figure 4.16: *Total alpha spectrum is shown in black. The events identified as coming from the decays of ^{220}Rn and ^{216}Po are shown in red and blue, respectively.*

Then, we built a preliminary calibration function using these ^{220}Rn and ^{216}Po identified lines and, taking it as a guide, the expected alpha energy values from ^{238}U and ^{232}Th chains are assigned to the seven main peaks observed in the spectrum, see the position of the peaks and the energy assigned in Table 4.10 and in Figure 4.17 the linear fit.

Channel	E_α (MeV)
75	4.20
94.5	4.78
114	5.30
136.5	6.00
146.55	6.29
164.2	6.78
198.58	7.69

Table 4.10: *Position of the main peaks in the alpha spectrum (shown in Figure 4.16) with the energy associated to each of them.*

The result is

$$E_\alpha(MeV) = (0.0284 \pm 0.0003) \cdot Ch + (2.0885 \pm 0.0464) \tag{4.3}$$

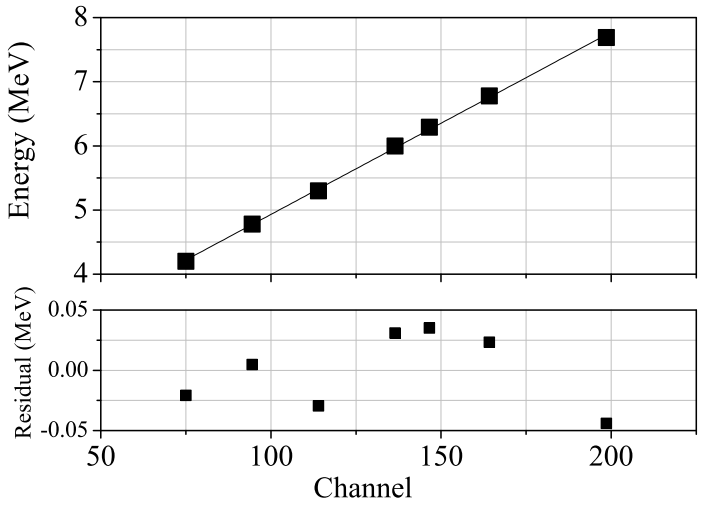

Figure 4.17: *Alpha calibration using all the lines shown in Table 4.10:* $E_\alpha(MeV) = (0.0284 \pm 0.0003) \cdot Ch + (2.0885 \pm 0.0464)$. *Reasonable linearity is observed.*

The fit seems reasonable and residuals are neither are too large, nor hint at any suspicious systematic effect. Anyway, validity of this calibration is limited, because the peaks observed in the spectrum corresponds to the addition of different contributions (see later).

Then, the calibrated alpha spectrum is fitted to a sum of gaussian peaks, one for every alpha decaying isotope in the ^{238}U and ^{232}Th chains, letting as free parameters the six independent activities (A1 to A6) and an additional R parameter to consider the reduced ^{214}Po intensity peak by dead time effects, fixing the position of the expected alpha peaks at their nominal values, and a common width for all them, fixing sigma at 0.11 MeV, in order to reduce the number of free parameters (this value is derived from the fit of the ^{220}Rn and ^{216}Po peaks singled out by the delayed coincidence). A0 has been supposed to be equal to A1, as no arguments for broken equilibrium between these two branches have been found. Results are shown in Figure 4.18 and Table 4.11.

Looking at the results, it can be concluded that secular equilibrium is broken in both chains. The derived activities are on the limit of the ANAIS requirements. Anyway, for ANAIS new crystals is expected to reduce these contaminations, specially in ^{210}Pb, that affects stronger the low energy region, where the dark matter is searched for. Alpha events observed below 3.5 MeV (see Figure 4.18) are possibly related with a surface alpha contamination component, whose contribution to the low energy background is discussed in sections 3.1 and 4.3.3.

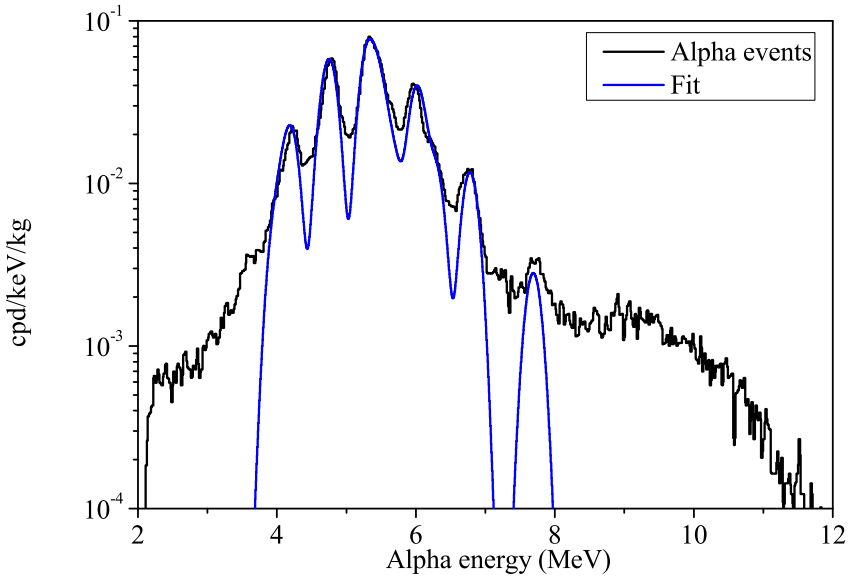

Figure 4.18: *Alpha spectrum (black) and fit to a sum of gaussian peaks (blue). See text for explanation of the fit details.*

Parent Isotope	Activity	Activity (mBq/kg)
$^{238}U/^{234}U$	A0/A1	0.075 ± 0.005
^{230}Th	A2	0.023 ± 0.007
^{226}Ra	A3	0.098 ± 0.004
^{210}Pb	A4	0.188 ± 0.005
^{232}Th	A5	0.013 ± 0.005
^{228}Th	A6	0.035 ± 0.003

Table 4.11: *Specific activities of the different ^{238}U and ^{232}Th chain branches for the ANAIS-0 crystal derived from the analysis of the alpha spectrum. Equilibrium is broken in both chains.*

Finally, the temporal distribution of the α events along ANAIS-0 set-up 2 measurements has also been studied and it is shown in Figure 4.19. An average value of $777.7 \pm 2.1\,\alpha$/day is obtained without relevant fluctuations.

Cosmogenic Isotopes

The ANAIS-0 detector was taken underground after its encapsulation at the University of Zaragoza, from 10/03/09 to 24/04/09, as explained in section 2.1. While the crystal was stored at surface laboratories, cosmogenic isotopes were being created by the interaction of cosmic radiation till equilibrium was reached (decay rate = production rate) and activity

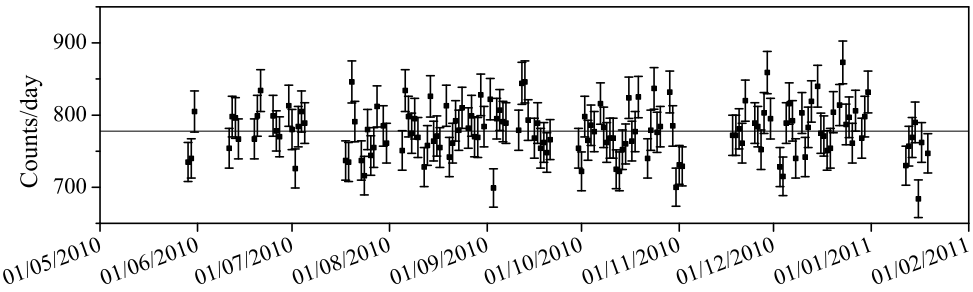

Figure 4.19: *Rate of alpha events selected in ANAIS-0 crystal during set-up 2 measurements, selected by the PSA technique. Average value of* 777.7 ± 2.1 *counts/day is shown as horizontal line.*

saturated. Fortunately, NaI has few cosmogenic activation processes and most of the isotopes produced are short-lived. Their decays were detected in the first operation runs carried out at the Canfranc underground laboratory (since 05/05/09).

The main lines with cosmogenic origin observed with ANAIS-0 in the first weeks of data are:

- The peak around 30 - 35 keV seen in the first week of measurement underground, blue line in Figure 4.20, is attributed to isotopes decaying by K-shell EC to Sb (30.8 keV K-shell energy) or to Te (31.8 keV K-shell energy), see section 5.2, so no quantitative description of activation yields can be derived from this peak. In the spectrum of the last week of set-up 1 (after 50 days underground) this peak was strongly reduced, which is compatible with an origin related to short lifetime isotopes.

- The peak around 70 keV (see also Figure 4.20) is explained by the addition of the X-rays (or Auger electrons) following the K-shell EC decay of ^{125}I (amounting 31.8 keV) with the 35.5 keV from the deexcitation of the daughter nucleus ^{125}I; this isotope has a half-life of 59.40 days.

- Also the presence of the 144.8 keV line from ^{125m}Te with a half-life of 57.40 days has been identified. This line is not seen in the ANAIS-0 module data because of the higher radioactivity level of the PMTs used, however in the PIII it has been observed during the Phase III of the ^{40}K measurement, when the PIII was brought underground and ULB PMTs were coupled (see Figure 4.20.b).

- ^{129}I is expected to be present in the crystals. As the half-life of this isotope is very high, the ^{129}I activity is not seen to decrease during the ANAIS-0 measurement time. It is not easy to quantify the ^{129}I activity because it depends on the geologic

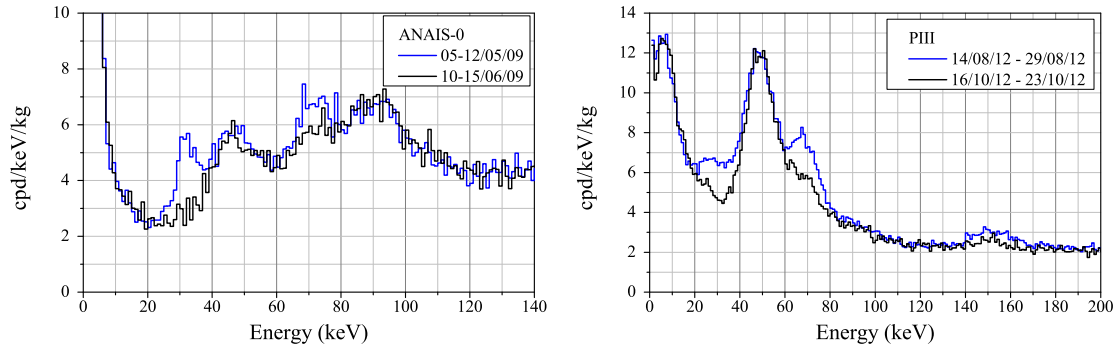

Figure 4.20: *(a) Spectrum from the first week of measurement underground with ANAIS-0, after being stored in surface for several years, compared to the spectrum of the last week of measurement of set-up 1. (b) Spectrum from the first week of measurement underground with PIII, after being in surface for several months, compared to the two months later spectrum corresponding to the Phase III of the ^{40}K coincidence set-up. Cosmogenic lines at around 30 - 35 keV, 70 keV and 145 keV lines are observed. Only raw data are shown.*

history of the iodine used to grow the crystal, however, we will try to quantify ^{129}I content in the ANAIS-0 crystal in section 4.3.1. The ^{129}I decay scheme is shown in Figure 4.21.

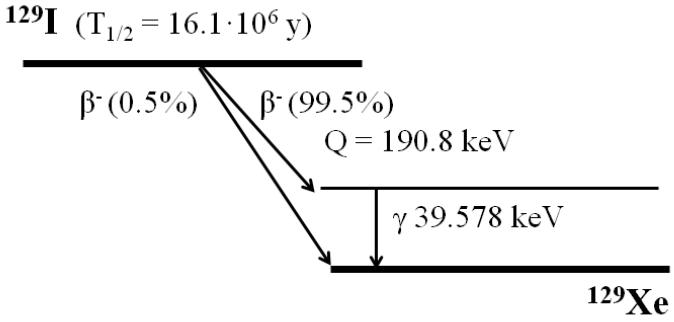

Figure 4.21: *Simplified ^{129}I disintegration levels diagram [127]. It disintegrates by β^- to the excited level of 39.6 keV in ^{129}Xe the 99.5% of the decays.*

4.2 Background simulation

The complete ANAIS-0 set-up has been simulated taking into account the most relevant internal and external contributions to the ANAIS-0 module background using the Geant4 code, version Geant4.9.4.p01 [156].

4.2.1 Geant4 simulation description

The main characteristics of the simulation carried out are:

- Physical processes and models commonly used in the fields of underground experiments and search for rare events have been implemented (the underground physics example of Geant4 has been followed) for interactions of alpha, beta, and gamma particles; for example, the low energy models based on the Livermore data libraries for the electromagnetic interactions.
- The Geant4 Radioactive Decay Module has been used for simulating the decay of radioactive contaminations, after checking carefully the energy conservation in the decay of all the considered isotopes. Problems with energy conservation had been found in previous works, as also is reported in [157].
- Range cut values of $10\,\mu m$ have been used typically for electrons and of $100\,\mu m$ for photons. They are converted into the corresponding energy cuts for every material.
- The simulated geometry (see Figure 4.22) includes the main components of the ANAIS-0 module and its shielding: the NaI crystal, Teflon and reflector lining, quartz windows, light guides (optional), photomultipliers, copper encapsulation, Mylar window, HV divider circuit and its mechanical support, and the shield made of both, archaeological and standard low activity lead. Calibration sources have been also implemented for specific simulations of the calibration procedure.

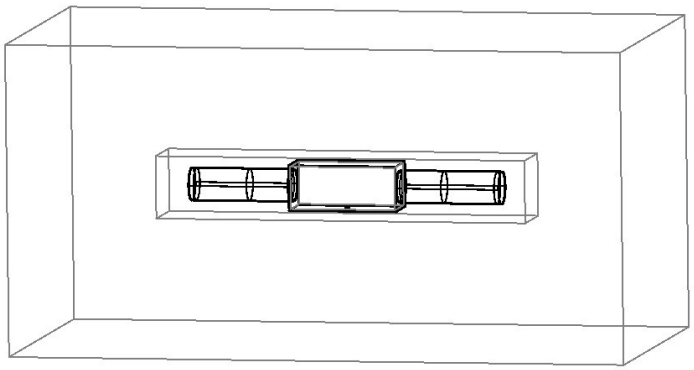

Figure 4.22: *Geometry of the ANAIS-0 set-up used in the simulation.*

- Decays of radioactive impurities in the most relevant materials of the experimental layout, including mainly ^{238}U and ^{232}Th chains and ^{40}K, have been simulated assuming (unless otherwise stated) a uniformly distributed bulk contamination in the different components.

- For each simulated event, defined considering an energy integration time of 1 μs, the energy deposited in the NaI crystal by different types of particles has been recorded separately in order to build afterwards the total energy spectrum, correcting each component with the corresponding quenching factor (see section 3.6).

- ANAIS-0 acquisition dead time effects have been also considered in the simulations. Events occurring in a 4 ms period after a previous one, are not considered in the building of the simulated spectra.

- Simulated spectra shown hereafter have been convoluted with the response function of the detector to take into account energy resolution effects. A gaussian response is considered with the σ (energy dependent) obtained experimentally. In the high energy region, a linear dependence $\sigma^2 = 1.1006 \cdot E(keV^2) + 6.3111$ is considered, derived from the calibration lines at 122.1 keV (from a ^{57}Co calibration), 511 keV, 1275 keV and 1786 keV (from a ^{22}Na calibration). In the low energy region, $\sigma =$ 0.86 keV is considered up to 5 keV (derived from the 3.2 keV background line from bulk ^{40}K), and above 5 keV, $\sigma^2 = 0.4184 \cdot E(keV^2) + 3.4684$ is used, obtained from ^{133}Ba, ^{137}Cs, ^{109}Cd and ^{57}Co calibration lines.

4.2.2 Distribution of contaminants

The most relevant contributions to the ANAIS-0 module background are coming from radioactive isotopes located at or near the NaI crystal. Because of that, we have taken into account contributions of alpha, beta, and gamma emissions coming from internal sources of radiation, bulk distributed in the NaI crystal and external sources of radiation located in PMTs, quartz optical windows, optical coupling grease, light guides, copper encapsulation, lead shielding and the inner volume air.

Internal radioactive contaminants

First, we have considered for the NaI(Tl) crystal the contaminations in the bulk coming from uranium and thorium natural radioactive chains, ^{40}K and ^{129}I isotopes. The values for every NaI crystal bulk contamination used in the background model of ANAIS-0 module are summarized in Table 4.12.

- The ^{40}K bulk content is the most relevant contribution to the background in the ANAIS-0 module and it was estimated in a dedicated set-up, as it is detailed in section 4.1.2, the result is $(12.7 \pm 0.5)\, mBq/kg$ as shown in Table 4.7.

- Activities of the different isotopes in the ^{238}U and ^{232}Th chains, without imposing secular equilibrium, have been quantified after identifying their alpha emissions by means of Pulse Shape Analysis (PSA) technique (also detailed in section 4.1.2 and results shown in Table 4.11).

- Concerning the activity of ^{129}I, cosmogenic isotope usually found in iodine compounds in a very broad range of activity values (depending on the ore origin), the value deduced for DAMA/LIBRA crystals [97], produced (as the ANAIS-0 module crystal) by Saint Gobain company has been used: $^{129}I/^{nat}I = (1.7 \pm 0.1) \times 10^{-13}$ and $T_{1/2} = 1.57 \times 10^7\, y$, which corresponds to a specific activity of $0.96\, mBq/kg$.

- Other isotopes such as ^{227}Ac, ^{87}Rb, ^{85}Kr or ^{235}U have also been considered and studied, but no evidence of their presence has been found in the data and they have not been included in the ANAIS-0 background model.

Isotope	Activity (mBq/kg)
^{40}K	12.7 ± 0.5
^{129}I	0.96 ± 0.06
^{232}Th	0.013 ± 0.005
^{228}Th	0.035 ± 0.003
$^{238}U/^{234}U$	0.075 ± 0.005
^{230}Th	0.023 ± 0.007
^{226}Ra	0.098 ± 0.004
^{210}Pb	0.188 ± 0.005

Table 4.12: *Isotopes and activities considered in the simulation distributed in the bulk of the NaI crystal of the ANAIS-0 module.*

External radioactive contaminants

Besides the NaI crystal, PMTs are usually the main background contribution in scintillation detectors. For the rest of the components only upper limits for the different radioactive isotopes searched for have been obtained. For most of these external components High Purity Germanium (HPGe) spectrometry at LSC has been used to screen the radioactive contaminations (results are reported in Table 2.1).

- Several low background Electron Tubes and Hamamatsu PMT models have been tested with the ANAIS-0 module. All of them were previously measured at the HPGe test bench at the LSC, see section 2.1.3. The activities of ^{238}U, ^{226}Ra, ^{232}Th,

^{60}Co and ^{40}K, shown in Table 2.5, have been taken into account. Equilibrium in the natural chains has been observed except if otherwise is explicitly stated.

- For quartz windows, light guides, optical coupling grease, and copper encapsulation the upper limits (95% C.L.) on the activities considered in the simulations are shown in Table 4.13 and have been obtained at the HPGe test bench at the LSC. Upper limits for ^{238}U are worse than those obtained for other isotopes because of the low intensity of its gamma emissions; in this case, equilibrium in the natural chains has not been imposed.

- For archaeological lead, upper limits on ^{210}Pb, ^{232}Th and ^{238}U activities quoted in [158] have been used.

- For radon content in the air filling the inner volume of the shielding, there is no real estimate. Radon content in the laboratory air is being continuously monitored, and the inner volume of the shielding is flushed with boil-off nitrogen to guarantee its radon-free quality. An arbitrary value for the radon content in the inner volume air of about one hundredth of the external air radon content has been assumed in our background model (0.6 Bq/m^3), compatible with the absence of lines coming from radon daughter isotopes in the measured background. Nevertheless, this contribution should be considered as an upper limit, as no direct evidence of the presence of radon in the data has been found.

Contributions from neutrons and environmental gamma background have been also simulated, being negligible at the present level of sensitivity. Contribution from muons interacting in the crystal (and other muon related events) can be vetoed by the coincidence with a signal in the plastic scintillators covering the ANAIS-0 shielding. Although the coverage was only partial in the experimental layout, the corresponding residual background contribution has been estimated to be negligible, see section 2.3.

4.2.3 Code validation and analysis of systematic effects

Energy spectra for different calibration sources have been simulated to validate the code. Systematic effects, specially at very low energy, are expected to be higher for external than for internal sources and are not easy to evaluate. With such a purpose, experimental and simulated spectra for all the radioactive sources measured with ANAIS-0 have been compared. The energy sources used for the high energy range are: ^{22}Na, ^{152}Eu, ^{133}Ba and ^{137}Cs, whereas low energy ones are: ^{57}Co, ^{109}Cd, ^{133}Ba and ^{137}Cs. In the Figures

Detector component	Isotope	Activity
Copper encapsulation	^{40}K	$< 11\,mBq$
	^{232}Th	$< 4.1\,mBq$
	^{238}U	$< 140\,mBq$
	^{226}Ra	$< 2\,mBq$
	^{60}Co	$< 0.94\,mBq$
Quartz optical window	^{40}K	$< 12\,mBq/kg$
	^{232}Th	$< 2.2\,mBq/kg$
	^{238}U	$< 100\,mBq/kg$
	^{226}Ra	$< 1.9\,mBq$
Light guides	^{40}K	$< 21\,mBq/guide$
	^{232}Th	$< 4.1\,mBq/guide$
	^{238}U	$< 120\,mBq/guide$
	^{226}Ra	$< 4.7\,mBq/guide$
Optical coupling grease	^{40}K	$< 200\,mBq/kg$
	^{232}Th	$< 200\,mBq/kg$
	^{238}U	$< 2000\,mBq/kg$
	^{226}Ra	$< 30\,mBq/kg$
Archaeological lead	^{210}Pb	$< 20\,mBq/kg$
	^{232}Th	$< 0.3\,mBq/kg$
	^{238}U	$< 0.2\,mBq/kg$
Inner volume air	^{222}Rn	$< 0.6\,m^3$

Table 4.13: *Upper limits given at 95% C.L. for the content on the main radioactive isotopes in the different components of the ANAIS-0 module layout.*

4.23 and 4.24 the experimental calibrations are compared with the simulations normalized to the activity of the sources (known only at a level of $\pm\,10\%$ accuracy, except for ^{152}Eu, whose activity is better known at $\pm\,1.5\%$). Response functions to take into account energy resolutions effects are different at high and low energy ranges, as it has been previously explained.

With the same goal, radon was allowed to enter into the shielding in order to have data for an homogeneously distributed contamination in the air around the ANAIS-0 module. In Figure 4.25 experimental (after subtracting the background) and simulated spectra are shown for radon contamination in the inner cavity air, normalizing both spectra to the same total number of counts. The radon content required to match both spectra is $58.2\,Bq/m^3$. The radon level in the laboratory has been continuously monitored along the corresponding period with an AlphaGUARD detector (mean value, in this period, of $65\,Bq/m^3$), see section 2.6.

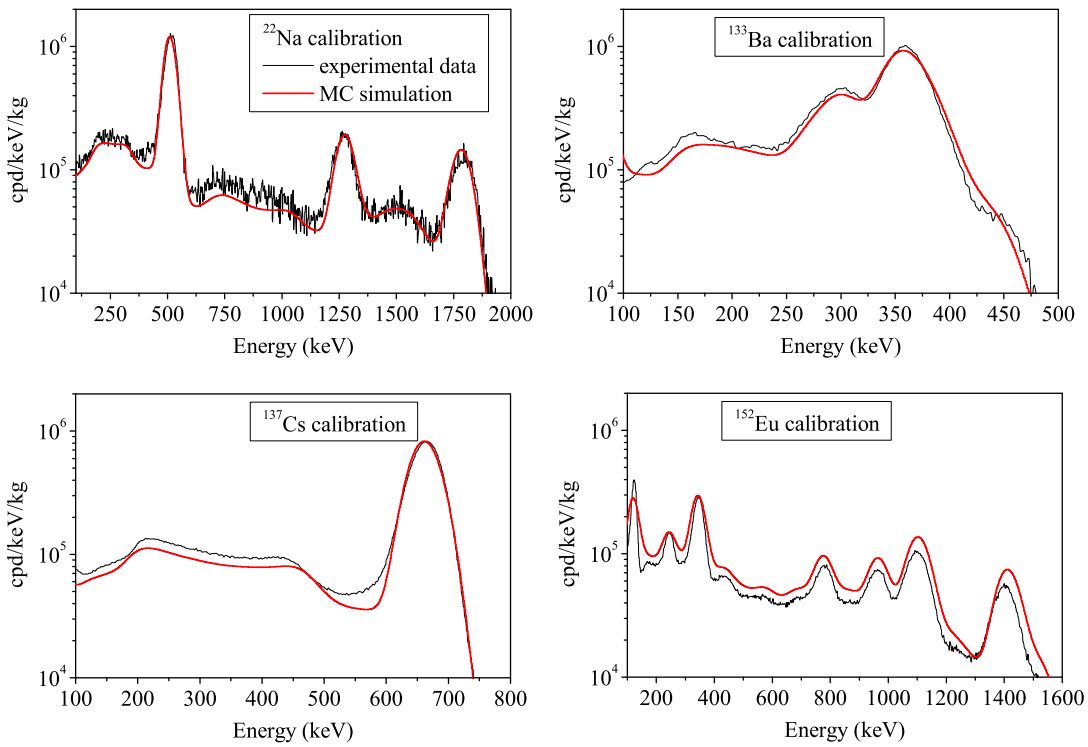

Figure 4.23: *Measured and simulated spectra for different calibration sources in the high energy range:* ^{22}Na, ^{133}Ba, ^{137}Cs *and* ^{152}Eu. *Simulations have been normalized to the nominal activity of the sources.*

From the comparison between simulations and measured data, it can be concluded that simulation reproduces qualitatively very well all the measurements. Concerning the quantitative estimate of the activity, some systematics have been identified for external gamma calibration data, specially at the lowest energies; they could be related with our imprecise knowledge of the sources geometry and possible misplacement of the source with respect to the Mylar window, but we cannot discard a reduced scintillation yield or bad light collection efficiency for events corresponding to interactions of very low energy X-rays in the first microns of the crystal surface, that could explain, for instance, the non-linear response evidenced for the iron X-rays in Figure 4.24 and already brought forward in section 2.7.

Comparing simulation and measurement (see Table 4.14) we can state that simulations agree with experimental data at the accuracy level of our knowledge of activity and other source details when using for the normalization the total number of detected counts, except for the ^{152}Eu calibration source. However, some differences in Compton vs. photopeak relative event rates have been identified in the simulations (see Table 4.14): this suppression of Compton vs. peak event rates in the simulation can be possibly ascribed to

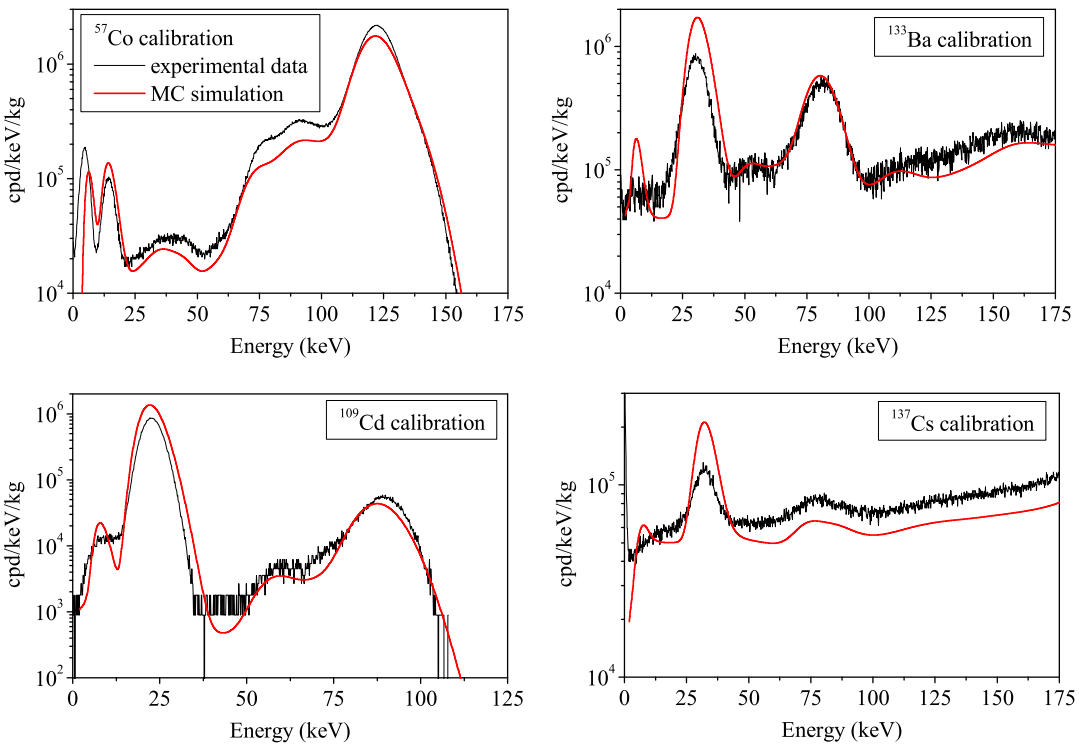

Figure 4.24: *Measured and simulated spectra for different calibration sources in the low energy range:* ^{57}Co, ^{133}Ba, ^{109}Cd *and* ^{137}Cs. *Simulations have been normalized to the nominal activity of the sources.*

some energy loss mechanisms in the detector performance, f.i. because of inhomogeneity in the light collection efficiency, resulting in less events contributing to the peaks but the same total rate. This Compton/peak defect between experimental and simulated data has been quantified as 75% with the ^{22}Na calibration (using the 1275 keV gamma line intensity and the number of events in the region from 600 to 1100 keV).

The lines associated to X-rays are systematically badly reproduced by the simulation (see Figure 4.24); this could be explained by a malfunction of Geant4 mechanism for the generation of the atomic electromagnetic deexcitation cascades after a nuclear process. There is also some error present in the ^{152}Eu simulation: it does not follow the same tendency as the other sources do. However, no explanation has been found for the large overestimate, in particular, of the high energy gamma lines.

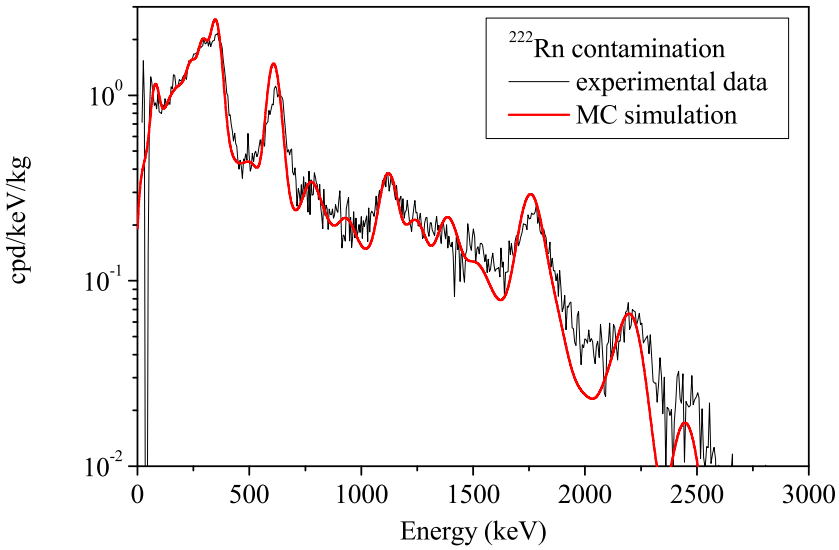

Figure 4.25: *Comparison of simulation (red) vs. experimental data (black) for a homogeneously distributed radon contamination in the air around the detector, inside the shielding.*

Source	Activity	Estimated activity (A)	Estimated activity (B)
^{22}Na	(1 ± 0.1) μCi	1.08 μCi	0.95 μCi
^{137}Cs	(1 ± 0.1) μCi	1.07 μCi	0.99 μCi
^{152}Eu	(1.07 ± 0.02) μCi	0.78 μCi	0.87 μCi
^{57}Co	(1 ± 0.1) μCi	1.18 μCi	1.09 μCi
^{133}Ba	(1 ± 0.1) μCi	0.83 μCi	0.90 μCi
^{222}Rn	(63 ± 3.4) Bq/m^3	58.2 Bq/m^3	37.2 Bq/m^3

Table 4.14: *Comparison between nominal and derived from the simulation activities for the different calibration sources used with the ANAIS-0 module. Activities are derived using the total number of counts in the spectrum (A) and a single line (B): 1275 keV for ^{22}Na, 662 keV for ^{137}Cs, 344 keV for ^{152}Eu, 122 keV for ^{57}Co, 81 keV for ^{133}Ba and 609 keV for ^{222}Rn.*

4.3 Background model

The total energy spectrum in ANAIS-0 has been simulated for the different contaminations reported in section 4.2.2 and the different available experimental set-ups shown in Table 2.6.

4.3.1 Background model

Internal background

The contributions of internal radioactive contaminants, clearly dominant in the ANAIS-0 module background, are shown separately for alpha particles (see Figure 4.26) and beta/gamma ones, in this case together with the corresponding uncertainties at $1\,\sigma$ level (see Figure 4.27). For these contaminants, the same contribution is expected for all the set-ups.

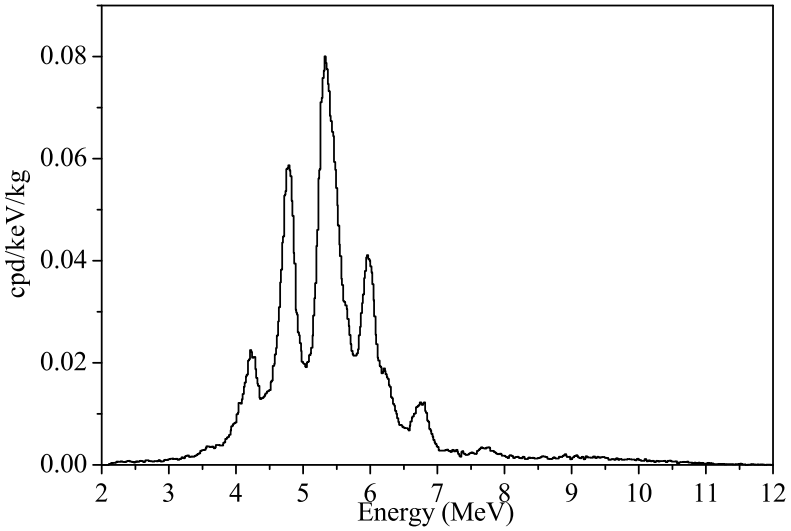

Figure 4.26: *Simulation of the alpha spectrum, for the bulk crystal contaminations in U and Th chains.*

The Geant4 version used in this work presents a very relevant modification, related with the shape of the ^{40}K beta spectrum, because the proper shape factor for the third unique forbidden beta decay has been used, see Figure 4.28. It can be seen a much better accordance with the measured background spectrum shape at 1 MeV for the latter version: in both cases $12.7 \pm 0.5\,mBq/kg$ of ^{40}K have been considered, as deduced from the analysis of coincidences.

External background

In Figure 4.29 the contributions of the external radioactive contaminants (placed in PMTs, optical windows, light guides, optical coupling grease, copper encapsulation, inner volume

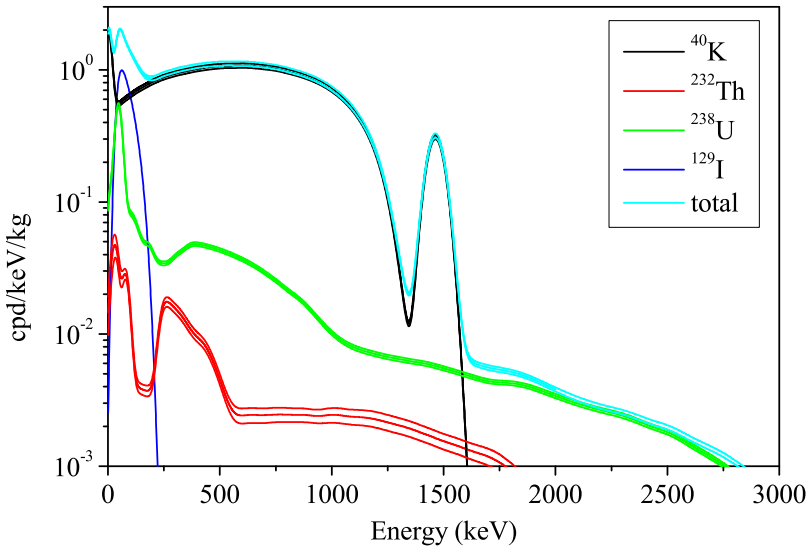

(a)

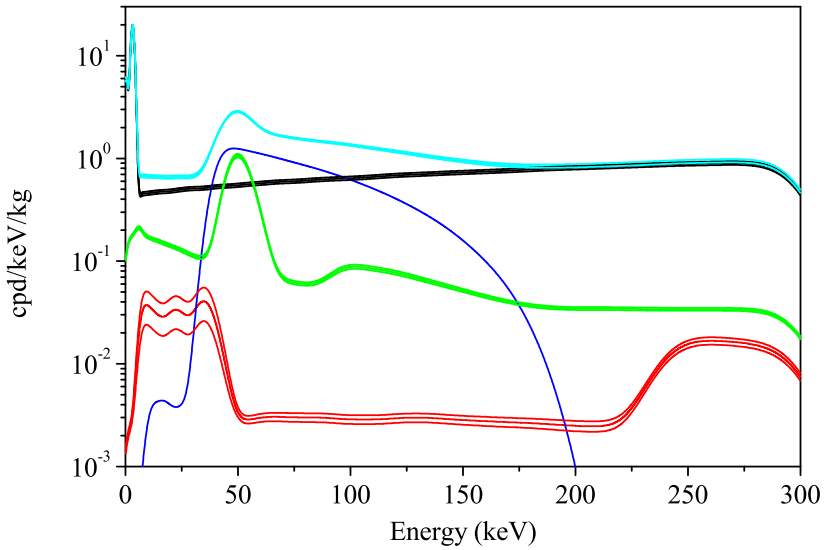

(b)

Figure 4.27: *Contribution to the background from internal radioactive contaminants for the ANAIS-0 crystal at high (a) and low energy (b). Uncertainties in the estimates of the contamination values used at 1 sigma level are shown in the figure.*

air, and archaeological lead shielding) to the background are shown for the different set-ups.

In Figure 4.30 the total contributions to the background coming from external components are shown for every simulated set-up. It has to be noticed that for most of

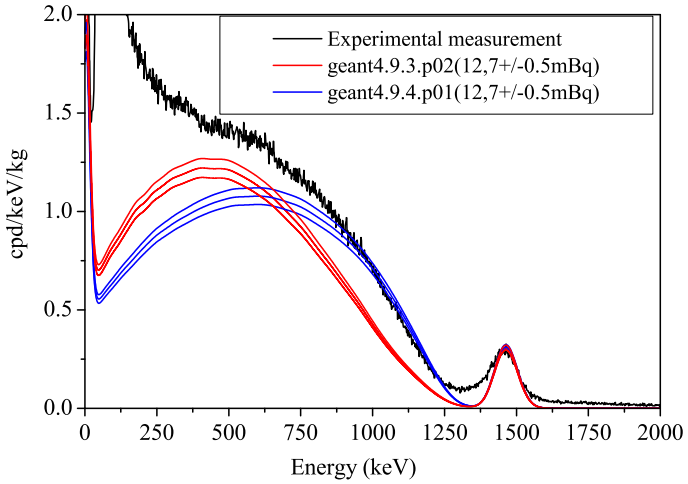

Figure 4.28: *Simulated spectra for bulk ^{40}K contamination in the ANAIS-0 NaI crystal are shown both for an allowed beta spectrum shape (Geant4.9.3 version) in red and taking into account the proper shape factor for the third unique forbidden beta decay (Geant4.9.4 version) in blue. The latter is the Geant4 version used throughout this work.*

these contaminations only upper limits have been derived, so the contributions to the background shown should be also taken as upper limits at 95% C.L.

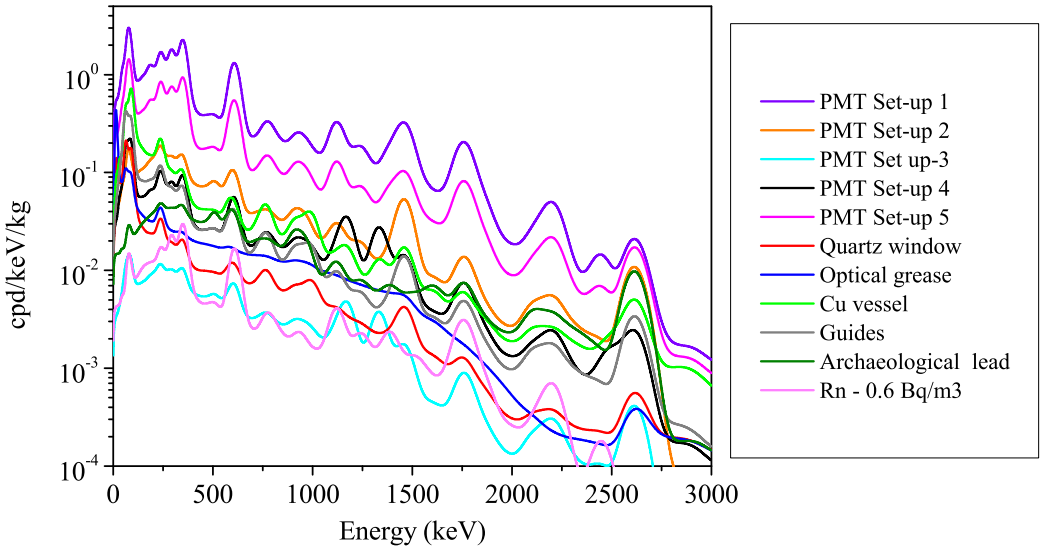

Figure 4.29: *Background contribution from every external component of the ANAIS-0 set-ups.*

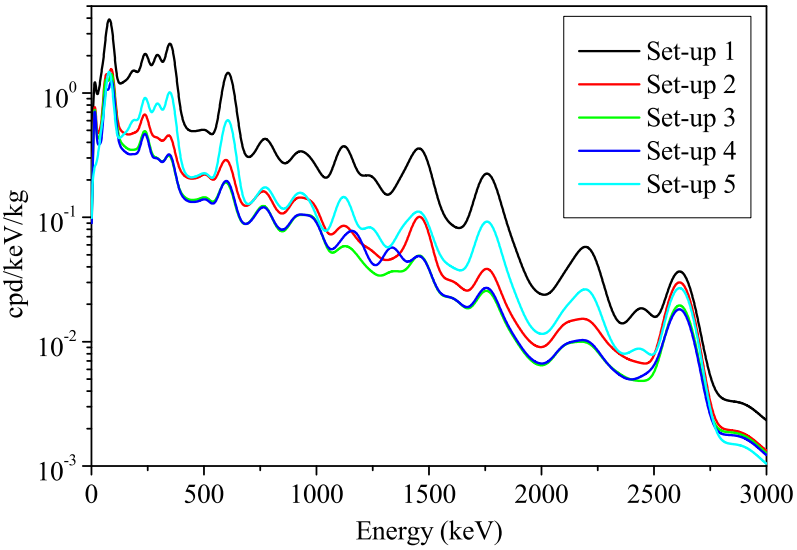

Figure 4.30: *Total contribution to the background for every simulated ANAIS-0 set-up coming from contaminations in external components.*

4.3.2 Comparison between background simulations and measurements

The background measurements for the ANAIS-0 set-ups (summarized in Table 2.6) have been compared with the addition of the simulated contribution of the different components. First, the simulated alpha spectrum is compared with the alpha spectrum from the set-up 2 (the alpha contribution to the background should be the same for all the set-ups). Then beta/gamma spectra at high and low energy are compared for set-ups 1 - 5.

The energy spectrum corresponding to alpha particle energy depositions, discriminated by PSA as stated in section 4.1.2 has been compared with the corresponding simulation, assuming a homogeneous bulk distribution of ^{238}U and ^{232}Th, and daughter isotopes in the NaI crystal with the activity values deduced and shown in Table 4.12. Above 6 MeVee the experimental spectrum shown in Figure 4.31 is the total spectrum in order to show all the $^{212}Bi - Po$ events.

Effect of acquisition dead time on ^{214}Po emission detection efficiency and the summing of alpha and beta emissions for the $^{212}Bi - Po$ sequence in the charge integration window have been properly taken into account in the simulated data (see Figure 4.31). Quenching factor for alpha particles vs. electrons has been fitted to properly match experimental data and simulation in the Bi-Po events (above 9 MeV in alpha energy).

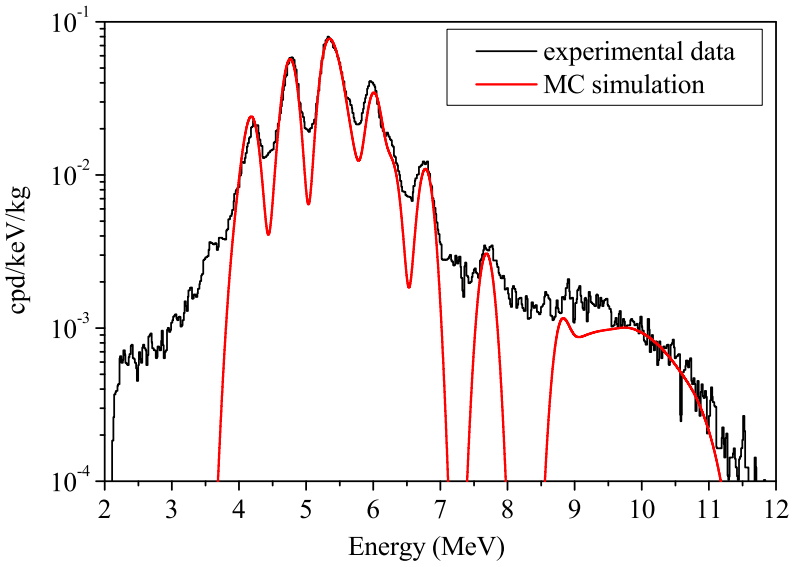

Figure 4.31: *Simulation of the alpha spectrum (red line) vs. experimental data (black line) selected by PSA. The $^{212}Bi - Po$ coincident events, summing of the beta and alpha emissions, above 9 MeV, are also shown.*

A good agreement between simulation and measurement supports the validity of the model. From the difference between the number of events in the simulated spectrum and that in the experimental one for an energy window from 3.5 MeV to 12 MeV (17% less events in the simulation) and the consideration that efficiency for the detection of alpha events should be 100% in an ideal detector, we can conclude that our contamination levels derived from the study of the alpha emissions are probably slightly underestimated and that a surface component, implying some degradation of the energy below the nominal alpha energy value, is present. Events observed below 3.5 MeV support the argument given in section 3.1 regarding surface contamination.

Beta/gamma high energy spectra, experimental and simulated, corresponding to set-up 4 are compared in Figure 4.32, and in Figure 4.33 for the rest of setups.

Above 500 keV the measured background seems to be nicely reproduced by the simulated considered contributions, having in mind that some of them are actually, upper limits. ^{40}K from the bulk NaI crystal is clearly the dominant background source from 500 to 1500 keV.

Below 20 keV, raw background data show an important contribution (dominant below 10 keV) of events not attributable to bulk NaI scintillation, making necessary to apply convenient filtering procedures, see section 3.1. Different events populations appear in that

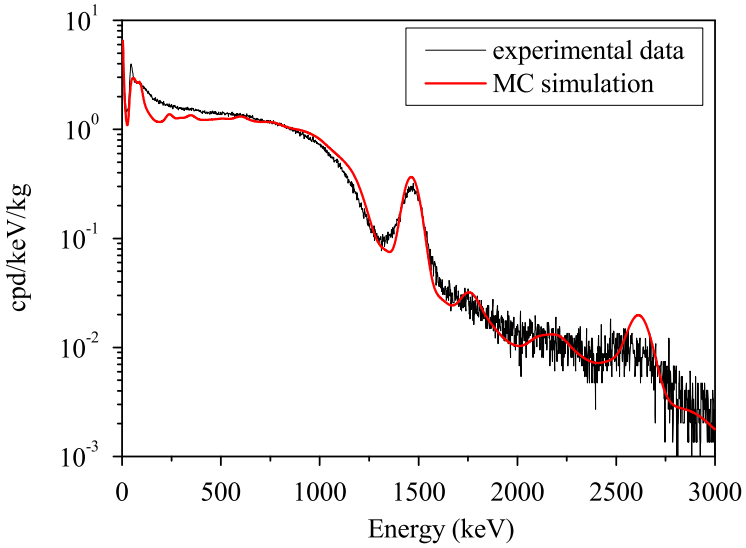

Figure 4.32: *Comparison between simulations and measured data at high energy for the ANAIS-0 module in set-up 4.*

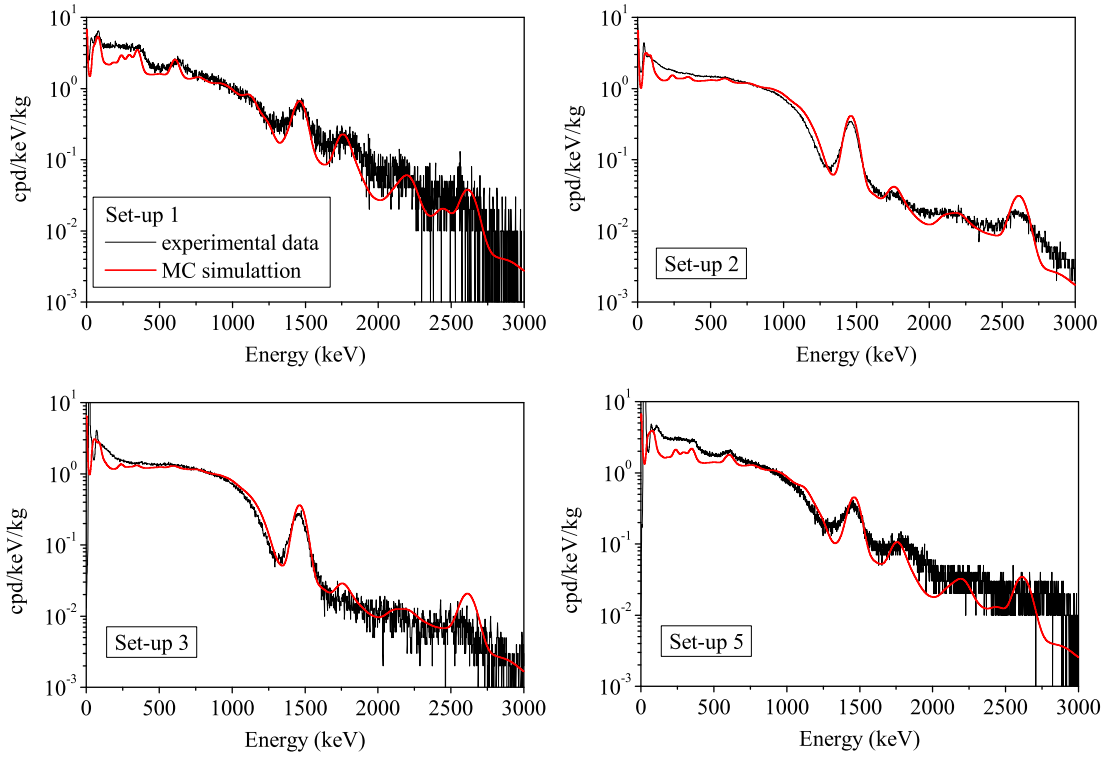

Figure 4.33: *Comparison of simulations (in red) and experimental data (in black) for the different ANAIS-0 set-ups, other than set-up 4.*

low energy regime, being the most relevant: electronic noise, events originated in the PMTs (reduced but not completely suppressed by the coincidence), and anomalous fast events not compatible with NaI scintillation time constant. Efficiency of that filtering for accepting real bulk scintillation events in NaI crystal originated by beta/gamma interactions is estimated with low energy calibration data (using ^{57}Co and ^{109}Cd sources).

In the low energy region, agreement between the measured data (filtered spectrum obtained in section 3.1) and the total simulated contributions is worse (see Figure 4.34), pointing to some non explained background components. Different possibilities have been analyzed trying to better model backgrounds at low energy without compromising the good agreement at higher energies: ^{210}Pb surface contamination in the NaI crystal, ^{210}Pb surface contamination in the copper encapsulation, ^{3}H bulk contamination in the NaI crystal, and fast neutrons. Slight (and motivated) modifications in the assumed activities for some isotopes with respect to the upper limits given in section 4.2.2 have been also considered as hypothesis and will be described in next section.

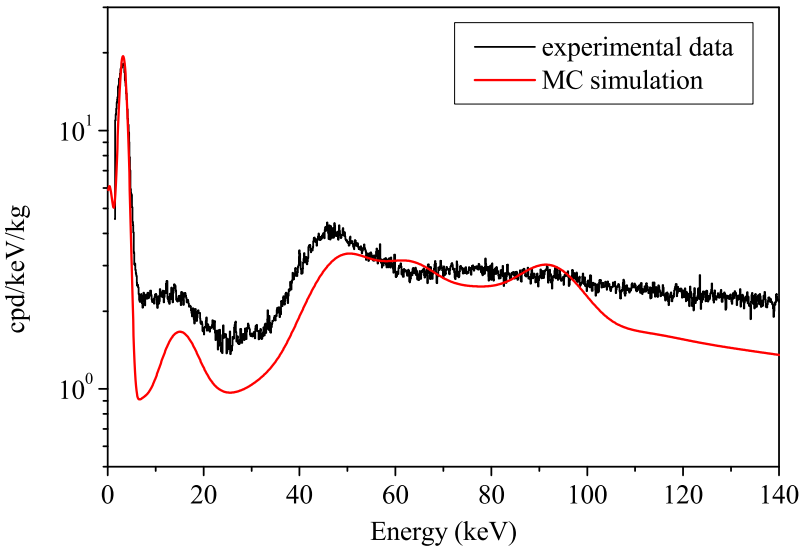

Figure 4.34: *Comparison between simulations and measured data at low energy for the ANAIS-0 module in set-up 4.*

The total simulated contribution to the ANAIS-0 background has been evaluated and compared with the experimental raw data (without filtering, unless for set-up 5) for the rest of experimental configurations available (Figure 4.35). Drawn conclusions are equivalent for all the available configurations, either from the high or the low energy regions of the spectra; the only relevant distinction was the presence of some cosmogenic lines below

100 keV, not included in the simulations, for the set-up 1 which was first operated, shortly after the handling of the detector at sea level, see section 4.1.1.

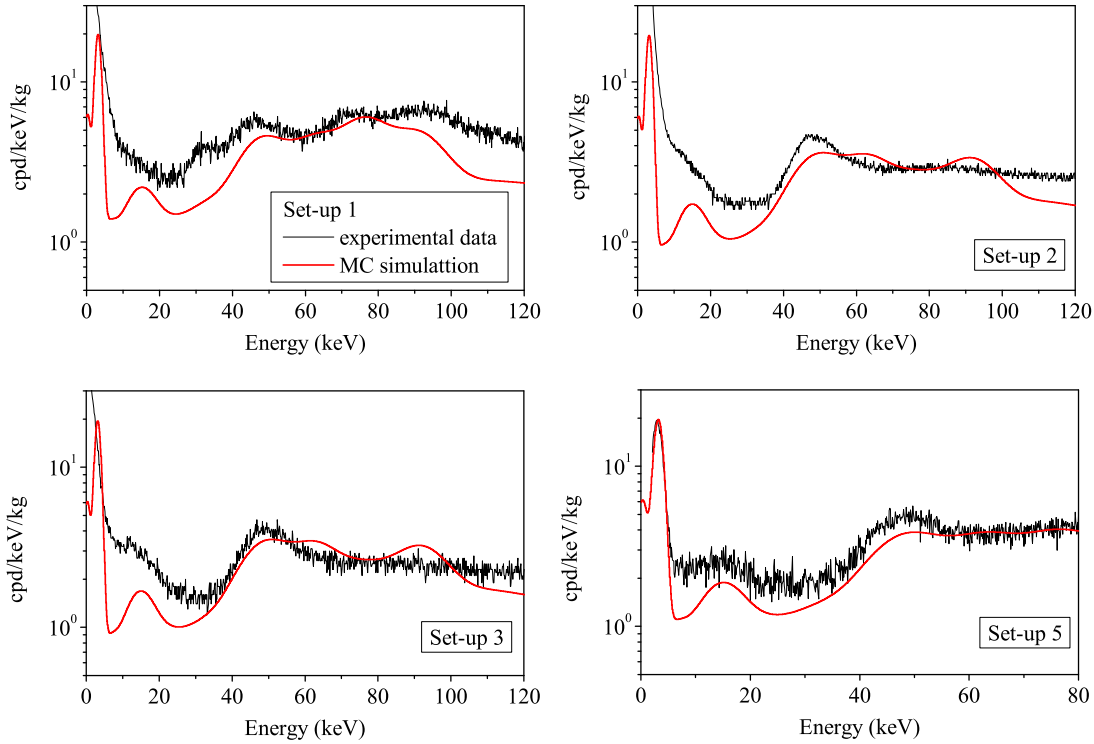

Figure 4.35: *Comparison of simulations (in red) and experimental data (in black) for the different ANAIS-0 set-ups, other than set-up 4, at low energy. Raw data are shown for setups 1, 3, and 4; for set-up 5 data have been filtered up to 80 keV. Cosmogenic lines observed in set-up 1 have not been simulated.*

4.3.3 Other hypothetical background sources

Some of the most realistic hypotheses analyzed, able to explain a part of the missed background events at low energy are shown in Figure 4.36, after adding each of them separately to the background model presented in previous section:

- 1.7 mBq of ^{210}Pb surface contamination on NaI crystal (reducing correspondingly the ^{210}Pb bulk contamination). This value stems from the assumption of a bulk crystal contamination of ^{210}Pb in equilibrium with ^{226}Ra, and the excess of ^{210}Po (daughter of ^{210}Pb) alpha events as originated by a ^{210}Pb contamination in the crystal surface.
- 75 mBq of ^{210}Pb surface contamination on copper encapsulation distributed in a 1 μm layer (^{210}Pb contamination out of equilibrium is difficult to trace because of

the low efficiency for detecting its gamma emissions with the HPGe spectrometer used at LSC).

- 90 μBq/kg of ^{3}H (cosmogenic origin) in the bulk NaI (upper limit derived in [97] for similar crystals from the same supplier).
- 50% extra of ^{129}I contamination in the bulk NaI.
- 1 Bq/kg extra ^{210}Pb contamination in the lead shielding (bremsstrahlung produced by electrons coming from ^{210}Bi decay could contribute to fill the missing background component above 100 keV, but this contribution is limited by the associated production of lead X-rays that easily exceeds the measured spectrum).

In Figures 4.37 and 4.38, the measured background is shown at high and low energy (as black solid line) as well as the previously explained hypotheses added to the background model presented before, slightly modified in the following points (shown as red solid line):

- reduction of the ^{232}Th contamination in the lead shielding from the upper limit of the measurement (see Table 4.13) down to 0.1 mBq/kg.
- reduction of the ^{238}U contamination from the upper limit of the measurement down to the equilibrium with ^{226}Ra contamination values in copper, quartz windows, and optical coupling grease (see Table 4.13).

Other possible hypothesis is shown as blue solid line in Figure 4.37, which corresponds to a slight modification of that shown as red solid line and explained in the previous paragraphs: letting the uranium out of equilibrium with radium in the optical coupling grease and reducing the ^{210}Pb contamination in the copper surface down to 50 mBq. A very similar background at low energy is obtained, pointing at the requirement of improving the sensitivity of our radiopurity assessment for that contaminants in order to identify the origin of the missing low energy background contribution(s). At high energy no difference between both hypotheses can be noticed.

A very remarkable agreement (except in the region above 100 keV and between 20 and 40 keV) can be observed. No fitting of the experimental data to a combination of these contributions has been attempted and we only want to stress that plausible background components at reasonable activity levels can be responsible of the observed background in the low energy region. However, these possible background sources should be taken into account in the estimates of achievable background levels for ANAIS experiment.

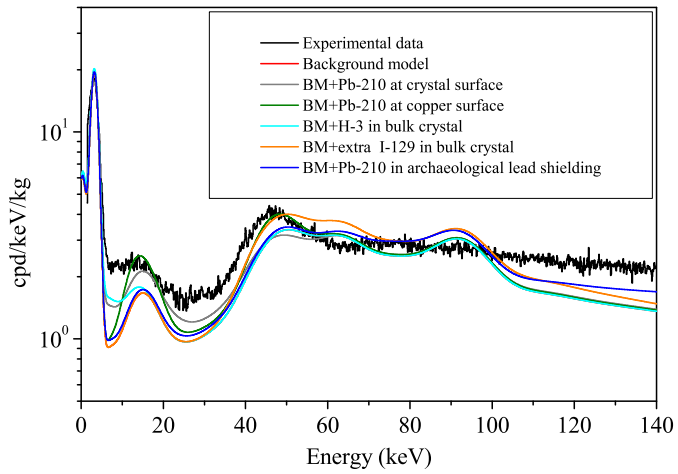

Figure 4.36: *Comparison between simulations and measured data at low energy for the ANAIS-0 module in set-up 4 taking into account separately different hypotheses added to the background model described in section 4.3.1.*

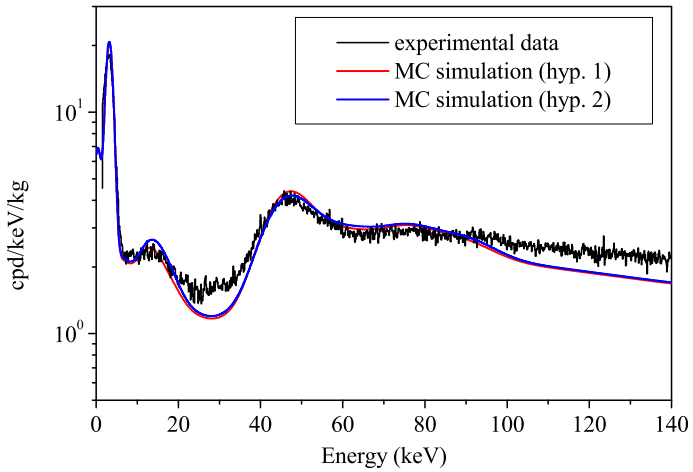

Figure 4.37: *Comparison between simulations and experimental data at low energy for the ANAIS-0 module in set-up 4 adding some hypotheses to the background model. In black solid line, measured data are shown. In red and blue solid lines two different combination of hypotheses about possible background contributions at low energy are shown (see text for details), both explaining quite well the measured spectrum.*

Other possible background sources as, for instance, ^{227}Ac, ^{87}Rb and ^{85}Kr have been considered. No direct evidence of their presence in our data has been found and they have not been included neither in our background model nor in our shown hypotheses.

Also, the possible contribution from fast neutrons, coming in deep underground environment mainly from muon induced reactions, ^{238}U spontaneous fission and (α, n) reac-

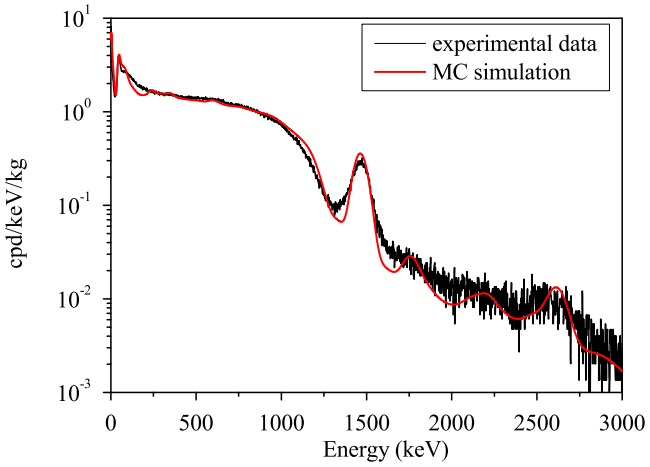

Figure 4.38: *Comparison between simulations and experimental data at high energy for the ANAIS-0 module in set-up 4 adding some hypotheses to the background model. In black solid line, measured data are shown. In red solid line a combination of hypotheses about possible background contributions is shown (see text for details).*

tions, and very relevant usually in the search for dark matter, is worth of some comment: it has been simulated for a typical flux of the order of 10^{-6} $neutrons/cm^2/s$ [159], and being negligible with respect to the rest of the contributions shown, it has not been included in the background model at the present level of sensitivity.

Possible contaminations in the Teflon reflecting foil wrapping the crystal have been studied also as complementary hypothesis, although there is no direct evidence of contamination in any of the different Teflon foils or tapes screened. Possible background contribution of surface ^{210}Pb contamination in the Teflon would produce similar effects to that included in the copper in our previously shown hypotheses; however, we find in our simulations a higher relative contribution of events below 20 keV that is more difficult to match with our low energy data.

4.4 Conclusions from the comparison

We summarize the simulation results in Tables 4.15 and 4.16 for the ANAIS-0 set-up 4, in the high (from 150 to 3000 keV) and low energy regions (from 5 keV to 150 keV and from 2 keV to 20 keV), respectively. Table 4.17 summarizes the results for the different isotopes present in the NaI(Tl) crystal (from 2 keV to 50 keV). Contributions of the different components to the background in counts/kg/day, as well as the background percentage explained by the simulations are shown, for the background model proposed in

section 4.3.1 and in parentheses for that model adding extra hypotheses as proposed in section 4.3.2. It is to remark that more than 92% of the background in the region from 150 to 3000 keV is explained with our proposed background model, increasing up to 98% when some hypotheses are added. More than 77% of the low energy background is also explained, increasing up to a 99% when adding the referred hypotheses.

Simulated component	Background contribution 150 - 3000 keV	
	cpd/kg	%
Crystal	1000.2 (1002.7)	77.5 (77.7)
Copper encapsulation	67.8 (47.5)	5.3 (3.7)
Quartz window	13.5 (6.6)	1.0 (0.5)
Optical coupling grease	21.4 (7.2)	1.7 (0.6)
Ham ULB PMT	47.2	3.7
Lead shielding	36.0 (145.0)	2.8 (11.2)
Inner volume air	9.1	0.7
Total	1195.2 (1265.3)	92.6 (98.1)

Table 4.15: *Contribution to the background of ANAIS-0 module in set-up 4 from the different simulated set-up components: total rate derived from simulation from 150 keV to 3000 keV and corresponding percentage of the measured background. Rates and percentages shown in parentheses correspond to the background model including extra hypotheses.*

Simulated component	Background contribution 5 - 150 keV		2 - 20 keV	
	cpd/kg	%	cpd/kg	%
Crystal	196.0 (255.0)	53.0 (68.8)	49.6 (65.0)	64.8 (84.8)
Copper encapsulation	46.1 (31.4)	12.5 (8.5)	1.4 (8.0)	1.8 (10.5)
Quartz window	15.5 (2.5)	4.2 (0.7)	1.8 (0.2)	2.4 (0.3)
Optical coupling grease	15.7 (3.3)	4.2 (0.9)	5.8 (0.9)	7.6 (1.2)
Ham ULB PMT	15.4	4.2	0.5	0.7
Lead shielding	3.2 (33.7)	0.9 (9.1)	0.3 (1.3)	0.3 (1.8)
Inner volume air	1.2	0.3	0.1	0.1
Total	293.2 (342.1)	79.3 (92.5)	59.5 (76.0)	77.7 (99.3)

Table 4.16: *Contribution to the background of ANAIS-0 module in set-up 4 from the different simulated set-up components: total rate derived from simulation from 5 keV to 150 keV and from 2 keV to 20 keV and corresponding percentage of the measured background. Rates and percentages shown in parentheses correspond to the background model including extra hypotheses.*

After this analysis was completed, a new estimate of the ^{40}K content of ANAIS-0 crystal was derived using data from the phase III ^{40}K coincidence setup (see section

Simulated component	Background contribution 2 - 50 keV	
	cpd/kg	%
^{40}K	61.5	40.7
^{232}Th	1.1	0.7
^{228}Th	0.1	0.1
^{238}U	2.5	1.7
^{226}Ra	5.4	3.6
^{210}Pb	4.7 (18.5)	3.1 (12.2)
^{129}I	14.4 (21.5)	9.5 (14.3)
^{3}H	- (6.8)	- (4.5)
Total crystal contribution	89.7 (117.5)	59.4 (77.8)

Table 4.17: *Contribution to the background of ANAIS-0 module in set-up 4 from the different isotopes simulated in the crystal of NaI: total rate derived from simulation from 2 keV to 50 keV and corresponding percentage of the measured background. Rates and percentages shown in parentheses correspond to the background model including extra hypotheses (see text).*

2.2). Corresponding results are shown in Figure 4.39 and Table 4.18. Very nice and stable operation can be reported and results are compatible with those of phase I (see Table 4.6), slightly higher than those of phase II, pointing at some coincident events loss in phase II attributable to instability in PIII high energy data.

Detector	Phase	^{40}K Activity (mBq/kg)		
		$1\,\sigma$	$2\,\sigma$	$3\,\sigma$
ANAIS-0	III	14.5 ± 0.6	14.3 ± 0.5	15.1 ± 0.5

Table 4.18: ^{40}K *activity calculated for ANAIS-0 phase III using different widths coincidence windows.*

Our conclusion is that the ^{40}K activity we assumed for ANAIS-0 (derived from the coincident 3.2 keV peak intensity, by averaging the estimates from phase I and II) is underestimated in about a 10%. However, the limit for ^{40}K derived from the 1461 keV gamma line in the background is more hardly compatible with such a higher ^{40}K bulk content. Further study is required to solve this issue, but systematics on Geant4 simulations can be responsible: for instance, possible energy loss mechanisms previously mentioned could affect in about such a percent the conclusions derived from our analysis.

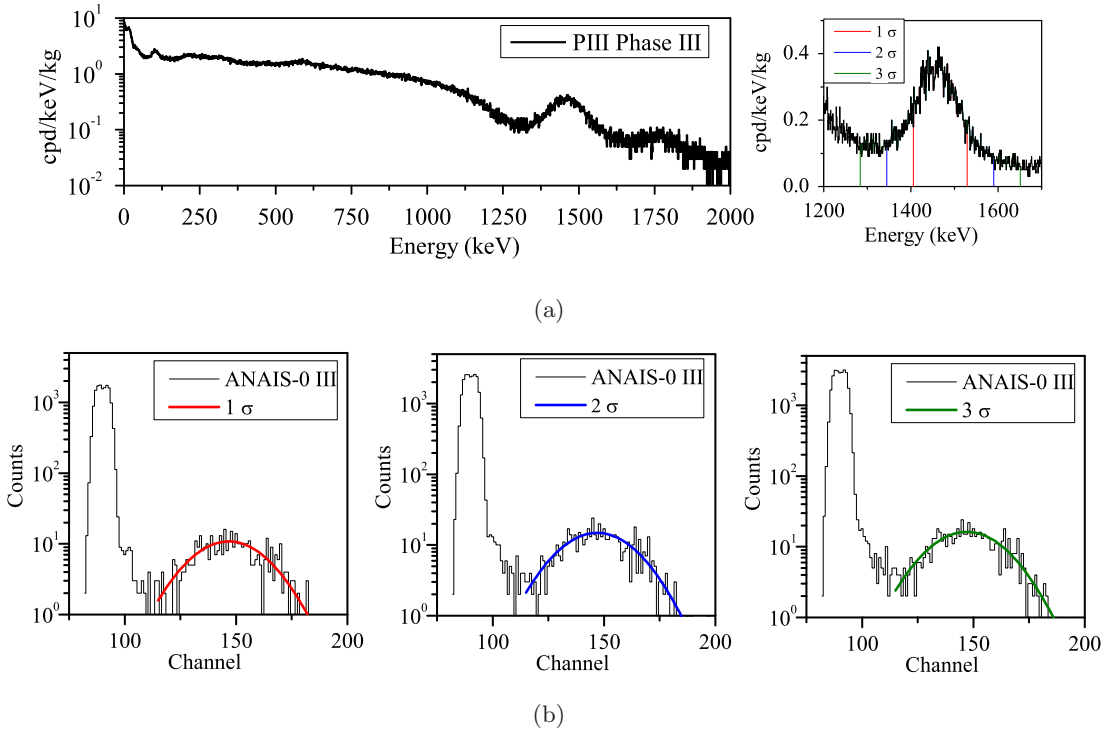

Figure 4.39: *(a) High energy spectrum of PIII corresponding to the phase III of the ^{40}K-coincidence setup (left) and zoom showing the 1461 keV line and the 1σ (red), 2σ (blue) and 3σ (green) coincidence windows (right). (b) Low energy coincident events for the 1σ, 2σ, and 3σ (c) coincidence windows, and gaussian fits of the events above the threshold, see section 4.1.2 for the equivalent analysis of phases I and II.*

We can conclude, that the proposed background model for ANAIS-0 prototype is able to reproduce notably the high energy background of the experiment, for alpha as well as for beta-gamma components. At low and medium energies some non-explained background components are present. For the analysis of the dark matter annual modulation with the final ANAIS modules, a complete understanding of the background will be required.

Chapter 5

Towards the ANAIS experiment

The ANAIS experiment is the large scale conclusion of previous studies carried out with different prototypes, described in the preceding chapters. The complete experiment will use 250 kg of NaI(Tl) crystals to study the expected annual modulation in the galactic dark matter signal, in order to confirm the effect evidenced by the DAMA/NaI and DAMA/LIBRA experiments using the same target and technique [56, 97]. For this goal, background at low energy should be kept as low as possible. Hence, the hexagonal NaI(Tl) crystals, 10.7 kg each, made by BICRON, which were originally thought as ANAIS target, were discarded after the full background assessment carried out because of the ^{40}K bulk crystal contamination identified. More radiopure crystals, specially in ^{40}K bulk content, were required, implying the development of NaI powder purification techniques and the search for new providers (section 5.1).

Furthermore, an energy threshold below 2 keV should be achieved in order to improve sensitivity for the annually modulated WIMP signal. This goal is addressed by testing new photomultiplier tubes: PMTs having higher quantum efficiency and PMTs of very low (or even ultra-low) radioactive background that could allow direct coupling to the crystal (without light guides) (section 5.2).

As result of this work, two crystals have been prepared with the most radiopure NaI powder found and are taking data at LSC. We refer to them as ANAIS-25 and preliminary results will be presented in chapter 6. In their building it has been applied all the experience acquired with ANAIS-0 and all the investigations summarized in this chapter.

5.1 Ultrapure NaI(Tl) crystals

The radiopurity of the NaI crystals has been identified as the main limiting issue, requiring to be overcome to allow an important improvement in sensitivity. The ANAIS experiment was conceived to be made with 10 hexagonal NaI(Tl) crystals of 10.7 kg each, made by BICRON (now Saint Gobain) (see section 1.3.2). One of them was chosen to be further studied and modified: it has been used in ANAIS prototypes I, II and III. As main result of the study of these prototypes the natural potassium content of the bulk crystal was measured to be 0.46 ± 0.2 ppm (13.7 ± 0.6 mBq/kg of ^{40}K), too high to allow their use in a dark matter search experiment. Subsequently, all the available crystals were characterized, see section 4.1.2, resulting natural potassium contaminations in the range from 0.46 to 0.71 ppm (from 13.7 ± 0.6 to 21.2 ± 0.4 mBq/kg of ^{40}K). This result implied a significant change in the ANAIS experiment timeline.

Hence, the ANAIS research team started to look for new NaI(Tl) crystals with very low content in potassium (less than 20 ppb). Saint Gobain [160] was contacted as the first option to produce the new crystals, as it had low radioactive background state-of-the-art NaI(Tl) detector technology: they had previously built DAMA/LIBRA detectors with similar background requirements. In fact, some years before, a 9.6 kg NaI(Tl) crystal was bought to that company as similar to those made for DAMA collaboration to be tested as first step in this direction. This crystal was used to build the ANAIS-0 module. Levels of ^{40}K of that crystal were not enough for ANAIS, as it has been confirmed in this work, see section 4.1.1. Unfortunately, the contacts with the company to develop more radiopure crystals were not successful.

At this point, the search for radiopure enough crystals turned out more complicated because no other company had an state-of-the-art technology and new potassium purification techniques for NaI powder had to be developed before trying to grow crystals. In this direction ANAIS searched for new possibilities and contacts with different enterprises and research groups at international level were established.

On the other hand, ^{210}Pb can be also an important background source, specially if the contamination is placed on the surface of the crystals or in the encapsulation materials and should be avoided by conveniently cleaning and/or polishing the surface of the crystal and carefully selecting the encapsulation material. Efforts in this direction were also done.

5.1.1 Measurement techniques and NaI reference samples

Accurate potassium content measurements at a few ppb level in NaI powder were required to guarantee the radiopurity of the samples. HPGe spectrometry was not able to reach that level even for high mass samples. For example, to reach the sensitivity level of 100 ppb in potassium at 95% C.L, our HPGe spectrometer would require roughly 1 kg of sample and a measurement time of one month. Going below that level is basically background limited, being the improvement achieved by measuring longer not much significant. Because of that, and in order to test many small samples as it would be required to certify any purification procedure applied, other analytical techniques had to be searched for.

The research group MARTE (Métodos de Análisis Rápidos con Técnicas Espectroscópicas) from the Department of Analytical Chemistry of the University of Zaragoza [161], was contacted in order to explore the possibility of reaching such low sensitivity in potassium content by Atomic Absorption Spectroscopy measurements (AAS).

Atomic spectroscopy [162] is the technique for determining the elemental composition of an analyte by its electromagnetic or mass spectrum. Atomic Absorption occurs when a ground state atom absorbs precise amounts of energy (i.e. light of specific wavelenghts) to reach specific excited states of the atom. The amount of light absorbed at the atom characteristic wavelengths searched for will increase as the number of atoms of the selected element in the light path increases. The relationship between the amount of light absorbed and the concentration of analytes present in known standards can be used to determine absolute unknown sample concentrations by measuring the amount of light they absorb. But relative measurements of sample concentrations could be more precise, not being affected by possible systematics in the comparison of standards and unknown samples.

The AAS equipment used by the MARTE group is a high resolution continuous source one, model ContrAA 700 (HR-CS-AAS) of Analytic Jena AG (Jena, Germany) with graphite furnace. It includes an arc lamp of Xe in *hot spot* mode as radiation primary source, a double monochromator of high resolution and a CCD array (588 pixels). It allows mass sample precision measurements ($1\,\mu g$ precision), and disposes of automatic solid sampler and graphite pyrolytic tubes and platforms for introducing and atomizing solid samples. Calibration is carried out with aqueous standard K samples. The main advantage of the ContraAA with respect to other AAS equipments is that it can study two different wavelengths at a time with very good resolution. In our case, the doublet at 404.4 nm and 404.7 nm of potassium spectral lines was chosen.

To validate the analytical procedure, commercial NaI samples from different providers were bought to be used as reference samples, see Table 5.1 and Figure 5.1. Because of the NaI hygroscopic character, samples were always manipulated in glove box with dry atmosphere, tightly stored in special containers, and also were dehydrated before weighting for the AAS measurements. The glove box is used only by the ANAIS members and exclusively NaI samples are handled there to avoid possible accidental contaminations. In Figure 5.2 different steps of the samples preparation at the glove box are shown.

(a) Sample 1 (b) Sample 3 (c) Sample 4 (d) Sample 5

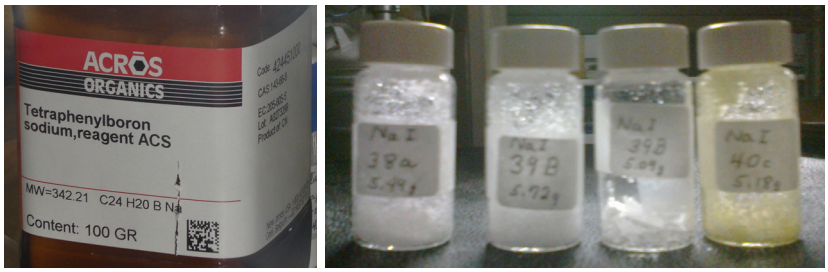

(e) Sample 6 (f) Samples 7, 8, 9 and 10

(g) Sample 11 (h) Samples 12 and 13 (i) Sample 14

Figure 5.1: *Pictures of some NaI and NTPB samples. They are not to scale. Respective masses and providers of the samples are listed in Table 5.1.*

All the samples heavier than 100 g were screened for K, U and Th with the HPGe test bench available at LSC, the results are shown in Table 5.2. By AAS, only K content was studied and corresponding results are also shown in Table 5.2. Both techniques should have been combined in order to monitor the progress of the purification procedure, but first, compatibility between both should also be guaranteed. Sample 3 was selected as

Figure 5.2: *Pictures of the preparation of different NaI samples at the glove box, at the University of Zaragoza.*

reference sample to validate the analytical procedure and it was measured several times by AAS.

5.1.2 Ultrapure NaI powder samples

Due to the fact that no commercial radiopure enough NaI powder was found, a new purification procedure had to be developed. Contacts with various international companies were established and different NaI samples were measured until an ultrapure NaI powder (below 100 ppb potassium) was found. At the same time, a company able to grow the NaI(Tl) crystals with this ultrapure powder was looked for.

Electrochemical Systems Inc.

The Electrochemical Systems Inc. (ESI) company of Knoxville (U.S.A.) proposed us the development of a new purification procedure able to reach less than 100 ppb potassium, starting from commercial NaI powder. This radiopurity goal was limited more by the analytical techniques than by the purification process, according to ESI.

A protocol was agreed by ESI and the University of Zaragoza, consisting in three phases: Phase I had as goal the determination of possible NaI powder purification methods and the choice of the most convenient(s) for the purification of around 250 kg NaI as

#	Provider	Description	Mass
1	Merck	Reference NaI powder (Ref. 106519; 99.99; K $\leq 2\,ppm$) (Ref. 43447; 99.98; K $\leq 5\,ppm$)	100 g
3	Alfa Aesar	Reference (Ref. 11665; 99.9; K $\leq 50\,ppm$)	500 g
4	Alfa Aesar/ESI	Starting NaI powder (Ref. 11665; 99.9; K $\leq 50\,ppm$)	115 g
5	ESI	Purified NaI powder	2.3 g
7	ESI	Purified once NaI powder	5.49 g
8	ESI	Purified twice NaI powder	5.72 g
9	ESI	Purified twice NaI crystalline sample	5.09 g
10	ESI	Purified 3 times NaI powder	5.18 g
11	ESI	Highly purified NaI powder	1007.4 g
12	AS	Starting NaI powder	1000 g
13	AS	Selected NaI powder	1000 g
14	AS	Cubic NaI crystal	1000 g
6	ESI	NTPB	100 g

Table 5.1: *General data from the different NaI and NTPB powder samples studied. ESI stands for Electrochemical System Inc. and AS for Alpha Spectra (see text for details).*

required for ANAIS; the goal of Phase II was the testing of the selected purification process and production of reference purified samples up to 1 kg; finally, Phase III would consist in the production and delivery of the total amount of the required purified powder (250 kg).

Phase I concluded that the use of chemical getters was the most convenient method to attain the required potassium purity level in NaI powder, being economically feasible for the required amount of powder to purify. Sodium tetraphenylborate, $NaPh_4B$ (NTPB) was selected as the first getter to be tested.

During Phase II, different raw and purified samples, described in Table 5.1, were sent by Electrochemical Systems Inc. These samples had been analyzed before the sending by ICP-OES (Inductively Coupled Plasma Optic Emission Spectroscopy) and AAS by the Galbraith Laboratory [163], and we measured all of them short after reception at the University of Zaragoza, if possible, with the two available methods (HPGe Spectrometry and AAS). The results of all those measurements for potassium content are shown in Table 5.2.

Samples from ESI were received in three shipments, and in the following we summarize the most relevant results derived from our analysis. Those results were shared with ESI and helped to take some of the following steps.

First shipment:

- Sample 4: 115 g of ESI raw NaI powder (same provider and reference number than Sample 3). HPGe results (see Table 5.2) showed compatible potassium levels in both samples. AAS results were not compatible with HPGe ones (see comments later).
- Sample 5: 2.3 g of purified NaI powder. As only a few grams were sent, it was measured only by AAS (see Table 5.2). Comparing results from samples 4 and 5, no hints of purification were observed.
- Sample 6: 100 g of the getter used for the purification. It was measured at the HP Ge test bench in Canfranc (see results in Table 5.2). It showed a potassium contamination level higher than the raw NaI sample. This result moved Electrochemical Systems Inc. to change their procedure in order to remove potassium from the getter as first step.

Second shipment:

- Samples 7 - 10: purified NaI samples taken in different steps of the process. All of them were about 5 g. These samples were crystalline, due to the purification procedure applied, and had to be ground before the AAS measurement. ESI analytical results are shown in Table 5.2. Differences between analysis results from ESI and UZ were so important that a more thorough cross-checking of the analytical techniques used and possible systematics was mandatory. Meanwhile this issue was under study, ESI was required to prepare a large mass purified NaI sample to be measured at the HP Ge spectrometer at LSC.

Third shipment:

- Sample 11: 1 kg purified NaI powder. Results are shown in Table 5.2. A significant purification was observed but the required K content was not achieved. Important difference between AAS and HPGe results for the potassium content of the samples was again obtained. Preliminary analysis of possible systematics in the AAS measurements was not able to explain those results, although, for instance, the dilute nature of the reference samples used for the AAS calibration versus the solid character of the samples studied in this work could play a significant role.

#	Galbraith AAS	ICP-OES	UZ Contra-AAS		LSC HPGe		
	K (ppm)	K (ppm)	K (ppm)		K (ppm)	U (ppb)	Th (ppb)
1	-	-	21.1 ± 3.5	(1)	1.5 ± 0.7	< 18	3 ± 1.5
3	-	-	16.5 ± 2.0	(1)	1.59 ± 0.14	< 1	< 0.33
			1.42 ± 0.18	(3)			
			1.64 ± 0.10	(4)			
4	2.02	107	36.5 ± 2.1	(2)	3.4 ± 1.4	< 13	< 2.8
5	1.02	50	48.0 ± 6.9	(2)	-	-	-
7	0.33	-	1.70 ± 0.50	(3)	-	-	-
8	0.07	-	0.99 ± 0.28	(3)	-	-	-
10	0.11	-	1.22 ± 0.60	(3)	-	-	-
11	< 0.07	-	1.38 ± 0.11	(4)	0.32 ± 0.08	< 1.7	< 0.24
12	-	-	0.69 ± 0.05	(4)	0.117 ± 0.045	-	-
13	-	-	0.74 ± 0.07	(4)	< 0.09	< 1.6	< 0.13
6	137 ± 15	254	-		87 ± 5	< 21	< 4

Table 5.2: *Analytical results from Galbraith Laboratory using AAS and ICP-OES techniques (sent by ESI), from the MARTE group of the University of Zaragoza by the Contra-AAS technique and from the HPGe Spectrometer at LSC. Contra-AAS measurements were done in different batches, being the batch number shown in parentheses.*

Alpha Spectra Inc.

In the meantime, contacts with another U.S.A. scintillator supplier, Alpha Spectra Inc. (AS) in Colorado, started. Initially, it was only thought to grow the crystals from the ESI purified powder, but they offered us to measure their starting NaI powder, standard (sample 12) and selected (sample 13), and a crystal grown with the selected powder (sample 14). Samples 12 and 13 were measured at the HPGe spectrometer at LSC. Results are shown in Table 5.2. Sample 13 gave a result consistent with the background and only an upper limit at 95% C.L. for the potassium content was derived. A powder having a potassium content below 90 ppb fulfilled our purification goal, because although ANAIS would require potassium content below 20 ppb, to test such a low level another measurement technique was required. Hence, two large crystals (grown from the selected NaI powder) were ordered to Alpha Spectra in order to measure directly the ^{40}K contamination level by the coincidence technique. Only after confirming the potassium content of those prototypes is at or below 20 ppb, the total 250 kg NaI detection mass will be ordered to AS. Description of these two crystals and their encapsulation will be done in chapter 6. Preliminary results derived from the first weeks of data will be also presented.

Hilger Crystals

Contacts with an UK scintillator company (Hilger Crystals) started in parallel, because they had the technology to grow crystals in low background conditions, and could also provide a radiopure powder. As the Alpha Spectra powder already fulfilled our purification goal, this line was not further evaluated.

5.2 Photomultipliers

Several Electron Tubes Limited (ETL) and Hamamatsu (Ham) photomultipliers (PMTs) models have been tested to choose the best option for the ANAIS experiment. In section 2.1.3, the PMT models tested and their main features were described. As it was explained there, a compromise between high quantum efficiency and low background features of the different PMT models was looked for.

Before coupling the PMTs to a NaI crystal, first tests were carried out at the University of Zaragoza in a very simple and specially designed set-up. This PMT test bench consisted of a light-tight cylinder in which one or two PMTs could be placed. It was a simple and versatile set-up to allow the measurement of different properties of the PMTs. The light emitted by an UV-LED is guided through an optical fiber inside the cylinder, coming into a Teflon disk acting as light diffuser. The light intensity arriving to the PMTs can be selected by using two polarizers, at a minimum when they are crossed, plus an optional absorptive filter. A pulse generator can be added to the LED circuit in order to produce pulses with different shape, either single ones or pulse chains at different frequencies. To test the PMTs with NaI scintillation pulses, a small cylindrical NaI(Tl) crystal ($43\,\mathrm{mm}\,\phi \times 34\,\mathrm{mm}$) could be placed inside the cylinder, being the scintillation excited with a radioactive source. A picture and a sketch of the test bench are shown in Figure 5.3.

The PMT output signal is recorded with a digital phosphor scope and analyzed off-line with a software similar to that described in section 2.5.

All the PMTs were previously measured at the HPGe test bench at the LSC. Results of such radioactive screening have been presented in Table 2.5 (see section 2.1.3 for more information). Their contribution to the background has been studied in chapter 4, in the following sections their behaviour in terms of light output is going to be studied.

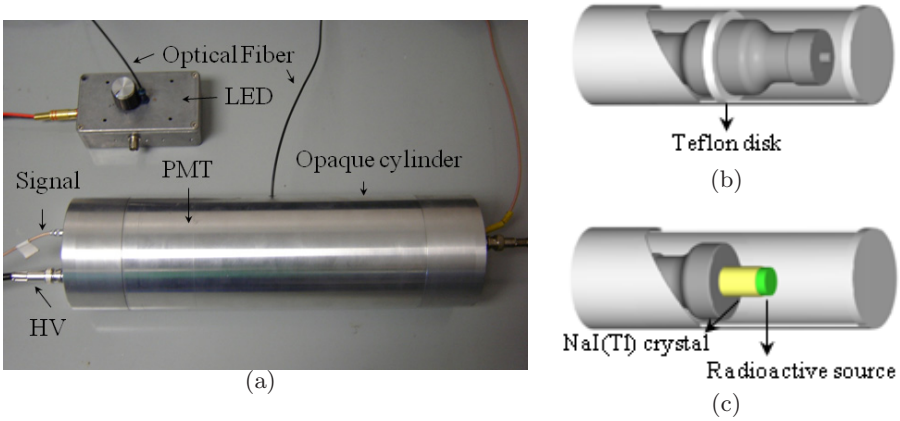

Figure 5.3: *(a) PMT test bench consisting of a light tight cylinder designed to allow the measurement of two PMTs in coincidence mode (b) or coupling one PMT to an small NaI(Tl) crystal plus a radioactive source (c). In the coincidence measurement, UV light from an external LED source is introduced (through an optical fiber) into a Teflon disk, acting as light diffuser, at the middle of the cylinder.*

5.2.1 Gain

The gain of a PMT is defined as the ratio of the anode output current to the photoelectric current from the photocathode. Measuring the gain so defined, and shown in Table 2.3 (as quantified by Hamamatsu) is not possible for us, because we cannot measure the cathode output current in our present set-up. Moreover, because the intensity and position of the LED were not reproducible, comparison between different measurements were only meaningful in relative gain terms. Only relative gain was measured with the PMT test bench in Zaragoza to verify the correct PMT performance, to determine the best operation point and to compare the gain - HV dependence for the different PMT models under study. The PMTs relative gain was tested as they were arriving, in different sets of measurements. Results of those relative gain tests are shown in Figure 5.4, one plot for each set of measurements. The measurements of each set are normalized to the gain at the recommended operation voltage of HQE 1066DA PMT in Figure 5.4.a, b and c; relative to ULB BA0057 at 1400 V in Figure 5.4.d and to VLB ZK 5902 at 1400 V in Figure 5.4.e.

LB and HQE PMTs have similar gain behaviour. ETL PMTs show higher gain, but this has not proved to be crucial for the achievable resolution (see section 5.2.4) or energy threshold. ULB and VLB PMTs have less homogeneous gain behaviour. HV operation point has to be chosen for every PMT trying to optimize the PMT photoelectron response, that is decisive for the triggering of ANAIS, but also to adjust similar gain factors in the two PMTs coupled to the same detector module. Our measurements revealed that the

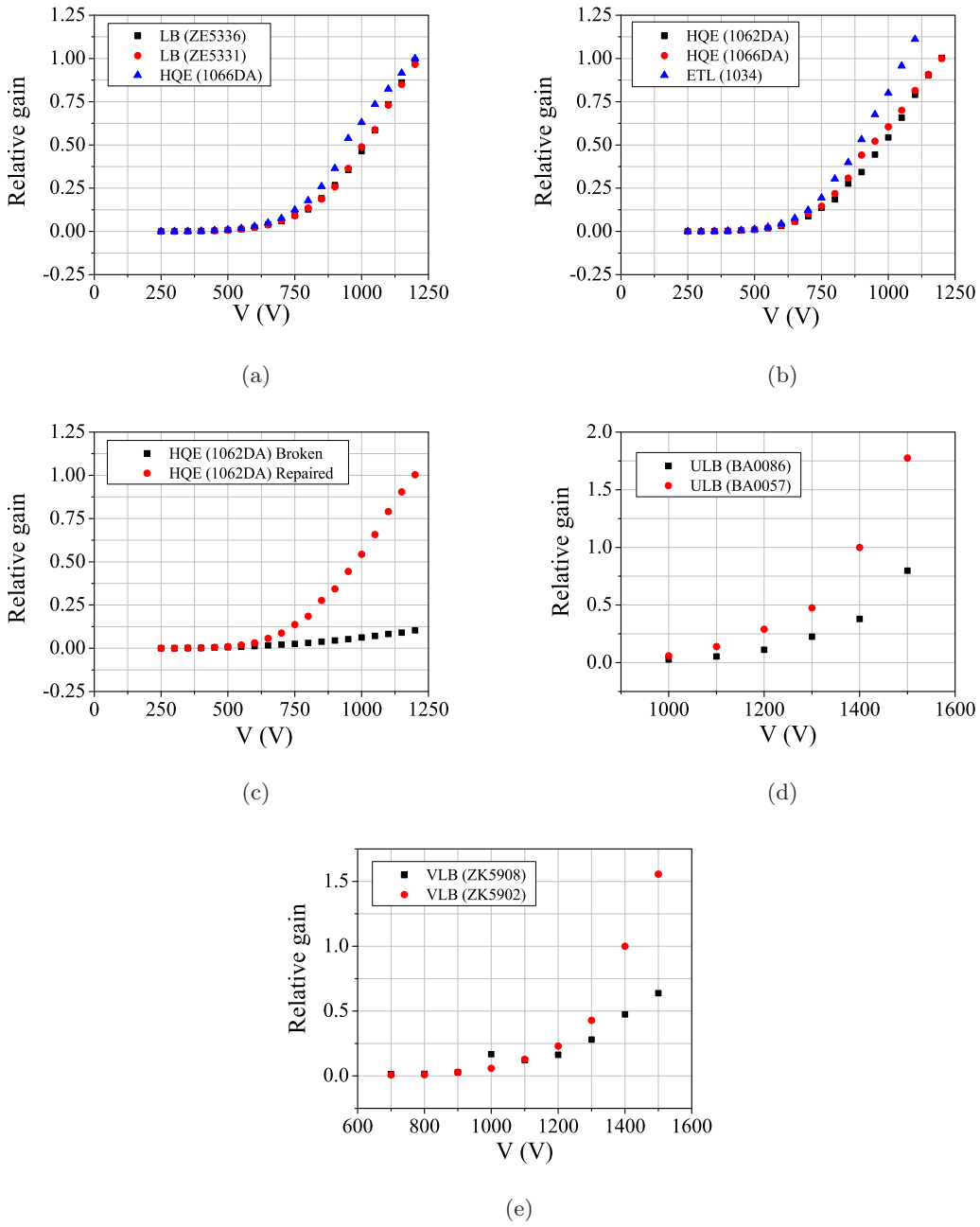

Figure 5.4: *Results of the relative gain measurements at the PMT test bench in Zaragoza, exciting the PMT with UV light from a LED. Gain is shown relative to HQE 1066DA PMT at 1200 V in plots (a), (b) and (c); relative to ULB BA0057 at 1400 V in plot (d) and to VLB ZK5902 at 1400 V in plot (e).*

photomultiplier 1062DA (HQE) had a broken dynode and was sent back to Hamamatsu to be repaired, see Figure 5.4.c.

5.2.2 Gain dependence with rate

An important issue concerning the operation of the ULB PMTs was detected when they were installed at the LSC in the set-up 3. They showed a non linear gain behaviour when excited with high frequency light pulses. The different dynode structure of the ULB PMTs with respect to the other PMT models seemed to be responsible of such a feature.

This problem was identified in high energy gamma calibrations of the ANAIS-0 module. The 1275 keV line of the ^{22}Na source was observed at a much higher equivalent energy, almost superposing the 1461 keV line from ^{40}K in the background spectrum (see Figure 5.5). This effect was clearly dependent on the position of the source, main factor determining the events rate.

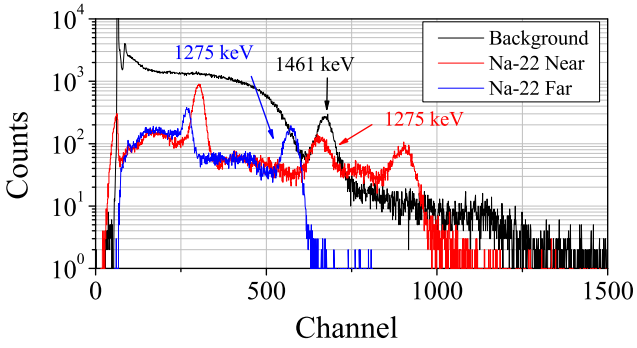

Figure 5.5: *High energy spectra for background (black line) and ^{22}Na calibrations. The 1275 keV line is seen to move depending on the source position (in red if it is placed near the crystal, in blue if it is moved away). PMT gain dependence on the rate is responsible of that effect. If the source is far from the detector, the sum peak at 1786 keV (1275 keV +511 keV) is strongly suppressed.*

Calibrations with other available radioactive sources were done to study this effect: ^{137}Cs, ^{57}Co, ^{60}Co, ^{133}Ba and ^{54}Mn. All the sources used had 1 μCi of activity in October 2009, although they emit with different intensity one or more gamma lines in very different energy ranges, producing very different energy depositions in the detector and very different detection rates. In Figure 5.6 the positions (in channels) of the different gamma and X-rays lines from all the sources used are shown for the high (left) and the low (right) energy ranges. In the case of ^{22}Na and ^{60}Co lines (both having emissions above 1 MeV) the different gain is clearly evidenced by the different slope in the channel vs energy plot.

In order to check and quantify the effect, tests were done in the Zaragoza test bench, placing a PMT in the cylinder and exciting it with light pulses from a LED source at low and high amplitude and different frequencies. Results show that LB PMT model presents

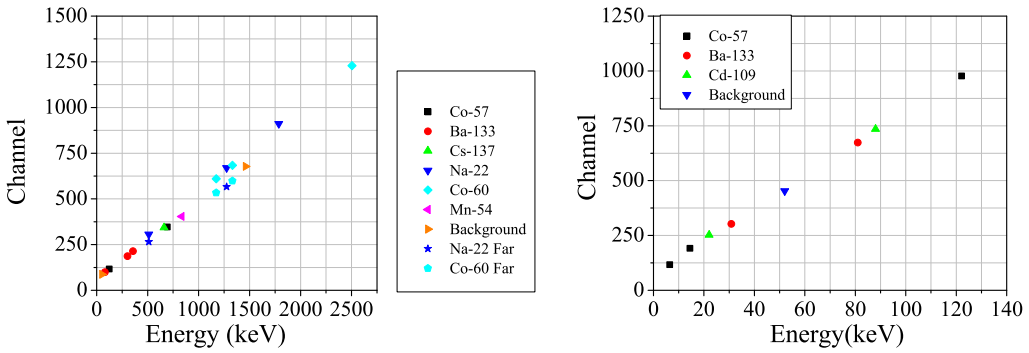

(a) (b)

Figure 5.6: *Positions (in channels) of the different gamma and X-rays lines from all the sources used (^{22}Na, ^{137}Cs, ^{57}Co, ^{60}Co, ^{133}Ba and ^{54}Mn) and for all the background lines, at high (a) and low (b) energy regions. All the sources were placed in the regular calibration position, but ^{22}Na and ^{60}Co were also placed far from the detector (labeled far in the legend). All the sources had 1 μCi of activity in October 2009.*

almost no variation of gain with excitation rate. However, ULB PMT model shows a very different behavior even at low frequency for high amplitude UV light excitation.

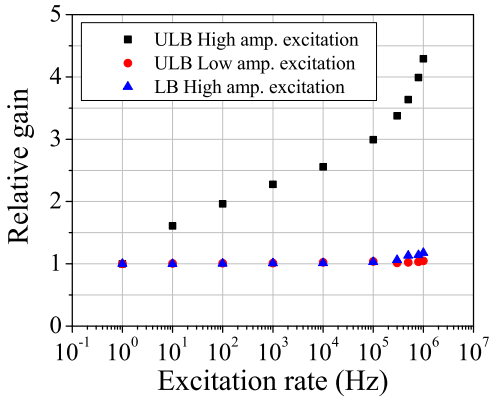

Figure 5.7: *Relative gain vs UV light excitation rate dependence derived from tests done in the Zaragoza PMT test bench. LB PMT presents almost no variation of gain with rate, whereas ULB shows a strong increase in gain with the excitation rate for high amplitude UV excitation.*

This effect is not a real problem for the background measurements of ANAIS, being the trigger rate below 1 Hz per ANAIS-module, but for the calibration of the experiment could be an issue to consider. Anyway, being the study of the low energy region the goal of ANAIS, only low energy gamma sources are mandatory and no apparent effect has been observed for them.

5.2.3 Single Electron Response

Triggering at photoelectron level is required for ANAIS. To ensure this condition is fulfilled, a good knowledge of the S.E.R. (Single Electron Response) of every PMT at the operation HV used is required. Some preliminary tests were done at the Zaragoza test bench [164]. As it was explained in sections 2.5 and 3.1, an algorithm has been implemented in the ANAIS data analysis to find the peaks in the pulse (attributable to single photoelectrons if the total number is low enough). The last peak in pulses having a low number of peaks is considered to be a good single photoelectron population, as far as the probability of arriving more than one photon simultaneously is very low, and the trigger efficiency does not bias the selection. However, the threshold level in the algorithm for peak identification is an issue and has to be made as low as possible. Pulses with less than 10 peaks have been considered to avoid peaks overlapping and only pulses where the last peak is placed at the end of the pulse are taken into account in order to not being influenced by the trigger efficiency. With the selected population for each ANAIS-0 set-up, area, width and height distribution are calculated. The single photoelectron response in terms of area for the different setups is shown in Figure 5.8, the peak is gaussian fitted and the results of the fit for all the setups tested in ANAIS-0 are shown in Table 5.3. In section 3.5, where the trigger efficiency was studied, the S.E.R. was shown in terms of amplitude, see Figure 3.28.

Set-up	PMT model	Photoelectron area			
		PMT 0		PMT 1	
		Mean	σ	Mean	σ
		mV·ns			
1	ET	224.3 ± 1.1	85.5 ± 1.1	232.3 ± 1.3	90.9 ± 1.2
2	LB + LG	193.8 ± 1.6	48.6 ± 1.4	139.2 ± 0.6	38.8 ± 0.8
3	ULB + LG	151.8 ± 1.8	68.4 ± 1.3	198.3 ± 2.6	105.5 ± 2.0
4	ULB	144.0 ± 2.3	62.8 ± 1.5	159.0 ± 2.1	80.4 ± 1.7
5	VLB	176.6 ± 1.1	89.9 ± 1.1	214.6 ± 3.9	142.8 ± 3.6

Table 5.3: *Photoelectron area calculated for the different ANAIS-0 set-ups. Direct comparison is meaningless because PMTs gain was adjusted in a different way at each setup.*

To better study the photoelectron shape, the selected pulses are averaged around the position of the last peak. Figure 5.9 shows the photoelectron average in the different setups. In Figure 5.9.f all the PMT models are compared normalizing to 1 their amplitude. It can be seen that LB and VLB PMT models present a wider photoelectron response. It is specially relevant the bounce, probably due to the PMT voltage divider design in

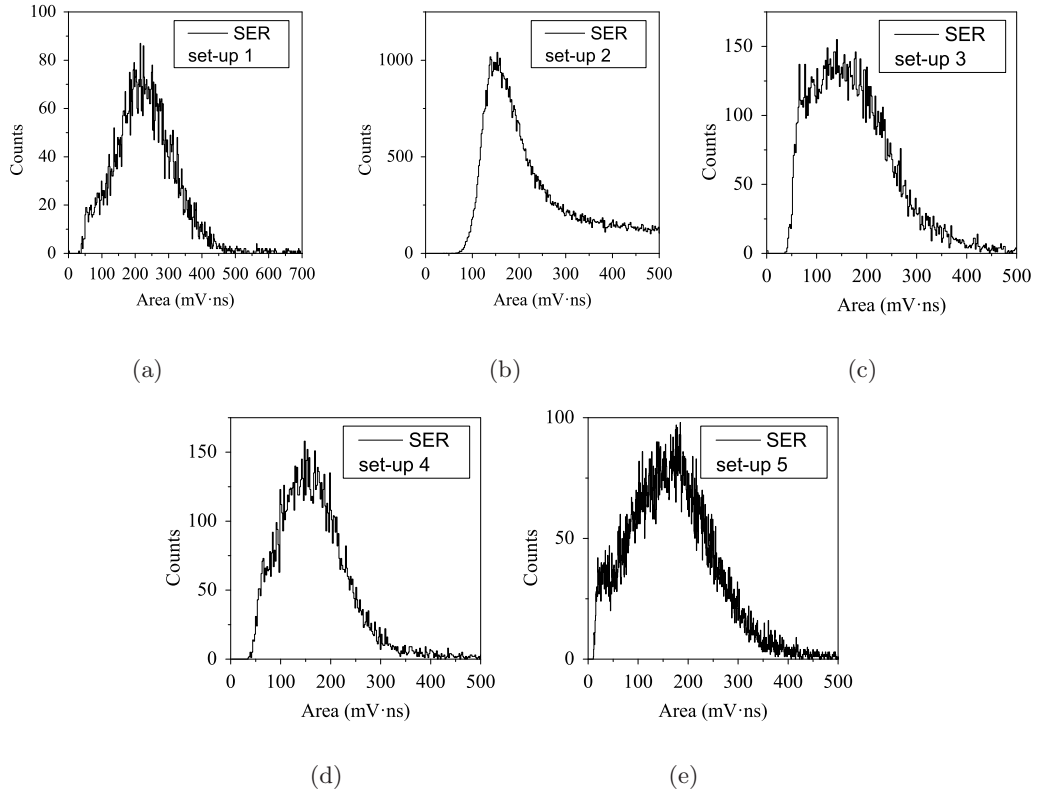

Figure 5.8: *Area distribution of the Single Electron Response for the PMT signal 0 from ANAIS-0 set-up 1 using ETL PMTs (a), dset-up 2 using LB PMTs with LG (b), set-up 3 using ULB PMTs with LG (c), set-up 4 using ULB PMTs (d), and set-up 5 using VLB PMTs (e).*

the ULB and VLB PMTs. This issue is relevant for the cleanliness of the signal and an improved design of the HV divider and charge collection circuit is being sought. However, preliminary tests did not improve the S.E.R. signal quality.

5.2.4 Light collection efficiency

To compare the light collection in the different setups, the number of photoelectrons per keV has been estimated from the S.E.R. area distribution and the area of a low energy line from calibration spectra: the area of the 22.6 keV line from ^{109}Cd, (see Table 5.4) is divided by the mean photoelectron area (obtained by studying the distribution of the last peak area, as explained above) and the nominal energy of the line used.

Results for all the set-ups are shown in Table 5.5. It can be seen that light guides worsen about 25% the light collection efficiency. Comparing the different PMTs used, VLB PMTs present the best number of phe/keV (set-up 5) supporting the better QE they have, according to manufacturer data. Also according to manufacturer data, ETL

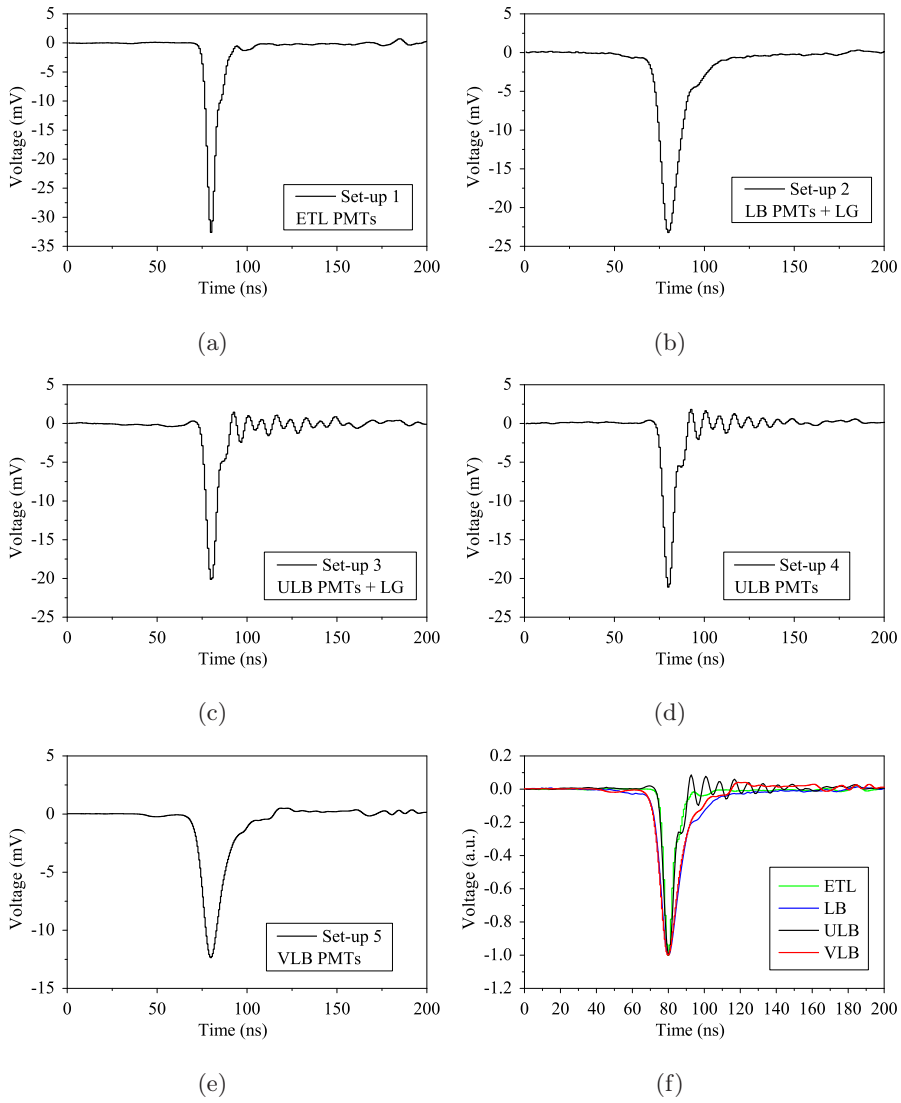

Figure 5.9: *Average S.E.R. built by averaging those individual photoelectron pulses selected with the last peak of pulses having very few peaks: (a) S.E.R. for ETL PMTs in setup 1, (b) S.E.R. for LB PMTs with light guides in setup 2 , (c) S.E.R. for ULB PMTs with light guides in setup 3, (d) S.E.R. for ULB PMTs in set-up 4, and (e) S.E.R for VLB PMTs in set-up 5. (f) Comparison of average pulses corresponding to the S.E.R. for all the PMT models tested with ANAIS-0. They have been all normalized to the same amplitude.*

PMTs should not have better QE than the rest of the models; hence, the higher than expected light collection efficiency corresponding to them (set-up 1) could be due to a better optical coupling between crystal and quartz window that degraded afterwards, worsening the performance of the following set-ups.

Set-up	PMT model	22.6 keV line area			
		PMT 0		PMT 1	
		Mean	σ	Mean	σ
		mV·ns			
1	ETL	16189 ± 4	2556 ± 3	16514 ± 4	2555 ± 4
2	LB + LG	7626 ± 3	1600 ± 3	7412 ± 3	1538 ± 3
3	ULB + LG	7682 ± 6	1690 ± 4	7963 ± 6	1888 ± 4
4	ULB	8726 ± 4	1681 ± 3	9546 ± 4	1800 ± 2
5	VLB	14614 ± 5	1970 ± 5	18017 ± 5	2678 ± 5

Table 5.4: *Area of the 22.6 keV line coming from the ^{109}Cd calibration source. It has been calculated for the different set-ups. Direct comparison is meaningless because PMTs gain was adjusted in a different way at each setup.*

Set-up	PMT model	Photoelectrons/keV		
		PMT 0	PMT 1	PMT0+PMT1
1	ETL	3.19 ± 0.01	3.15 ± 0.02	6.34 ± 0.02
2	LB + LG	2.41 ± 0.03	2.36 ± 0.01	4.77 ± 0.03
3	ULB + LG	2.24 ± 0.03	1.78 ± 0.02	4.02 ± 0.04
4	ULB	2.68 ± 0.04	2.66 ± 0.03	5.34 ± 0.05
5	VLB	3.66 ± 0.02	3.71 ± 0.07	7.38 ± 0.07

Table 5.5: *Photoelectrons per keV derived from 22.6 keV line (^{109}Cd calibration) data. They have been calculated for the different set-ups by dividing the the mean value of the 22.6 keV area by the mean photoelectron area (see Tables 5.3 and 5.4). The error has been estimated propagating the deviation of both measurements.*

5.2.5 Quantum efficiency

Energy resolution measurements have been done at the Zaragoza test bench and with the different set-ups of the ANAIS-0 module in the LSC using low energy calibration data from ^{57}Co, ^{133}Ba and ^{109}Cd radioactive sources.

Energy resolution is not an inherent property of the PMT, because it depends also on many other external factors. However, comparing similar set-ups energy resolution can be a tracer of the PMT quantum efficiency, assuming the rest of external factors are the same.

First, resolution was measured at the Zaragoza test bench. Inside the cylinder, a small NaI(Tl) crystal was coupled to the PMT and low energy gamma calibrations were carried out, see Figure 5.3. Results of these tests concerning Full Width at Half Maximum (FWHM) of the studied lines are shown in Figures 5.10 and 5.11 and listed in Table 5.6 for

the different PMT models available. It can be seen that Hamamatsu PMTs showed better energy resolution than ETL PMTs. This is consistent with the better nominal quantum efficiency of the Hamamatsu models.

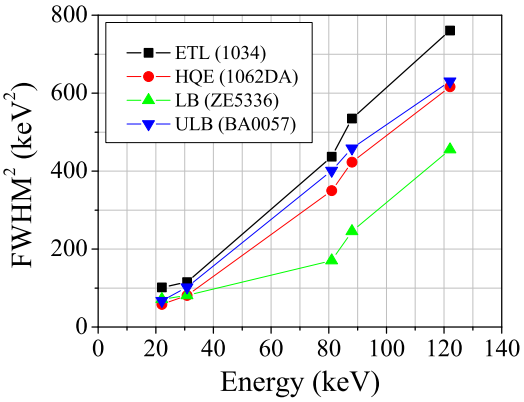

Figure 5.10: *Square of the full width half maximum (FWHM) of the different gamma lines measured at the Zaragoza test bench corresponding to low energy calibration data.*

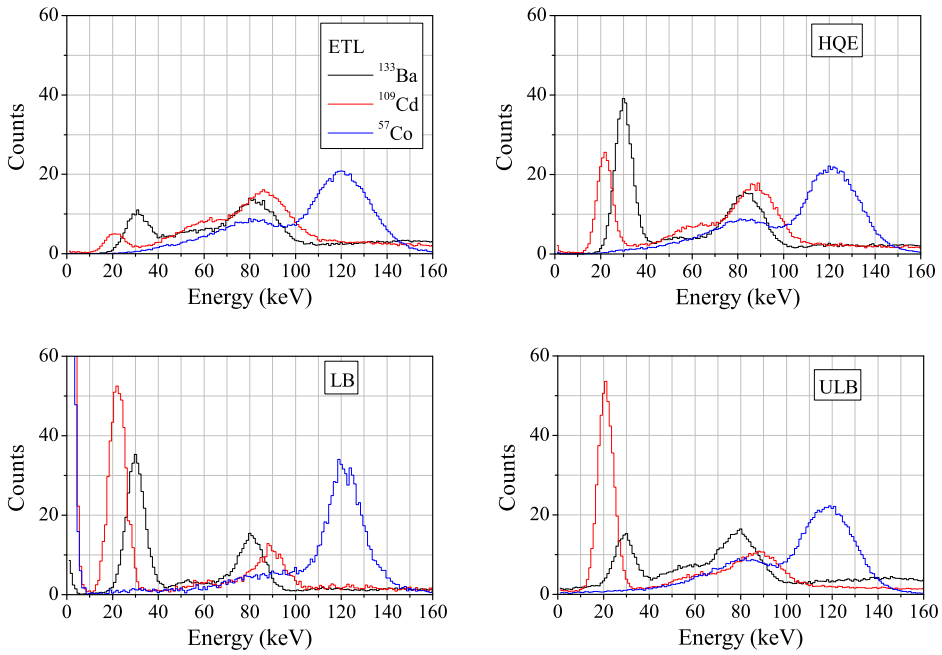

Figure 5.11: *Low energy spectra for the different radioactive sources and PMTs obtained in the PMT test bench by coupling every PMT unit to a small NaI(Tl) crystal.*

Second, energy resolution has been measured for all the available PMTs (except the HQE model) in the different ANAIS-0 setups at LSC. Results, shown in Figure 5.12, are compatible with the tests carried out at the PMT test bench. VLB PMT model resolution

Energy (keV)	Resolution (%)			
	ETL	HQE	LB	ULB
22.6	19.41	14.65	16.27	15.79
31.7	14.80	12.40	12.43	13.95
81.0	10.98	9.83	6.86	10.53
88.0	11.18	9.94	7.57	10.35
122.1	9.61	8.65	7.44	8.75

Table 5.6: *Energy resolution (%) values derived from measurements at the PMT test bench in Zaragoza for the different lines in low energy calibration data.*

was not measured in Zaragoza, but in sight of the ANAIS-0 measurements, it can be stated that their resolution is quite good, supporting the high light collection efficiency of the corresponding set-up (see Table 5.5 and the high nominal quantum efficiency of that model). The effect of the light guides in reducing light collection efficiency can be also observed in Figure 5.12 and Table 5.7 and it can be concluded that avoiding light guides would improve the resolution in a factor between 20-25%.

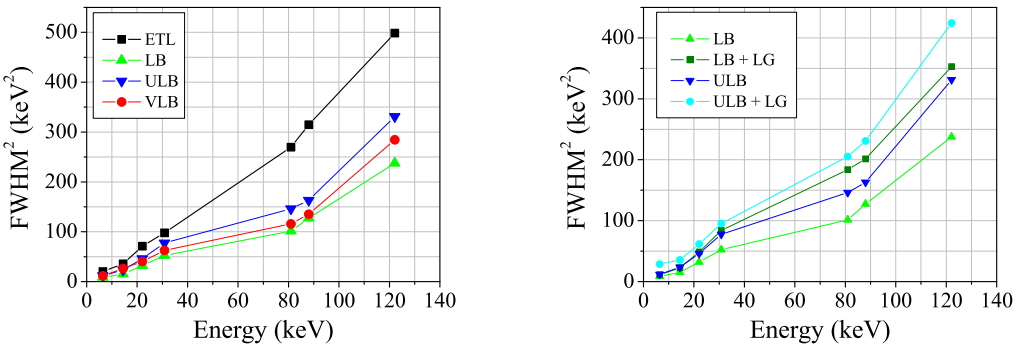

(a) (b)

Figure 5.12: *Square of the FWHM for the different gamma lines measured at LSC in ANAIS-0 module. (a) Comparison between the different PMT models and (b) effect of adding light guides in two different set-ups.*

5.2.6 Conclusions

Different PMTs which could be used in ANAIS have been tested. The first option was to use low background PMTs from Electron Tubes Limited, but PMTs with higher quantum efficiency from Hamamatsu have proved to be a better option. Low background PMTs from Hamamatsu would probably require using light guides, because their contribution to the background of the experiment can be important. In terms of background, the best option

Energy (keV)	Resolution (%)					
	ETL	LB	ULB	VLB	LB + LG	ULB + LG
6.4	29.85	19.54	22.92	22.62	22.25	35.67
14.4	17.63	11.51	14.36	15.18	14.07	17.60
22.1	16.23	10.90	13.08	12.19	13.45	15.12
30.9	13.64	9.98	12.15	10.93	12.64	13.46
81.0	8.63	5.29	6.35	5.66	7.12	7.53
88.0	8.57	5.46	6.17	5.62	6.86	7.34
122.1	7.78	5.37	6.34	5.88	6.55	7.18

Table 5.7: *Energy resolution (%) results for the different gamma lines measured at LSC in ANAIS-0 module. Light guides worsen the energy resolution an average of 24% for the LB PMTs and of 17% for the ULB ones.*

would be the ULB PMTs. However, the results of our tests point out that the ULB PMTs have lower quantum efficiency values than LB or VLB ones, which entails disadvantages on the light collection efficiency. With the VLB PMTs, having better radiopurity than LB model, a lower energy threshold could be achieved if they could be used without light guides. Tests of the two Alpha Spectra prototypes at the LSC are trying to solve this issue in a definitive way.

Hence, due to the high cost of the ULB PMTs and the quantum efficiencies guaranteed by Hamamatsu (33% for the VLB and 30% for the ULB), 42 units of the VLB PMTs (one of them is shown in Figure 5.13) have been purchased to be used in the ANAIS experiment.

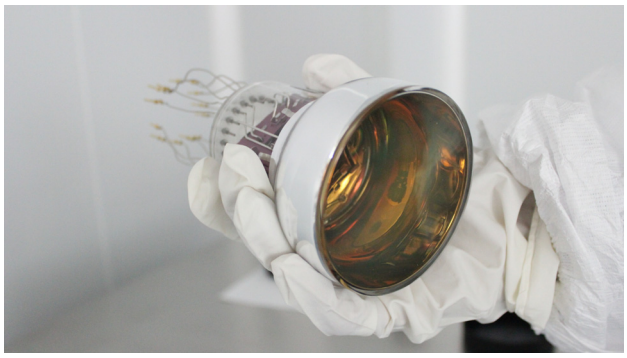

Figure 5.13: *VLB Hamamatsu photomultiplier which will be used for the ANAIS experiment.*

Chapter 6

ANAIS-25

The ANAIS experiment requires the use of ultrapure NaI(Tl) crystals. A NaI powder having a potassium level under the limit of the analytical techniques used was found (see section 5.1), and then, two crystals were grown to measure the potassium content using the coincidence technique (see section 4.1.2). The encapsulation of the crystals was discussed with the manufacturer, Alpha Spectra, in order to guarantee the use of ultra low background materials and procedures in the machining of the different components, as well as to have a good light collection (section 6.1.1). This two NaI(Tl) crystals of 12.5 kg each from Alpha Spectra form the ANAIS-25 set-up.

The two modules arrived at the LSC the 27^{th} November 2012 and, after coupling the PMTs, they were directly installed in the ANAIS experimental space (section 6.1.2). Since then, the background measured by these two modules has been carefully studied, but work is still in progress (section 6.2): their natural potassium content in the bulk has been quantified (section 6.2.1), as well as the uranium and thorium radioactive chains presence in the bulk through the discrimination of the corresponding alpha evens by PSA (section 6.2.2), and due to the fast commissioning, the contribution from cosmogenic activated isotopes is clearly identified and their decay observed along the first months of data taking (section 6.2.3). Longer-life isotopes are still contributing to the background and further study is ongoing. Background results are supported by the background model carried out with a Geant4 simulation (section 6.2.4).

Following the procedures established with ANAIS-0 and previous prototypes (see chapters 3 and 5) it has been studied the best procedure to select bulk NaI(Tl) scintillation events (sections 6.3.1), the asymmetry in the energy sharing between the two PMTs in each module (section 6.3.3), the long scintillation timing constants in NaI(Tl) (section 6.3.4), and light collection efficiency (section 6.4).

6.1 ANAIS-25 experimental procedure

The need for new crystals for the ANAIS experiment had been clearly established (see section 4.1.2) and, as soon as a NaI powder with the lowest potassium content that could be assessed by the available analytical techniques was found (see section 5.1), two large crystals were ordered. They have been taking data at LSC in order to determine their potassium, uranium and thorium bulk content. The results derived from those measurements will be decisive to order the rest of the modules required to complete the ANAIS detection mass (18 modules more, 12.5 kg mass each).

6.1.1 Growing and encapsulation at Alpha Spectra

While the Alpha Spectra (AS) selected powder was being measured at the HPGe test bench in the LSC, see section 5.1, discussions about growing and encapsulation procedure were going on with the company. AS started to grow with that selected powder a large mass NaI(Tl) ingot. As soon as the upper limit of 90 ppb potassium in the selected powder was verified by the University of Zaragoza (UZ) measurement, an agreement between AS and the UZ about the building of two prototypes, 12.5 kg each, using that NaI(Tl) ingot already grown, was quickly prepared and signed. In Figure 6.1.a, a picture of the bare crystals can bee seen.

The knowledge acquired at the University of Zaragoza with the previous prototypes, specially with ANAIS-0, and the AS expertise on the field were put together to select the materials and to design the encapsulation. The crystals were encapsulated in OFHC copper with two synthetic quartz windows allowing the PMTs coupling in a second step, as it was done with ANAIS-0. Indeed, the encapsulation was designed to allow the use of the same ANAIS-0 PMTs housing and to ease the PMTs coupling at the UZ. In Figure 6.1.b, the copper encapsulation machining at Alpha Spectra is shown. Only white Teflon was used as light diffuser, wrapping the crystal, inside the copper encapsulation. A Mylar window, built following UZ specifications and very similar to that of ANAIS-0, allows to calibrate at low energy both detectors. Unlike ANAIS-0, an special silicon optical interface, instead of optical grease, is used to optically couple the NaI crystal to the quartz. Protocols for low-background machining and surface cleaning procedures were proposed by the UZ, discussed and agreed by AS. A glove box was designed on purpose for encapsulating these detectors at AS, and it can be seen in Figure 6.1.c. The copper cleaning protocol proposed to AS was that applied to the cleaning of the ANAIS-0 PMT copper casings, as explained

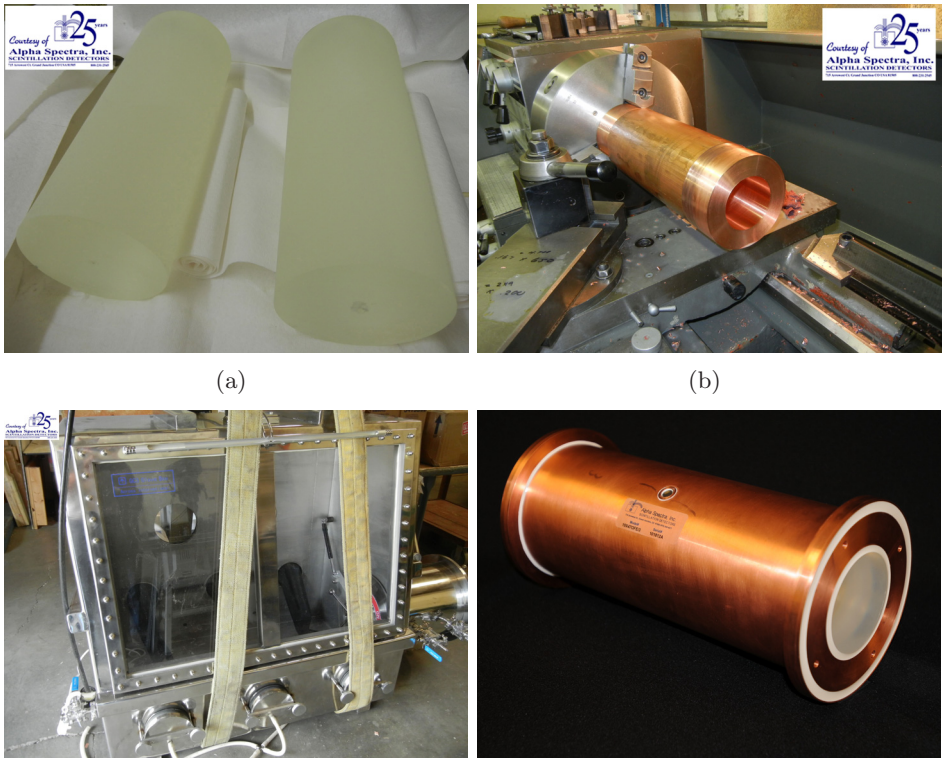

(a) (b)

(c) (d)

Figure 6.1: *Pictures sent by Alpha Spectra: (a) crystals of 12.5 kg each grown from the ultrapure NaI(Tl) powder, (b) copper housing machining, (c) specially built glove box used at Alpha Spectra for encapsulating ANAIS crystals in ultra-low background conditions, and (d) one of the crystals after the encapsulation, before shipment to LSC.*

in section 2.1.3. One of the detectors made by AS ready to be shipped to LSC is shown in Figure 6.1.d.

Shipping was done by surface transportation, to minimize cosmogenic activation of the detectors. These two detectors arrived at the Canfranc Underground Laboratory the 27/11/12.

6.1.2 Installation at LSC

Detectors were brought to the LSC clean room, where the PMTs were coupled, see Figure 6.2. Two units of VLB Ham PMTs and two units of ULB Ham PMTs, previously tested in ANAIS-0, have been coupled to the detectors, directly to the quartz windows, without light guides to achieve the higher light collection efficiency. The optical quality of the crystals was very good by visual inspection, specially the detector 0. For this reason the VLB PMTs (with higher QE) were coupled to it. Table 6.1 summarizes the serial

number of the detectors and the PMT models coupled to each module. Figure 6.3 shows the final aspect of the two modules.

(a) (b)

Figure 6.2: *PMT coupling to the ANAIS-25 modules in the LSC clean room: (a) connecting the PMT flying leads into the voltage divider connectors, and (b) PMT with the optical grease on it, just before coupling it to the quartz window.*

Detector	Serial Number	PMTs	Light guides
0	101812B	VLB	No
1	101812A	ULB	No

Table 6.1: *Serial number and PMTs used in the two modules of the ANAIS-25 set-up.*

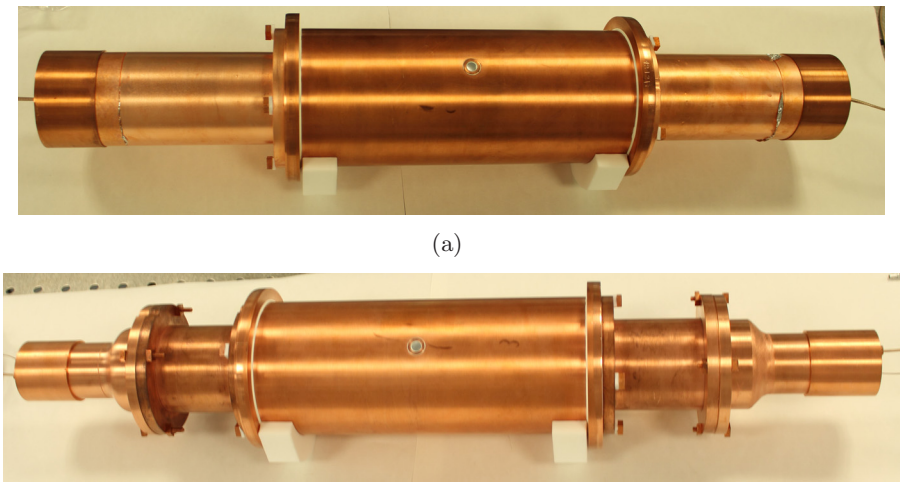

(a) (b)

Figure 6.3: *Final appearance of ANAIS-25 modules after the coupling of the PMTs and placement of their copper casings at the LSC clean room: detector 0 with VLB PMTs (a) and detector 1 with ULB PMTs (b). Despite the different appearance of the modules, light guides were not coupled to none of them.*

Then, the detectors were installed in the LSC Hall B, inside a convenient shielding, at ANAIS experimental space the 30/11/12, see Figure 6.4. The same shielding of ANAIS-0 (see section 2.3) was adapted to be used with the new detectors: 10 cm ancient lead, 20 cm low radioactive lead, anti-Rn box and three active vetoes anti-muons. Data taking started almost immediately after mounting because electronics and acquisition system had been already fine-tuned and tested with ANAIS-0 and PIII, see section 2.5. The Figure 6.5 is an artistic view of the ANAIS-25 experimental layout at LSC, consisting of active and passive shielding.

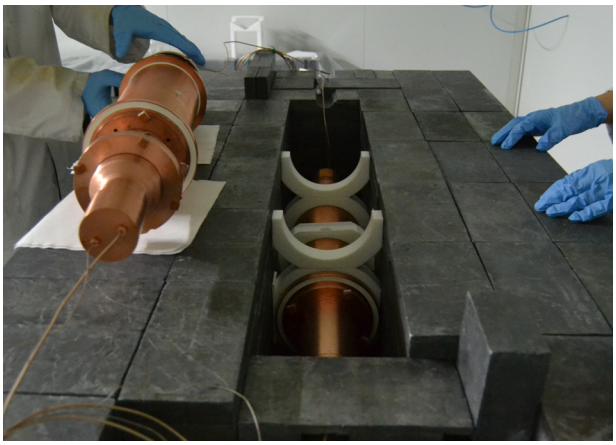

Figure 6.4: *Installing the ANAIS-25 modules in the shielding.*

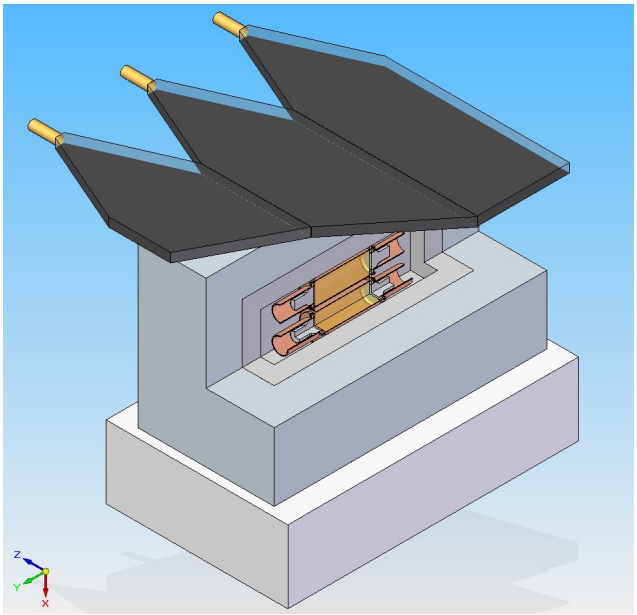

Figure 6.5: *Schematic drawing of the ANAIS-25 experimental layout. It can be seen the NaI(Tl) crystals, the copper encapsulation, PMTs, ancient lead, low activity lead, a polyethylene base, and three vetoes anti-muons.*

The stability of all the environmental parameters (radon, temperature, pressure and humidity) has been also monitored through the ANAIS-25 operation.

6.1.3 Data taking

ANAIS-25 began taking data the 30/11/12, and the preliminary results corresponding to the first three months underground of the two detectors are presented in this chapter. Stable data taking corresponds to 49.8 days of live time (from the 26/12/12 to the 20/02/13). For the ^{40}K content analysis, 70.4 days of live time have been used to increase the statistics in spite of some instabilities in the first weeks of data (specially in detector 1, that had as consequence that only data from PMT 1 of that detector have been considered). It has to be noted here, that a full study of the ANAIS 25 background has not yet been carried out and only preliminary results are presented, derived by applying directly the procedures used for ANAIS-0 in previous chapters.

6.1.4 Energy calibration of ANAIS-25 modules

Calibration of the ANAIS-25 modules is carried out using the same sources and procedures than in ANAIS-0 set-ups, see section 2.7. Because of the very high light collection efficiency of ANAIS-25 modules (see section 5.2.2), PMTs signals saturate at much lower equivalent energies than in previous setups and stronger gain dependence on the events rate is observed for ANAIS-25 data. This implies that calibration at high energy is much difficult. The high energy region will be calibrated in the following with the background lines.

Non-linear effects are produced even in background measurements and complicate enormously the calibration of the high energy spectra. Because of this, calibration is done dividing the high energy spectra in two regions: from 0 to 500 keV and from 500 to 2000 keV. This issue is under study and modifications in the voltage dividers could help to solve them.

However, the low energy region can be calibrated with the lines from low energy sources, as done in ANAIS-0. Calibration spectra for ^{57}Co and ^{109}Cd sources are shown in Figure 6.6. A clear improvement in energy resolution with respect to that of ANAIS-0 is observed and will be quantified in section 6.4.

The anomalous behavior after excitation with a high energy radioactive source identified in ANAIS-0 (see section 2.7) has also been detected with the ANAIS-25 modules,

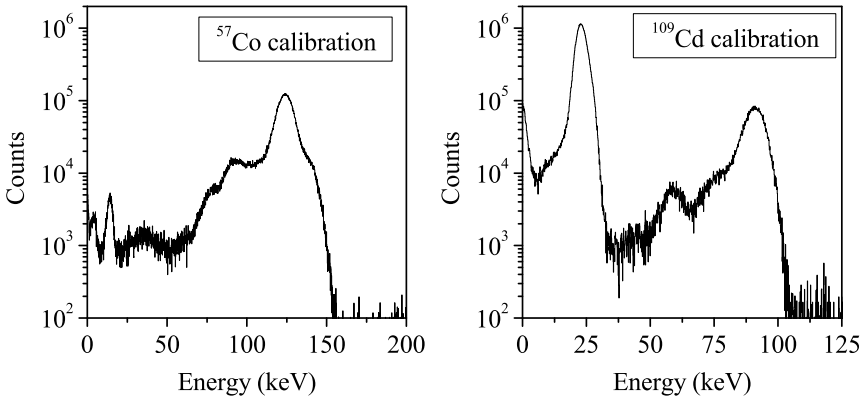

Figure 6.6: *Calibration spectra from ^{57}Co (left) and ^{109}Cd (right) sources taken with ANAIS-25 detector 1. 6.4 and 14.4 keV lines are clearly observed after going through the Mylar window.*

specially with the detector 0, see Figure 6.7.a. In Figure 6.7.b the total trigger rate just after removing the ^{22}Na source has been fitted to three exponential decays (the best fit achieved), to the function shown in 2.3, for the detector 0 and the results derived are shown in Table 6.2. When trying to fit similarly the detector 1 rate, a good fit is obtained with the scintillation times fixed to those of the detector 0, but with a much smaller amplitude.

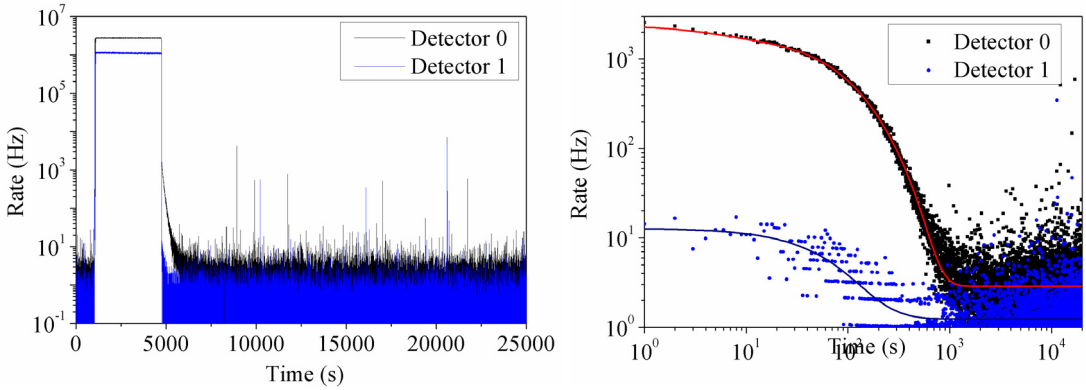

Figure 6.7: *(a) Trigger rate before, during and after a ^{22}Na calibration for ANAIS-25 detectors 0 and 1. (b) Trigger rate after removing the ^{22}Na source and the exponential decay fit to the function shown in 2.3. Fit results are shown in Table 6.2.*

The two crystals have been cut from the same ingot, and no differences in their past have been found able to explain such a different behavior. However, PMTs coupled to each detector are not the same: VLB PMTs for the detector 0 and ULB PMTs for the detector 1. The larger QE of the former could imply a larger sensitivity to effects of this kind, but the several orders of magnitude effect seen in Figure 6.7.b is beyond expectations. In next

Detector	τ_1 (s)	A_1 (Hz)	τ_2 (s)	A_2 (Hz)	τ_3 (s)	A_3 (Hz)
0	4.2 ± 0.9	582 ± 9	56 ± 10	963 ± 5	132 ± 14	864 ± 3
1	4.2(*)	3.5 ± 1.4	56(*)	9.3 ± 0.7	132(*)	2.2 ± 0.4

Table 6.2: *Exponential decay fit results of the trigger rate after a ^{22}Na calibration for ANAIS-25 modules. Values marked with * have been fixed in the fit.*

months, VLB PMTs will be coupled to both modules and further understanding of the origin of this behavior could be achieved.

Moreover, this behavior could be related with the higher trigger rate observed in detector 0 since the data taking underground began. This trigger rate is mostly due to single photons producing chance coincidences, found at a much higher rate in detector 0 than in detector 1, and it has been decreasing with time as shown in Figure 6.8.a. Detector 1 presents, on the contrary, a constant rate since the beginning. If events having more than 3 peaks (see section 3.1) are selected, rate is constant in both detectors along the whole acquisition (after solving a cross-talk problem), see Figure 6.8.b.

Although both effects seems to be related, an explanation is still to be found and work in this direction is in progress. However, we can conclude that exposition to high intensity high energy calibration sources and to light sources should be avoided as much as possible.

6.2 Background understanding

Main goal of ANAIS-25 setup was to determine the potassium content of the crystals by the coincidence technique, as done with ANAIS-0 module (see section 4.1.2). At the same time, ^{238}U and ^{232}Th chains isotopes content in the crystal has to be determined as well as a general background assessment of the detectors. As the modules started to take data just a couple of days after their arrival, cosmogenic activation was clearly observable. Hence, background spectra have been carefully studied to extract as much information as possible for the different background contributions.

The normalized background spectra (see section 6.1.3) for both ANAIS-25 modules are shown in Figure 6.9 for the low energy region and in Figure 6.10 for the high energy region. It is worth remarking that these spectra correspond to raw data, and no filtering at low energies has been applied, in section 6.2.1 the filtering procedure will be described.

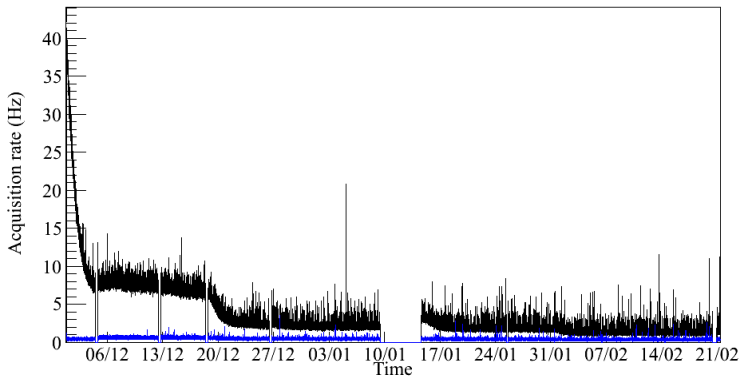

(a)

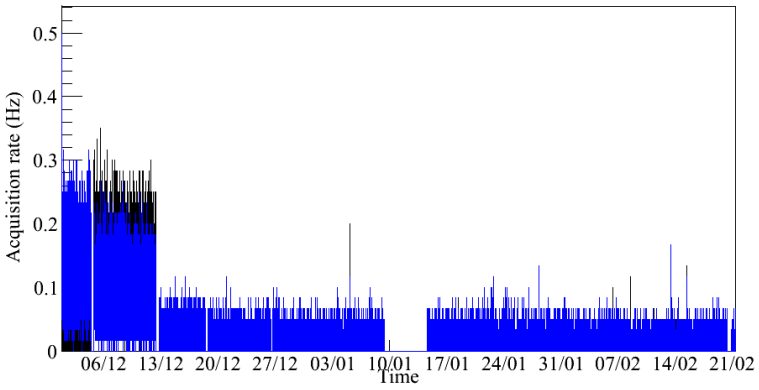

(b)

Figure 6.8: *ANAIS-25 background trigger rate for detector 0 (black) and 1 (blue). The 18/12/12 the anti-Rn system was placed and the ANAIS hut was closed (reducing the light coming into the hut). The 12/12/12 the HV power supply of detector 1 was changed to avoid the cross-talk problem. The 14/01/13 the shielding was opened. In (a) all events are shown and in (b) only those with more than 3 peaks in each PMT signal.*

In the low energy region $E < 80\,\text{keV}$, no meaningful differences are observed between the two modules background. However, they should be compared after the events filtering, see section 6.3.1. In the energy range above 500 keV, higher background is observed in detector 0 with respect to detector 1, attributable to the contribution of the VLB PMTs.

Total background contribution in both ANAIS-25 modules is lower than in ANAIS-0, as it will be shown in the next sections. Moreover, some cosmogenic isotopes contribution are still present in the shown data. However, the background in the low energy of ANAIS-25 is not better than that of ANAIS-0, and although more time is required before the cosmogenic contributions fade away, it does not seem to be possible to reach a background level below 2 cpd/keV/kg.

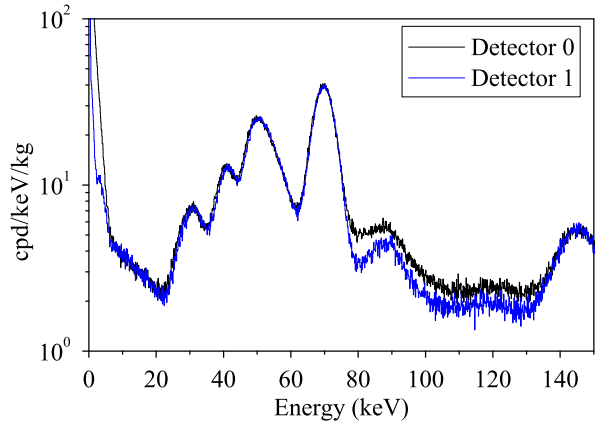

Figure 6.9: *Comparison of the low energy spectra for the two ANAIS-25 modules. Only raw data corresponding to 49.8 days of live time are shown.*

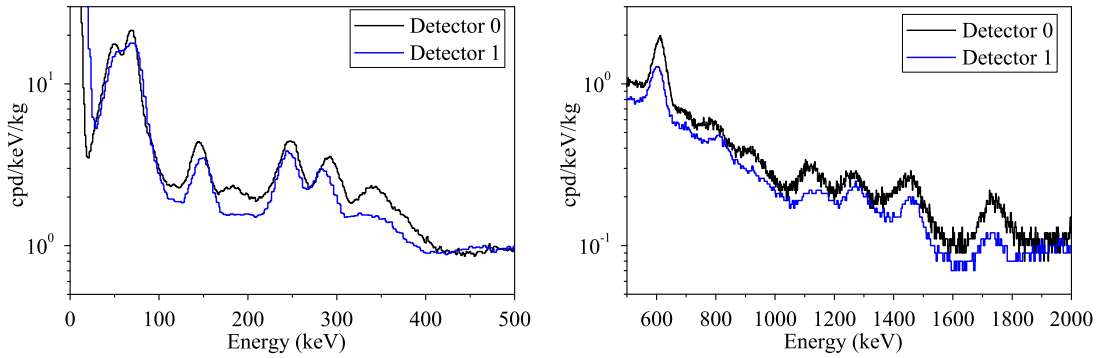

Figure 6.10: *Comparison of the high energy spectra for the two ANAIS-25 modules in the regions from 0 to 500 keV (a) and from 500 to 2000 keV (b). Raw data corresponding to 49.8 days of live time are shown.*

6.2.1 ^{40}K bulk content

The potassium content of the ANAIS-25 modules has been carefully analyzed using the same technique explained and applied to previous prototypes in section 4.1.2. That previous work and thorough understanding of the technique have been crucial to analyze ANAIS-25 data without time delay and promptly derive, with the required accuracy, the potassium bulk content of both crystals.

The first step is to select the ^{40}K gamma events at 1461 keV in one detector: different windows widths ($1\,\sigma$, $2\,\sigma$ and $3\,\sigma$) have been considered to select the coincident events in the other detector. High energy spectra of both detectors are shown in Figure 6.11 (left) and a zoom around the 1461 keV line (right). The bad resolution observed is a consequence of the instabilities in PMTs gain, specially in detector 1 where only data from PMT 1 have

been considered. The low energy spectra in coincidence with the $1\,\sigma$ window around the 1461 keV line in the other detector, are shown in Figure 6.12.

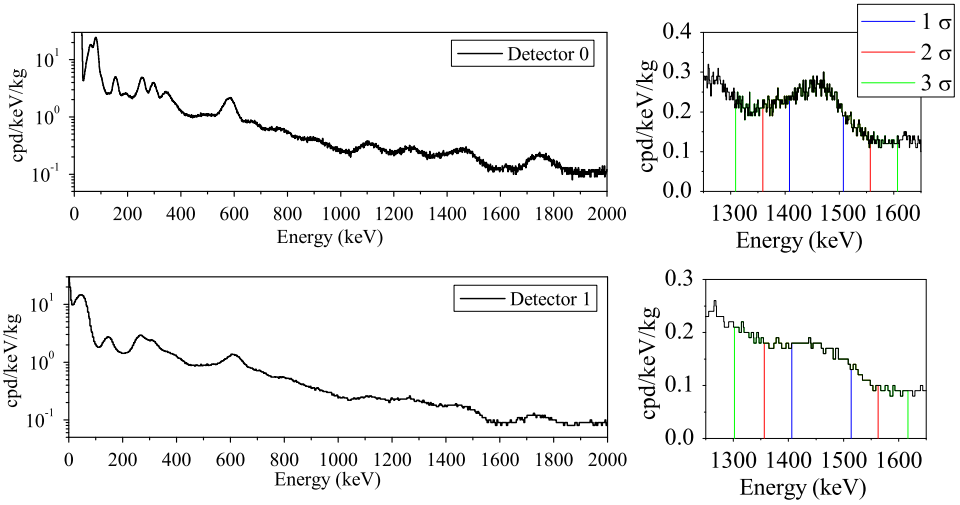

Figure 6.11: *High energy spectra of the ANAIS-25 modules corresponding to 70.4 days (left), and zoom showing the 1461 keV gamma line in the right. The $1\,\sigma$ (red), $2\,\sigma$ (blue) and $3\,\sigma$ (green) coincidence windows are also shown.*

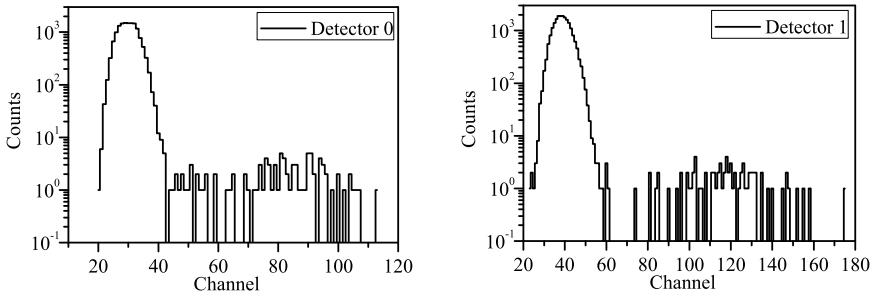

Figure 6.12: *Low energy spectra in coincidence with $1\,\sigma$ windows around the 1461 keV line (shown in Figure 6.11) in the other crystal for detector 0 (left) and 1 (right).*

Only a small fraction of the events selected by the coincidence are attributable to ^{40}K decay, and are distributed in a peak around 3.2 keV, the rest are mostly baseline noise and a few fortuitous coincidences. A simple selection of ^{40}K events is done, considering those above a threshold. The choice of such a threshold is done just by visual inspection and the thresholds used are channel 60 for the detector 0 and channel 70 for the detector 1.

In order to check the ^{40}K origin of the low energy events selected by the coincidence, the effect of changing the high energy window above and below the 1461 keV position has been studied. For this purpose, the coincidence is done with $1\,\sigma$ windows centered in channels $2\,\sigma$ above and below 1461 keV. Also another window more energetic is selected,

centered $11\,\sigma$ above the 1461 keV position (see results in Figure 6.13). Assuming gaussian shape for the 1461 keV line, the corresponding percentage of real ^{40}K events selected should be 68% for $\mu \pm \sigma$, 16% for $\mu + 2\sigma \pm \sigma$, 16% for $\mu - 2\sigma \pm \sigma$, and 0 for the $\mu + 11\sigma \pm \sigma$. The highest window should only present fortuitous coincidences and allow us to estimate their contribution in the other windows. Number of counts over these threshold for every coincidence window are shown in Table 6.3. On view of the results, compatible between both detectors as expected, it seems that events selection has been done correctly in spite of the instabilities.

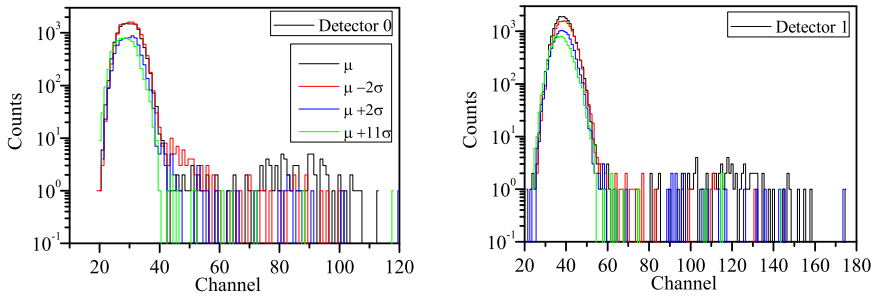

Figure 6.13: *Low energy spectra in coincidence with* $1\,\sigma$ *width windows around 1461 keV, 1461 keV-*$2\,\sigma$*, 1461 keV+*$2\,\sigma$ *and 1461 keV+*$11\,\sigma$ *in the other crystal for detector 0 (a) and 1 (b).*

Detector	μ	$\mu - 2\,\sigma$	$\mu + 2\,\sigma$	$\mu + 11\,\sigma$
0	82	25	16	7
1	78	22	21	10

Table 6.3: *Events above the analysis threshold (channel 60 for detector 0 and channel 70 for detector 1), among those selected by the coincidence with an event in a window centered at, below, or above the 1461 keV gamma position (*$1\,\sigma$ *width).*

The ANAIS-25 setup has been simulated with Geant4, in order to evaluate the probability that, after a ^{40}K disintegration in one crystal, the 1461 keV photon escapes and releases the full energy in the other detector. The corresponding efficiency for the coincidences between both ANAIS-25 modules is $1.08 \cdot 10^{-3}$, just a bit lower than that obtained for ANAIS-0 and PIII because of the higher mass, that decreases the probability for the escape of the gamma without losing any energy.

The activities of ^{40}K for each ANAIS-25 crystal have been estimated for the different width coincidence windows, see equation 4.1. The area of the 3.2 keV peak is obtained by fitting to a gaussian the events above the threshold. The fits are shown in Figure 6.14. The ^{40}K activity is calculated for each detector using three different coincidence window

widths (1σ, 2σ and 3σ) around 1461 keV energy. Results for each detector are shown in Table 6.4.

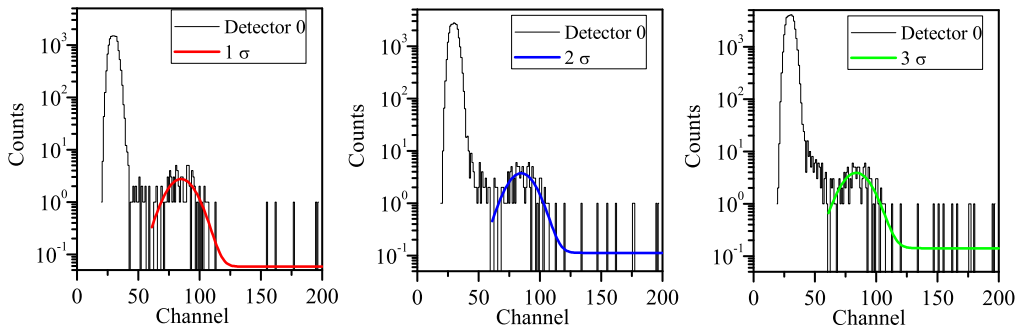

(a)

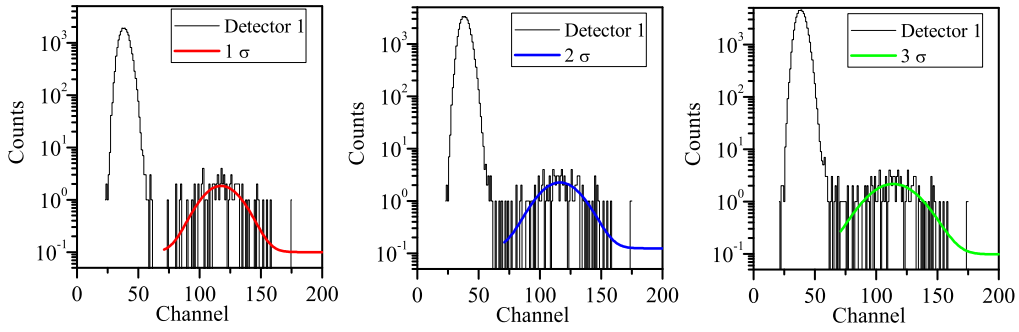

(b)

Figure 6.14: *Low energy spectra in coincidence with $1\,\sigma$, $2\,\sigma$, and $3\,\sigma$ windows around 1461 keV line in the other crystal for ANAIS-25 detector 0 and 1.*

Detector	^{40}K Activity (mBq/kg)		
	$1\,\sigma$	$2\,\sigma$	$3\,\sigma$
0	1.34 ± 0.13	1.16 ± 0.11	1.31 ± 0.11
1	1.15 ± 0.18	1.08 ± 0.16	1.21 ± 0.20

Table 6.4: *^{40}K Activity calculated for the two ANAIS-25 crystals using different widths coincidence windows.*

Good agreement between results derived for both detectors is observed, as expected. Results of the $2\,\sigma$ window width seem to be underestimated. Averaging the $1\,\sigma$ window results for the two crystals, we can conclude that ANAIS-25 crystals have a ^{40}K content $\sim 1.25 \pm 0.11$ mBq/kg (37.4 ± 3.3 ppb of potassium) much lower potassium content than ANAIS-0 crystal, see Figure 6.15. However, the 20 ppb goal has not been achieved and before ordering the additional 18 modules required to complete the ANAIS total detection mass, careful analysis of the situation in collaboration with Alpha Spectra is required.

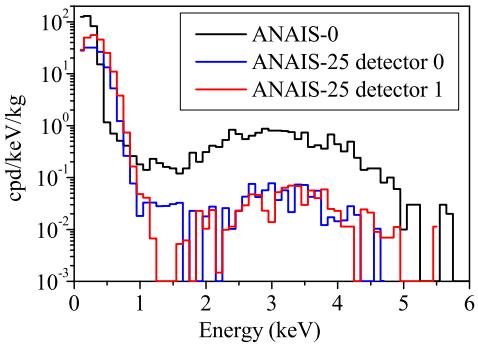

Figure 6.15: *Low energy spectra in coincidence with* $1\,\sigma$ *windows around 1461 keV line in the other crystal for ANAIS-0 (black), ANAIS-25 detector 0 (blue), and ANAIS-25 detector 1 (red).*

6.2.2 ^{238}U and ^{232}Th chains isotopes content

Activities of the different branches in the ^{238}U and ^{232}Th chains have been studied after identifying their alpha emissions. In this case a special digitization line, with independent readout, was implemented for the high energy events, in parallel to the standard electronic chain and acquisition system. Detector 0 PMT signals saturated both in the alpha energy region and only analysis of the detector 1 has been possible. In Figure 6.16 pulse area versus pulse amplitude of the high energy events in ANAIS-25 detector 1 is shown. The events identified as produced by alpha interactions in the crystal are marked in red.

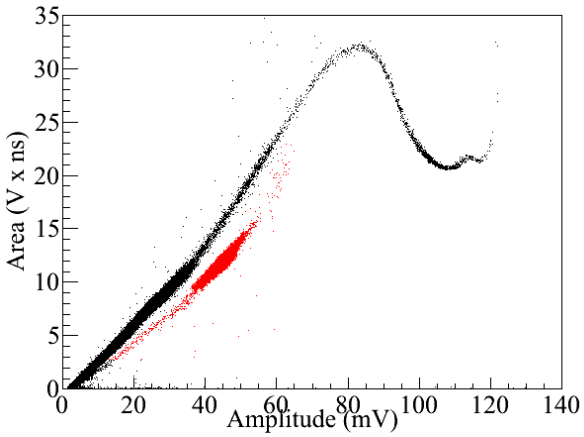

Figure 6.16: *Pulse area as a function of the pulse amplitude. Alpha events (faster) are shown in red and those corresponding to beta/gamma and muons in black. Pulses with amplitude over 80 mV correspond to PMT saturated signals.*

The calibration of the alpha spectrum obtained has been attempted by following the same procedure as was done with ANAIS-0 data. First, ^{220}Rn and ^{216}Po alpha lines (from

the ^{232}Th chain) have been searched for and identified in the following sequence of fast alpha decays:

$$^{220}Rn \xrightarrow{55.6s} {}^{216}Po \xrightarrow{0.145s} {}^{212}Pb \tag{6.1}$$

Looking at the time interval between one alpha event and the following (Δ_{post}) or previous (Δ_{pre}) alpha event, ^{220}Rn (if $\Delta_{pre} < 55\,\mathrm{s}$ and $\Delta_{post} < 0.15\,\mathrm{s}$) and ^{216}Po (if $\Delta_{pre} < 0.15\,\mathrm{s}$) lines are identified in the alpha spectrum (see Figure 6.17). Few statistics is available and a calibration from these lines can not be carried out for the moment.

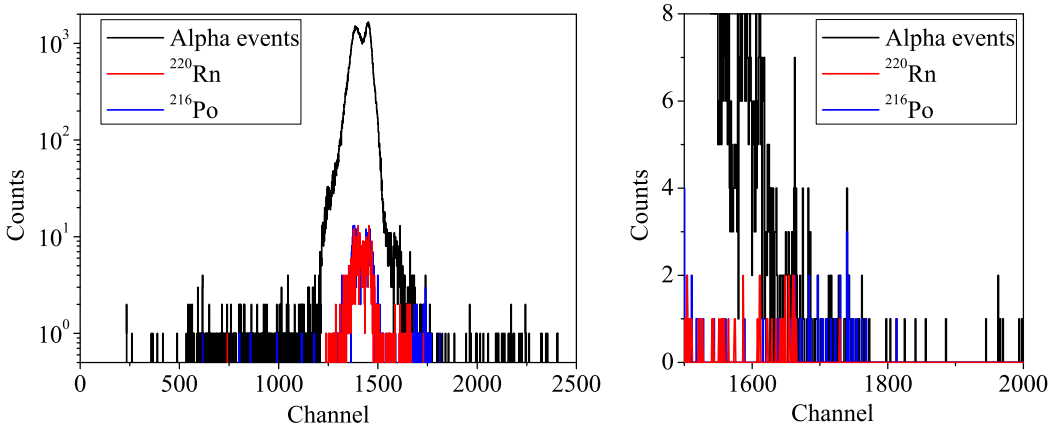

Figure 6.17: *(a) Total alpha spectrum from ANAIS-25 Detector 1 in black. The events selected as coming from the decays of ^{220}Rn and ^{216}Po are shown in red and blue, respectively (most of them are chance coincidences). (b) Zoom of (a) in the region where the ^{220}Rn (6.29 MeV) and ^{216}Po (6.78 MeV) seem to be identified.*

On view of Figure 6.17, the ^{232}Th natural chain seems to be really suppressed in ANAIS-25 crystals. This is confirmed also by the few $^{212}Bi - Po$ events that can be seen, in comparison to those found in ANAIS-0 data, for instance. Although the acquisition dead time per event ($\approx 2\,\mathrm{ms}$, see section 2.5) complicates the observation of those isotopes having lifetimes below a few ms, in the case of ^{212}Bi and ^{212}Po, both events fall in the digitization window and can be identified by the difference in the positions of the pulse minimum and the pulse onset, as it was done in ANAIS-0, see Figure 4.12.

However, the total alpha rate measured is $272\,\alpha$/kg/day (3.15 mBq/kg), much higher than that of ANAIS-0, and as far as we have shown the ^{232}Th chain is suppressed, we have to attribute such a rate to isotopes from the ^{238}U chain, probably one or more of its branches out of equilibrium, because we do not see the expected alpha lines structure. With the tentative calibration derived from ^{220}Rn and ^{216}Po lines, most of the alpha

contributions to the measured spectrum are below 6 MeV. The lower part of the ^{238}U chain is found out of equilibrium because of possible contaminations of ^{222}Rn during the growing or machining of the detectors. After a few weeks, only ^{210}Pb would remain. We will show later the presence of ^{210}Pb events in the low energy range, confirming the assumption that most of the alpha events observed could be coming from this branch of ^{238}U chain. More statistics is required in order to properly calibrate the alpha spectrum and to determine the precise contribution from each component. In the meantime, AS has been asked to revise the growing procedure trying to understand the possible origin of the contamination.

6.2.3 Cosmogenic activation

ANAIS-25 modules started to take data very soon after their arrival to Spain and delivery at LSC (27/11/12). This allowed to observe short-life isotopes activated during the stay on surface of all detectors components, mainly the NaI crystals. Despite the transportation was done by surface to avoid higher activation rates associated to air travel, cosmogenic activation has been observed much better in ANAIS-25 than in previous prototypes. Besides the prompt data taking starting at LSC, low radioactivity level of the modules and very good resolution have contributed significantly to that issue.

Figures 6.18 and 6.19 show the spectra in the high and low energy regions corresponding to the the first week of measurements and those obtained 75 days after. Several lines are clearly attributable to cosmogenic activation in the subtracted spectra of both modules (see Figures 6.9.b and 6.9.d). Main isotopes identified are shown in Table 6.5. The presence of the ^{121}Te isotope has been checked by looking at the coincidences in the other detector, see Figure 6.20: gamma lines in coincidence with Sb K-shell and L-shell binding energies (31.8 keV and 4.7 keV, respectively) emitted following EC are clearly identified.

6.2.4 Background model

The same simulation code developed for ANAIS-0 (see section 4.2) has been extended to the ANAIS-25 set-up by changing the geometry. For the moment, only NaI bulk crystal contaminations have been simulated. In Figure 6.21 the contribution to the background of 1.25 mBq/kg of ^{40}K and 3.15 mBq/kg of ^{210}Pb (corresponding to the total alpha rate) in the crystal are shown together with the low energy background spectra of ANAIS-25.

Background in the R.O.I. (2-6 keV) is over the 2 cpd/keV/kg required. Specially, bulk ^{40}K and ^{210}Pb are contributing to this region. Potassium content of these crystals is much

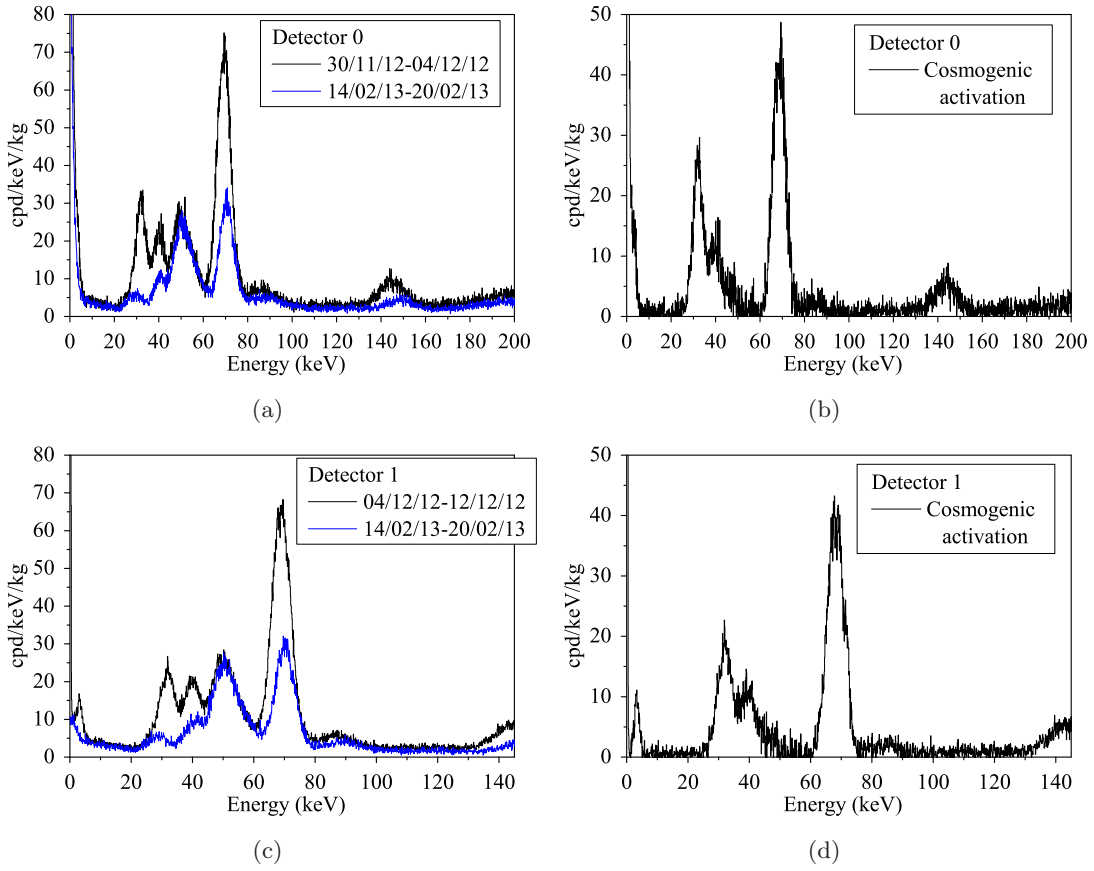

Figure 6.18: *(a) Low energy spectra corresponding to the first week of data underground (LT = 3.5 days) taken with detector 0 (black) and to a week (LT = 7.4 days) 75 days after (blue). (b) Subtraction of the two spectra shown in (a). Corresponding data for for detector 1 are shown in (c) (LT = 3.4 days), and (d). Only raw data are shown.*

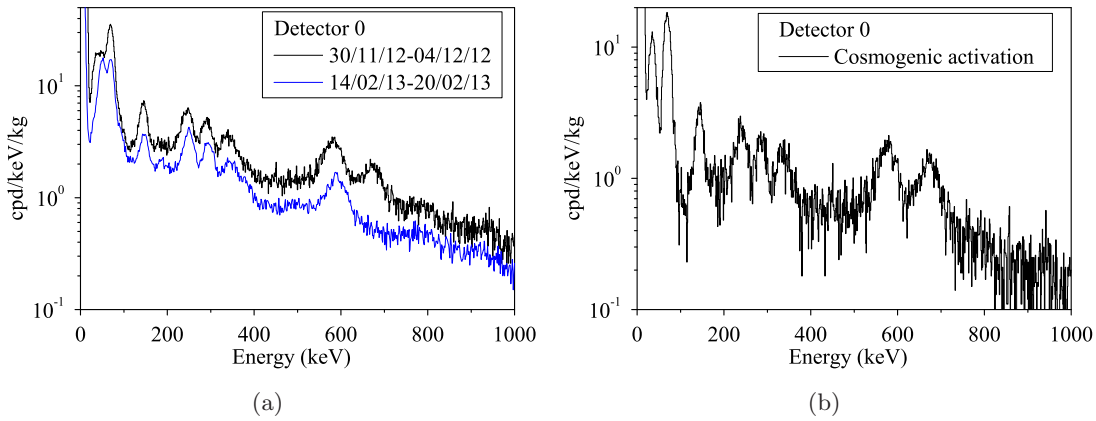

Figure 6.19: *(a) High energy spectra corresponding to the first week of measurement underground with detector 0 and to a week 75 days after. (b) Subtraction of the two spectra shown in (a).*

Isotope	Lifetime	Decay	Main γ emissions
	days		keV
^{126}I	13.11	EC, β^-	666.0
^{125}I	59.4	EC	35.5
^{121m}Te	154	IT, EC	294.0
^{121}Te	16.8	EC	507.6, 573.1
^{125m}Te	57.4	IT	144.8
^{127m}Te	109	IT,β^-	88.3

Table 6.5: *Main cosmogenic isotopes identified in the first weeks of data with the ANAIS-25 modules underground. The lifetime, decay, and main emission are shown. Data obtained from [127, 165].*

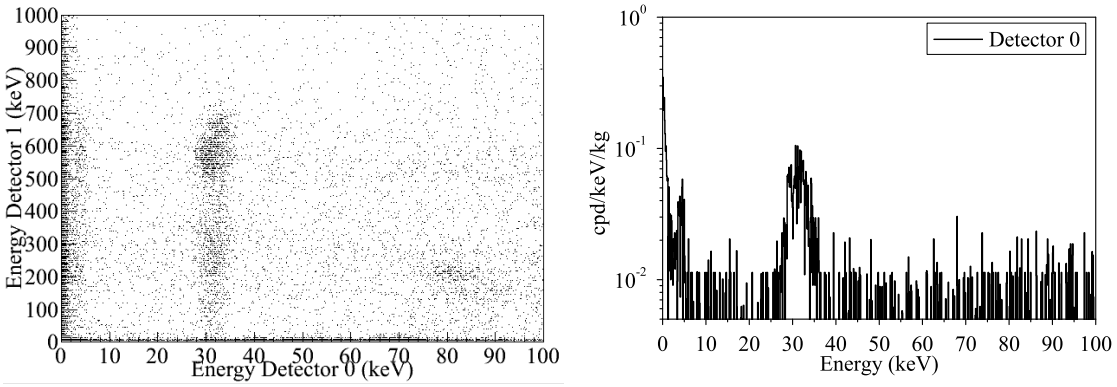

(a) (b)

Figure 6.20: *High energy events in detector 1 versus low energy events in detector 0 (a). Low energy spectrum of detector 0 in coincidence with* $1\,\sigma$ *window around the 573 keV line in detector 1 (b).*

lower than the old ones, but still an improvement in the crystal radiopurity is required for the final ANAIS crystals, in particular ^{210}Pb contamination at the observed level is the most limiting factor to reach the ANAIS background goal.

6.3 ANAIS-25 data analysis

6.3.1 Scintillation events selection

Rejection of non bulk NaI scintillation events is required to reduce the effective threshold, because event rate below 10 keV is dominated by non bulk NaI scintillation events, specially in detector 0. The events selection protocol for ANAIS-25 data is not completed yet, but a preliminary filtering procedure has been applied, following that developed for ANAIS-0

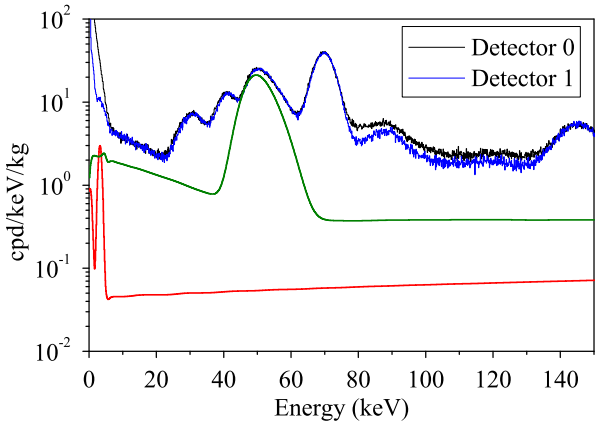

Figure 6.21: *Total background spectra of detector 0 (black) and 1 (blue), only raw data are shown. Simulated contamination of 1.25 mBq/kg of ^{40}K (red) and 3.15 mBq/kg of ^{210}Pb (green) are also shown.*

(section 3.1). Events with anomalous baseline estimate have been rejected by applying the same cut developed for ANAIS-0 events and explained in section 3.1. As in ANAIS-25 set-up two modules are taking data, an anticoincidence cut has been also implemented: events where the other detector made trigger can be discarded: they correspond to real scintillation events but they are not attributable to dark matter. At last, the cut on the peaks number of the event has been used. For the detector 1 the same criterion as in ANAIS-0 (see section 3.1) has been followed and events having less than 3 peaks in any of the PMT signals have been discarded. As detector 0 presents a higher dark current rate, events having less than 5 peaks in any of the PMTs are rejected. In both detectors this cut implies an effective analysis threshold below 1 keV, because of the excellent light collection efficiency of the ANAIS-25 modules (see section 6.4 for the estimate of the corresponding light collection efficiencies). In Figure 6.22 the filtered spectra of both ANAIS-25 modules are shown.

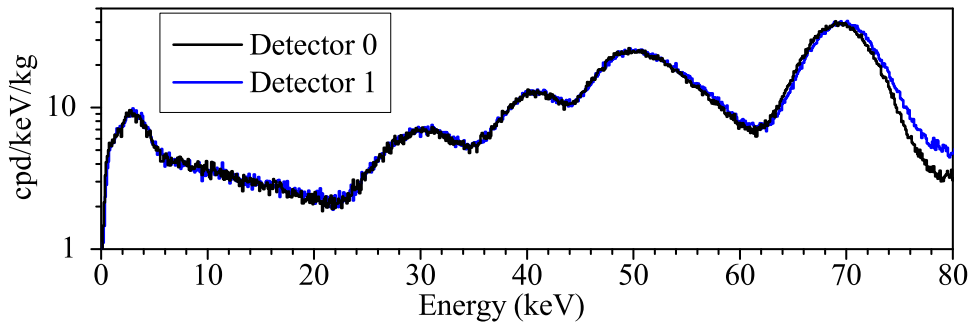

Figure 6.22: *Low energy spectra of ANAIS-25 after having applied all the cuts described in text.*

As shown in Figure 6.8, detector 0 presents an anomalous high trigger rate. However, these data have not been discarded because few data are still available and moreover, these anomalous events seem to be effectively removed by the cuts. Active vetoes have not been working during the first operation period of the ANAIS-25 set-up, and events coincident with a a plastic veto signal can not be rejected. Moreover, PMT signals saturate and muons (very high energy events) cannot be tagged and the anomalous high rate caused by them cannot be discounted. Cut on events faster than typical NaI(Tl) bulk scintillation has neither yet been applied. However, this cut seems to be less important than in ANAIS-0 data, because ANAIS-25 modules do not present such a high rate of anomalous events in the P1s distribution as observed in ANAIS-0 (see Figure 6.23). These cuts are going to be optimized soon, specially the P1s cut.

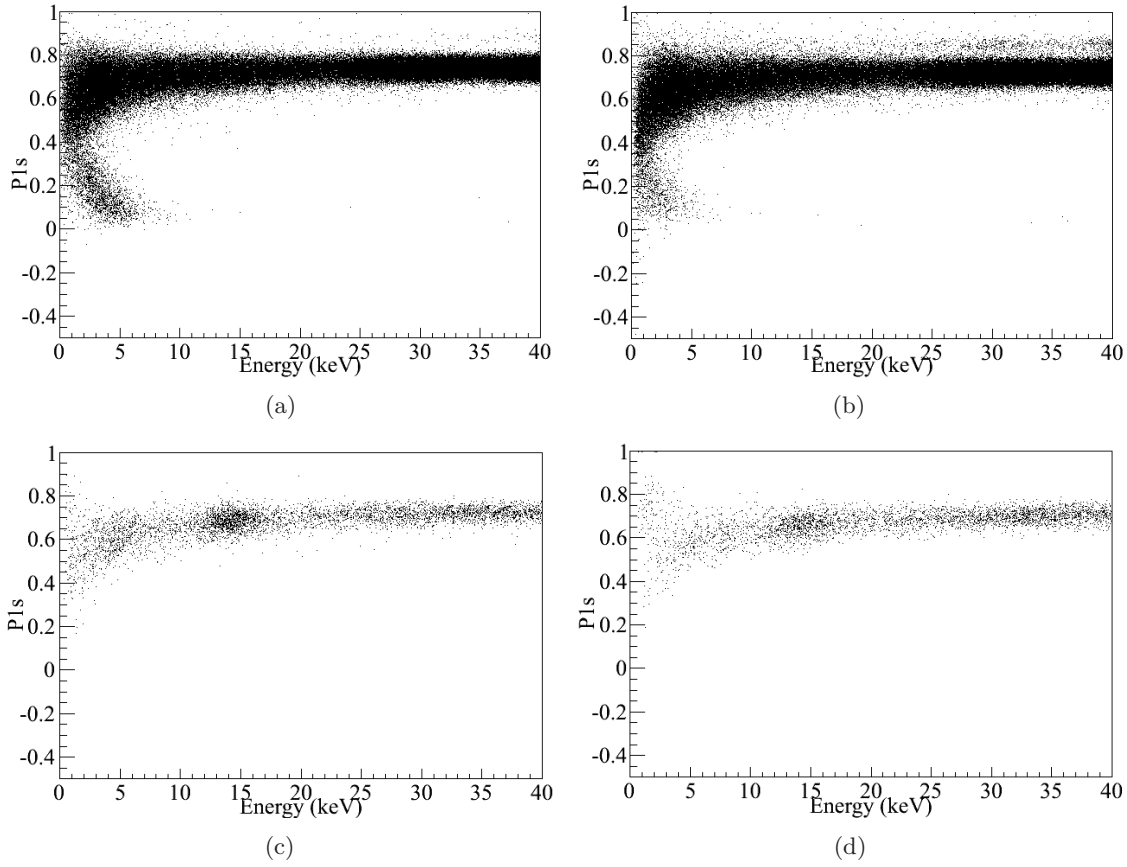

Figure 6.23: *P1s parameter as a function of the energy for background data of ANAIS-25 detector 0 (a) and 1 (b) and for a ^{57}Co calibration for detector 0 (c) and 1 (d) after the cuts described in the text.*

After the explained (and limited) filtering procedure applied, both detectors present the same background, and if this is confirmed, VLB PMTs would not be contributing in the low energy region and hence, light guides could be avoided. However, the background is still higher than expected.

6.3.2 Asymmetry

Asymmetric events have been also observed in background data from ANAIS-25 by looking at the different sharing of light between the two PMT channels but the spread is smaller than in ANAIS-0 module, see Figure 3.17.

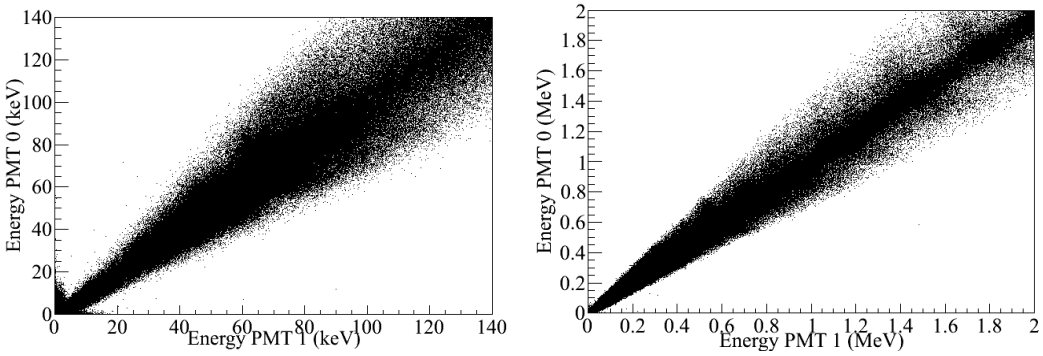

Figure 6.24: *Energy sharing between the two PMT signals at low (a) and high (b) energy in background data taken with the ANAIS-25 detector 0. Similar data are observed with detector 1.*

From the comparison of asymmetric events from ANAIS-25, PIII and ANAIS-0 modules, we can conclude that is related with the shape of the crystal: parallelepipedic crystal shows higher asymmetry than hexagonal prism and cylindrical crystals. It is foreseen to carry out calibrations of ANAIS-25 modules placing the source in different positions along the crystal axis to determine more precisely this dependence on the light collection asymmetry with the interaction position as done in section 3.3 with the previous prototypes.

6.3.3 Trigger efficiency

The efficiency of the triggering at photoelectron level has been also studied for the ANAIS-25 setup data by using the same methods developed for ANAIS-0 module. The distribution of the S.E.R. amplitude is compared to the amplitude of the first peak (at the trigger position), and the 3.2 keV events population, selected by the coincidence, has been profited to confirm the so derived efficiencies.

Figure 6.25 shows the amplitude distribution of photoelectrons derived from the last peak of pulses having a low number of peaks and that corresponding to the first peak (responsible of the trigger) for pulses having only one peak per PMT. The spectra have been conveniently scaled. The photoelectron amplitude spectra have been gaussian fitted: mean values and standard deviations are shown in Table 6.6. From the first peak amplitude distribution an effective threshold (an amplitude that effectively triggers) can be deduced

and is also shown in Table 6.6. Comparing this threshold with the mean value and standard deviation of the S.E.R. amplitude distribution gaussian fit, the number of sigmas above the mean is calculated and, hence, the percent of the S.E.R. distribution effectively triggering. Trigger efficiency could be improved by lowering the CFD threshold or increasing the HV of the PMTs, but this would imply probably more non-linear effects in the high energy region, and a compromise has to be taken. Detector 1 presents a worse trigger efficiency than detector 0 and this could be causing the higher acquisition rate of detector 0, see Figure 6.8.

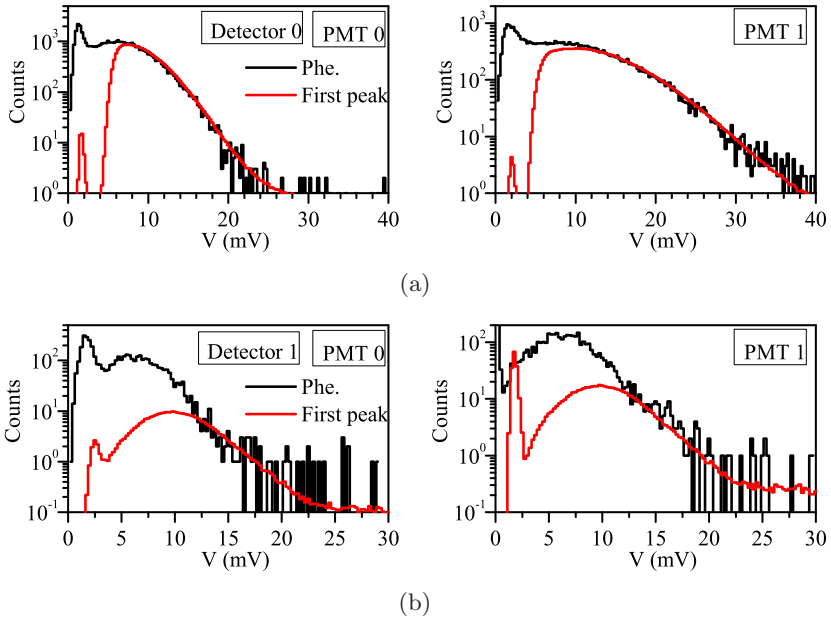

Figure 6.25: *Photoelectron and first peak amplitude distribution for the two ANAIS-25 detectors, conveniently scaled.*

Detector	Signal	S.E.R. Mean	S.E.R. σ	Trigger level		Over T.L.
		mV	mV	mV	$n \cdot \sigma$	% of S.E.R.
0	PMT 0	6.03 ± 0.04	3.92 ± 0.04	8	0.50 ± 0.01	30.8
	PMT 1	7.77 ± 0.15	13.76 ± 0.27	10	0.16 ± 0.01	43.6
1	PMT 0	6.07 ± 0.03	5.31 ± 0.06	12	1.12 ± 0.01	13.24
	PMT 1	6.30 ± 0.02	5.52 ± 0.05	12	1.03 ± 0.01	15.09

Table 6.6: *Photoelectron amplitude mean value, standard deviation, trigger level and percent of the photoelectron distribution that triggers (fraction of the S.E.R. above trigger level). Data are shown for the four PMTs used in the ANAIS-25 detectors.*

The trigger efficiency has also been estimated with the selected population of 3.2 keV events after ^{40}K decay, as it was done in section 3.5. The Pattern Unit module saves

the trigger configuration of the event in the variable T and the effective threshold of the acquisition is checked with this variable (see Table 3.6 for the possible values of T). In Figure 6.26 spectra of the detectors 0 and 1 in coincidence with the 1461 keV line in the other detector are shown. ^{40}K events should make trigger in both detectors, if a 2 keVee threshold has been achieved. A good trigger efficiency is observed in the coincidence events: 99% of the events avobe 1.5 keV are triggering in detector 1, and 97% in detector 0. It is worht noting that chance coincidences in detector 0 arrive up to higher energies, and that in detector 1 baseline could be triggering.

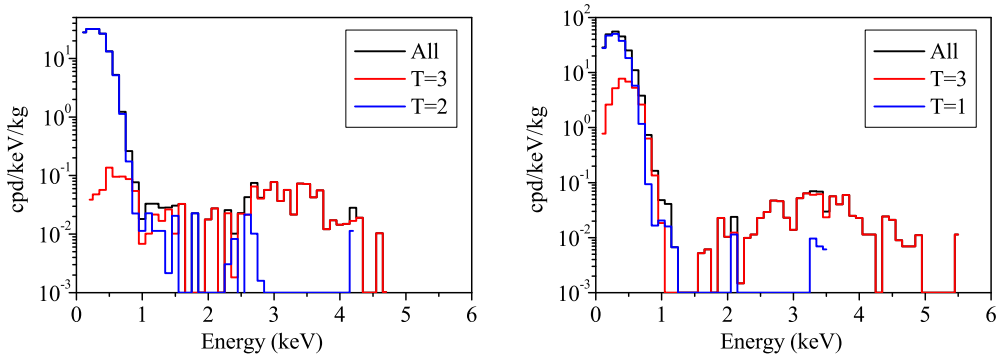

Figure 6.26: ^{40}K *events at low energy, identified by the coincidence with a high energy gamma, considering T variable for the ANAIS-25 detector 0 (a), and detector 1 (b). Events with T=2 (T=1) have not triggered in detector 0 (1), whereas events with T=3, have triggered in both detectors.*

6.3.4 Long scintillation constants in NaI(Tl)

The long scintillation constants observed in ANAIS-0 and PIII crystals, see section 3.6, have been also observed in data from ANAIS-25 detector 0, and are being presently measured for detector 1. The special branch in the electronic chain designed for data acquisition in the very long timeline basis has been also implemented, see Figure 3.30 and Table 3.7.

Following the same procedure, alpha events are separated from beta/gamma/muon events by a discrimination based on the different relationship between pulse height and area of the fast pulse. Events with the same area for the fast pulse have been selected: this region corresponds from 2.5 to 3 MeVee (from 4.2 to 5 MeV for the alphas). Photoelectrons have been identified individually by the peak search algorithm at a given position of the pulse, and an histogram has been produced with the corresponding temporal distribution, separately, for all the alpha and beta/gamma/muons events in the region. The

corresponding pulses, normalized to the same area of the fast pulse, can be seen in Figure 6.27.a.

In order to derive the long decay time constants, a fitting to two exponential decays using the range from 4 to 320 ms after the onset of the pulse has been done, see Table 6.7 and Figure 6.28. On view that in both cases the scintillation constants seem to be the same, and a combined analysis has also been attempted. The most relevant difference between both pulses in this long timescale is the total number of photoelectrons in these slow components: gamma or muon events excite much more efficiently the long-lived states contributing to this very slow light emission. The distributions of the total number of photoelectrons for events of the alpha and gamma/muon populations are shown in Figure 6.27.b. There is more than a factor of two different average values (0.0029 ± 0.005 for alpha particles vs. 0.064 ± 0.029 for gammas/muons). By cause of the scope sampling and peak search algorithm required for building the photoelectron distribution, we can not rely on the absolute number of photoelectrons assigned to a given energy depositions. However, relative values between the both analyzed populations should be trustworthy.

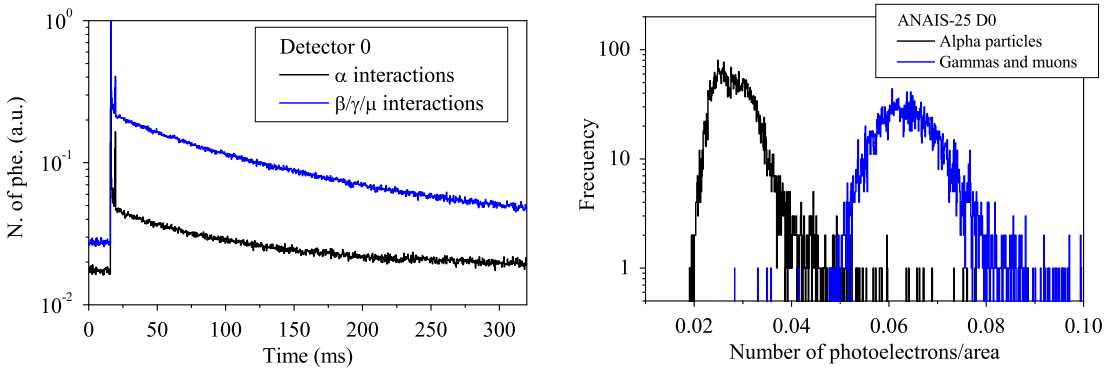

(a) (b)

Figure 6.27: *(a) Pulses from alpha particle events (black) vs. those produced by gammas and muons (blue) in a 320 ms temporal scale, registered with the ANAIS-25 detector 0. Events from both populations correspond to the same pulse area, dominated by the fast scintillation components. (b) Distribution of the number of photoelectrons per area unit identified in the longest timescale for alpha particles (black) and gammas/muons (blue) interacting in the detector 0.*

The decay time of the scintillation does not match with the ANAIS-0 and PIII results, however it confirms that very slow scintillation components are present in NaI(Tl) crystals, and that probably they have non-intrinsic origin, because different crystals produce different time constants. Moreover, this slow scintillation seems to be related to the activation of the crystals exposure to high energy and high intensity gamma sources (section

	Detector 0			
	Independent fit		Dependent fit	
	α	$\beta/\gamma/\mu$	α	$\beta/\gamma/\mu$
τ_1 (ms)	54.05 ± 3.8	52.5 ± 2.44	52.6 ± 1.7	
τ_2 (ms)	174.44 ± 17.5	171.5 ± 4.2	171.6 ± 3.0	
A_1/A_2	1.74	0.66	1.6	0.66

Table 6.7: *Results of the fit between 4 and 320 ms after the pulse onset for ANAIS-25 detector 0.*

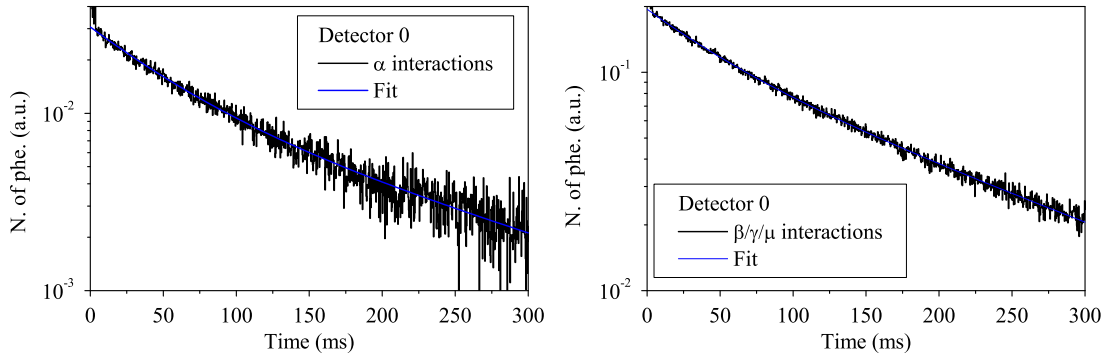

(a) (b)

Figure 6.28: *Pulses corresponding to the interaction of alpha particles (a), and gammas and muons (b), in a 320 ms window, registered with the Tektronix 207 for the ANAIS-25 detector 0 are shown in black. The fit of the data shown in Table 6.7 are shown in blue. Events from both populations correspond to the same pulse area, dominated by the fast scintillation components.*

6.1.4). Further research in this line is in progress, and results derived from the analysis of detector 1 data could help.

6.4 Light collection efficiency

The light collection of both ANAIS-25 modules has been studied similarly as what was done with the ANAIS-0 module in the different setups (see section 5.2). First, the S.E.R. is analyzed for the four PMTs, then the light collection efficiency can be obtained. Finally, energy resolution of the ANAIS-25 module has been studied.

Single photoelectron response has been obtained by identifying the last peak in the pulse with the same criteria explained in section 5.2.3. The area distribution of the S.E.R.

for the four PMTs used in the ANAIS-25 modules are shown in Figure 6.29. They are fitted to gaussians and the results of the fits are shown in Table 6.8.

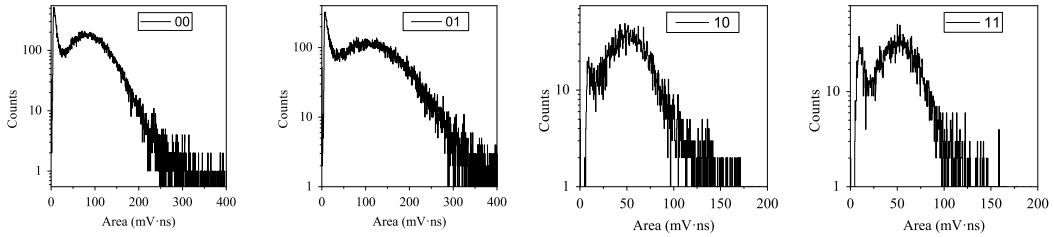

(a) (b) (c) (d)

Figure 6.29: *Single electron response for the PMT signals corresponding to both ANAIS-25 modules: Detector 0 VLB PMT 0 and PMT 1 (a, b), Detector 1 ULB PMT 0 and PMT 1 (c, d).*

Detector	PMT model	Photoelectron area			
		PMT 0		PMT 1	
		Mean	σ	Mean	σ
		mV·ns			
0	VLB	82.2 ± 0.4	47.1 ± 0.3	98.8 ± 7.8	74.8 ± 0.6
1	ULB	51.6 ± 0.7	24.2 ± 0.9	48.3 ± 0.7	20.2 ± 0.8

Table 6.8: *Parameters from the fit to a gaussian of the S.E.R. area distribution for the four PMTs used in ANAIS-25 setup.*

To study the light collection efficiency of the ANAIS-25 modules, the number of photoelectrons per keV has been estimated from the S.E.R. area distribution and the area of the 22.6 keV line from ^{109}Cd calibration spectra, see Table 6.9. The 22.6 keV line area is divided by the mean photoelectron area (shown in Table 6.8) and the nominal energy of the line used (22.6 keV). Results for the two detectors are shown in Table 6.10.

Detector	PMT model	22.6 keV line area			
		PMT 0		PMT 1	
		Mean	σ	Mean	σ
		mV·ns			
0	VLB	14432 ± 3	1621 ± 2	18656 ± 4	2149 ± 3
1	ULB	6790 ± 2	844 ± 2	7378 ± 2	870 ± 2

Table 6.9: *Area of the 22.6 keV line coming from the ^{109}Cd calibration source.*

The obtained light collection efficiencies are consistent with the better QE of VLB PMTs, used in detector 0 from ANAIS-25 setup, already stated with ANAIS-0 data (see

Detector	PMT model	Photoelectrons/keV		
		PMT 0	PMT 1	PMT0+PMT1
0	VLB	7.77 ± 0.04	8.36 ± 0.66	16.13 ± 0.66
1	ULB	5.82 ± 0.08	6.76 ± 0.10	12.58 ± 0.13

Table 6.10: *Light collection efficiencies (ph.e./keV) for ANAIS-25 setup detectors, derived from the 22.6 keV line (^{109}Cd calibration) data.*

section 5.2.4). However, the light collection efficiencies of the ANAIS-25 modules are much better than those previously obtained with ANAIS-0 and PIII: more than a factor of two has been gained in total light collection efficiency with respect to the ANAIS-0 module with the same PMTs (see Table 5.5). This remarkable improvement is attributed to the much better optical coupling of the new modules and the excellent optical quality of the NaI(Tl) crystal. Pulses at very low energy (4.7 keV) for the two detectors of ANAIS-25 setup are shown in Figure 6.30: the high light collection efficiency can be clearly noticed.

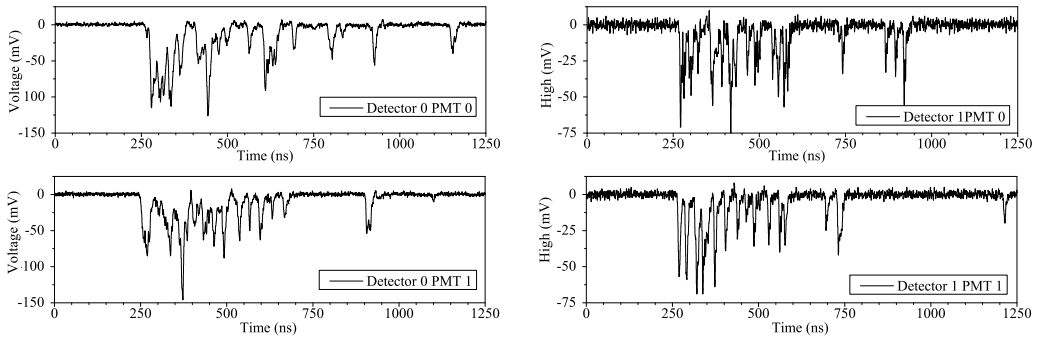

(a) (b)

Figure 6.30: *Pulses at very low energy (4.7 keV) obtained with ANAIS-25 detector 0 (a) and detector 1 (b).*

Results for the FWHM of the ANAIS-25 modules are shown in Figure 6.31, compared to that of the ANAIS-0 module (section 5.2.5). The significant improvement observed in energy resolution for both modules is consistent with the clear improvement in light collection efficiency, previously reported. Resolution results for the available lines below 150 keV can be seen in Table 6.11

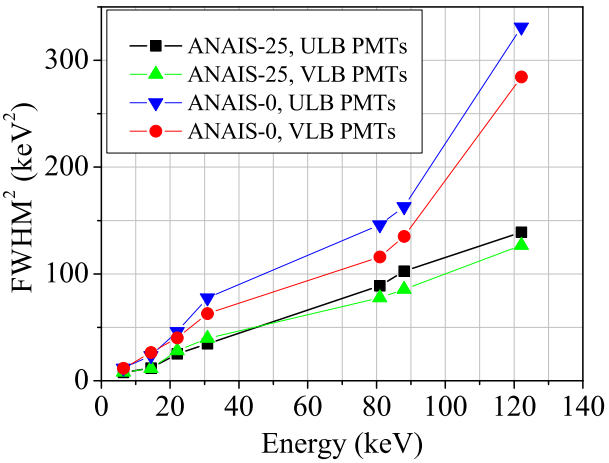

Figure 6.31: *$FWHM^2$ for the different gamma lines measured at LSC in ANAIS-25 modules compared with the ANAIS-0 results when using the same PMTs.*

Energy (keV)	Resolution (%)	
	D0 VLB	D1 ULB
6.4	18.46	18.68
14.4	10.20	10.00
22.1	9.65	10.21
30.9	8.12	8.70
81.0	4.95	4.63
88.0	4.89	4.47
122.1	4.11	3.92

Table 6.11: *Resolution (%) for the different gamma lines measured at LSC with the ANAIS-25 modules.*

Conclusions

The feasibility of carrying out the ANAIS experiment at the Canfranc Underground Laboratory has been studied in this work. The ANAIS experiment will look for dark matter annual modulation with 250 kg of ultrapure NaI(Tl) crystals. The three main experimental requirements are: energy threshold below 2 keV, background at low energy as low as possible, and very stable operation conditions. Most of this feasibility study has been carried out with the ANAIS-0 module, a 9.6 kg NaI(Tl) crystal, placed in the same experimental space and conditions of ANAIS, but it has been extended to the preliminary analysis of the first weeks of data from ANAIS-25 modules. ANAIS-25 consists of two crystals 12.5 kg NaI(Tl) each, that have been built as conclusion of all the previous ANAIS experience in the operation of prototypes.

The ANAIS experiment was conceived to be made with 10 hexagonal NaI(Tl) crystals of 10.7 kg each, made by BICRON (now Saint Gobain). However, the natural potassium content was measured to be too high (from 0.46 to 0.71 ppm) to allow their use in a dark matter experiment. This result involved a significant change in the ANAIS experiment timeline. The search for more radiopure crystals implied the development of new potassium purification techniques, a good knowledge of available analytical techniques to reach sensitivity at ppb level in potassium, and the application of low background technology for the growing and encapsulation:

- Accurate potassium content measurements at a few ppb level in NaI powder were required to guarantee the radiopurity of the samples. HPGe spectrometry was not able to reach that level, even for high mass samples, and analytical techniques as AAS were investigated.
- Commercial samples from different providers were bought to be used as reference samples and cross-checking of the different analytical procedures have been thoroughly carried out. As result, analytical techniques have not been able to trace the

potassium level, even in the ppm range, and only data from the HPGe test bench at LSC have been considered in the decision taking.

- Powder purification procedure proposed and investigated by ESI company was unsuccessful, not reaching potassium contents below 320 ± 8 ppb.

- A powder fulfilling the radiopurity requirements was found and two crystals, 12.5 kg mass each, were grown by Alpha Spectra company from it (ANAIS-25 modules). Encapsulation materials selection and protocols for machining and cleaning the components were proposed by the UZ to the manufacturer. ANAIS-25 modules were delivered to LSC in November 2012.

In the meantime, the ANAIS-0 module was built at the University of Zaragoza, consisting of a 9.6 kg NaI(Tl) crystal made by Saint Gobain, and similar in shape and dimensions to those built for DAMA collaboration. The main conclusions derived from the ANAIS-0 experimental procedure are:

- ANAIS-0 crystal was encapsulated at the UZ using ETP copper, and two synthetic quartz windows to tightly close the detector, preventing humidity from reaching the crystal. This design allowed the direct coupling of different PMT models to these quartz windows and the optional inclusion of light guides.

- An aluminized Mylar window was included in the detector design to allow calibration at very low energy (below 20 keV) with external gamma sources. Radioactive sources have been used to calibrate the ANAIS-0 module, to check the gain stability, and to get reference NaI(Tl) scintillation events for the data analysis, to search for systematic effects in the simulations. Emissions of 6.4 and 14.4 keV from ^{57}Co, 22.6 keV from ^{109}Cd can be used to calibrate the low energy range through this window.

- The ANAIS-0 module has been taking data in the old and new facilities of the LSC, under 2450 m.w.e. The ANAIS-0 experimental layout was moved into the Hall B of the LSC in February 2011, to a hut specially designed for the ANAIS experiment.

- The ANAIS-0 module was operated inside a shielding very similar to the projected for ANAIS: 10 cm of ancient lead, 20 cm of low activity lead, an anti-radon box closing the shielding to prevent the entrance of airborne radon inside the experimental space and three plastic scintillators ($0.5 \times 1 \times 0.05\, m^3$ each) to monitor the muon rate in the laboratory and reject the corresponding background contribution.

- Electronic chain, acquisition software and analysis hardware have been optimized and upgraded along the ANAIS-0 operation. The electronic chain final design is compact and homogeneous, combining VME and NIM modules. MATACQ digitizer has shown excellent performance since installation. All the system is easily scalable to a high modularity experiment, up to 40 (2×20 PMTs) channels.

- Monitoring of experimental and environmental parameters, specially at LSC Hall B, has been done. As most outstanding results we can remark that after 19 months of measurements, mean value of the radon air content in Hall B is $80.9 \pm 0.3\,\mathrm{Bq/m^3}$. A seasonal fluctuation has been identified in the radon and humidity values, being compatible with a yearly period having the maximum around 25^{th} July. Both modulations are clearly correlated, being the amplitude higher for humidity (31%) than for radon content (15.5%). Nevertheless, more data are needed to confirm such a modulation and to identify its origin. As far as the inner volume of the shielding is continuously flushed with radon-free gas, this seasonal radon fluctuation is not expected to contribute to the experiment background. Temperature fluctuations in Hall B are large. LSC thermostat is placed in Hall A, therefore, local temperature variations in Hall B, related for instance to the human presence, can not be corrected. Correlation of ANAIS-0 trigger rate with temperature at the electronics rack has been observed in some periods of ANAIS-0 data taking, disturbing considerably the acquisition. This issue was solved after the upgrading to the new electronics and repair of some faulty modules.

- Energy calibration near threshold has been studied with low energy radioactive sources. Superficial effects have been identified for 6.4 and 5.9 keV lines and some non-linearities have proven to affect the threshold estimate. The population of 3.2 keV coincident events from ^{40}K should not be affected by superficial effects and it has been used for the calibration at low energy, together with 14.4 keV from ^{57}Co and 22.6 keV from ^{109}Cd.

- Muon coincident events have been identified in the ANAIS-0 set-up using the time after the last muon event in the plastic scintillators. An increase in the muon coincident events rate is observed after the moving to the new LSC facilities, as expected, since there is less rock overburden. Results are compatible with available measurements.

ANAIS-0 data have been thoroughly analyzed and direct conclusions derived are the following:

- A protocol to reject the non NaI scintillation events has been designed with the ANAIS-0 data. First, periods of anomalous high rate are discarded, in particular 0.5 s after a high energy event (over 9 MeVee), being the corresponding live time deducted. Events coincident with a plastic veto signal are rejected. Events having anomalous baseline estimate are also rejected, because pulse dependent parameters would not be properly calculated. An algorithm designed to count the number of peaks in the pulse has been implemented, and events with few photoelectrons per PMT can be discarded: a cut has been chosen implying an analysis threshold equivalent to about 1 keV if peaks are associated to ph.e. Events faster than typical NaI(Tl) bulk scintillation were found in ANAIS-0 and a timing parameter able to distinguish them was optimized, P1s, profiting from the full pulse information from both PMT signals. Efficiency for the cut on this parameter has been estimated with events from low energy calibrations. A 2 keVee analysis threshold can be confirmed, although being cuts conservative, a residual contribution from anomalous events in the acceptance region can not be discarded. ANAIS-25 filtering protocol is still under development. However, some of the previous cuts will not be probably required. Preliminary analysis of data, hints at a very good analysis threshold (down to 1 keVee), because of the very high light collection efficiency achieved.

- Neutron calibration data have been analyzed, showing that although nuclear recoil events are faster than beta/gamma events, discrimination on an event by event basis is not possible. However, a correction to the efficiency for the cut on the P1s parameter in the dark matter analysis has been calculated from data in a 5 to 30 keV window. Although this analysis is done with old data from PIII detector, it comes out from an intrinsic property of NaI(Tl) and can be extended to other crystals.

- Asymmetric events on the sharing of the energy between the two PMTs have been studied in ANAIS-0 and ANAIS-25 data. However, they do not seem to be a significant contribution to the low energy background, being easily removed by previous cuts. Origin of these events has been traced back to PMTs and light guides, mostly. The rate of events in coincidence with muons in the plastic vetoes (strongly asymmetric) increases ∼20% when light guides are used (86% from 1 to 100 keV), pointing to muon interactions in the light guides producing scintillation able to trigger ANAIS acquisition and contributing to the low energy background.

- Different low energy estimators have been considered and analyzed in order to determine the one with the best resolution (capacity to reconstruct correctly the energy) and signal-to-noise discrimination (separation between signal and noise distribu-

tions). QDC and area parameters perform quite well in both features and seem to be equivalent.

- Trigger at photoelectron level in ANAIS-0 and ANAIS-25 setups is achieved. The percentage of the photelectron distribution effectively triggering has been determined for every setup. In the case of the VLB PMTs, the fraction of the ph.e. distribution triggering is still low and could improve by lowering the CFD threshold. However, the efficiency of the trigger estimated with the 3.2 keV population following ^{40}K decay selected by the coincidence with the high energy gamma at 1461 keV is almost 100% in most of the setups, pointing at a very high trigger efficiency above 2 keV, even though trigger at photoelectron is only partially achieved in some of those setups.

- NaI(Tl) scintillation constants have been derived for the different interacting particles. Fast NaI(Tl) scintillation constant has been reported to be 219.3 ± 0.5 ns for alpha particles and 287.4 ± 0.5 ns for gamma particles. Also different rise times of the pulses have been clearly observed for both particle interactions. This fast scintillation behavior is compatible with all the bibliography on the subject, being associated to thallium doping. However, long scintillation constants observed in the ms scale with ANAIS-0, PIII and ANAIS-25 crystals have probably a different origin. ANAIS-0 and PIII crystals showed long scintillation constants of about 20 and 80 ms, ANAIS-25 detector 0 showed constants of 52 and 172 ms and detector 1 is being measured at the moment. Moreover, this slow scintillation seems to be related to the anomalous behavior after excitation with high energy and high intensity radioactive sources identified with ANAIS-0 and ANAIS-25 crystals. Long-life excited states seem to be activated in the crystal producing in their decay a large number of photons in a few hours following the irradiation. Very large amplitude effect is observed for ANAIS-0 crystal, and also for ANAIS-25 detector 0. No explanation of differences between detector 0 and 1 behavior has been found.

Light collection efficiency has been studied in the different setups with the aim of determining the best configuration for ANAIS:

- Five models of photomultipliers tubes have been studied in this work in terms of gain, single electron response, light collection, resolution, and its contribution to the background. On view of the results, the VLB PMT model (Hamamatsu R6956 MOD) has been chosen for ANAIS because: it has a high quantum efficiency that provides a very good light collection (7.38 ± 0.07 ph.e./keV with ANAIS-0 and

16.13±0.66 ph.e./keV with ANAIS-25), about a 30% more than the ULB PMT model (Hamamatsu R11065 SEL) in similar experimental conditions; its contribution to the background can be afforded without using light guides.

- Light guides have been tested to minimize the contribution to the background of the PMTs. However, they worsen light collection efficiency about a 30% and they scintillate under high energy depositions, introducing an additional contribution to the low energy events rate and some systematics in the annual modulation analysis, because muons are able to generate such a scintillation and muon flux is known to have an annual modulation.

ANAIS-0 background has been carefully studied to understand the main contributions in the different energy ranges. A good background understanding is required as first step for its reduction:

- The ANAIS-0 ^{40}K bulk content has been determined in this work with the coincidence measurement. It consists in measuring in one detector X-ray/Auger electron emissions of argon amounting a total energy release of 3.2 keV following the K-shell EC of ^{40}K in coincidence with a 1461 keV gamma fully absorbed in another detector sharing the experimental space. From the measured coincidence rates and Geant4 estimated efficiencies, the potassium content of the ANAIS-0 crystal has been deduced to be 460 ppb, and the same analysis has been applied to the new radiopure ANAIS-25 crystals obtaining 37 ppb. Sensitivity of the technique down to a few ppb potassium content in the NaI(Tl) crystal can be concluded.

- Activities of the different branches in the ^{238}U and ^{232}Th chains have been studied after identifying their alpha emissions for ANAIS-0 and ANAIS-25 crystals. As α events are faster in NaI(Tl) than β/γ ones, they can be discriminated by PSA techniques. Looking at the results, it can be concluded that secular equilibrium is broken in both chains and in all the studied modules. The derived activities for the ANAIS-0 crystal are on the limit of the ANAIS requirements: 0.75 mBq/kg is the total alpha activity, where the higher contribution are 0.188±0.005 mBq/kg of ^{210}Pb. For ANAIS-25 crystals, the ^{232}Th natural chain seems to be really suppressed, but as the total alpha activity (3.15 mBq/kg) is much higher than that of ANAIS-0, such a rate is attributable to isotopes from the ^{238}U chain, probably one or more of its branches out of equilibrium, because we do not see the alpha lines structure corresponding the chain in equilibrium. Possible contaminations of ^{222}Rn during the growing or machining of the detectors could have taken place. Measurements

are on-going in order to properly calibrate the alpha spectrum and derive more quantitatively conclusions.

- ANAIS-0 and ANAIS-25 modules started to take data very soon after their installation underground. This allowed to observe short-life isotopes activated during the stay on surface of all detectors components, mainly the NaI crystals. Cosmogenic activation has been observed much better in ANAIS-25 than in previous prototypes, because of the prompt data taking starting at LSC, low radioactivity level of the modules, and very good resolution. Some of the identified isotopes are: ^{125}I, ^{129}I, ^{121}Te, o ^{125m}Te.

- The complete ANAIS-0 set-up has been simulated taking into account the most relevant internal and external contributions to the ANAIS-0 module background using the Geant4 code. Energy spectra for different calibration sources have been simulated to validate the code. Systematic effects, specially in lines associated to X-rays and to Compton-to-peak ratio, are observed. The simulated results have been compared to the experimental spectra and it is to remark that more than 92% of the background in the region from 150 to 3000 keV is explained with our proposed background model, increasing up to 98% when some hypotheses are added (such as ^{210}Pb surface contamination, or tritium presence). More than 77% of the low energy background is also explained, increasing up to a 99% when adding the referred hypotheses. The same simulation code has been extended to the ANAIS-25 set-up by changing the geometry. For the moment, only NaI bulk crystal contaminations have been simulated. ^{40}K contribution at the 37 ppb present in ANAIS-25 is not limiting strongly the low energy background, howver, ^{210}Pb contamination at the level identified (and compatible with the alpha total rate) is an important issue, compromising the ANAIS background goal. Discussions with Alpha Spectra about the possible mechanisms for the introduction of such a contamination in the crysal are going on and next steps are being agreed.

Resumen y conclusiones

De las medidas de las anisotropías de la radiación cósmica de fondo realizadas por la sonda WMAP se han derivado precisas estimaciones de los parámetros del modelo cosmológico estándar. Los datos acumulados de 9 años confirman un Universo plano, en expansión acelerada y que, en la actualidad, está compuesto por un 72% de energía oscura y un 28% de materia. Una gran variedad de observaciones tanto a escala de galaxias y cúmulos de galaxias como a escala cosmológica, y obtenidas con diversas técnicas, apoyan este modelo. Sin embargo, a pesar de su éxito, todavía quedan importantes aspectos del mismo pendientes de aclaración, en particular, respecto a un nuevo tipo de materia, más allá del Modelo Estándar de la Física de Partículas, que se precisa para explicar la mayor parte de la masa del Universo, y que se denomina materia oscura. Una denominación genérica para las partículas candidatas a materia oscura es WIMP, Weakly Interacting Massive Particles, el acrónimo en inglés de partículas masivas que interaccionan débilmente.

Diferentes estrategias experimentales se aplican a la detección de la materia oscura. Los productos de la aniquilación de las partículas de materia oscura en los halos galácticos o en los cúmulos de galaxias, pueden llevar a su identificación indirecta. Por otro lado, los experimentos de detección directa, buscan las interacciones de las partículas de materia oscura por dispersión elástica con los núcleos de un detector adecuado. El movimiento de traslación de la Tierra en torno al Sol, con periodo anual, genera una modulación en la velocidad de los WIMPs relativa al detector que se traduce en una modulación anual en los ritmos de detección asociados a la señal de materia oscura. El experimento DAMA/LIBRA, en operación en el Laboratorio Nacional del Gran Sasso, que utiliza NaI(Tl) como material blanco y ha tomado datos correspondientes a 13 ciclos anuales, ha observado una modulación en su ritmo de sucesos en la región de 2 a 6 keV con un significado estadístico de $8.9\,\sigma$. Sin embargo, otros experimentos que utilizan materiales blanco y técnicas de detección diferentes, y que han alcanzado un alto grado de sensibilidad excluyen la mayor parte del espacio de parámetros de los WIMPs compatible con la señal de DAMA-LIBRA. Es importante remarcar que la comparación de resultados obtenidos

con blancos diferentes y distintas técnicas es dependiente del modelo considerado tanto para el WIMP como para el halo, y que posibles efectos sistemáticos relacionados con la técnica específica pueden alterar los resultados de dicha comparación de forma considerable. En este sentido es de particular importancia una medida precisa de los factores de eficiencia relativa de centelleo para retrocesos nucleares.

El experimento ANAIS (Annual Modulation with NaI(Tl) Scintillators) tiene como objetivo confirmar la señal de DAMA/LIBRA usando el mismo blanco y técnica en el Laboratorio Subterráneo de Canfranc (LSC). Se usarán 250 kg de NaI(Tl) ultrapuro como blanco, divididos en 20 módulos, acoplados cada uno a dos fotomultiplicadores, dentro de un blindaje adecuado para minimizar la contribución al fondo del radioactivo experimento de la radioactividad ambiental. Los principales requisitos del experimento son: bajo fondo radioactivo, bajo umbral energético y condiciones de operación muy estables. La Figura 1, muestra visión esquemática del diseño del experimento ANAIS.

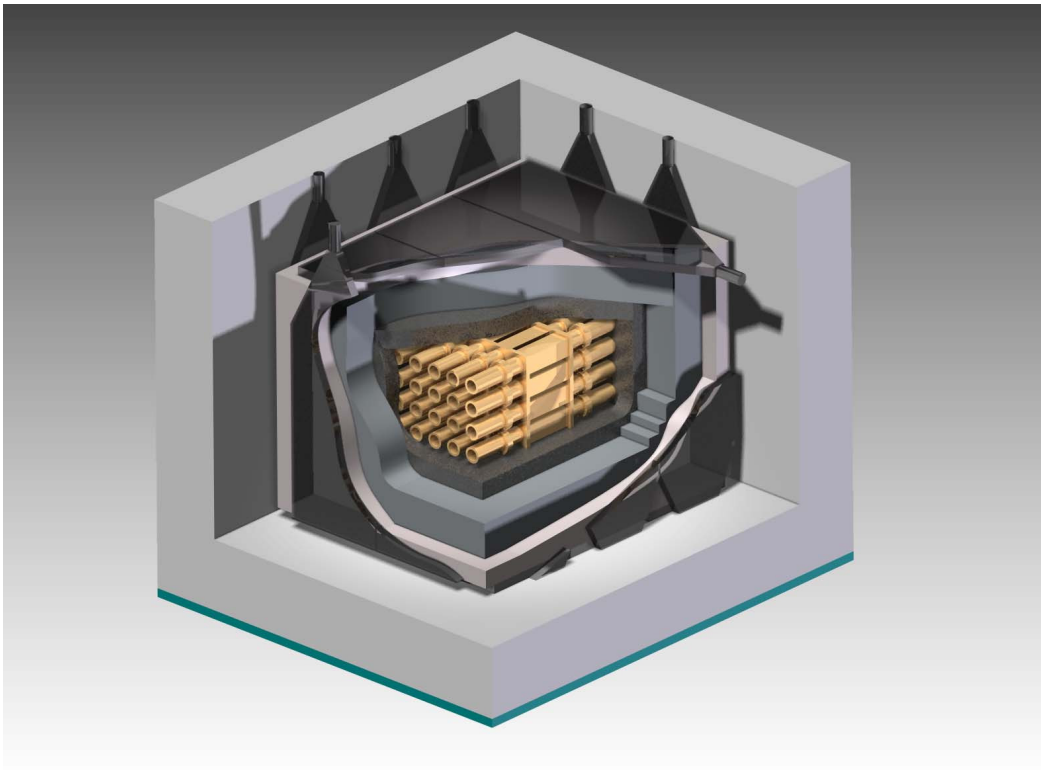

Figura 1: *Esquema del experimento ANAIS.*

En este trabajo se ha estudiado la viabilidad del experimento ANAIS en el LSC. La mayor parte de este estudio se ha llevado a cabo con el módulo ANAIS-0, un cristal de 9.6 kg de NaI(Tl), fabricado por Saint Gobain y que fue encapsulado en la Universidad de Zaragoza usando cobre ETP y dos ventanas de cuarzo sintético. ANAIS-0 ha estado

tomando datos en el LSC en el mismo espacio que alojará al experimento ANAIS en el futuro y, previsiblemente, en similares condiciones ambientales y experimentales. El estudio se ha ampliado al análisis preliminar de las primeras semanas de datos de los módulos de ANAIS-25. ANAIS-25 consiste en dos cristales, de 12.5 kg de NaI(Tl) cada uno, que se han construido aplicando toda la experiencia adquirida con los prototipos previos y gracias a la disponibilidad de un polvo de NaI con adecuada radiopureza.

El experimento ANAIS se concibió para ser llevado a cabo con 10 cristales hexagonales de NaI(Tl) de 10.7 kg cada uno, fabricados por BICRON (ahora Saint Gobain). Sin embargo, al medir su contenido en potasio natural (entre 0.46 y 0.71 ppm), éste resultó ser demasiado alto para usarlos en un experimento de búsqueda de materia oscura. Este resultado conllevó un cambio significativo en la cronología del experimento. La búsqueda de nuevos cristales implicó el desarrollo de nuevas técnicas de purificación en potasio, un buen conocimiento de las técnicas analíticas adecuadas para alcanzar sensibilidades al nivel de ppb en la identificación de dicho elemento y la aplicación de técnicas de bajo fondo para el crecimiento y encapsulado de los cristales:

- Para garantizar la radiopureza de las muestras, se requiere una determinación precisa del contenido en potasio de polvo de NaI, hasta niveles del orden de unas pocas ppb. La técnica de espectrometría gamma utilizando un detector de Germanio hiperpuro (HPGe) no es capaz de alcanzar ese nivel ni siquiera con muestras de gran masa, y por ello se consideraron otras técnicas analíticas como la Espectroscopia por Absorción Atómica (AAS).

- Se adquirieron muestras comerciales de polvo de NaI a diferentes suministradores para usarlas como muestras de referencia y comprobar la validez de los distintos procedimientos analíticos. Tras la realización de varios tests cruzados, se concluye que las técnicas analíticas consideradas no cuantifican el nivel de potasio adecuadamente, ni siquiera en el rango de las ppm y, por ello, en este trabajo solo se han considerado los datos de espectrometría gamma realizados en el banco de medidas del LSC para la toma de decisiones.

- Electrochemical System Inc. propuso un método de purificación de polvo de NaI, partiendo de muestras de calidad comercial, que no ha resultado exitoso, puesto que no se han podido alcanzar niveles de potasio por debajo de 320 ± 8 ppb.

- Finalmente se ha encontrado un polvo de NaI cumpliendo los requisitos de pureza iniciales (menos de 90 ppb en potasio natural, al límite de sensibilidad del detector hiperpuro de germanio utilizado en el LSC para la medida de materiales). La empresa

Alpha Spectra creció dos cristales de 12.5 kg cada uno con el polvo seleccionado (nos referiremos a ambos, conjuntamente, como ANAIS-25). Los materiales utilizados y los protocolos para la limpieza de las piezas y encapsulado de los cristales fueron propuestos por la Universidad de Zaragoza (UZ) al fabricante, aplicando todos los conocimientos adquiridos con los prototipos previos de ANAIS, encapsulados en la UZ. Los detectores de ANAIS-25, llegaron al LSC en noviembre de 2012.

Mientras tanto, en el LSC se ha seguido trabajando con el módulo ANAIS-0, que está formado por un cristal de 9.6 kg de NaI(Tl) fabricado por Saint Gobain, similar en forma y tamaño a los del experimento DAMA. Como aspectos más relevantes del diseño de ANAIS-0, su instalación y operación en el LSC podemos destacar:

- El cristal de ANAIS-0 fue encapsulado en la UZ con cobre ETP y dos ventanas de cuarzo para cerrar herméticamente el detector. Ha funcionado perfectamente, aislando el cristal de NaI(Tl) fuertemente higroscópico, de la humedad ambiental. El diseño permite acoplar directamente diferentes modelos de fotomultiplicador (PMT) a las ventanas de cuarzo, y opcionalmente la incorporación de guías de luz entre el cuarzo y el PMT. En la Figura 2 puede verse el cristal antes, durante y después del encapsulado.

- Se incluyó una ventana de Mylar en el diseño del detector para permitir su calibración con fuentes gamma externas de muy baja energía (por debajo de 20 keV). En la Figura 2.c se muestra un detalle de la ventana de calibración. Las fuentes radioactivas se han usado no sólo para calibrar sino también para comprobar la estabilidad de la ganancia, obtener sucesos de centelleo en NaI(Tl) que puedan ser usados como referencia en el análisis de datos y analizar la posible presencia de efectos sistemáticos en las simulaciones.

- ANAIS-0 ha tomado datos en las viejas y en las nuevas instalaciones del LSC, bajo 2450 m.w.e. El montaje experimental de ANAIS-0 se trasladó al Hall B del LSC en febrero de 2011, a una caseta especialmente diseñada para el experimento ANAIS. En la Figura 3 se puede ver la ubicación de las distintas instalaciones del LSC así como una fotografía de la estructura que aloja el experimento ANAIS para aislarlo de las interferencias con el resto de las actividades que se desarrollan en el Hall B.

- El módulo ANAIS-0 ha operado dentro de un blindaje muy similar al que está proyectado para el experimento ANAIS: 10 cm de plomo antiguo, 20 cm de plomo de baja actividad, una caja anti-radón de PVC que es mantenida bajo sobrepresión de

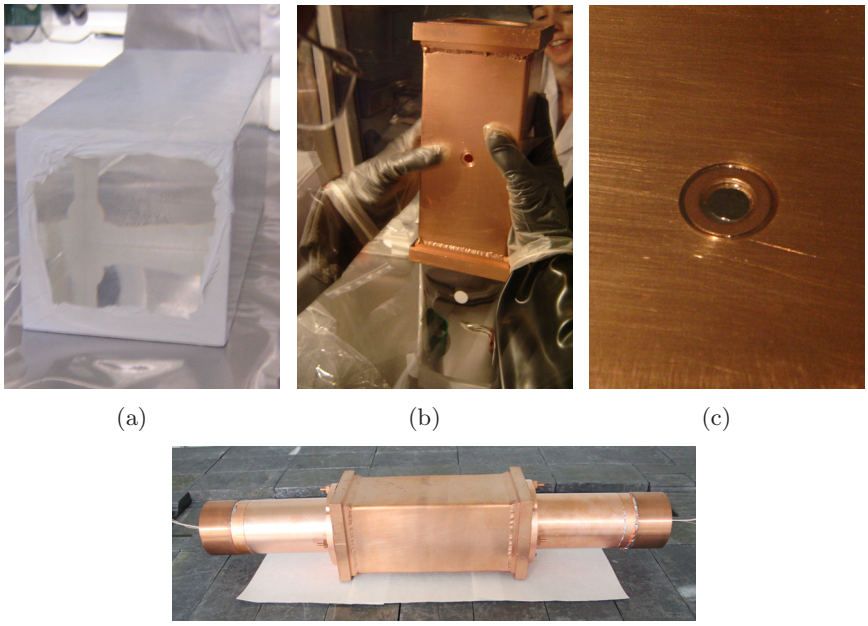

(a) (b) (c)

(d)

Figura 2: *Imágenes de ANAIS-0: (a) cristal recubierto de Teflon, (b) durante el encapsulado, (c) detalle de la ventana de Mylar y (d) aspecto final de ANAIS-0 después de acoplar los PMTs.*

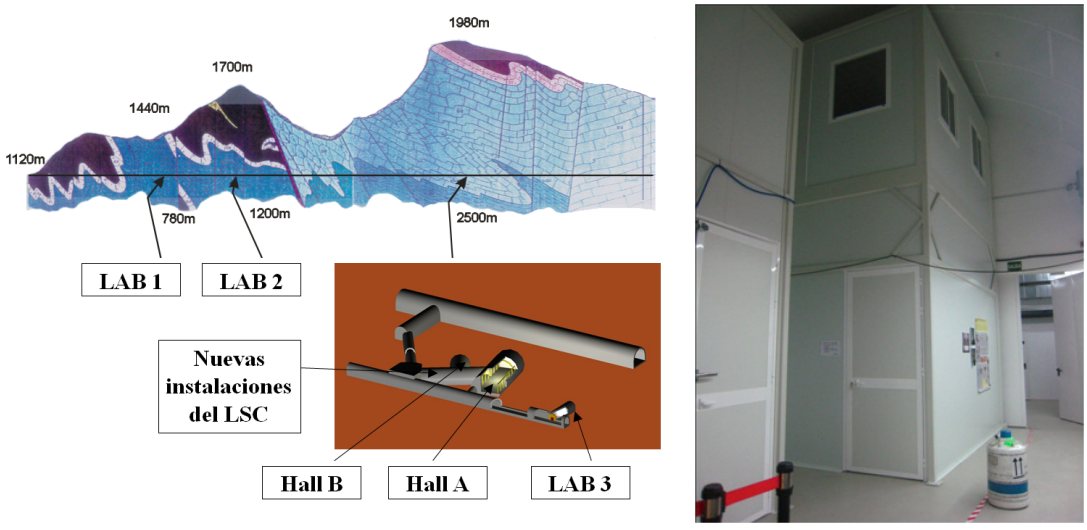

(a) (b)

Figura 3: *(a) Perfil de la cobertura de roca a lo largo del túnel de Somport. La máxima cobertura se encuentra bajo el Tobazo (1980 m de altura). Las diferentes ubicaciones de las instalaciones del LSC a lo largo del túnel de ferrocarril están indicadas. (b) Caseta diseñada para albergar el experimento ANAIS en el Hall B de las nuevas instalaciones del LSC.*

nitrógeno gas evaporado de líquido para evitar la entrada del aire del laboratorio (que contiene radón) en el interior del blindaje y tres centelleadores plásticos colocados

en la parte superior del blindaje ($0.5 \times 1 \times 0.05\, m^3$ cada uno) para monitorizar el ritmo de muones en el laboratorio y eliminar su contribución al fondo radioactivo de ANAIS-0, ver Figura 4. Para el experimento ANAIS, este blindaje se completará con el blindaje de neutrones (consistente en tanques de agua y ladrillos de polietileno borado) y se cubrirá completamente con plásticos centelleadores como sistema de veto activo.

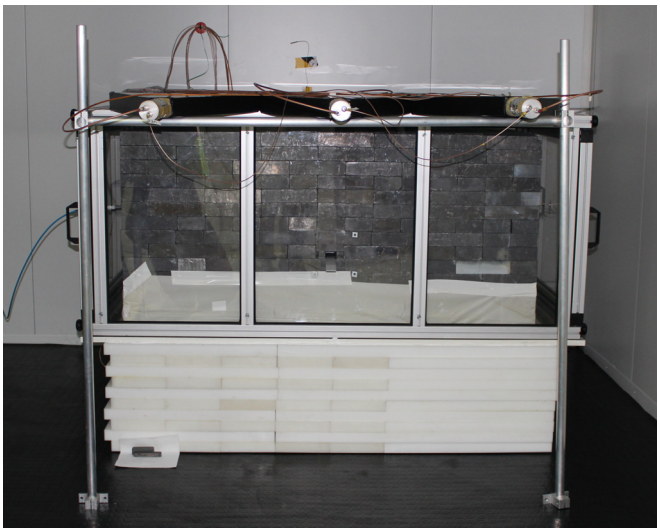

Figura 4: *Blindaje completo de ANAIS-0 compuesto por una base de polietileno, plomo, una caja anti-radón y vetos anti-muones.*

- La cadena electrónica, el sistema de adquisición y el programa de análisis de datos han sido optimizados y mejorados durante la operación de ANAIS-0. El diseño final de la cadena electrónica es compacto y homogéneo combinando módulos NIM y VME. La placa digitalizadora MATACQ ha mostrado un comportamiento excelente desde su instalación. El sistema es fácilmente escalable a un número elevado de módulos, hasta los 40 canales (2×20 PMTs) del diseño final de ANAIS.

- Se ha llevado a cabo la monitorización de los parámetros experimentales y ambientales (especialmente en las nuevas instalaciones del LSC) para controlar la estabilidad del experimento. Respecto a los resultados, hay que resaltar que tras 19 meses de medida se ha obtenido una actividad media de 80.9 ± 0.3 Bq/m^3 de radón en el aire del Hall B. Además, se ha observado una fluctuación estacional en los valores de radón y humedad, compatible con un periodo anual con máximo en torno al 25 de julio. Ambas modulaciones están claramente correlacionadas, aunque la amplitud es mayor en la humedad (31%) que en el contenido de radón en el aire (15.5%). Se requieren más datos para confirmar esta modulación e identificar su origen. Como se introduce constantemente nitrógeno gas en el volumen interno del blindaje, esta fluctuación

estacional no se espera que contribuya al fondo del experimento de una forma significativa. Las variaciones de temperatura en el Hall B son grandes: el termostato del LSC se encuentra en el Hall A y, por tanto, variaciones locales en la temperatura del Hall B, relacionadas por ejemplo con la presencia humana, no pueden ser corregidas. Se ha encontrado correlación entre el ritmo de trigger de ANAIS-0 y la temperatura del Hall B, pero sobre todo la temperatura de la electrónica, en algunos periodos de la toma de datos, causada principalmente por el mal funcionamiento de algunos módulos que tuvieron que ser reparados.

- Se ha estudiado la calibración cerca del umbral con fuentes radioactivas de baja energía. Efectos superficiales han sido identificados en las líneas de menor energía estudiadas, 6.4 y 5.9 keV, por lo que estas líneas no han sido consideradas en la calibración final de la región de baja energía. La población de eventos de 3.2 keV correspondientes a la desintegración del ^{40}K y seleccionados por la coincidencia con un gamma de 1461 keV en un segundo detector, no está sujeta a estos efectos superficiales y, por lo tanto, ha sido utilizada para la calibración calibración final de la región de baja energía, junto con las líneas de 14.4 keV y 22.6 keV de fuentes externas de ^{57}Co y ^{109}Cd, respectivamente

- Sucesos de ANAIS-0 en coincidencia con un muón en los vetos centelleadores han sido identificados y estudiados. Un aumento en el ritmo de eventos coincidentes con muón se ha observado tras el traslado a las nuevas instalaciones del LSC, tal y como se esperaba debido al menor cubrimiento de roca.

Los resultados del análisis de los datos de ANAIS-0 se pueden resumir en los siguientes puntos:

- Se ha diseñado un protocolo para rechazar los eventos que no han sido producidos por centelleo en el cristal de NaI. En primer lugar se descartan los periodos de ritmo anómalamente alto, en particular 0.5 s después de un evento de muy alta energía (> 9 MeVee), descontando el correspondiente tiempo vivo. También se rechazan los eventos en coincidencia con una señal en los centelleadores plásticos y los eventos con la línea de base mal calculada, porque los parámetros del pulso dependientes de su valor no se podrán calcular adecuadamente. Se ha diseñado un algoritmo para contar el número de picos en el pulso, que ha sido implementado para rechazar los pulsos con pocos fotoelectrones por PMT, el corte derivado implica un umbral de análisis equivalente a 1 keV en ANAIS-0 si los picos son asociados a fotoelectrones. Por último, en ANAIS-0 se identificaron eventos más rápidos que los correspondientes

al centelleo del NaI(Tl) y han sido rechazados optimizando el parámetro temporal P1s para incluir la información de los dos PMTs. La eficiencia de este corte ha sido determinada con datos correspondientes a las calibraciones a baja energía, ver Figura 5. Se puede concluir que se ha conseguido un umbral de análisis de 2 keV, habiendo elegido un corte conservador que hace posible que en la región de aceptación de sucesos queden algunos de la población anómala. El protocolo de filtrado para los datos de ANAIS-25 todavía está siendo optimizado, pero es posible que algunos de los cortes anteriores no sean necesarios, pues se observan menos eventos más rápidos que los correspondientes al centelleo del NaI(Tl), ver Figura 6. El análisis preliminar apunta a que es posible alcanzar un umbral del orden de 1 keV, gracias a la buena recogida de luz conseguida, especialmente en uno de los dos módulos. Los espectros finales, tras la aplicación del filtrado de datos antes explicado, tanto para ANAIS-0 como para ANAIS-25 se muestran en la Figura 7.

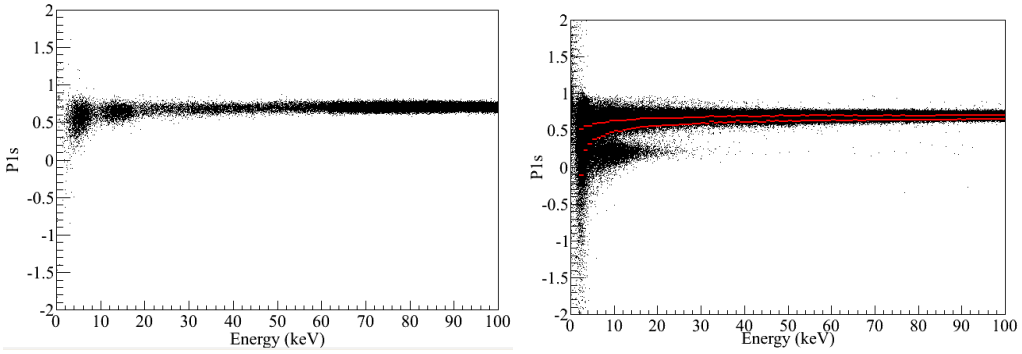

(a) (b)

Figura 5: *Distribución del parámetro P1s en función de la energía para una calibración de ^{57}Co (a), y el fondo (b) durante la toma de datos de ANAIS-0 con ULB PMTs. La línea roja superior representa el valor medio de P1s obtenido de las calibraciones y la inferior el valor de corte elegido, que conlleva una aceptación del 97.7% de eventos de centelleo en NaI(Tl).*

- Se han analizado los datos antiguos de una calibración realizada con una fuente de ^{252}Cf, que emite un espectro continuo de neutrones. Los retrocesos nucleares son más rápidos que los eventos beta/gamma en NaI(Tl), sin embargo esta diferencia es tan pequeña que no es posible distinguirlos suceso a suceso mediante el análisis de pulsos. No obstante, se debe incluir una corrección en el cálculo de la eficiencia del corte P1s para hacer un análisis de materia oscura. Este análisis se ha realizado con datos del PIII, pero se entiende que es una propiedad intrínseca del NaI(Tl) que puede ser extendida a otros cristales.

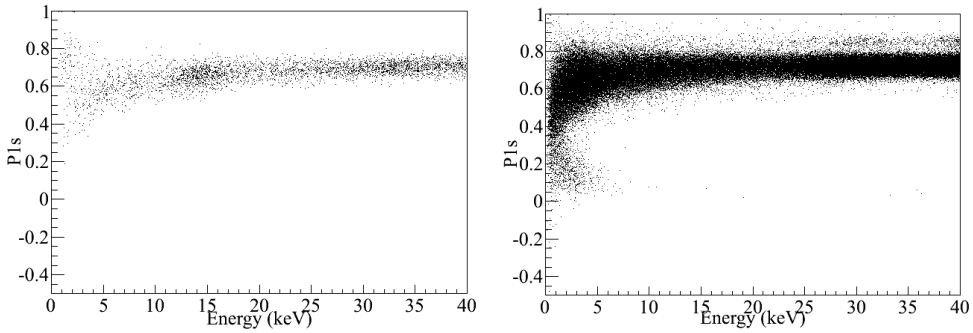

(a) (b)

Figura 6: *Distribución del parámetro P1s en función de la energía para una calibración de ^{57}Co (a), y el fondo (b) durante la toma de datos de ANAIS-25 con ULB PMTs.*

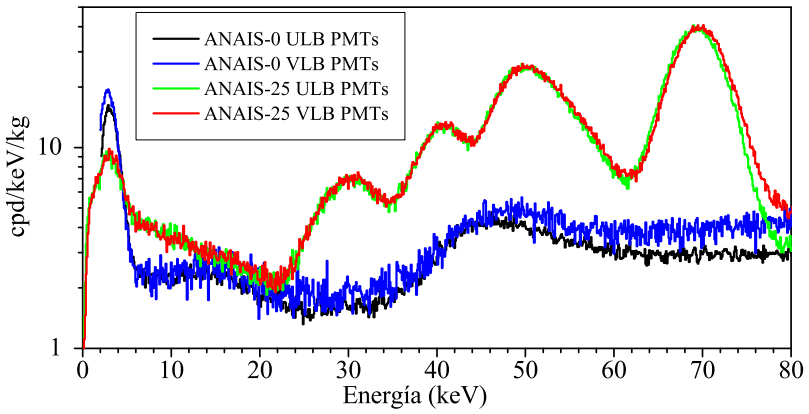

Figura 7: *Espectros de baja energía de ANAIS-0 y de los dos detectores de ANAIS-25 después de aplicar el protocolo de filtrado de datos.*

- La asimetría en el reparto de la energía por parte de los dos PMTs en los datos de ANAIS-0 y ANAIS-25 ha sido estudiada. No representan una contribución significativa al fondo de baja energía y son eliminados por los cortes descritos anteriormente. El origen de estos sucesos puede vincularse a centelleo en las guías de luz y a sucesos originados en los PMTs. El ritmo de eventos en coincidencia con muón (fuertemente asimétricos) aumenta ∼20% cuando se usan guías de luz (un 86% de 1 a 100 keV), apuntando a interacciones de muones en las guías que producen centelleo capaz de disparar la adquisición de ANAIS y contribuyen al fondo de baja energía de ANAIS.

- Se han considerado diferentes estimadores de la energía para su aplicación a sucesos con pocos fotoelectrones, en los que se puede identificar la llegada discreta de cada uno de ellos, con el objetivo de determinar cuál presenta mejor resolución y discriminación de señal frente a ruido. Los parámetros QDC y área han mostrado ser equivalentes en la versión mejorada de la electrónica, utilizando como tarjeta

digitalizadora la MATACQ. Otros interesantes estimadores como el área bajo los picos del pulso, han demostrado buena reconstrucción de la energía de los sucesos, pero peor definición del umbral.

- Se ha conseguido disparar la adquisición en el fotoelectrón, tanto en ANAIS-0 como en ANAIS-25. El porcentaje de la distribución de fotoelectrón capaz de disparar ha sido determinado en los diferentes montajes. En el caso de los PMTs VLB, la fracción de la distribución de fotoelectrón que dispara es todavía baja y habría que aumentarla bajando el umbral del CFD. Sin embargo la eficiencia de disparo estimada con la población de 3.2 keV siguiendo la desintegración de ^{40}K y seleccionada con la coincidencia con la línea gamma de 1461 keV es casi del 100% en todas las configuraciones, indicando una eficiencia de disparo muy buena por encima de 2 keV.

- Se han derivado las constantes de centelleo del NaI(Tl) para las diferentes partículas interaccionantes. La constante de centelleo rápida en NaI(Tl) obtenida es 219.3 ± 0.5 ns para partículas alfa y 287.4 ± 0.5 ns para partículas gamma, acorde con las medidas que recoge la bibliografía. Además diferentes tiempos de subida han sido medidos para pulsos correspondientes a ambos tipos de partículas. También se han observado constantes más lentas, del orden de los ms, en los cristales de ANAIS-0, PIII y ANAIS-25 cuyo origen es probablemente distinto. Los cristales de ANAIS-0 y del PIII muestran constantes de aproximadamente 20 and 80 ms, mientras que el detector 0 de ANAIS-25 de 52 and 172 ms (el 1 está siendo medido actualmente). Este centelleo lento parece estar relacionado con el comportamiento anómalo mostrado por los cristales de ANAIS-0 y ANAIS-25 tras una excitación con fuentes de calibración de alta energía. Parece que se excitan estados de larga vida que producen en su decaimiento un gran número de fotones durante las horas posteriores a la irradiación. En el cristal de ANAIS-0 se ha observado una gran amplitud asociada a este efecto, también importante en el caso del detector 0 de ANAIS-25, sin haber encontrado explicación para la diferencia con el detector 1 o el PIII (salvo que la recogida de luz sea mucho peor en estos montajes, lo que no aparece acorde con el resto de los resultados experimentales obtenidos).

Se ha estudiado la eficiencia en la recolección de luz en las diferentes configuraciones de PMTs y guías de luz probadas, con el objetivo de determinar la óptima para ANAIS:

- En este trabajo se han valorado cinco modelos de PMT en función de su ganancia, respuesta al fotoelectrón, recogida de luz, resolución y su contribución al fondo radioactivo. En vista de los resultados, se ha seleccionado el modelo VLB (Hamamatsu

R6956 MOD) para ser usado en ANAIS (ver Figura 8), debido a su buena eficiencia en la recogida de luz (7.38 ± 0.07 ph.e./keV en ANAIS-0 y 16.13 ± 0.66 ph.e./keV en ANAIS-25), del orden de un 30% superior a la conseguida con el modelo ULB (Hamamatsu R11065 SEL); en condiciones experimentales similares; además, gracias a su baja contribución al fondo, puede usarse sin guías de luz.

- Se ha demostrado que las guías de luz reducen de forma importante la contribución al fondo radiactivo de los PMTs, sobre todo en la región de media y alta energía. Sin embargo, empeoran la eficiencia en la recolección en un 30% y centellean cuando se deposita en ellas una gran cantidad de energía, introduciendo una contribución adicional al ritmo de interacción a baja energía. Esta contribución al fondo puede afectar de forma importante al estudio de la modulación anual dado que los muones son capaces de generar dicho centelleo, y el flujo de muones en subterráneo se espera que muestre también una modulación anual. Por ello se evitará la utilización de guías de luz en el experimento ANAIS.

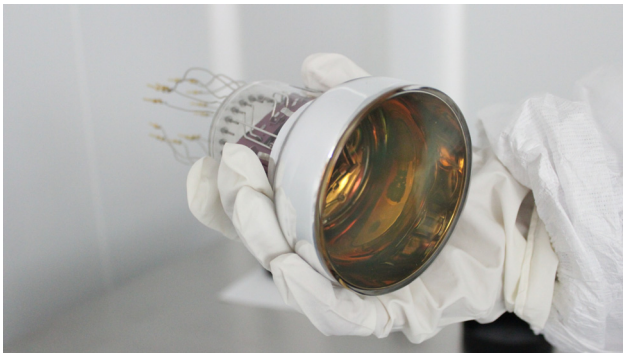

Figura 8: *Fotografía del fotomultiplicador Hamamatsu VLB (R6956 MOD) que ha sido seleccionado para acoplar a los 20 módulos del experimento ANAIS.*

El fondo radioactivo de ANAIS-0 ha sido estudiado cuidadosamente para identificar las principales contribuciones en todos los rangos energéticos. Una buena comprensión del fondo radioactivo es imprescindible como primer paso para su reducción.

- El contenido en ^{40}K de ANAIS-0 se ha determinado en este trabajo con la medida en coincidencia. Consiste en medir en un detector las emisiones de rayos-X y de electrones Auger que siguen a la captura en capa K del ^{40}K y que suman la energía de ligadura de dicha capa, 3.2 keV, en coincidencia con el gamma de 1461 keV que es completamente absorbido en un segundo detector ubicado en el mismo espacio experimental. La eficiencia de la coincidencia se ha estimado con una simulación de Geant4 y se ha determinado el contenido de potasio en el cristal de ANAIS-0,

resultando 460 ppb. El mismo análisis ha sido aplicado a los cristales de ANAIS-25 y se ha obtenido un resultado preliminar de 37 ppb. Se ha demostrado por tanto que la técnica garantiza la determinación de contenidos de unas pocas ppb de potasio natural en cristales de NaI(Tl). En la Figura 9 se muestra el espectro de baja energía en coincidencia con ventanas de $1\,\sigma$ de anchura centradas en la línea de 1461 keV en el otro cristal montado en el mismo espacio experimental para los datos de ANAIS-0 y ANAIS-25.

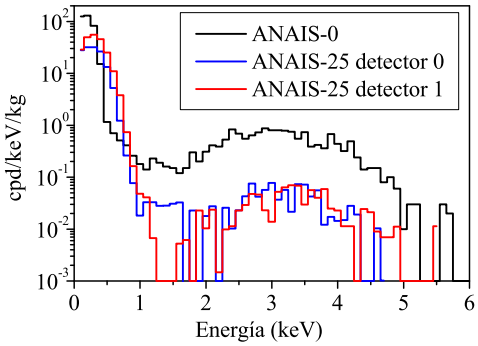

Figura 9: *Espectros de baja energía en coincidencia con ventanas de* $1\,\sigma$ *de anchura centradas en la línea de 1461 keV en el otro cristal montado en el mismo espacio experimental. Se muestra en negro el espectro correspondiente a ANAIS-0, en azul el detector 0 de ANAIS-25 y en rojo el detector 1 de ANAIS-25. Los niveles de potasio derivados del análisis son 460 ppb en el cristal de ANAIS-0 y 37 ppb en los de ANAIS-25.*

- Las actividades de las cadenas naturales de ^{238}U and ^{232}Th han sido determinadas a partir de sus emisiones alfa. Como los eventos α en NaI(Tl) son más rápidos que los β/γ, pueden ser discriminados a partir de la forma de los pulsos. Los resultados indican que el equilibro está roto en ambas cadenas. Las actividades correspondientes al cristal utilizado en ANAIS-0 están en el límite de las requeridas para la consecución de los objetivos de fondo del experimento ANAIS: el ritmo total de sucesos de origen alfa es 0.75 mBq/kg, donde domina la contribución de ^{210}Pb, 0.188 ± 0.005 mBq/kg. En ANAIS-25, la cadena de ^{232}Th parece bastante suprimida y, sin embargo, el ritmo total de sucesos de origen alfa en ANAIS-25 es muy elevado (3.15 mBq/kg), con la información a nuestra disposición en estos momentos se atribuye a la cadena del ^{238}U, probablemente con el equilibrio roto, al menos en el ^{210}Pb. Una posible contaminación de ^{222}Rn durante el crecimiento de los cristales podría haber tenido lugar. Las medidas continúan para poder calibrar el espectro alfa adecuadamente y determinar de forma precisa las actividades de los diferentes isótopos.

- Tanto ANAIS-0 como ANAIS-25 comenzaron a tomar datos inmediatamente después de su instalación en subterráneo. Esto permitió observar el progresivo decaimiento de los isótopos de vida corta que se habían activado en el periodo en que los cristales se encontraron en superficie. La activación cosmogénica se ha observado mejor en ANAIS-25 por la mayor prontitud en el comienzo de la toma de datos, su alta radiopureza y buena resolución. Algunos de los isótopos identificados son: ^{125}I, ^{129}I, ^{121}Te y ^{125m}Te.

- El montaje correspondiente a ANAIS-0 ha sido simulado considerando las contribuciones más relevantes al fondo radiactivo, tanto internas como externas, usando el código Geant4. El código ha sido probado y validado simulando las distintas fuentes de calibración, a alta y a baja energía: se han encontrado efectos sistemáticos, especialmente en las líneas asociadas a rayos-x y en la relación de sucesos en el fotopico frente a los correspondientes a la región compton. Los resultados de la simulación se han comparado con los espectros experimentales (ver Figura 10). Cabe destacar que más del 92% del fondo en la zona entre 150 y 3000 keV es explicado por el modelo de distribución de contaminantes propuesto, aumentantdo al 98% si se añaden algunas hipótesis plausibles tales como suponer contaminación superficial de ^{210}Pb en el cristal. El mismo código ha sido extendido a la geometría de ANAIS-25. Por el momento, sólo se ha simulado la contaminación interna de los cristales, ver Figura 10. La contribución de 37 ppb de potasio en ANAIS-25 no está limitando fuertemente el fondo de baja energía, sin embargo la contaminación de ^{210}Pb al nivel identificado (y compatible con el ritmo total alfa) supone un importante problema, comprometiendo el objetivo de bajo fondo de ANAIS. Conversaciones con Alpha Spectra para determinar el origen de dicha contaminación y evitarla están teniendo lugar en el momento de presentar este trabajo y de ellas se derivarán los siguientes pasos a dar para cumplir los objetivos del experimento ANAIS.

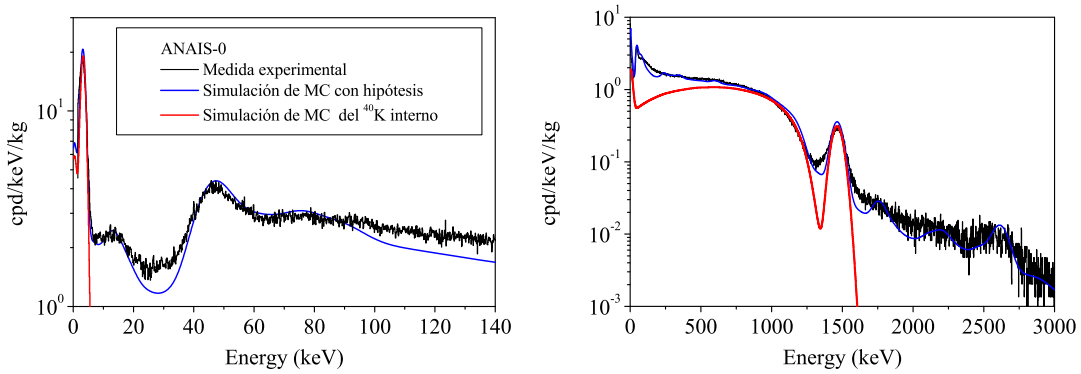

Figura 10: *Comparación entre simulación (azul) y datos experimentales (negro) a baja (a) y alta energía (b) para datos de ANAIS-0 con ULB PMTs tras añadir algunas hipótesis. En las gráficas se muestra destacada en rojo la contribución al fondo de una contaminación de 12.7 mBq/kg de ^{40}K en el cristal de ANAIS-0.*

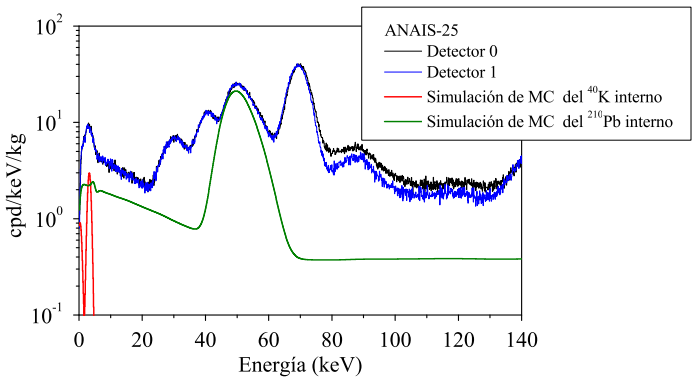

Figura 11: *Epectros totales de los detectores 0 (negro) y 1 (azul) de ANAIS-25, junto con las simulaciones de 1.25 mBq/kg de ^{40}K (rojo) y 3.15 mBq/kg de ^{210}Pb (verde) en los cristales de ANAIS-25.*

Agradecimientos

En primer lugar quiero dar las gracias a mi directora la Prof. María Luisa Sarsa, por guiarme desde el primer hasta el último día con una paciencia y dedicación insuperables. Ha supuesto un soporte fundamental con sus conocimientos y apoyo en el comienzo de mi carrera investigadora.

El trabajo descrito en esta memoria se ha conseguido con la colaboración de muchas personas. En particular, quiero agradecer al Prof. Jose Ángel Villar su confianza en mí en todo momento. A los profesores Jorge Puimedón, Eduardo García y Julio Amaré, sus buenas ideas y su criterio científico que han sido imprescindibles. A la Prof. Susana Cebrián sus enseñanzas, su tiempo y su modo de trabajar que resulta un ejemplo a seguir.

A María Martínez, que con sus aportes a este proyecto, ha trazado un camino por el que ha sido más sencillo continuar. A Carlos Pobes y a Miguel Ángel Oliván, puesto que sin su preciada ayuda habría resultado imposible conseguir estos resultados. A Alfonso Ortiz de Solórzano cuyo entusiasmo por el laboratorio me transmitió desde el primer momento. Así como al resto del equipo, siempre dispuestos para colaborar.

No me puedo olvidar de mencionar a todos los miembros del grupo, gracias a los cuales no sólo he adquirido gran cantidad de conocimientos, sino que además hemos pasado muy buenos ratos. En especial quiero destacar el toque humano de Asun y todo lo que he compartido con Laura, mucho más que un despacho.

Me gustaría agradecer la acogida y el trato de todo el equipo de CUORE durante mi estancia en el Laboratorio de Gran Sasso, también a MultiDark que ha permitido aumentar mis conocimientos sobre materia oscura y a todo el equipo del Laboratorio Subterráneo de Canfranc que siempre nos facilita el trabajo.

Quiero mostrar por último mi gratitud a mis amigas, que tanto me valoran, a mi familia y especialmente a mis padres, por el inmensurable cariño sin el cual nada sería posible, y a Rubén, por haberme elegido para compartir aventuras.

Bibliography

[1] G. Gale and N. Shanksf. Methodology and the birth of modern cosmological inquiry. *Stud. Hist. Phil. Mod. Phys.*, 27:279–296, 1996.

[2] J.R. Primack. Precision cosmology. *New Astronomy Reviews*, 49:25–34, 2005.

[3] J.R. Primack. Precision cosmology: Successes and Challenges. *Nuclear Physics B Proc. Suppl.*, 173:1–5, 2007.

[4] Particle Data Group. `http://pdg.lbl.gov/2012/reviews/rpp2012-rev-bbang-cosmology.pdf`.

[5] W. Freedman. Colloquium: Measuring and understanding the universe. *Mon. Not. R. Astron. Soc.*, 220:249:523–537, 1991.

[6] A. Liddle. *An Introduction to Modern Cosmology*. Wiley, 2003.

[7] G. Bertone. *Particle Dark Matter*. Cambridge University Press, 2010.

[8] D. Hooper G. Bertone and J. Silk. Particle Dark Matter: Evidence, Candidates and Constraints. *arXiv.org*, arXiv:0404.175v2, 2004.

[9] D.J. Fixsen. The temperature of the Cosmic Microwave Background. *The Astrop. Journal.*, 707:916–920, 2009.

[10] G.Hinshaw et al. Nine-year Wilkinson Microwave Background Probe (WMAP) observations: cosmological parameter results. *arXiv.org*, arXiv:1212.5226v2, 2013.

[11] N. Aghanim et al. Planck intermediate results I. Further validation of new Planck clusters with XMM-Newton. *Astronomy and Astroph.*, 543:A102, 2012.

[12] WMAP. `http://wmap.gsfc.nasa.gov/`.

[13] R. Keiser et al. A measurement of the damping tail of the Cosmic Microwave Background power spectrum with the South Pole Telescope. *Astroph. Jour.*, 743:28, 2011.

[14] S. Das et al. Detection of the Power Spectrum of Cosmic Microwave Background Lensing by the Atacama Cosmology Telescope. *Phys. Rev. Lett.*, 107:021301, 2011.

[15] Particle Data Group. `http://pdg.lbl.gov/2011/reviews/rpp2011-rev-cosmological-parameters.pdf`.

[16] Particle Data Group. `http://pdg.lbl.gov/2006/reviews/hubblerpp.pdf`.

[17] K. A. Olive B. D. Fields. Big bang nucleosynthesis. *Nucl. Phys. A*, 777:208–225, 2006.

[18] Vera C. Rubin. The rotation of spiral galaxies. *Science*, 220:1339–44, 1983.

[19] A. H. Broeils K. G. Begeman and R.H. Sanders. Extended rotation curves of spiral galaxies - dark haloes and modified dynamics. *Mon. Not. R. Astron. Soc.*, 220:249:523–537, 1991.

[20] F. Zwicky. Spectral displacement of extra galactic nebulae. *Helb. Phys. Acta*, 6:110–127, 1933.

[21] Hubble Telescope. `http://hubblesite.org/newscenter/archive/releases/2006/39/image/a/`.

[22] Hubble Telescope. `http://hubblesite.org/newscenter/archive/releases/exotic/dark-matter/2012/10/`.

[23] L. Bergström. Dark Matter Candidates. *arXiv.org*, arXiv:0903.4849v4, 2009.

[24] F. D. Steffen. Dark-Matter Candidates. *Eur. Phys. Journ.*, 59:557–588, 2009.

[25] K. Griest and M. Kamionkowski. Supersymmetric dark matter. *Physics Reports*, 333:167–182, 20090.

[26] Dan Hooper and Stefano Profumo. Dark matter and collider phenomenology of universal extra dimensions. *Physics Reports*, 453:29–115, 2007.

[27] S. Chatrchyan et al. Search for Dark Matter and Large Extra Dimensions in pp Collisions Yielding a Photon and Missing Transverse Energy. *Phys. Rev. Lett.*, 108:261803, 2012.

[28] S. Chatrchyan et al. Search for dark matter and large extra dimensions in monojet events in pp collisions at $\sqrt{s} = 7\,\text{tev}$. *JHEP*, 09:094, 2012.

[29] A. Abramowski et al. Search for Dark Matter Candidates and Large Extra Dimensions in events with a photon and missing transverse momentum in pp collision data at $\sqrt{s} = 7\,\text{tev}$ with the ATLAS detector. *Phys. Rev. Lett.*, 110:011802, 2013.

[30] European strategy for astroparticle physics (ASPERA) roadmap. `http://www.aspera-eu.org/index.php?option=com_content&task=view&id=35&Itemid=72`.

[31] C. Muñoz. Indirect dark matter searches and models. *Nucl. Instrum. Meth. A*, 692:13–19, 2012.

[32] C. Rott. Review of Indirect WIMP Search Experiments. *Nuclear Physics B Proceedings Suplement*, 00:1–8, 2012.

[33] G. Bertone. The moment of truth of WIMP dark matter. *Nature*, 468:389, 2010.

[34] T. Bringmann and C. Weniger. Gamma ray signals form dark matter: Concepts, status and prospects. *Phys. of the Dark Universe*, 1:194–217, 2012.

[35] M. Ackermann et al. Fermi LAT Search for Dark Matter in Gamma-ray Lines and the Inclusive Photon Spectrum. *Phys. Rev. D*, 86:022002, 2012.

[36] C. Weniger. A Tentative Gamma-Ray Line form Dark Matter Annihilation at the Fermi Large Area Telescope. *arXiv.org*, arXiv:1204.2797v1, 2012.

[37] A. Abramowski et al. H.E.S.S. constraints on Dark Matter annihilations towards the Sculptor and Carina Dwarf Galaxies. *Astrop. Phys.*, 34:608, 2011.

[38] E. Aliu et al. Upper Limits on the VHE gamma-ray Emission from the Willman 1 Satellite Galaxy with the Magic telescope. *Astrophys. J.*, 697:1299, 2009.

[39] J. Aleksic et al. Searches for Dark Matter annihilation signatures in the Segue 1 satellite galaxy with the MAGIC-I telescope. *JCAP*, 1106:035, 2011.

[40] E. Aliu et al. VERITAS Deep Observations of the Dwarf Spheroidal Galaxy Segue 1. *Phys. Rev. D*, 85:062001, 2012.

[41] The CTA consortium. Design concepts for the Cherenkov Telescope Array CTA: an advanced facility for ground based high-energy gamma-ray astronomy. *Exp. Astron.*, 32:193–316, 2011.

[42] J. L. Feng. Dak Matter and Indirect Detection in Cosmic Rays. *arXiv.org*, arXiv:1211.3116v1, 2012.

[43] P. Picozza et al. PAMELA - A payload for antimatter matter exploration and light-nuclei astrophysics. *Astrop. Phys.*, 27:296–315, 2007.

[44] O. Adriani et al. PAMELA Measurements of Cosmic-Ray Proton and Helium Spectra. *Science*, 332:69, 2011.

[45] J.H. Adams et al. The Pierre Auger Observatory I: The Cosmic Ray Energy Spectrum and Related Measurements. *arXiv.org*, arXiv:1107.4809, 2011.

[46] J.H. Adams et al. An evaluation of the exposure in nadir observation of the JEM-EUSO mission. *Astrop. Phys.*, 44:76–90, 2013.

[47] R. Abbasi et al. All-Particle Cosmic Ray Energy Spectrum Measured with 26 IceTop Stations. *Astrop. Phys.*, 44:40–58, 2013.

[48] J. D. Zornoza et al. Dark matter search with the ANTARES neutrino telescope. *arXiv.org*, arXiv:1204.5066v1, 2012.

[49] L. Baudis. Direct dark matter detection: The next decade. *Phys. of the Dark Universe*, 1:94–108, 2012.

[50] G. Gelmini and P. Gondolo. Weakly interacting massive particle annual modulation with opposite phase in late-infall halo models. *Phys. Rev. D*, 64:023504, 2001.

[51] D. Jordan et al. Neutron background at the Canfranc underground laboratory and its contribution to the IGEX-DM dark matter experiment. *Astrop. Phys.*, 21:523–533, 2004.

[52] Y. F. Wang et al. Predicting neutron production from cosmic-ray muons. *PRD*, 64:013012, 2001.

[53] G. Heusser. Low-radioactivity background techniques. *Ann. Rev. Nucl. Part. Sci.*, 45:543–59, 1995.

[54] J. Amaré et al. Recent developments on scintillating bolometers for WIMP searches: ROSEBUD status. *J. Phys. Conf. Ser.*, 39:133–135, 2006.

[55] G. Angloher et al. Results from 730 kg days of the CRESST-II Dark Matter search. *Eur. Phys. J. C*, 72:1971, 2012.

[56] R. Bernabei et al. New results from DAMA/LIBRA. *Eur. Phys. J. C*, 67:39–49, 2010.

[57] F. Avignone et al. Searching direction dependent daily modulation in dark matter detectors. *arXiv.org*, arXiv:0807.3758v1, 2008.

[58] S.C. Kim et al. New Limits on interactions between Weakly Interacting Massive Particles and Nucleons Obtained with CsI(Tl) Crystal Detectors. *Phys. Rev. Lett.*, 108:181301, 2012.

[59] K. Abe et al. Light WIMP search in XMASS. *Phys. Lett. B*, 719:78–82, 2013.

[60] E. Aprile et al. Dark Matter Results from 225 Live Days of XENON100 Data. *Phys. Rev. Lett.*, 109:181301, 2012.

[61] D. Yu. Akimov et al. WIMP-nucleon cross-section results from the second science run of ZEPLIN-III. *Phys. Lett. B*, 709:14–20, 2012.

[62] C. E. Aalseth et al. Search for an Annual Modulation in a p-Type Point Contact Germanium Detector. *Phys. Rev. Lett.*, 107:141301, 2011.

[63] E. Armengaud et al. Final results of the EDELWEIS-II WIMP search using a 4-kg array of cryogenic germanium detectors with interleaved electrodes. *Phys. Lett. B*, 702:329–335, 2011.

[64] Z. Ahmed et al. Dark Matter Search Results from the CDMS II Experiment. *Science*, 327:1619, 2010.

[65] Z. Ahmed et al. Results from a Low Energy Analysis of the CDMS II Germanium Data. *Phys. Rev. Lett.*, 106:131302, 2011.

[66] E. Behnke et al. First dark matter search results from a 4-kg CF_3I bubble chamber operated in a deep underground site. *Phys. Rev. D*, 86:052001, 2012.

[67] M. Felizardo et al. Recent results from the SIMPLE dark matter search. *J. Phys. Conf. Ser*, 375:012011, 2012.

[68] S. Archambault et al. Constraints on low-mass WIMP interactions on ^{19}F from PICASSO. *Phys. Lett. B*, 711:153–161, 2012.

[69] E. Aprile et al. The XENON100 dark matter experiment. *Astrop. Phys.*, 35:573–590, 2012.

[70] Z. Ahmed et al. Combined limits on WIMPs from the CDMS and EDELWEISS experiments. *Phys. Rev. D*, 84:011102(R), 2011.

[71] R. Bernabei et al. Performances of the 100 kg NaI(Tl) set-up of the DAMA experiment at Gran Sasso. *Riv. Nuovo Cim. A*, 112:545, 1999.

[72] Z. Ahmed et al. Search for annual modulation in low-energy CDMS-II data. *arXiv.org*, arXiv:1203.1309v2, 2012.

[73] M. Kuzniak et al. Surface roughness interpretation of 730 kg days CRESST-II results. *Astrop. Phys.*, 36:77–82, 2012.

[74] F. Alessandria et al. The low energy spectrum of TeO_2 bolometers: results and dark matter perspectives for the CUORE-0 and CUORE experiments. *arXiv.org*, arXiv:1209.2519v2, 2013.

[75] H. Kraus et al. EURECA. *PoS*, IDM 2010:109, 2011.

[76] D.G. Cerdeño et al. Complementarity of dark matter direct detection with bolometric targets. *To be published.*, 00:00, 2013.

[77] P. L. Brink. Conceptual Design for SuperCDMS SNOLAB. *J. Low Temp. Phys.*, 167, 2012.

[78] R. Alarcon et al. Max: Multi-ton argon and xenon. *FERMILAB-PROPOSAL-1001*, 0:24, 2009.

[79] L. Baudis. DARWIN: dark matter WIMP search with noble liquids. *PoS*, IDM 2010:122, 2011.

[80] L. Miramonti. Study of the nuclear recoil response of a NaI(Tl) scintillator detector with a ^{252}Cf neutron source. *Nucl. Instrum. Meth. B*, 194:337–342, 2002.

[81] G. Gerbier et al. Pulse shape discrimination and dark matter search with NaI(Tl) scintillator. *Astrop. Phys.*, 11:287–302, 1999.

[82] H. Chaganiet al. Measurement of the quenching factor of Na recoils in NaI(Tl). *J. Inst.*, 3:P06003, 2008.

[83] T. Jagemann et al. Measurement of the scintillation light quenching at room temperature of sodium recoils in NaI(Tl) and hydrogen recoils in NE 213 by the scattering of neutrons. *Nuc. Ins. Meth. A*, 564:549, 2006.

[84] E. Simon et al. SICANE: a detector array for the measurement of nuclear recoil quenching factors using a monoenergetic neutron beam. *Nuc. Ins. Meth. A*, 507:643, 2003.

[85] V.I. Tretyak. Semi-empirical calculation of quenching factors for ions in scintillators. *Astrop. Phys.*, 33:40–53, 2010.

[86] D. Tovey et al. Measurement of scintillation efficiencies and pulse-shapes for nuclear recoils in NaI(Tl) and CaF_2(Eu) at low energies for dark matter experiments. *Phys. Lett. B*, 433:150, 1998.

[87] N. Spooner et al. The scintillation efficiency of sodium and iodine recoils in a NaI(Tl) detector for dark matter searches. *Phys. Lett. B*, 321:156, 1994.

[88] J. I. Collar. Quenching and Channeling of Nuclear Recoils in NaI[Tl]: Implications for Dark Matter Searches. *arXiv.org*, arXiv:1209.2519v2, 2013.

[89] M. Martínez. *Diseño de un prototipo para un experimento de detección directa de materia oscura mediante modulación anual con centelleadores de ioduro de sodio.* PhD thesis, Universidad de Zaragoza, 2006.

[90] Y. Ortigoza et al. Light relative efficiency factors for ions in BGO and Al_2O_3 at 20 mK. *Astrop. Phys.*, submitted.

[91] M. Martinez et al. Study of parylene-coated NaI(Tl) at low temperatures for bolometric applications. *Astrop. Phys.*, submitted.

[92] M. L. Sarsa et al. Dark matter searches at the canfranc tunnel. *Nucl. Phys. B (Proc. Suppl.)*, 35:154–158, 1994.

[93] M. L. Sarsa et al. Searching for annual modulations of WIMPs with NaI(Tl). *Phys. Lett. B*, 386:458–462, 1996.

[94] M. L. Sarsa et al. Results of a search for annual modulation of WIMP signals. *Phys. Rev. D*, 56(4):1856–1862, 1997.

[95] S. Cebrián. *Estudio del fondo radioactivo en experimentos subterráneos de búsqueda de sucesos poco probables: CUORE (Cryogenic underground Observatory for Rare Events) y ANAIS (Annual Modulation with NaI(Tl)).* PhD thesis, Universidad de Zaragoza, 2002.

[96] M. A. Oliván. Sistema de adquisición de datos para un experimento de detección directa de materia oscura (ANAIS). Master's thesis, Universidad de Zaragoza, 2012.

[97] R. Bernabei et al. The DAMA/LIBRA apparatus. *Nucl. Instrum. Meth. A*, (592):297, 2008.

[98] Heraus Suprasil 2 Grade B Quartz data sheet. http://optics.heraeus-quarzglas.com/en/productsapplications/productdetail_4103.aspx.

[99] D. C. Herrera. Estudio del posible centelleo en cuarzo natural. Master's thesis, Universidad de Zaragoza, 2009.

[100] 3M Vikuiti^{TM} Enhanced Specular Reflector Film data sheet. http://www.3m.com/.

[101] Electron Tubes Limited. http://my.et-enterprises.com/pdf/9302B.pdf.

[102] Hamamatsu. http://sales.hamamatsu.com/en/products/electron-tube-division/detectors/photomultiplier-tubes/part-r6233-100.php.

[103] D.S. Akerib et al. An ultra-low background PMT for liquid xenon detectors. *Nucl. Instrum. Meth. A*, 703:1–6, 2013.

[104] A. Wright et al. The DarkSide Program at LNGS. *arXiv.org*, arXiv:1109.2979, 2011.

[105] Hamamatsu. http://sales.hamamatsu.com/assets/pdf/catsandguides/p-dev_2012_TOTH0020E02.pdf.

[106] R. Bernabei et al. Performances of the new high quantum efficiency PMTs in DAMA/LIBRA. *Journal of Instrum.*, 7:P03009, 2012.

[107] F. Alessandria et al. Validation of techniques to mitigate copper surface contamination in CUORE. *arXiv.org*, arXiv:1210.1107, 2012.

[108] D. Fortuño. Instrumentación electrónica asociada a un experimento de detección de materia oscura. Master's thesis, Universidad de Zaragoza, 2013.

[109] A. Alessandrello et al. Measurements of internal radioactive contamination in samples of roman lead to be used in experiments on rare events. *Nucl. Instrum. Meth. B*, 142:163–172, 1998.

[110] Canfranc Underground Laboratory. http://www.lsc-canfranc.es/en/.

[111] A. Morales et al. Particle dark matter and solar axion searches with a small germanium detector at the Canfranc Underground Laboratory. *Astrop. Phys.*, 16:325–332, 2002.

[112] S. et al. Cebrián. First results of the ROSEBUD dark matter experiment. *Astrop. Phys.*, 15:79–85, 2001.

[113] S. Cebrián et al. Bolometric WIMP search at Canfranc with different absorbers. *Astrop. Phys.*, 21:23–34, 2004.

[114] J. Amaré et al. Light yield of undoped sapphire at low temperature under particle excitation. *App. Phys. Lett.*, 87:264102, 2005.

[115] Y. Ortigoza et al. Energy partition in sapphire and bgo scintillating bolometers. *Astrop. Phys.*, 34:603–607, 2011.

[116] N. Coron et al. Measurement of the L/K electron capture ratio of the ^{207}Bi decay to the 1633 keV level of ^{207}Pb with a BGO scintillating bolometer. *Eur. Phys. J. A*, 48:89, 2012.

[117] A. Morales et al. A search of the neutrinoless decay of ^{76}Ge to the first excited state of ^{76}Se in the Canfranc tunnel. *J. Phys. G (Nucl. Phys)*, 17:211, 1991.

[118] C. Sáenz et al. Results of a search for double positron decay and electron-positron conversion of ^{78}Kr. *Phys. Rev. C*, 50:1170–1174, 1994.

[119] C. E. Aalseth et al. IGEX ^{76}Ge neutrinoless double-beta decay experiment: Prospects for next generation experiments. *Phys. Rev. D*, 65(9):092007, 2002.

[120] J. Argyriades et al. Results of the BiPo-1 prototype for radiopurity measurements for the SuperNEMO double beta decay source foils. *arXiv.org*, arXiv:1005.0343, 2010.

[121] A. Marchionni et al. ArDM: a ton-scale LAr detector for direct Dark Matter searches. *arXiv.org*, arXiv:1012.5967v1, 2010.

[122] V. Álvarez et al. NEXT-100 Technical Design Report. Executive Summary. *arXiv.org*, arXiv:1202.0721, 2012.

[123] C. Pobes. *Optimización de la respuesta de un sistema multidetector de cristales de centelleo para un experimento de materia oscura (ANAIS)*. PhD thesis, Universidad de Zaragoza, 2006.

[124] R. Brun and F. Rademakers. Root - an object oriented data analysis framework. In *Proceedings AIHENP'96 Workshop, Lausanne, Sep. 1996*. Nucl. Instrum. Meth. A 389 (1997) 81-86. `http://root.cern.ch`.

[125] M. Morhac et al. Identification of peaks in multidimensional coincidence γ-ray spectra. *Nucl. Instrum. Meth. A*, 443:108–125, 2000.

[126] Genitron AlphaGUARD. http://www.genitron.de/download/ag_fb_gb_01_a4.pdf.

[127] Nucleide. http://www.nucleide.org.

[128] J. B. Birks. *The Theory and Practice of Scintillation Counting*. Pergamon Press Ltd., 1964.

[129] P. Dorenbos et al. Non-proportionality in the scintillation response and the energy resolution obtainable with scintillation crystals. *IEEE Transactions on Nuclear Science*, 42:2190, 1995.

[130] A.J.L. Collison et al. The fluorescent response of NaI(Tl) and CsI(Tl) to X rays and γ rays. *Proceedings Physical Society*, 81:883, 1963.

[131] L.R. Wayne et al. Response of NaI(Tl) to X rays and electrons. *Nucl. Instrum. Meth. A*, 411:351, 1998.

[132] L.F. Requicha Ferreira et al. Energy non-linearity effects in the response of ionic crystal scintillators to X rays with energy in the region of the K absorption edges: experimental results. *Nucl. Instrum. Meth. A*, 516:486, 2004.

[133] T. Tojo. Nonlinear scintillation response of thin NaI(Tl) crystals. *Nucl. Instrum. Meth. A*, 238:153, 1985.

[134] Kfir Blum. DAMA vs. the annually modulated muon background. *arXiv.org*, arXiv:1110.0857, 2011.

[135] Enrique Fernández-Martínez and Rakhi Mahbubani. The Gran Sasso muon puzzle. *arXiv.org*, arXiv:1204.5180v2, 2012.

[136] D. Nygren. A testable conventional hypothesis for the DAMA-LIBRA annual modulation. *arXiv.org*, arXiv:1102.0815, 2011.

[137] R. Bernabei et al. No role for muons in the DAMA annual modulation results. *arXiv.org*, arXiv:1202.4179v3, 2012.

[138] A. Bettini. http://benasque.org/2012imfp/talks_contr/294_Betini.pdf.

[139] S.C. Kim et al. Low energy fast events from radon progenies at the surface of a CsI(Tl) scintillator. *Astrop. Phys.*, 35(12):781–784, 2012.

[140] P. Lecoqet al. *Inorganic scintillators for detector systems*. Springer-Verlag Berlin Heidelberg, 2006.

[141] R. Hofstadter. The detection of gamma-rays with Thallium-Activated Sodium Iodide crystals. *Phys. Rev.*, 75:796, 1949.

[142] J.C. Robertson and J.G. Lynch. The luminescent decay of various crystals for particles of different ionization densities. *Proc. Phys. Soc.*, 77:751, 1961.

[143] F.S. Eby and W.K. Jentschke. Fluorescent response of NaI(Tl) to nuclear radiations. *Phys. Rev.*, 96:911, 1954.

[144] J.S. Schweitzer and W. Ziehl. Temperature dependence of NaI(Tl) decay constant. *IEEE Trans. Nucl. Sci.*, 30:380, 1983.

[145] S. Koički et al. The investigation of the 0.15 s phosphorescent component of NaI(Tl) and its application in scintillation counting. *Nucl. Instrum. Meth.*, 108:297, 1973.

[146] C.R. Emigh and L.R. Megill. The long-lived phosphorescent components of thallium-activated sodium iodide. *Phys. Rev.*, 93:1190, 1954.

[147] et al. P. Doll. Pulse shape discrimination with a large NaI crystal. *Nucl. Inst. Meth. A*, 285:464, 1989.

[148] J.C. Barton. Assessment of heavy radioactive elements in sodium iodide scintillators. *Appl. Rad. Isot.*, 47:997, 1996.

[149] et al. K. Ichihara. Highly sensitive measurement of α-rays in NaI(Tl) scintillators by pulse shape discrimination with charge-sensitive analog-to-digital converter. *Nucl. Instr. Meth. A*, 515:651, 2003.

[150] et al. C. Bacci. WIMPs search with low activity NaI crystals. Preliminary results. *Phys. Lett. B*, 293:460, 1992.

[151] et al. D.R. Tovey. Measurement of scintillation efficiencies and pulse-shapes for nuclear recoils in NaI(Tl)/and CaF_2(eu) at low energies for dark matter experiments. *Phys. Lett. B*, 433:150, 1998.

[152] et al. V. Kudryavtsev. Characteristics of alpha, gamma and nuclear recoil pulses from NaI(Tl) at 10-100 kev relevant to dark matter searches. *Phys. Lett. B*, 452:167, 1999.

[153] Hamamatsu. `http://www.hamamatsu.com/us/en/index.html`.

[154] J. Pradler et al. On an unverified nuclear decay and its role in the DAMA experiment. *Physics Letters B*, 2013.

[155] S. Agostinelli et al. GEANT4 a simulation toolkit. *Nucl. Instrum. Meth. A*, (506):250–303, 2003.

[156] S. Cebrián et al. Background model for a NaI(Tl) detector devoted to dark matter searches. *Astrop. Phys.*, 37:60–69, 2012.

[157] V. Kudryavtsev et al. The expected background spectrum in NaI dark matter detectors and the DAMA result. *Astrop. Phys.*, (33):91–96, 2010.

[158] S. Cebrián et al. Perforances and prospects of the rosebud dark matter search experiment. *Astrop. Phys.*, (10):361, 1999.

[159] D. Jordan et al. Measurement of the neutron background at the Canfranc Underground Laboratory. *Astrop. Phys.*, 42:1–6, 2013.

[160] Saint Gobain. `http://www.saint-gobain.com/en`.

[161] M. Resano et al. On the possibilities of high-resolution continuum source graphite furnace atomic absorption spectrometry for the simultaneous or sequential monitoring of multiple atomic lines. *Spectrochimica Acta Part B*, 66:321–328, 2011.

[162] Perkin Elmer. `http://www.perkinelmer.com/Content/RelatedMaterials/Brochures/BRO_WorldLeaderAAICPMSICPMS.pdf`.

[163] Galbraith. `http://www.galbraith.com/`.

[164] C. Cuesta. Optimización de los detectores del experimento anais. Master's thesis, Universidad de Zaragoza, 2009.

[165] The Berkeley Laboratory Isotopes. `http://ie.lbl.gov/education/isotopes.htm`.